CHARACTERISATION OF TABLETS AND ROLLER-COMPACTED RIBBONS WITH TERAHERTZ TIME-DOMAIN PULSED IMAGING

L. Alex Wall

Leicester School of Pharmacy, De Montfort University

Date: *06/2015*

PhD Thesis

In partial fulfilment of the requirements for the degree of

Doctor of Philosophy

Submitted to

De Montfort University

Declaration

I, Alex Wall, confirms’ that the content presented within this thesis is of my own work. I confirm that information derived from other sources has been indicated accordingly in this thesis.

Abstract

The pharmaceutical process of dry granulation using roller-compaction (DG/RC) is effectively a non-batch based procedure orientated to deliver a continuous stream of material free of a pre-defined batch-size with reduced plant equipment/scale-up R&D resources and an enhanced work-throughput, particularly suitable for moisture sensitive formulation. The desirable accreditations of DG/RC are many; yet by the nature of a more flexible approach than (i.e. wet-granulation), it must be highly monitored and controlled to accomplish higher-throughput rates and reduced 'static' material testing stages. To monitor rapidly and in-line with production, pre-granulated ribbons of RC (which highly correlates to the post milled granulates), terahertz time-domain spectroscopy (TDS) is used to elucidate the key physical attributes of post-compression density and thickness uniformity, key to end-product consistency.

Invariably a great number of conditions apply to DG/RC (*viz*: System design, material characteristics, environmental and unit configuration), although widely regarded as the key processing parameters (PP's) are roll-pressure and roll-gap [1-4]. The target of the study is to derive a strategy to position TDS as PAT to DG/RC.

Two terahertz time-domain TD methods of a conventional transmission setup and reflection (TPI) THz analysis are used on standards of glass slides for verifying the interpretational foundations of the TD methods. Achieving RI/thickness error-discrepancies +2.2 to -0.4% c.f. literature ([150]) values provides foundations to test the solid-fraction ratios of pharma tablets with regard to RI's being surrogate values to SF/path-length ($R^2 = 1$). Combining transmission principles to the portion of reflected EMR removes the pre-requisite for RI or path-length knowledge, giving +1.5 to +2.4% RI agreement (vs. frequency-domain attained results) thus enabling thickness estimations to be above 95% against physical micrometre judgement in all models. Augmentation of the TD methods, refined in *Experimental chapter 2* ,then chiefly focuses on TPI as the principle THz-TD method (as the most ideal tool for PAT) for adopting the RI measures for ribbon uniformity analysis in *Experimental chapter 4* in an off-line environment again resulting in RI and thicknesses < 5 error of known parameters of thickness and further use of RI as a proxy porosity equivalent to gas pycnometry. Elucidated in the work are the limitations encountered with tablets and RC's, data interpretation of industrial considerations. *Experimental chapter 3* diverges from RI to differentiate thickness in-order to assess the FD transmission for non-destructive mechanical assessment. This demonstrates a clear relationship between compaction force and the surrogate value for density, following a linear trend below a certain threshold of force. The 'threshold' value is observed for less massive tablets, snd concluded is that the mechanistic interplay and permanent (plastic) consolidation is greater in instances where compaction-force increases proportionally with target-fill weights, and thus the various behaviour of MCC to stress.

Table of Contents

List of Figures

List of Tables

List of abbreviations and terms

General terms

THz = Terahertz, 10^{-12} *Hz*
RI, n_0 = Refractive index in free-space, *c (m/s)*
TPI = Terahertz pulsed imaging
TDS = Time-domain spectroscopy
DG/RC = Dry granulation/roller-compaction
OD = Optical time-delay, *ps*
c_t = Speed of light during transmission, *m/s*
I_R = Intensity (following reflection), *a.u.*
ps = Picoseconds, 10^{-12} *s*
ms = Microseconds, 10^{-6} *s*
$\tilde{v}$ = Wavenumber, cm^{-1}
EMR = ElectroMagnetic Radiation

TPS = Terahertz pulsed spectroscopy
RI_T, n_t = Rerfrative index ratio to RI_0/n_t
v, f = Frequency, *Hz*
FDS = Frequency-domain spectroscopy
a.u. = Arbitrary units
c or c_0 = Speed of light in free-space: (2.998×10^8), *m/s*
I_0= Intensity (detected), *a.u.*
I_T= Intensity (following tranmission), *a,u.*
nm = Nanometres, 10^{-9} *m*
π = 3.141,592
fs = Femtoseconds, 10^{-15} *s*
FFT = fast Fourier Transformation

Method abbreviations

TPI= THz-Time-Domain Reflection Imaging.
TDT-SD = THz-Time-Domain Transmission optical signal delay-time, *ps.*
FDT = THz-Frequency-Domain transmission spectroscopy.
$E(\tilde{v})$= Detected *E-Field* recorded at detection antennae, *a.u.*

THz-TD/TDT= THz-Time-Domain optical delay.
TD-ID = THz-Time-Domain Transmission optical internal delay-time, *ps.*
$E_0(\tilde{v})$ = Detected *E-Field* of a reference profile at detection antennae, *a.u.*

Geometry/Force

Thk^n = Substrate thickness, *mm*
SF = Solid-fraction % (*air/solid ratio)*

ρ , density, mg/mm^3 or g/cm^3
F, Newton's (*mass × area ÷ time*), *N/m*

Regulatory/Industry terms

PAT = Process analytical tool.
ICH = International conference of harmonisation.
CQA = Critical quality attributes.

QbD = Quality by Design.
CPP's = Critical control parameters.
PPs = Process parameters.

Off-line = Samples of the processed material are removed following a critical process and analysed while the material-stream is quarantined, pending results.
At-line = Operators remove material from sampling ports in-process and present the sample for analysis to determine quality in respect to the MA.
In-line = Measurements are made in the process stream and analysed in real-time by operators.
On-line = A sampling system that examines the processed material in real-time using PAT and knowledge-based systems to validate or constrain CPP's for optimal product quality.

Optical physics

E = Electric-Field, *V/m*
B = Magnetic-flux density, $(v\text{-}s)/m^2$
σ = Conductivity, A/m^2
ω = Angular frequency vector, $\omega = 2\pi f$
κ = Angular wavenumber, $1/\lambda$
α = Absorbance coefficient, *a.u.* $[\text{Log}(E(\tilde{v})/E_0(\tilde{v})]$
∇ = Curl operator.
ρ_ϕ = Free charge density, $Coulombs/m^3$
$\partial/\partial t$ = Derivative with time.
$v(t)$ = Charge carrier velocity.

D = Electric displacement field, $Coulombs/m^2$
H = Magnetic-Field, *A/m*
G_τ = Optical carrier generation rate, *Siemens/t*
$T(\tilde{v})$= Transmittance, *a.u.* $[E(\tilde{v})/E_0(\tilde{v})]$
J_f = Free current density, A/m^2
ϕ = Unwound transmission phase, *radians*
N = carrier charge density, m^{-3}
q, Q = Charge, *Coulomb*
γ = Dimensional property of the photo-induced semiconductor
m^* = Charge carrier mass.

μ = Permeability, *Henries/m* [$\mu_0 = 1.26\times10^{-6}$ *Henries/m*]
ε = Permittivity, *Farads/m* [$\varepsilon_0 = 8.85\times10^{-12}$ *Farads/m*]

Mathematical operators

$\Re$ = Real part of a complex number
$z/z^\star$ = Complex number/ complex conjugate to $z^\star$

$\Im$, i = Imagery part of a complex number
$|x|$ = Absolute, modulus value of x

Acknowledgements

In comprehendible is the nature of *chaos*. Seemingly arising to allow growth of language, shapes, all in order to express amongst ideas between individual minds. Aside from the mystical, duly and truly tangible acknowledgements must be spread between an inordinate number of people who have interjected knowledge, direction, inspiration, and illumination. And to the people who have curbed my vaudeville mood from a seemingly vision of a brooding Victorian slate-grey sky to a more facetious swing their friendliness. Thankyou.

Citation utters upon a large number of key aides during this enjoyable period of growth including my supervisory team. Working together with the thought-provoking and forever inquisitive Dr Geoff Smith, mention is made in his belief in me with this investigative project and to Dr Irina Ermolina; stemming from them a grounding I have founding in empirical research, and fruition necessary to implement an idea and question unexpected hypothesises. Accreditation is also made to DMU for funding a research scholarship and the initial funding by the EMEA (2009). Thanks are made to Kazem Nazari, Sohail Arshad, Amee Pandya, and specific acknowledgement must be made to Martin Müeller-Holtz for his computational, level-headedness and mathematical assistance.

Helping to absorb the strain of this study I would also like to wish my long-suffering partner Scarlett Q, my parents of their supporting nature (and the plain tolerance/patience of an often buzzing hornet's nest) and all souls along the way. To all, gratitude is wished and appreciation off all the opportunities that will probably stand indebted, irrevocably.

Part I

Introduction of concepts

The tablet accounted for 80% of all manufactured dosage forms at the turn of the century [5] and represents a highly acceptable and easy method for patients to administer drugs (most often orally). Popularity can also be attributed to safety, where tablet production can arguably, be a more scrutinized process and has been the conventional method (historically) established, building knowledge boundaries (e.g. chemical stability/dosage etc.) compared with relative, newer methods. Tablet manufacturing has rarely consists of a single processing step, such as compression of an active pharmaceutical ingredient (API) into a dosage vehicle. For example, if the API constituents a minor physical percent of the vehicles mass, rendering impractical device size for direct administration.

Numerous physicochemical and mechanical issues need to be considered to achieve an exact drug dosage delivery system for consistent and safe release within a specific region of the gastro-intestinal tract [6]. Inevitably, API vehicles have grown with a knowledge base of formulation, bio-pharma/co-dynamics, API/excipient compatibility to multi-component delivery vehicles [5-8], to match excipients for reproducible, cost-efficient product of optimally pre-defined specification.

Undesirable properties attributed to any composite of the dosage vehicles character must be understood from a myriad of properties. For instance, from a formulation standpoint[1], an API with low bulk density and flowability, volumetric filling uniformity. Given in *Table 1,* a general common, non-exhaustive inclusion of excipients can partially/fully be resolved[2] [9].

---

[1] A formulation is sometimes defined as the method to fulfil the requirements warranted for successful dosage form design, yet in most pharmaceutical senses a formulation is more indicative of the ingredients and the proportion of these in the dosage unit.

[2] The classes of excipients are not necessarily limited to only one function within the formulation. Multi-functional excipients may for instance exist as filler/diluents whilst displaying good disintegrant and binding behavior (e.g. microcrystalline cellulose).

Table 1: **Potential problems of tableting a pure drug substance and some common formulation solutions.**

Possible undesirable drug characteristics	Classes of excipients	Reconciliatory Role
Poor flow	Fillers/ Diluents/ Bulking agents	Agent improves the collective ability of the blend to flow and fill die spaces equally, as is so important with volumetric-metering
Low dose requirement, potent compound		A means to increase the volume/size of the end-point tablet for consumer practicality. Also, the act of *dilution* aids to reduce the statistical propagation of poor mixing and effectively broadens the assay-content specification limits in parallel to the scale-of scrutiny.
Poor compressibility		Agent will possess good compressibility giving more robust tablets
Segregation (with more than one powder)		Now that a multi-component blend is required, size/ shape and density mismatches of particles can lead to de-mixing. Careful choice of excipients can partially reduce this.
Insufficient ability of the compact to breakup to relinquish constituent particles in the GI tract	Disintegrating agents (*disintergrants, wetting agents)*	Disintergrants ordinarily absorb liquid from the GIT to cause the tablet to swell and disentangle to control dissolution of the API.
		To provide agents to improve the solubility of the active in the GIT
Many multi-component blends will now compact rigidly. Yet, may adhere to punch faces and cause frictional ware during tablet expulsion and possible capping/lamination	Lubricants	To reduce excessive frictional forces between the production machinery, lubricants are used in low concentrations and are often fragile in nature. Effective blending and other processes exploit this and allow fine coating of particles to facilitate lubrication.
Following granule formation non-uniform surfaces can potentially hinder granule flow	Glidants	Common to roller-compacted formulations glidants are added to improve the flowability of pre-compressed powder; essentially reducing friction among particles[7] .
Blend does not agglomerate or respond to densification steps to readily form granules – useful to combat flow/shape/size/density variation	Binding agents	The function of binders is to agglomerate excipients and API's to form stronger granules with a narrow range of particle size distribution, size, density and thus products of acceptable friability. In dry granulations these are usually plastic binders, with some brittle nature [8]

Conventionally practised unit processing stages include milling, drying, blending, granulation (giving an intermediary product – pertinent to capsules [9]) before finalising stages has been summarised in *Table 2.* As with each process, it's purpose is crucial to the formulator/MA [6, 10].

Table 2: **Common unit processes.**

Unit operations / Handling	Description	Requirement / Reconciliation
Inventory storage	Holding components at specific temperatures and relative humidity can positively influence flowability and stability (i.e. for hygroscopic materials).	To reduce agglomeration and instability.
Milling and screening / Fine bulk solid handling	The initial blend is frequently screened and milled to influence the final blends flowability and segregation. Selection of milling type, speed and time aswell as screen size and feed rate are fundamental considerations	Free flowing and reduction of segregation / Control of particle size, shape and density
Blending	Selecting a type of mixer of defined geometry the process time and vigour of the mixing is controlled to achieve uniform distribution of the active.	Final blending: To improve the distribution of excipients/actives and enhanced flowability of blend.
	Incorporating specific mixing methods the formulation is mixed a number of times with addition of certain excipients. For example, additional lubricants are often blended post granulation in order to effectively coat the granules before compaction. Addition before this point would result in agglomeration into the granule, reducing its role in later processing.	Ordered (pre/intermediary) blending: Typically utilised in forming granulated products to again aid flowability and uniformity.
Granulation (often followed by drying, milling and screening)	Adhering small particles into larger permanent masses, the individual physicochemical properties of each component are essentially normalised into a collective bulk.	As a size enlargement and densification process it is designed to improve material properties of the bulk blend to improve particle uniformity. Whilst also agglomerating 'packets' of blended powder into granules, flowability is increased and downstream segregation is reduced.

Compaction	Compaction into tablets can be achieved through a number of tableting machine types at various speeds and compression appliance.	To deliver a useful product of correct pharmacologically active product that has a durable mechanical strength.
Coating	Tablets can be coated for numerous reasons and are typically coated with polymeric or sugar based materials containing a dye, or even active component in a rotary drum with spraying apparatus or dipped.	Aesthetic, taste masking, stability and biological target control.

Particles of varying size, density and morphology are major issues causing poor flow and segregation [1], and orders for the blend to be agglomerated by granulation [11, 12]. In a report by Shangraw a value of 95% of tablet and capsule manufacturing lines incorporate a granulation step [13]. Perry's *Chemical Engineering Handbook*, provides a definition of granulation as a stage of processing "whereby small particles are gathered into larger, permanent masses in which the original particles can still be identified" [14, 15]. In contrast to the primary powder, benefits provided by granulation are given in *Table 3*.

Table 3: **Benefits provided by granulation.**

Granulation provides:
A blend of powders of differing size/morphology/densities will have a potential to de-mix or segregate during later processing and/or transportation between processing stages.
The flow rate of individual powders are likely to differ (particularly true for particle sizes less than 100 µm [1]) therefore potentiating non-uniform volumetric filling of tablet die wells which will substantially affect tablet size/weight and component content. This is critical to unit-to-unit API concentration (w/w).
Fine particles can present a contamination risk to additional processes and importantly staff (i.e. of air-borne fines).
Poor tabletabilty/compression character: increasing the solid fraction will in some cases improve bonding capacity and particle cohesion of agglomerates.

Granulation methods can be divided into two major types: wet granulation (WG) and dry granulation (DG). The principle difference between the two methods is the mechanism by which the particles are agglomerated. Wet granulation requires a liquid binding solution to form inter-particulate bridges, where after granules are achieved by a drying stage. Particulate agglomeration using DG is otherwise created by the application of force alone. Having excluded the use of liquid binding agents, DG becomes particularly attractive when processing formulations sensitive to water, heat (the latter being requirement of the drying stage) [1], and in regard to the complete production-process, requires fewer unit processes. Highlighted in *Figure 1*, the usual manufacturing steps through wet or dry granulation are compared. However, WG remains the dominant method and was. the most commonly used agglomeration method at the turn of century[3][16].

DG using roller-compaction (RC) is a two stage process where pre-blended material is drawn between two counter-rotating rolls and forced through a narrow gap to create cohesive compacts in the form of flakes, strips or ribbons. Thereafter, these are typically milled into granules and conveyed to a secondary (low-energy) blending process to lubricate the granules before further processing [17]. RC has become the preferred DG technique in modern manufacturing to the only other *dry* method; namely *slugging*[4] [18]. Highlighted in *Table 4*, comparisons of WG and DG by RC are listed.

Table 4: **Unranked list of benefits provided by roller-compaction as an alternative to conventional wet granulation processing.**

Eliminates aqueous and solvent granulating.	Facilitates continuous manufacturing.
Eliminates heat-induced degradation[5].	Roller-compaction is more scalable.
Simplifies processing.	Requires less man hours to operate.
Uses minimal energy to operate.	Reproduces consistent particle density.
Uses less raw materials.	Does not require explosion proof room/equipment.
Usually reduces manufacturing times.	Minimal need for powder lubricant [19].

There exists several reasons why the pharma industry has been reluctant to move away from WG to DG in the past. One reason often cited is that the current regulatory frameworks are rigid and adverse to the introduction of processes which could not offer acceptable levels of process control and consistency [20]. Another reason specific to RC by DG is the inability to often produce a narrow granule size distribution, the inability to cope with poor flow and variable density with the bulk blend [21, 22].

A recent increase in the uptake of RC equipment has enabled manufacturers to identify and develop new solutions to some of the causal issues with DG/RC. These include: batch-to-batch

---

[3] With more than 70% of the global industry's granulated output being produced with wet methods.

[4] Slugging was a popular dry-granulation technique in the 1950's-70's whereby the primary powder blend was filled into a large die, compacted under extreme pressure and then hammer-milled. Today slugging is referred to as a 'relic' in modern manufacture because of low processing throughput and inconsistency.

[5] Although it is recognized that heat is conveyed during compaction, and thus limiting this alternative [miller 2005 book]. Drying operations invariably exceed those of frictional interactions (i.e. RC can generate a temperature increase of up to 30°C [Singh, 2012]).

variability and insufficient product mechanical strength, and has been addressed through integration of instrumental and mechanical feedback technologies, providing responsive control of the process [18]. However, certain formulations cannot be consistently produced by DG.

The manufacture of tablets *traditionally* relies on a batch procedure and separates production into a routine of discrete stages. The assessment of critical quality attributes (CQA's) unique to the formulation are evaluated within those periods of inactivity between processing stages. This easily permits data to be acquired on a step-by-step basis to evidence that the quality of a product and its intermediates lie within the specification limits of the Marketing Authorisation, allowing the progression of material to the subsequent stage [23]. The major advantage of batch processing thus, easy material sampling/analysis, yet inter-stage process testing inherently lessens the transition time of worked material into the final product.

Batch manufacture does not generally allow linear process scale-up[6] due to the singular task ascribed to the equipment's in performing one task [24]. It is not often *linear* for example, to simply re-design larger equipment (in the x, y and z dimensions) and transpose other CPP's such as the speed of the impellor in a high-shear granulator, as one does not necessarily end up with consistent quality attributes for the product or its intermediates [25, 26]. The technicalities of batch-orientated manufacture scale-up are usually high when increasing production capacity in batch-orientated manufacture because of significant capital investments in plant, energy, human resources and process optimisation [23]. Scalability is commonly less of an issue, because the resultant batch size can be adjusted simply altering by altering the processing time, whilst retaining the same equipment scale and conditions. Obviating the need for scale-up is partially true for semi-continuous batch manufacturing too, as running a large number of small, equivalent operations will reduce the need of equipment scaling in-order to match the product

---

[6] Scaling-up a process from one machine to another whilst simultaneously increasing product capacity and keeping product properties equal.

throughput of one batch/pot processing [23]. In comparing the three manufacturing modes (*See Figure 1*) material-throughput output per unit time is illustrated. In a truly continuous production scheme (*See Figure 1a*) the product output is proportional to the production-time and so a batch size does not need to be pre-determined. Rather, the output requirement is met when sufficient time has elapsed (*See Figure 1b*). For semi-continuous processing (*See Figure 1c*), the product output gradually increases because the total batch size is sub-divided into a defined number of sub-batches [24], benefiting from a reduced scale-up routine. For instance, to compensate for the reduced output/unit-time of a small-scale continuous process, the process can be run over an increased time to supply feedstock to non-continuous processes in the cycle.

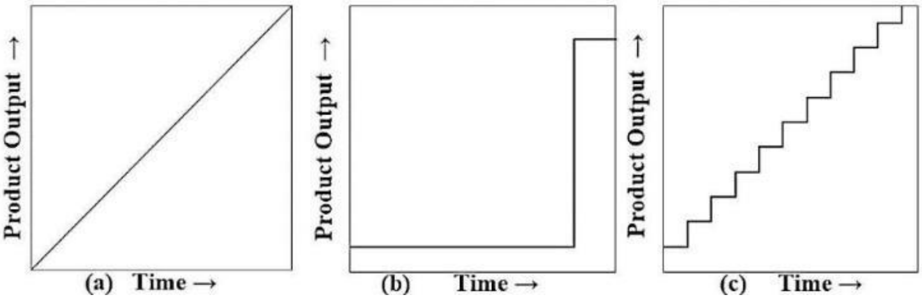

Figure 1: **Three modes of operation (a) continuous, (b) batch, and (c) semi-continuous.**

In evolving conventional batch-orientated manufacturing into a continuous one (as recognised by the regulatory bodies, such as the *FDA*, and the pharmaceutical industry) [27, 28], CQA requirements must be monitored in-line, with active and rapid analysis and feed-back control systems are necessary. Relying on timely in-line material measurements, interpretation of key characteristics against that of a knowledge-based data analysis system can either serve to verify that the process is between parameter limits (defined by the regulatory file) or if not, signal for rapid changes to the causal process parameters (i.e. responsive control of the process) [20, 29]. This has the potential to deliver:

1. Quantitative lowering of product failure.
2. Optimal material quality and performance attributes.
3. A time reduction of end-product testing.

4. Continued satisfaction of regulatory and MA constraints.

Continuous manufacture also provides a significant opportunity to reduce initial equipment and site capital costs, products handling (and thus product contact surfaces and cleaning), energy consumption, manufacturing time and, QA and validation systems (*Table 5* and *Table 6*).

Table 5: **Typical economic projections associated with (semi)/continuous RC dry granulation contrasted against a conventional batch-orientated wet granulation. Accessed by Gerteis® (2011) and reproduced from source [27].**

Activity	Unit Cost	Wet Granulation	DG/RC	Saving
Capital equipment cost		£1,600*k*	£650 *k*	£950 *k*
Building GMP area*	£9000/m^2	80 m^2	10 m^2	£620 *k*
Building technical area*	£1620/m^2	50 m^2	4 m^2	£60 *k*
Installation and commissioning*		£400 *k*	£40 *k*	£360 *k*
Scale Up		2 months	5 days	
Process Start Up		3 months	10 days	

Indirect cost benefits and potential savings	
Yield Savings	>60%
QA Saving	50%
Operator labour	50%
Electricity	70%
Compressed Air	80%
Potable Water	80%
Purified Water	80%

* Nominal market values have been used based on 200 Kg batch processed in 2 hours.
Figures will vary depending on application and configuration.

Table 6: **Included here to reduce bias for cost comparisons made by Gerteis® only, similar comparisons were made by the Fitzpatrick RC manufacturer.**

Activity	Wet Granulation	DG/RC
Capital equipment cost	Up to £800k	£240k –£280k
Process time	4 hours for 300 kg or 8 hours for 600 kg (2 batches)	8 hours for 600 kg
Energy consumption	About 80 kW for the total installation	Max 10 kW
Space/building requirements	135 m^3	36-50 m^3
Cleaning time	8 hours	4 hours
Labour input	12 hours	6 hours
Environmental in case of WG with solvents	Solvent recovery system or discharge (large investment)	Not required (dry)
Installation	Several weeks, complicated (costly)	Max. 1 week (simple)
Validation cost	Several processes (complicated)	Few parameters (simple)

The *FDA*'s quality initiative [30], incorporates a PAT framework for innovative to develop robust processes and efficiency gains. For instance, PAT assessment of blend uniformity, granular moisture and particle size distribution has been heavily researched and has invariably become adopted with the use of near-infra red spectroscopy (NIRS) in early stage manufacturing development [20, 27, 28, 31-35]. Similarly, other analytical techniques have been evaluated for wide ranging PAT applications in the literature [35-45]. However, firm QbD strategies to ensure desired levels of product quality have yet to be fully realised in-line to the process to achieve CQA the necessary control and feed-back control mechanisms [31].

DG/RC formulation and manufacturing currently rely on experience and empirical design of experimentations (DoE) to successfully fulfil crucial product quality indicators [27], and usually aligned with the requirements listed in *Table 7*. DG/RC is well positioned to integrate the guidance from the ICH for QbD and PAT innovations as a continuous agglomeration process with reduced scale-up, reduced resource usage [21, 46]. However, there is no well-established QbD type methodology to account for raw material/feed variation for efficient and controlled operation of RC process parameters on current instrumented equipment [27].

Table 7: **Requirements for successful roller-compaction as defined by sources [27, 47, 48].**

	Desirable steps to DG/RC.
i)	Uniform and continuous supply of powder to slip region/feeding zone.
ii)	Powder entering the slip and feeding zones must be wholly conveyed to the narrowest part of the roll gap.
iii)	Compaction pressure should be distributed as uniformly as possible over the entire roll-gripped mass.
iv)	Vacuum de-aeration must be adequately and effectively distributed before the nip roll region.
v)	Uniform pressure maintenance on the feedstock, independent of the fluctuating powder flow into the rolls, to maintain a consistent compact.
vi)	Systems to minimise primary powder leakage from the side of the rolls and ineffective compaction of feedstock.

It is the aim of this work to deliver a practical series of methods to evaluate the distribution of density and thickness of dry-granulated/roller-compacted ribbons using terahertz time-domain spectroscopy. These methods need to consider the practical implications of an industrial setting in order to serve as an in-line PAT tool capable of real-time feedback.

1 Dry granulation

Dry granulation (DG) can be characterised as a pressure-agglomeration process to create larger and denser cohesive forms (e.g. flakes, briquettes or ribbons) and are thereafter broken-up with a sizing technique, and usually screened to a desirable granule size [49].obviating the use of liquid binders [50]. During DG primary powder particles are agglomerated through the application of pressure It is an example of a particle-bonding process, where the theory of granule bond formation, as described by Miller [51] can be attributed to four key stages:

1. Particle rearrangement.
2. Particle deformation.
3. Particle fragmentation.
4. Particle bonding.

Physical cohesion during these four stages of granule formation specifically include mechanical interlocking, intermolecular/electrostatic bonding and surface-film bonding phenomena [52, 53]. High drug loading for poor compressibility and compaction properties demonstrate the key chief disadvantages of DG/RC because cohesive agglomeration originates from the yield stress alone[7]. Matching process variables/system parameters/setup to a formulation is vital in DG to produce granules of uniform flow, morphology, density and drug content (i.e. narrow CQA’s). By example, the binding agents must be evaluated to provide a mixed elastic, plastic and brittle nature to offer a high surface area under fracture (for particle-bonding and bulk reduction) and plastic deformation to contribute to physical interlocking mechanisms whilst enhancing further

---

[7] This is converse to wet-granulates in which capillary forces are established during the process and solid bridges formed during drying contribute largely to the overall mechanical strength.

compressibility of the granule at the *secondary* compression stage (usually for tableting) [11, 54, 55].

The pharma industry has used DG since the 1940's and favoured slugging until the 1970's [18, 56]. Slugging was carried out with a rotary press under exceptionally high pressures to create compacts of typically 25 *mm* in diameter and *10 -15 mm* thickness. The slugs/briquettes were then usually granulated by hammer-milling for capsule filling, sachets, powders for oral suspensions and tablet dosage forms. The use of this dry granulation method has largely ceased in pharmaceutical production lines for reasons highlighted in *Table 8*.

Table 8: **Unranked table listing the disadvantages of slugging multi-component powder mixes against roller compaction**

i) Poor process control.	vi) Excessive air and sound pollution.
ii) Poor economies of scale.	vii) Increased needs for manufacturing space.
iii) Single batch processing.	viii) Increased use of storage containers.
iv) Low manufacturing throughput per hour.	ix) Increase of logistical resources.
v) Frequent maintenance changeover and high machine maintenance.	x) More time and energy is required to produce 1Kg of slugged compacts rather than roller-ribbons.

The pharma industry has favoured roller-compaction as a DG process as the predecessor of slugging. Stated by Miller, 'roller-compaction is the key technology to future dry granulation' [18], and RC manufacturers have been quick to integrate/adopt new-system technologies to improve the flexibility of the process (for a broader range of formulations) and the precision and operational use of enhanced automation.

2 Roller compaction principles

Roller compaction (RC) is a continuous manufacturing process that can be sub-divided into three distinct sub-processes. Converting (*See Figure 2'1')* the loose powder-blend from a feed hopper to the main physical densification area, (*2*) into cohesive compacts. Thereafter, the compacts (*See Figure 2:3*) are milled into granules and usually screened to obtain the desired particle size [11]. DG/RC:

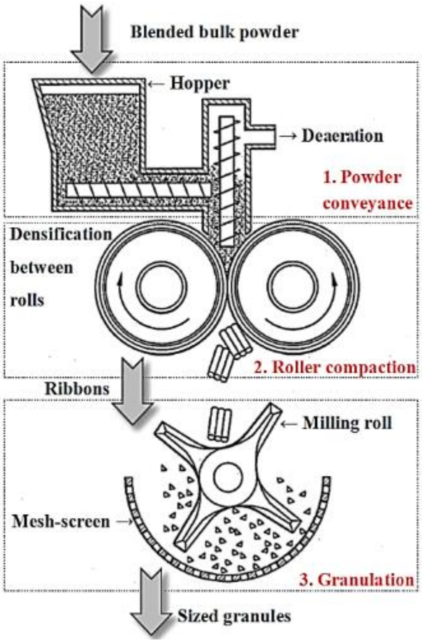

Figure 2: **Schematic representation of roller compaction as a unit-process situated between pre-blending and granulation.**

a) Powder conveyance

The feeding unit is responsible for transporting the pre-blended powder mixture from the pouring hopper to the region between counter-rotating rolls. As the bulk blend approaches the bottom of the hopper, particle rearrangement and powder densification occur (albeit, with very little, gravimetric force [54]).

b) Roller compaction

Compression is applied to the powder feed by two counter-rotating rolls designed to draw the blend towards a decreasingly narrow zone and motions the initial significant stage of rearrangement and densification [3, 19]. At the narrowest region between the rolls, the maximum stress is served. With sustained rotation, continual densification of the bulk powder blend occurs is expelled as ejection of a compacted.

c) Granulation

Granules are produced by milling (or grinding) the compacted material into particles post-compaction. Any remaining ribbons, adhered to the rolls is removed by a scraper in close contact with the rolls (*See Figure 8;* ‘*a’* & ‘*b’*). The compact then falls onto an oscillating wheel (milling-roll) closely situated above a wire mesh-screen at the base of the machine. Granules of a maximum size are formed through attrition between the milling-roll and a curved mesh screen (of equal central angle to the roll). This milling process operates in a similar manner across the known roller-compactors, while the (interchangeable) milling-roll’s surface texture is machine and formulation specific.

2.1 Theories of particle agglomeration

Multiple theories of compression led physical agglomeration of particles exist and also the extent to which each contributes to the resultant mechanical strength; the mechanisms of roll pressing is still not fully understood [57]. Parrott identified three mechanisms of compression bonding [58]:

1. Mechanical bonding arises from elastic, plastic and brittle deformation of individual particles leading to the formation of physically entwined, mechanical bonds.
2. Brittle fracturing during densification can lead to fresh creation of new surfaces and is purported to increase the affinity of intermolecular van der Waals forming from exposed surface ions For instance, particle fracture can create multiple new surfaces and contact points for inter-molecular bonding [51].
3. Parrott’s third theory of liquid-film bonding is less well documented in the literature, but describes creation of a thin moisture film at particle interfaces originating from compression. The existence of a thin liquid film subsequently acts as a binding agent and possible capillary attractions.

Of these three mechanisms, it is the mechanical interlocking which is often cited as the main contributing factor responsible for the cohesive nature of dry granulates.

2.2 Roller compaction equipment and process parameters

A brief overview of the management tools used to identify the CPP's and CQA's of a specific formulation are displayed in *Figure 3*, highlighting the framework of *FMEA* (Failure Mode and Effects management) and DoE (embodied in QbD concepts) in process optimisation.

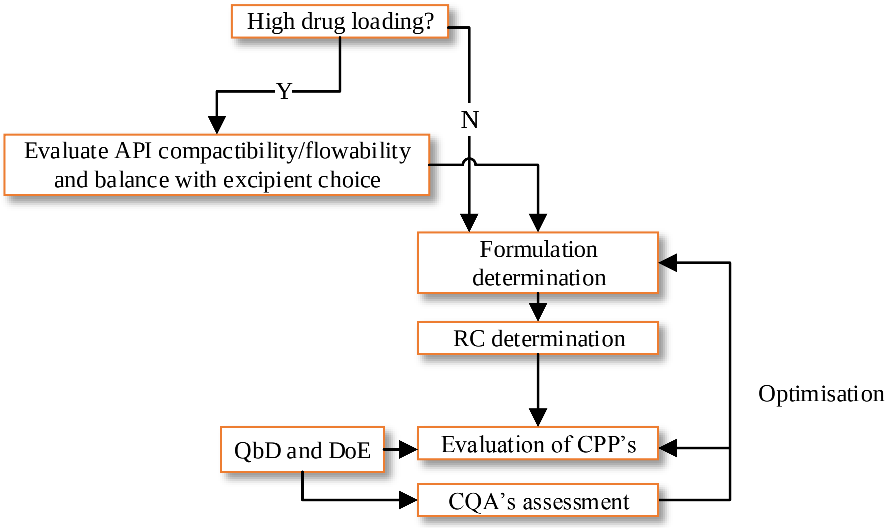

***Figure 3:* A brief flow chart for formulation and process development using roller compaction. Adapted from source [54].**

The chief process parameters of roll-force and roll-speed were identified by *Teng (1999)* as the main CPP's effect ribbon CQA's, while feed-rate is a secondary important consideration [54]. Additionally, *Singh et. al (2011)* states that the inter-relation of the chief CPP's of roll-force and roll-speed to achieve (specifically) uniform ribbon densification are crucial for optimal ribbons [29].

2.2.1 Feeder design

The feeding-configuration is an integral part of the design process and is given great attention in scale-up to not only convey the powder feed equally, but also in a manner to lessen opportunities to variable consolidate and de-mix. [54]. For instance a fully loaded hopper may cause a pressure differential from top-to-bottom, creating a consolidation difference. Conversely, the blend in the higher-regions of the hopper have a greater residence time in-order for particle rearrangement to occur if the blend is not continuously agitated.

Two distinct types of feeding systems are used to achieve this: gravity feeding (*Figure 5a)* and auger type systems (*Figure 4*) [59]. Transportation of the powder to the rolls, meanwhile are shown in *Figure 4*; *a-d*. Some RC's use a combination of these systems and different angular configurations. For example, in *Figure 7*, Gerteis's Macro-Pactor uses gravity to feed onto a horizontally mounted auger which then meets a diagonally mounted auger to meet the slip-zone (*See Figure 6 - Figure 7*).

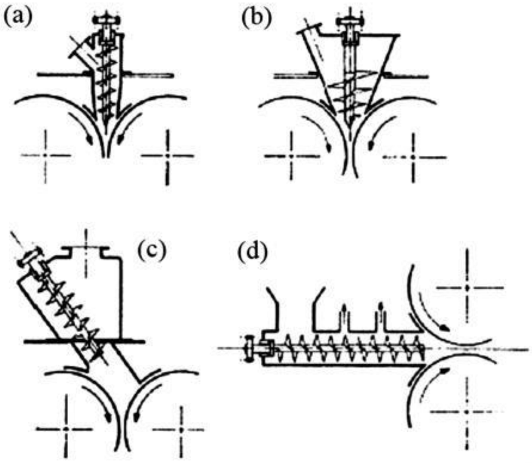

***Figure 4*: Screw arrangements to convey powder to the rolls. Adapted from source [51].**

Of the varieties available, gravity type (*Figure 5a*) is preferred for formulations of free-flowing powders with sufficient bulk density and compactibility. The use of gravity feeders for poor-flowing powders can result in air pockets forming as a result of a pressure differential between the top and bottom of the hopper (e.g. the capability of air to escape from the bottom, particularly when the hopper is fully loaded).

In order to address the issues of fine, light and poor flowing powders the majority of RC's use augers (others with pistons) to convey a consistent flow of particles to the slip region to reduce air pockets in the feed-stock.

***Table 9*: Comparison between roller-comparators.**

RC Manufacturer	Roll orientation	Feeder design
AlexanderWerk	Horizontal/vertical	Auger
Bepex	Horizontal	Auger/gravity
Fitzpatrick	Horizontal	Auger
Freud/vector	Horizontal	Auger
Gerteis	Horizontal/Inclined	Auger

Systems featuring multiple-auger systems (generally specific to production-scale manufacture) aide densification uniformity by exerting a pre-compaction force on the blend. The former, can be vertical: a pressure differential within the blend between the region, to offer resistance and thus, pre-compression if the feed-region is more densely filled. Intelligent system design offers variable rotational rates of the auger-screws are available to forestall these issues [3]. Furthermore, vacuum de-aeration of the powder prior to the nip region is frequently offered by many RC systems.

2.2.2 Compaction

The roll design can differ in terms of (1) mounting orientation and, (2) surface texture. Shown in *Figure 5*, rolls can be mounted on a horizontal-axis (*a*), vertically (*b*) or inclined (*c*). The boundaries between the rolls are confined by either, side sealing plates (*see Figure 5d*: *LHS* and *a*) or a rimmed-roll design (*See* Figure 5*d RHS* and *Figure 7*). Common surface textures of the rolls include smooth, knurled/latticed and fluted designs which are generally interchangeable to cope with different formulations. Knurled (and less frequently used fluted) wheels are more effective for powder blends which are not consistency gripped (or *drawn-in*) by smooth-rolls.

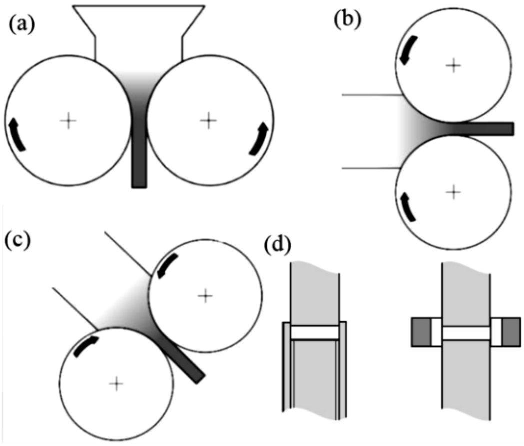

Figure 5: **Configuration of conveyance to the rolls and the preference usually favoured by a number of manufacturers (*a-c*). (*a*) Horizontal roll mounting: AlexanderWerk, Bepex, Fitzpatrick, Freud/Vector, and Komarek; (*b*) Vertical roll mounting: Some AlexanderWerk and Some Gerteis models and (*c*) Inclined roll mounting: Gerteis. Confinement of the pre-compacted powder-blend is illustrated in (*d*) from a rimmed roll (*LHS*) or side cheek plates (*RHS*).**

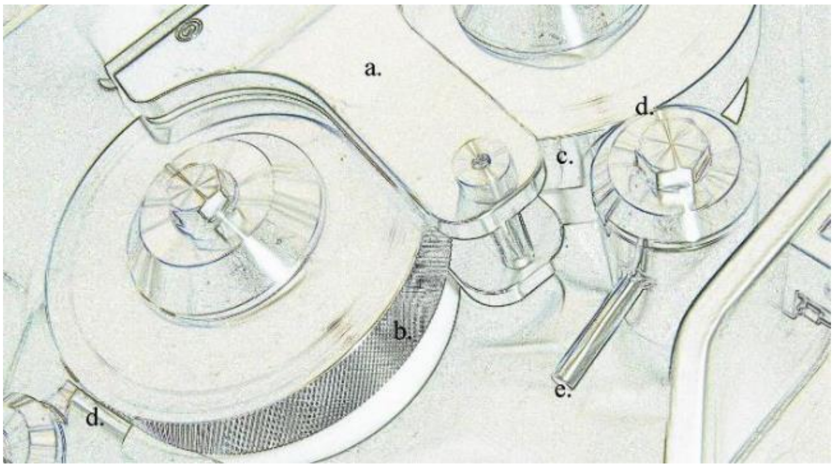

Figure 6: **A typical compaction stage: Gerteis's PolyGran®. The feedstock is contained in the slip and nip region, labelled *a,* whilst being drawn into the release region by roll rotation, these have different surface textures. Denoted, *b,* is a knurled roll and, *c,* is a smooth roll. Following compaction the ribbon may require removal from the rolls because of adhesion, which is aided by the scrapers (denoted *d*) or, be freely released and snapped into smaller pieces with collision with arm (denoted *e*).**

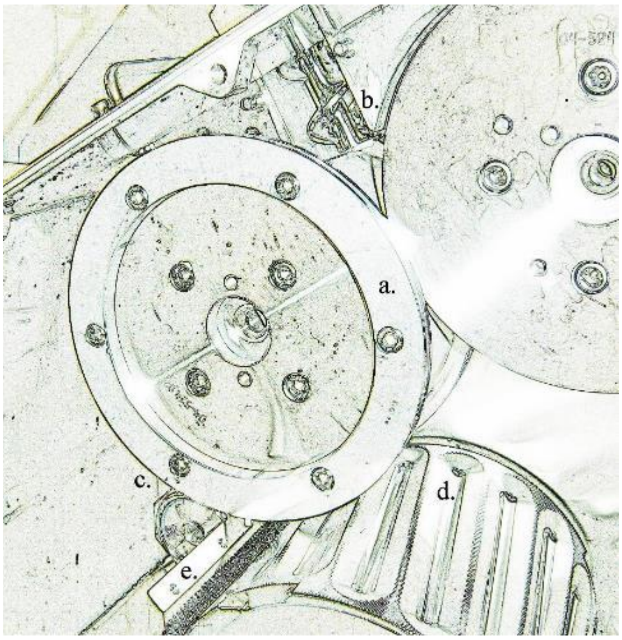

Figure 7: **Illustration of a typical compaction stage;: with equipment features of a Gerteis's Macro-Pactor® with the containment guard removed, revealing the tampering auger, *b*. In contrast also to the PolyGran® *a*, denotes a side-rimmed roll (instead of cheek-plates) whilst, *c* denotes the scrapers and the milling-mesh and mill-roll (*d* and *e*) respectively are displayed.**

Photos of the above illustrated RC's, are shown in appendix *Section 10.1*, while the equipment parameters are given in *Table 10*.

Table 10: **Technical specifications the Gerteis machines. Reproduced from source [60].**

Specification range	**PolyGran®**	**Macro-Pactor®**
Production scale	Medium: Max throughput *300 kg/h*	Development/Pilot/Full manufacture. Max throughput *400 kg/h*
Press range	*1 -15 kN/cm*	1 -20 *kN/cm*
Roller speed	*2 – 20 RPM*	1-30 *RPM*
Roller-gap	*2 – 5 mm*	1 – *6 mm*
Press roller surface	Knurled, smooth, toothed	Knurled, smooth, toothed
Roll diameter	*20 cm*	30 *cm*
Roll thickness	*5 cm*	15 *cm*

Identified in *Figure 8* (*a-c*), are the three distinct regions within the blend defined by the experienced strain between the rolls [3, 61] (*Figure 8*):

a) The slip region (or feeding zone).

b) The nip region (or compaction zone).

c) The release region (or extrusion zone).

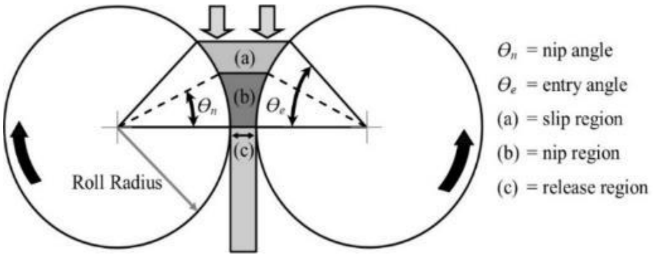

Figure 8: **Compression regions of roller-compaction described by Johanson's [62] rolling theory.**

Johanson is accredited as the first to model the pressure gradient at the slip and slip regions in RC [62]. He was able to establish a mathematical model for material behaviour mechanisms between the regions and formulated equation to predict the compressibility factor for the compacted material.

Bindhumadhavan later re-emphasised and validated experimentally the model proposed by Johanson's with good reproducibility to the original theories [2].

(a) The slip region

Characterised in *Figure 8a* refers to the slip-region or feeding-zone in which the blend begins to slip at the roll's surface and experiences particle rearrangement as individual particles move to displace interstitial voids. Dependent upon the frictional strain between the roll and material, stress is minimal and may only lead to a small degree of densification [3]. The start of this region is defined by the entry angle (*See Figure 8*, θ_e).

(b) The nip region

The nip-region or compaction zone begins at the nip angle, θ_n° (*See Figure 8 → Figure 9b*) and the narrowing significantly increases the powders' flow-rate, becoming equal with the rolls'. The next stage of drawing-in, is particle-interlocking which can be conceptualised as a mix of both elastic and permanent plastic deformation. Entering the 10° region (*Figure 9*'*a*'), the pressure exponentially increases towards a maximum, marginally before the minimum roll-gap distance. Parrot's theories suggest that brittle-particle fracturing is common at the maxima stress ‘*normal stress*’ (*See Figure 9b*) to create fresh-binding sites allowing further intermolecular binding to assist [7, 58].

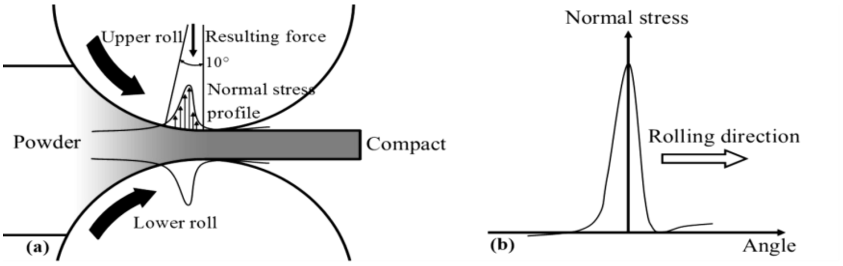

Figure 9: **Stress distribution in the nip region. Adapted from source [3].**

(c) The release region

The release-region (or extrusion-zone) is characterised by an increasing roll-gap after the neutral angle (*See Figure 9b*). The compressed ribbon may fall gravimetrically from the rolls or require forced removal by scrapers in close contact to the rolls (*See Figure 10*).

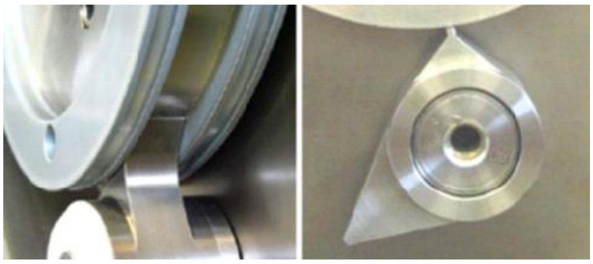

Figure 10: **The position of scrapers to aid removal of adhered ribbons.**

2.2.3 Accessories

2.2.3.1 De-aeration

Poorly flowing/low-bulk density blends can present upstream issues with air entrapment and can lead to weakened ribbons with high porosity, potentially causing ribbons to shatter [53].The use of de-aeration is thus crucial for some formulations in order to maintain consistent SF’s and narrow CQA’s. De-aeration methods used to enhance ribbon porosity are possible with the following techniques:

1. Mechanical de-aeration draws air from the pre-nipped powder-blend with via a negative vacuum (typically ~ 0.8 bar). This is made possible with filtered ports in the auger conduit, as visible in *Figure 5* (indicated by arrows).
2. During entry of the blend into the nip region non-assisted de-aeration can occur from the cheek plates and from gaps of the rimmed rolls.

2.2.3.2 Cheek-plates

Side seals (cheek-plates) or singular rimmed rolls serve to prevent leakage of the primary particles from the edges of the rollers, providing a route of de-aeration and potentially elevate frictional resistance at the ribbons edges [63].

2.3 Influence and impact of process parameters

The key operational goal in RC is to maintain a constant pressure on a consistent supply of feedstock, both in terms of rate and distribution. The compaction process is managed by controlling the input material, the quantity/unit time, the roll-speed, and the roll-gap in order to achieve the desired ribbon quality. The settings of the feeding system need to float to maintain a consistency of powder.

Roller compaction has a small number of control parameters that are process critical and focus chiefly on compaction force, roll-speed and the feeding design. Modern developments in RC instrumentation have significantly enhanced the stability (providing greater automation) and the degree of control in CPP maintenance. For example, the Gerteis's Micro-Pactor® is able to regulate the feed rate and roller gap distance to achieve user defined compaction force and roll speed, supported by mechanical monitoring (i.e. force displacement inducers) and software derived control (*See flow logic diagram Figure 11 for illustration of these inter-relationships*).

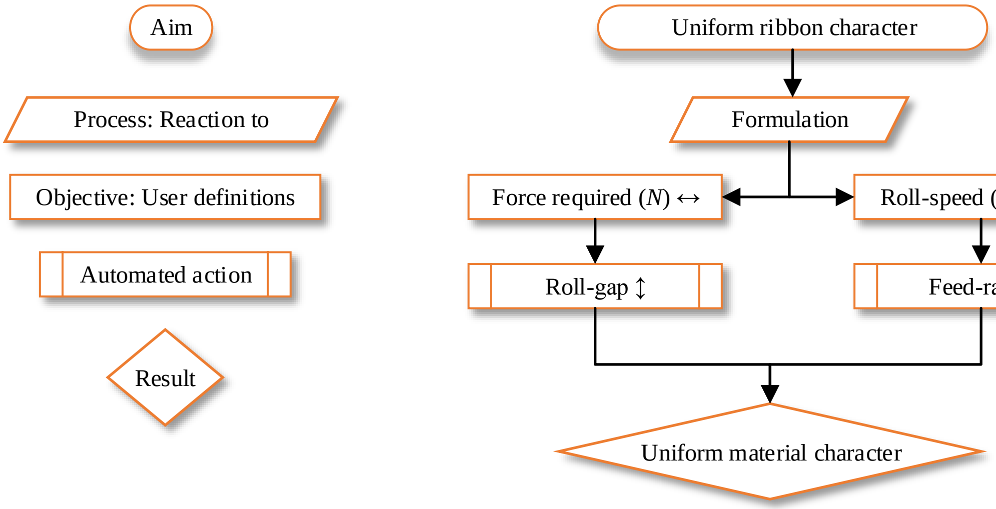

Figure 11: **Usual process control parameters of Gerteis Micro-Pactor®.**

2.3.1 Impact of feeder design types/parameters

Common problems leading to non-uniform ribbons and surface smoothness resulting from the feed process are listed in *Table 11* and chiefly concern ‘rat-holing’ or other conveyance issues.

***Table 11*: Consistency and evenness of the powder feed**

Gravity feed systems
When particles flow from the hopper there is usually a velocity gradient differentiation close to the wall due to friction, which resembles laminar flow in a pipe. Consequently, powder feeding consistency is poor at the edges of the rolls (particularly for poor flowing materials). The result is reduced compaction and potentially excessive leakage between rolls and the cheek plates due too inconsistent mass conveyance. Therefore, ribbons of such formulation attributes are inherently non-homogenous in terms of density, porosity, and strength; such granules tend to have a broad particle size distribution and excessive fines losses (i.e. contamination/reworking losses).
Screw feed systems
1) The force generated by a rotating flight produces a downward compression force that not only forces the powder into the compaction zone but also pre-densifies the powder [53]
2) Low screw speed may cause insufficient feeding to the nip and poor ribbon strength, while high screw speed may cause a highly densified zone in the nip area resulting the center portion of the nip stock being overfed while the edges are less populous. Problems of ribbons with thinner and more fragile edges and densified central banding can result if unresolved. Unsurprisingly, the screw diameter has a large bearing on radial banding. Unsurprisingly the screw diameter has screw diameters matched to 50% of roll diameter [53][8]. Further increases can be detrimental however.

---

[8] When two intercepting augers are used simultaneously for feeding, it is usual for the one furthest from the rollers to be more closely monitored than the second because particle reorientation in the augers are likely to fluctuate. Monitoring of the torque of the first auger can therefore reduce inconsistent particle re-orientation/deformation.

In work carried out by Guigon and Simon, two forms of conveyance systems were used to measure the uniformity of stress imparted on roller-compacted ribbons (recorded by force transducers bound in two concentric circles circumventing the rolls) [64]. The bespoke RC compared the applied strain on the ribbons made with equal blends/CPP’s from an auger feed design against a piston controlled system. The research results are summarised in *Figure 12* inset with shaded and quanitifed contour mapping of stress to accompany the piezoelectric transducer data. The principle observation was a variability in force for both conveyance systems evident with the periodic fluctuation of strain corresponding to the rotational speed of the conventional singular auger feed system (*Figure 12, RHS*). The strain corresponding to the piston system (*Figure 12, LHS*) meanwhile, indicated that equal conveyance force leads to a higher degree of compaction through the centre of the ribbon against the strain imparted at the sides. Of further note, it is apparent that as the auger screw rotated not only did the rate of powder increase ahead of the spline closest to the rolls but also, that slippage of the powder backwards against the rotation of the spline further adds to the recorded force differential. Guigon and Simon concluded that the geometry of both the screw and the piston designs intrinsically influence densification of the material and consequently the flux of pre-compacted material conveyed to the rollers [18, 64].

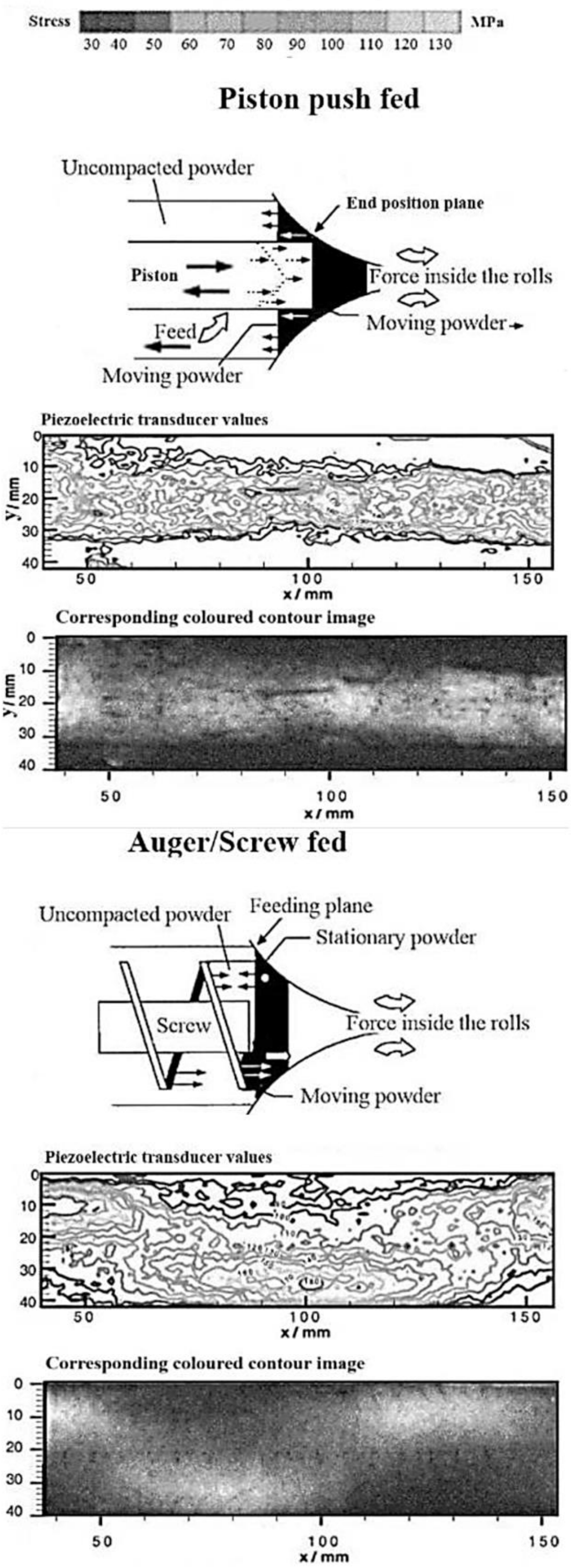

Figure 12: **Illustration of Simon and Guigon's results comparing auger and piston conveyance to the slip region. On the left–hand side, a schematic representation of the piston design is shown, followed beneath with the raw recorded piezoelectric transducer values and beneath, shaded contour representations corresponding to the stress key. To the right is the equivalent readings of an auger type roller compactor [18, 64].**

2.3.2 Compaction force and roll surface texture

A minimum compaction force of the feedstock is needed to compress the loose powder into ribbons.

Table 12: **CQA's implicated with compaction force/surface.**

	Compaction force
1)	At greater compaction forces, stronger ribbons with lower porosity and less fines are produced [65-67], however over-compaction can cause very brittle ribbons and result in poor granule quality in later tableting stages; excessively high compaction force (in RC) is well documented to reduce the compactibility of granules [68, 69]. As a result, tablets prepared from over-compressed granules may suffer from low hardness and high friability.
2)	Compaction force is considered the most important factor in controlling granule quality because fragmentation/interlocking is the main cited mechanism for bonding. Inghelbrecht and Remon [67] studied roller compaction of various formulations and found that compaction force was the most important factor to effects the quality of a compact. Wu and Sun [70] also pointed out that brittle material is less susceptible to compactibility loss.
	Roll surface
1)	Schoenert [71] studied the movement of particles in the slip region and observed that they stayed closer to the center of the material stream rather than to the roller walls, which was attributed to the centrifugal force induced by roller revelation. Described also was a certain fluidization due to the upward flow of air squeezed out from the feedstock. Naturally, this is seen detrimental to consistent densification, and the throughput of the roller press, particularly when the blend was extremely fine. An appropriate transfer of material can be achieved using proper roller design.
2)	Daugherity and Chu [72] report that rollers with knurled surfaces supply additional friction to *draw-in* the pre-compressed powder more effectively than with smooth-rolls during the slip and nip regions. Insufficient friction at the powder-roller interface can cause multiple ribbon issues, including system blockages over densification and temperature/content variance. Consequently, blends with low-shear/highly lubricated may require knurled rolls [21].

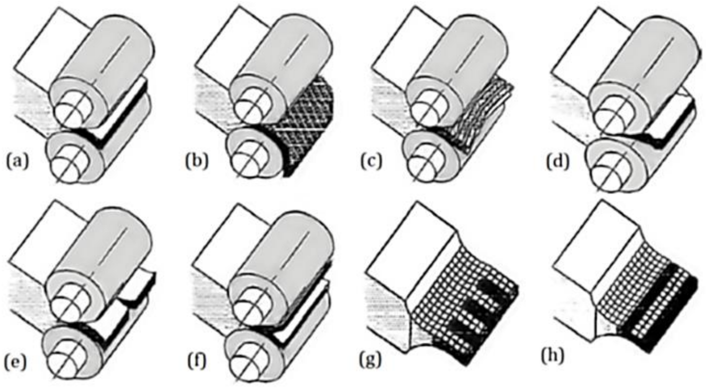

Figure 13: **Schematic diagram of roller compacted ribbons illustrating potential problems that can occur between smooth rolls and fine powders. (*a*) A dense good quality compact (*b*) ribbon is too powdery but has increased bulk density (*c*) compact breaks into regular pieces (*d*) no compaction at the edges (*e*) compact breaks in the middle to two strips (*f*) compact tears across its width (g) non-uniformity across roll width (*h*) non-uniformity in the transverse direction [73]. Readapted from source [3].**

2.3.3 Roll speed

Roll-speed controls the dwell time of the compaction cycle and as a consequence, the gross throughput of the RC. The selection of roll-speed depends on the formulation characteristics including flow-ability, plasticity and elasticity of the powder. For instance slower roll speeds are required for poor flowing formulations which are relatively resilient to elastic and plastic deformation.

Table 13: **Impact of roll-speed.**

For plastically deformed materials, such as MCC, which are sensitive to dwell time, a low roll speed tends to produce granules with better flow and lower friability [35]. However, a long dwell time may also cause the granule to lose compactibility (resulting in tablets with low hardness and high friability [54]).
High roll speeds and low screw speeds tend to minimize the dwell time dependency of the plastic material. Even for partially plastic deforming materials, such as lactose, a higher roll speed is preferred. Inghelbrecht and Remon [67] reported that at higher roll speed, granule quality improved and the tablet friability is lower.
For highly elastic material, the overall process throughput may be limited due to the physical property of starting material. For brittle materials, the compact strength tends to be independent of dwell time, because fragmentation is achieved rapidly and extended exposure tends to have a limited effect on the ribbon strength [53, 54, 74].

2.3.4 Recent RC innovations

Manufacturers of RC's have worked in co-operation with pharma firms to develop more sophisticated plant and software systems to improve production efficiency, consistency and precision, in order to reach the more stringent regulatory obligations. Measures of improvements have become manifest with greater feed-back information of the process (in-order to better control the compaction and milling parameters) which specifically include steady-state regulation of feed rate, roll-speed, compaction-force, roller-gap and mill speed. It is through continuous monitoring and control of the aforementioned system/process parameters that intentionally aim to narrow out of specification (o.o.s) stock/worked material to systematically increase the CQA's of products.

To provide methods for determining density and thickness uniformity several analytical techniques have been evaluated in recent years which broadly include optical techniques of NIR/Raman spectroscopy, powder χ-ray diffraction and χ-ray CT. An overview of each technique and the degree of success achieved by the methods is discussed within this *Section*, and also the limitations either reported by the authors or otherwise concluded.

2.4 NIR and Raman spectroscopy

The technique of near infra-red spectroscopy (NIRS) is showing premise of becoming a very versatile **optical process analysis tool (PAT), and is based on the absorption of NIR light with harmonics and overtones of intra-molecular bond vibrations. NIRS** has been used in methods to assess blend uniformity, drug assay, dissolution procedures, aswell as correlating spectral features with sample density, and also the hardness of compacts (with the industrial perception of a recurrence of continuous manufacturing [36, 75-78])**.**

Within the literature the reasonably well established technique of NIRS has been used in methods to assess blend uniformity, drug assay, dissolution procedures, aswell as correlating spectral features with sample density, and also the hardness of compacts (with the industrial perception of a recurrence of continuous manufacturing [36, 75-78]). Researchers have been increasingly investigating whether local and regional (batch-to-batch) densification and uniformity is quantifiable/predictable from spectral measures across ranges of formulations, while including tests for compaction-force variance on tablets and RC's [75, 79]. With individual tablet/compact spectra being representative of the intra-molecular vibrations of the sample in NIR and hence, conventionally production of many peaks [80], there is evidence that greater compaction-force appliance can be correlated with an upward shift across spectral amplitudes.

Resulting from shorter to longer wavelengths with increasing porosity, the method relies upon fitting a best-fit line over the series of compacts, which does seems an unconventional indicator, yet; the baseline gradients appear responsive to compaction forces used. Perhaps to the techniques detriment, *Donoso et. al. (2003)* reports that while porosity and hardness values are pseudo-correlated to compaction-force, that range of compaction-forces are likely an indicator to this prediction, but is predominately causal of the heightened specular reflection from smoother samples (i.e. that underlying the results is a strong potential for diffuse reflection associated with more porous samples leads to a lower absorbance mechanism [79]). The performance of NIRS is later generally tested by using multivariate models of PCA and PCR in which complex computational routines and training sets are needed which can greatly affect the reproducibility of any results (see sources [75, 79, 81-83]). Supported by *Gupta's* multiple papers *(2004, 2005)* mimicking *Donoso's et. al. (2003)* that the usefulness of an imposed NIR spectral slope (*See the error bars in Figure 14*) that, NIRS analysis of transmission/reflected probe-beams may in-directly indicate porosity to an extent [34, 35], but in practice, a new calibration model must be meticulously found for each NIRS run on different products. Limiting the practical durability of a porosity predictor.

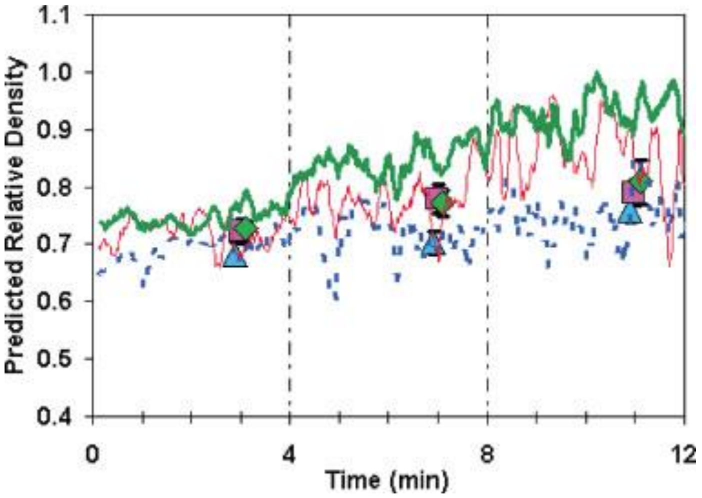

Figure 14: **PLS predicted values of relative density from the NIR data collected during real-time monitoring of roller compaction at different RH. Reproduced from source [35].**

Advancements in *NIR-CT* techniques for 3D profiling provide additional opportunites for process development [77].

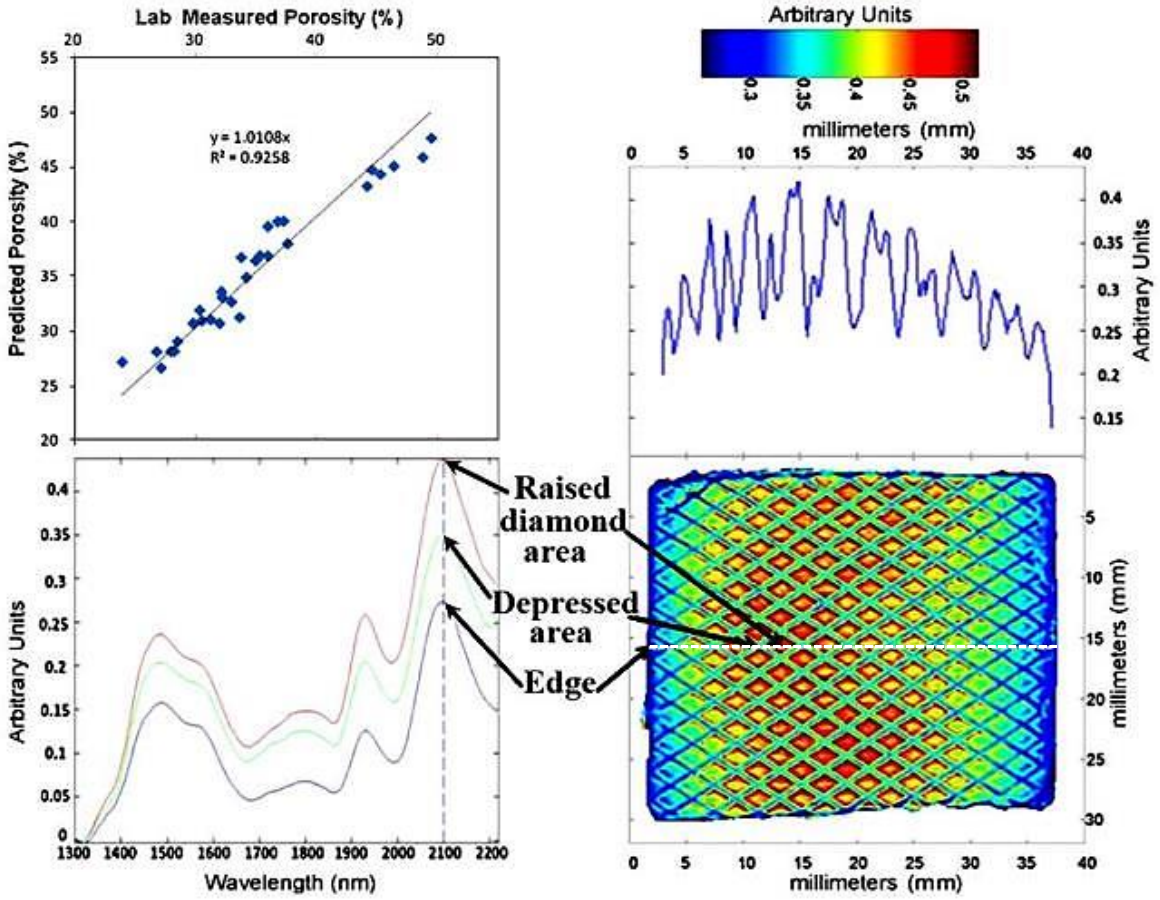

Figure 15: **Porosity 3D profiling with recent NIR-CT. Reproduced from source [77].**

Raman spectroscopy signal intensity has also been employed as a surrogate measurement for predicting the crushing strength of intact tablets [39, 84], although, Johansson *et al. (2005)* [84] noted that no significant effect upon the Raman signal were found due to changes to tablet density following compaction of tablets at different compressional forces. These contrasting observations signify that Raman spectroscopy requires a very accurate method, dependent on the materials used and particularly, the production parameters. For example, Wang *et al*. *(2002)* [85] assumed that density would increase when an increasing compaction force is applied to a confided, fixed mass of powder, giving rise to an increased Raman signal, yet it did not (in contradiction to KM theory; predicting that more elastic scattering would occur with increased density [85]). However, not until a sufficiently high compaction force was used, did the signal intensity rise significantly and thereafter the signal remained approximately constant with further increases in compaction force. It was concluded that the diffuse reflectance from the tablet’s surface increased until the density of the tablet became almost homogeneous and the surface became sufficiently smooth, and thus prevented in-elastic light scattering. Johansson *et al. (2005)* [84] later concluded that Raman spectroscopy is not as useful a tool for studying tablet compaction compared with NIR spectroscopy.

The sensitivity of the NIR baseline shift, relate to compaction force used over batches of equal compositional nature [75]. In this instance, with a defined and calibrated system and with equal tablet uniformity and thickness, a surrogate measurement for density is made, and in-directly this results in a hardness measurement. Raman and Mid-infrared (MIR) generated spectra are sensitive to intra-molecular vibrations of molecules which give rise to peak positions and signal magnitude. Due to this, MIR and Raman spectroscopy generally fail to directly probe inter-molecular dynamics. NIR produces a more complex situation than MIR alone because of the frequent inclusion of combinations and overtones of bands of the fundamental vibrations [80]. With Raman spectroscopy, and in light of the conclusions that *Wang et. al. (2002)* [85] noted, Raman is very sensitive to the effects of diffuse light-scattering as a consequence of the smoothness of the substrate. Hence, coupled with issues of sensitivity to intra-molecular dynamics (which are) only indirectly coupled to intermolecular bonding, tensile strength can only be broadly correlated to densification, and a limitation of these two techniques.

2.4.1 Powder χ-ray diffraction

The uses of χ-ray diffraction techniques are widely regarded as very powerful tools for elucidating atomic density distribution within materials. For instance Moore, M.D. *et. al*. [86] used advanced powder χ-ray diffraction (PχRD) to characterise the structure of anhydrous theophylline and an MCC binary mix. Consequently, they were able to analyse the PχRD data with PDF and PCA to successfully differentiate pattern changes consistent with theophylline and non-theophylline regions of material.

χ-ray based techniques (naturally) suffer from the issue of ionising radiation emission and incorporation into an established production line would present substantial investments in shielding apparatus, and engineering complexities.

2.4.2 χ-ray computed tomography

χ-ray CT is a non-destructive inspection technique which provides cross-sectional images in planes through a component. The component is placed on a precision turntable in the divergent beam of χ-rays generated by an industrial χ-ray source. A detector array (line or area array) is used to measure the intensities of the χ-ray beam transmitted through the component, as the component is rotated in the beam. A mathematical algorithm is then used to generate (or "reconstruct") the CT images from the measured transmitted intensities.

The resultant CT images (*See Figure 16*) are cross-sectional images, and show internal geometry with resolution within the micrometre scale [87].

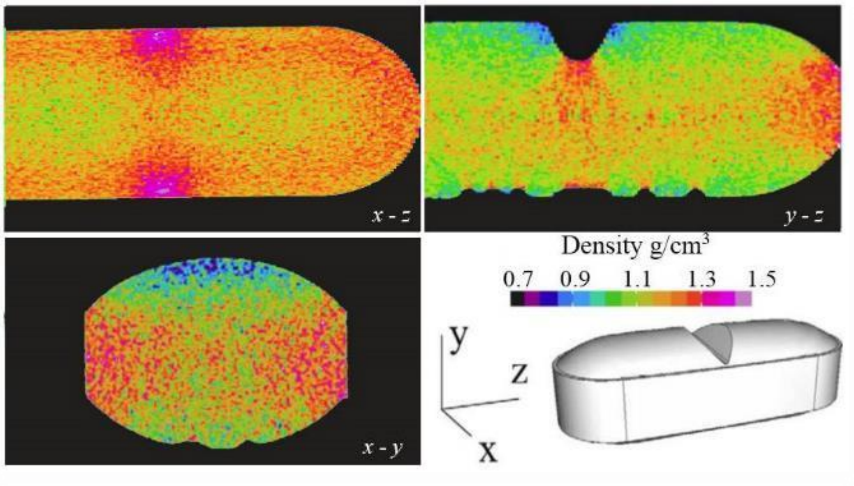

Figure 16: **Density distribution in three planes (bottom right) of a caplet resolved by χ-Ray CT. Reproduced from source [87].**

2.4.3 Critique of current PAT strategies

Excellent for uniformity verification, χ-ray techniques allow both qualitative and with interpretation quantitative information of the molecular distribution of a sample to be analysed to identify regions of variable mass distribution. Unfortunately the adverse feature of ionising EMR tools list caveats suchas difficulties in rapid interpretation of data (making χ –ray systems currently, atleast an off-line procedure regarding operator and formulation safety).

Similarly, the wavelengths characteristics of EMR at the blue end of the visible spectrum are of shorter frequency than χ, γ-rays yet convey greater energy than visible light to induce nuclei/electronic transitions [88]. In energetic terms, the differences between electronic transformations is approximately 100 times greater than compared with IR illuminated substances (whereby vibrational effects prevail), with greater wavelengths/frequencies (cm^{-1} or *Hz*) than in the NIR region [88]. In further regard to frequencies and energy conveyance, the wavelength/frequency of THz radiation is significantly larger than many pharma molecules and so, photon degradation is less likely. The effects associated with visible light (400-700 *nm*) will result in less molecular scattering [89, 90]. To the benefit of NIR-CT (*See Figure 15*), reflection imaging by NIR to produce density maps of similar detail to THz TPI, especially with CT capabilities.

However density determination using NIR-CT does have a number of considerable drawbacks. These commonly include a greater amount of resources (c.f. with THz-TPI) to prepare a sample for investigation, is not as robust as THz imaging in regard to the permissivity/transparency whilst also requiring many more probes to achieve comparable topology and depth scans.

In conclusion, the first notable adversities of highly energetic spectral tools are of risk to either the API or user; aswell as rapid quantification of porosity. Useful to assay determination and off-line analysis NIRS is deeply rooted as a useful assay/mixing-time indicator, while UV/γ & χ-rays are impractical or degradation assessment applications. Conversely, no-one technique is ideal for density uniformity testing. For instance, the broad wavelength and low conveyance of energy of THz TPI is both in regard to permissivity and low emission of photons (blackbody-radiation [91]); yet, longer wavelengths of TPI inhibit high resolution imaging with sensitivity to moisture. Thus off-line χ-ray diffraction permits good resolve to imaging and NIR for enhanced API distribution monitoring. TH result is that an ideal system for > CQA's is not achievable alone with one technique. Moreover, considering DG/RC is appraised for moisture free and continuous processing to rapidly acquire data may present the optimum tool to determine both porosity/density (via RI measurements) and the split capability of temporal recognition of analyte thickness; thus, timely feedback control of system CPP's and reaction to different material grades/batches of the many input permutations.

Naturally other techniques are available with optical dynamics to, for instance, gauge thickness and subsequently RI in a revere-type approach to the work presented herein.

2.5 Building quality into roller-compacted ribbons

To ensure DG/RC granules reach a desired quality during the unit-process, knowledge of practical design space is needed, whereby the range of the processing variables is understood for a given formulation. This is a form of risk management to ensure that the desired quality is built into a product [7], rather than that achieved by process control following manual stages of material testing.

The relatively modern implementation of automated sensory systems with computational feed-back routines has been very beneficial to the pharmaceutical industry, allowing increased consistency during densification and the production of more uniform granules. These process/equipment variables (including roll-gap, roll-speed, auger rotational-speed and compaction force) enhance steady maintenance of user-defined CPP's, in-turn adding to the design strategy to improve the range of products meeting the CQA's.

To ensure the quality of the formulation variables (see *Table 14*), compaction and milling usually lie as a singular stage within a production cycle, requiring stages such as blending (before addition to RC) is for this reason that the quality of the formulation must be ensured.

Table 14: **Formulation variables**

Characteristics	
Particle size	Flowability
Compactibility	Compressibility
Hygroscopicity	Loss on drying
Density	Particle distribution

3 Terahertz imaging

This chapter provides the key principles of THz generation and detection (*Section 3.1*) and then, addresses how a materials' porosity and thickness can be estimated majoritively by two distinguishing principles of EMR behaviour. Leading from passage of a THz probe-beam through an analyte, a comparative *time-delay* value is found to that of an empty-system. This is first established in a typical **transmission** setup and is illustrated in *Section 3.2;* alongside **reflectance** imaging, whereby the proportion of an angled probe-beam that is reflected and detected (vs. a gold mirror) is suggestive of the materials density. The basic phenomena of EMR (*Section 3.4*) is covered prior to establishing the methodologies through *Sections 3.5 - 3.6* and includes where germane; derivations of classical optics for the purpose of validating any mathematical models assumed in developing and enhancing method accuracy.

Increasingly attainable and sensitive forms of THz devices have rapidly proliferated spectral characterisation of non-conductive substances and has become a highly desirable technique in qualitative and (readily) quantitative time-resolution imaging. Many substances are firstly transparent to THz EMR, enabling non-destructive, sub-surface identification of artefacts with high temporal precision whilst remaining non-ionising and safe for analysing biological substrates. The transparency of many pharmaceutical substances to THz radiation furthermore, allows precise acquisition of RI's information (a useful surrogate parameter to SF) and/or dimensional properties. Many of these benefits are individually quantifiable with other light-based techniques; yet, the combined advantages are invariably unique to TPS/TPI, as are conveyed in *Section 3.7,* and undergoes exploration in the *gap of knowledge* to challenge current physical limitations and gaps in DG/RC manufacturing.

3.1 Introduction to the terahertz spectral region

Terahertz radiation ($THz = 10^{12}\,Hz$) lies within the EMR spectrum between the microwave and mid-infrared regions. More specifically, the THz gap is defined between the wavelength regions of $0.3\ cm^{-1} – 3\ cm^{-1}$ or alternatively, between the frequency band of 0.1 -$10\ THz$ [92].

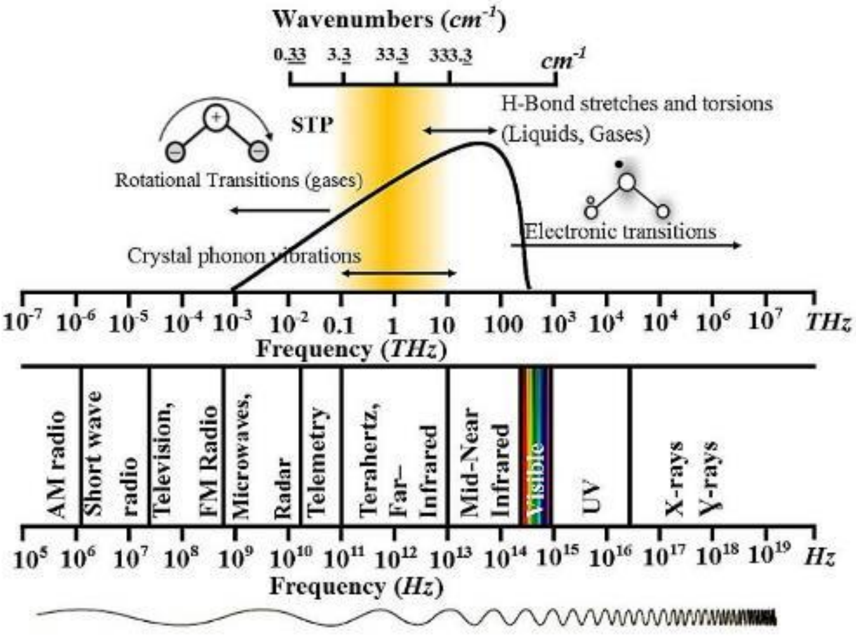

Figure 17: **The EMR spectrum. Top: Shaded orange is the spectral bandwidth accessible with most commercial THz instruments. The molecular illustrations are the typical molecular dynamics caused by THz excitation.**

3.2 Optical-gating and electronic detection of THz light

The TPS-3000 is reliant upon optical excitation from a femtosecond emitter (in the form NIR pulses: *See Figure 18*) at a wavelength of 800 *nm* from a Ti:Sapphire laser. Optical excitation is dealt with equally between both the THz source emitter and the detecting antenna along a variable length pump beam with equal power from the optical NIRsource [93].

The configuration of the TPS-3000 offers both a conventional orthogonal transmission-type setup (denoted ‘A’ in *Figure 18*, and reflection imaging (TPI) with the addition of an additional set of off-axis parabolic (OAP) mirrors (*See Figure 18B* for TPI measurements). The geometric alignment of the probe-beam is crucial for successful detection during reflectance imaging (TPI ‘*f*’) at *30°* from the normal angle of incidence.

3.2.1 The probe-beam

The probe-beam passes several OAP mirrors (*See Figure 18*) to transmit THz pulses through the substrate onto the detecting antennea.

3.2.2 The pump beam

The optical-pump beam passes through a rapidly-moving optical-delay rail containing a moving mirror (*See Figure 18 A,B, and E*). The travel distance within the system is unique ans so calls for a reference measure (≡ time) for gating the reciever. Therefore, a broad THz frequency range (*0.1–3.0 THz*) can be mapped out at sub-picosecond (< *ps*) intervals with a SNR of 4000:1 [94].

This configuration enables THz pulse detection by effectively activating the detecting antenna to obtain an *E-Field* (*t*) magnitude, while the beams phase is measured with an ammeter providing a near (pseudo) real-time parameter [92, 93, 95].

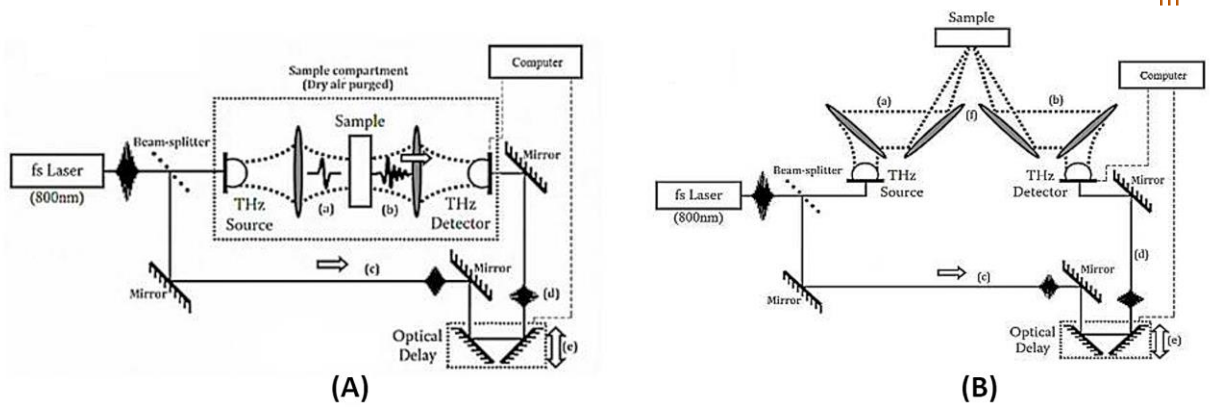

Figure 18: **Experimental configurations of the TPS-3000.for transmission measurements 'A', and *for* reflectance imaging with the Imaga1000™ module, 'B'. The images re-adapted from source [96].**

3.3 Generation and detection of THz EMR with excitation of a photoconductive device switch

The generation of THz radiation with photoconductive devices requires a primary laser source to optically excite and induce polarisation in a suitable semi-conductor (an Auston switch) [97]. Generation of a pulse of THz radiation occurs on the surface of the semiconductor (*See Figure 19*) initiated by the NIR optical probe-beam[9]. This causes photo-excitation every 100 fs onto a gap on the antennae between a 'bow-tie' designs of electrodes, separated by a narrow gap sufficient to separate the *E-Field*. With sufficient accumulation of energy, electron charge separation occurs on the semiconductors surface, creating a split ionic field (or an electron-hole gap). The heightening differential disparity eventually become a plasma field and becomes sufficiently great to bridge the band-gap between the electrodes (*See Figure 19*). With a regulated pulse of DC bias across the electrodes [98-100], the collapse of the electron-hole region is ostensibly instantaneous and reduces the μ, ε and σ (on the microscopic level) of the semiconductor, thereby emitting THz radiation. Following emission of a THz pulse, consistent accumulation of energy sourced from the optical-laser leads to a coherent, periodic emission of pulses.

---

[9] The NIR Ti: Sapphire laser has a bandwidth of ~ 800 nm

The photoconductive emitter and receiver (antennae) are functionally the same in the TPS-3000, however, a primary laser source) illuminates both conductors equally (labelled source and detector), as seen in *Figure 18* .

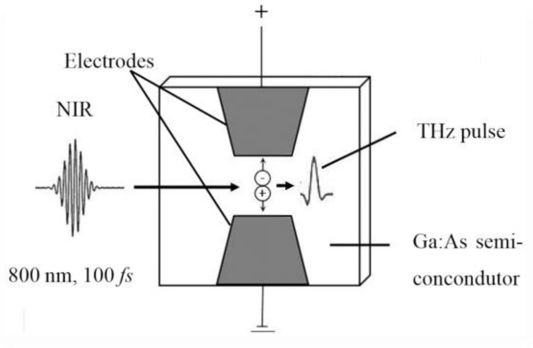

Figure 19: **Schematic image of the Ga:As substrate in the TPS-3000 with particular attention made to the 'bow-tie' layout of the electrodes. Note: The gap separating the electrodes is not to scale.**

The interrogatory pulse is collimated with OAP mirrors on the detecting antenna which bares many similarities to the emitter [101], except that the detector is gated (i.e. to form a charge separation) by the pump-beam which passes through a rapid delay-rail, to increase the propagation path-distance and thus map multiples times. The arrival of periodic THz pulses creates a DC bias on the semi-conductor, creating a photo-induced current induced by the THz wave to polarise the antennae. The charge difference between the bow-tie electrodes is de-codified by a low-noise current amplifier and is then computationally processed providing an instantaneous *E-Field*(t) of the THz pulse [95]. Being pulsed, the changing length of the probe-beam is able to map the THz *E-Field* as a function of time. This is known as optical gating.

3.4 Basic interaction of electromagnetic waves with matter

There are four main phenomena involved in the interaction of EMR waves with matter. These include light scattering, light reflection, absorption and refraction. The focus of this study places greater emphasis on the phenomena of light reflection and refraction (i.e. the substrates transparency and impedance of the velocity of c_0), however scattering and absorption are inevitably causally inter-related with our reflection and refraction interests.

Included in this section, the terms I_0, (as the incident radiation), I_T, as the light transmitted through a substrate, and I_R as the reflected portion of I_0 are common-terms in the field of optical-physics. Hence, terminology including I should not be confused with later usage of the parameter *Intensity*, discussed as the product of the Hilbert transformation.

3.4.1 EMR Absorption

Absorbance occurs with transference of energy into the electron clouds or the atomic/molecular structures within, proportional to the concentration of photon absorption during passage. The absorption coefficient (or specifically, energy conveyed by photons absorbed at specific frequencies) chiefly influences[10] the ratio of energy transmitted through a material.

3.4.2 EMR Refraction

Refraction of EMR invariably occurs at the boundary interface between two isotropic materials during any form of impedance spectroscopy. The transmittance of energy is impeded at a uniform rate in homogenous composites, which also results in a change in the angle of the propagated (internally transmitted) signal, θ_t° from the angle of incidence to the normal line.

Heterogeneous substrates do not allow such implicit rules to be stated in relation to uniform light propagation through the full path-length. Local regions within the subatrate may include internal artefacts such as laminar porosity changes or non-uniform chemical composition, which are equivalent to RI changes.

The RI of a material is an intrinsic property, simply defined in homogenous substrates (*see Equation 1*) as the quotient of the velocity of an EMR through free-space[11], c_0 with the velocity

---

[10] Other influencing factors common to transmitted EMR include light scattering (discussed later), yet the wavelength of THz radiation is generally stated to be less than most molecular species in the pharmaceutical industry [Taday, 2004].

[11] $c_0 = 2.9972 \times 10^8$ *m/s*

(determined by the time-delay) through the material, c_T (assuming the investigative materials have equal path-lengths).

$$RI = \frac{c_0(m/s)}{c_T\ (m/s)} \Rightarrow \left(\frac{c_0(\cancel{m/s})}{c_T\ (\cancel{m/s})}\right)$$

Equation 1

Additionally, the wavelength (λ) of light changes at the boundary interface of two isotropic materials, resulting in a further mathematical expression for RI: *Equation 2*.

$$RI = \frac{\lambda}{\lambda_t}$$

Equation 2

While the frequency, (*f*), of the incident light remains constant, velocity of the transmitted light to wavelength can be expressed as in *Equation 3.*

$$c_T = \lambda f$$

Equation 3

3.4.3 EMR Reflection

Illumination of a material transparent to EMR of a source of frequencies to which it is (fully/partially) transparent results in a proportion of the probe-source to be either/both reflected back into the dispersive media or transmitted into the substance. The transmitted probe-source can therefore be reflected at the initial interception (at the anterior surface) or transmitted internally and then reflected from artefacts within, including the posterior surface. In many instances, transparent media will cause both on these instances to occur whereby the posteriorly (or artefact) reflected pulse can be detected with transmission back into the anterior face of the dispersive media and detected (See *Figure 20A* and *Figure 21*).

- **Snell's law of reflection**

To model the relationship governing the angular aspects of incidence radiation to the normal angle of light interception (*0*°) to oblique angles. The general forms of Snell's law of reflection can be incorporates to indicate the effects of RI's '*n*', and geometry of angular propagation of incident radiation (to the normal angle), and any known RI's; generally of the dispersive media (*see Equation 4*). Introduced in *Figure 20,* inauguration of Snell's equation demonstrates the key principles for reflection and refraction.

$$n_i sin(\theta_i°) = n_t sin(\theta_t °) \leftrightarrows \frac{n_i}{n_t} = \frac{sin(\theta_t°)}{sin(\theta_i°)}$$

Equation 4

3.4.3.1 Physical influences effecting Snell predictions

- **Specular reflection**

The substrate must be partially reflective and planar with no indentations or pores of a greater size than the probe-beams wavelength. Illustrated with a simple *2D* pencil-ray diagram (*see Figure 20A*), n_t/RI_t corresponds to a planar and highly reflective mirror. This allows a confident reference value for I_R to be systematically used as a pseudo-I_0 value. The planar nature upholds to Snell's law (*see Equation 4*), such that the angle of light incident to the materials normal angle, θ^o_i is = θ^o_R. It is noteworthy to recall that the intensity of *EMR* received is highly unlikely to be equal with a perfect conductor or a perfect dielectric substance, due to EMR thermodynamic losses of heat, non-vector appreciation of the EMR source and, the potential losses due to excitation of molecular/phonon vibrations.

- **Diffuse reflection**

Diffuse reflection occurs from non-planar, yet reflective materials featuring surface imperfections (particularly with indentations greater in size than the wavelength of the investigative EMR). The result (highlighted in *Figure 20B*), expresses that, $\Sigma\theta_i^{\circ}$ may $\neq \Sigma\theta_r^{\circ}$ at the point of detection.

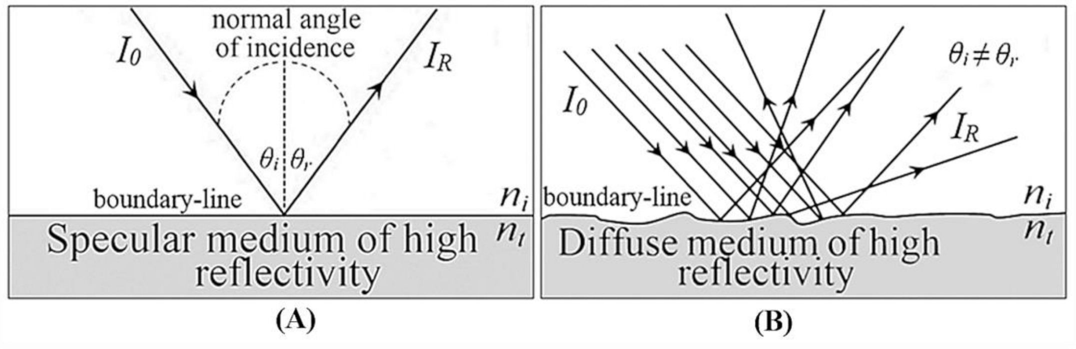

Figure 20: **Schematic of (A) Specular reflection, and diffuse reflection (*B*). The incident and reflected EMR beams and the lines of the norm. ∠ Incidence to the surface lie in only one plane.**

Conveyed schematically, Snell’s law addresses the passage of EMR as displayed *below* as a pencil-ray diagram (*in Figure 21*) in order to show the geometric terms of $\angle\ \theta_i^{\circ} = \theta_r^{\circ}$ (even after passage: $n_i \rightarrow n_t \rightarrow n_i$), and the influence to reduce θ_t° in comparison to θ_i° and the normal angle. With testing *with model values of* n_t, the greater the ΔRI the smaller θ_t° become[12].

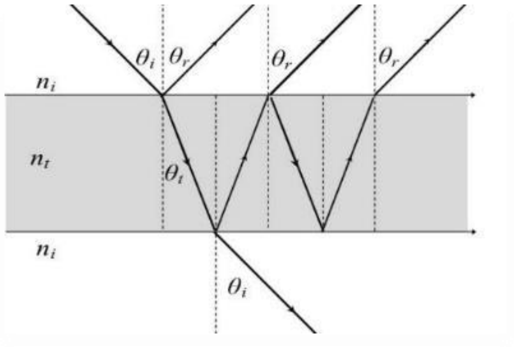

Figure 21: **Ray diagram depicting Snell’s law with a homogenous sample (n_t) suspended in a passive medium (where n_i =1, and $\theta_i^{\circ} = 0^{\circ}$ is the angle of incidence).**

---

[12] Generally, $n_i = 0$ in a passive medium and, n_t, relates to the denser medium. In this study the surrounding medium is N_2 which has a THz refractive index of 1.000,298. The contrasting RI of the investigative material will therefore be approximated to (i.e. RI within a vacuum).

3.5 Experimental time-domain transmission and TPI with the TPS-3000

3.5.1 Principles of experimentation

In transmission studies *E-Field* waveforms are acquired within the instruments' sample compartment as indicated in *Figure 22A*, (*See red arrow*) and reflection studies utilises TeraViews' Imaga1000™ module (*See Figure 22B: highlighted red - positioned over the sample compartment containing a mirror module to re-directed the THz pulses*). The visual system differences between the configurations are shown in '*A*' and '*B*' of *Figure 22*, respectively.

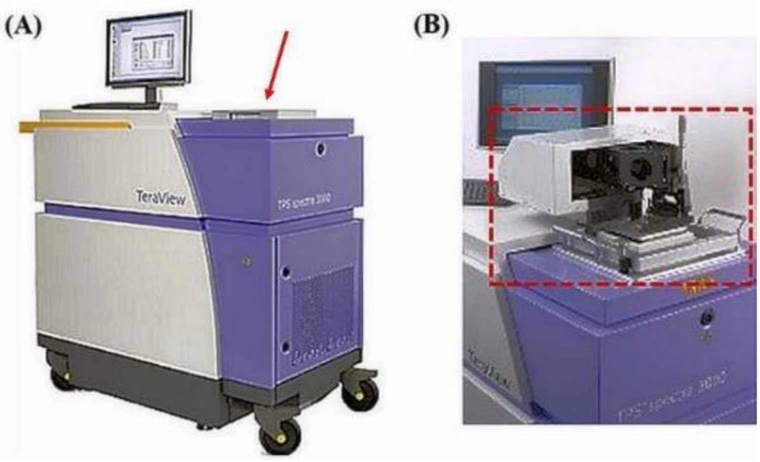

Figure 22: **Terahertz spectroscopy with the TPS-3000, 'A', and reflectance imaging with TeraViews' Imaga1000™ attachment, 'B'.**

Seen in *Figure 23a,* **transmission analysis** predominantly includes the parameters I_0 and I_T when referring to the propagation of a known quanta of light through a material (particularly in travelling one path-length, *d*). Operating in the TD means etalon resonance reflections (aka Fabry-Pérot reflection events, *FP's*) can be detected, although greatly attenuated, resulting from reflection of THz pulses internally transmitted between the anterior and posterior interfaces (*See Figure 23a: Bottom*). The system configuration does not permit quantification of the I_R of the EMR pulse initially reflected from the anterior surface for transmission work (as witnessed in *Figure 23b*).

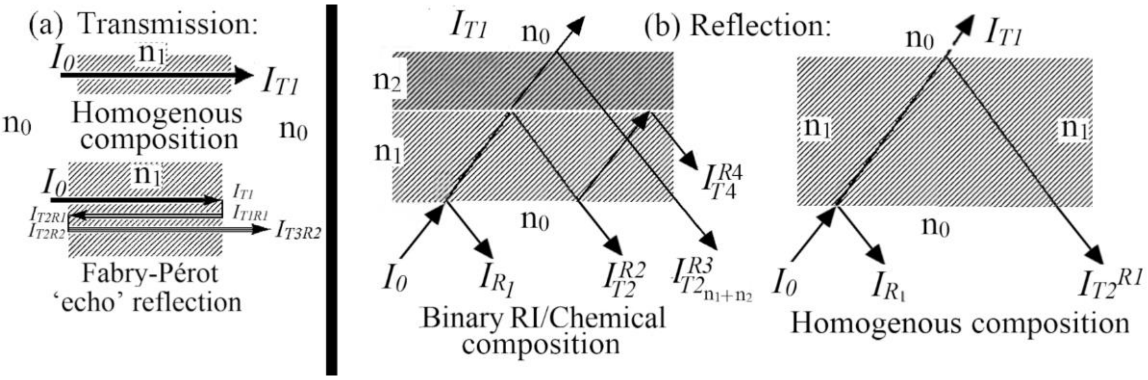

Figure 23: **Schematic ray-diagram of transmission and reflection mode (TPI) experimental configurations.**

TPI reflection analysis (*Figure 23b*) is analogous to transmission studies in regard to internal EMR propagation and reflection between the posterior & anterior surfaces. Detection of THz pulses using TPI importantly differs from transmission studies, because I_R values can be recorded from the initial interaction of EMR and the anterior face of the analyte. This is possible as the probe-beam is not perpendicular as would be the *normal line of incidence*, as illustrated in *Figure 23B*. TPI thus provides an I_{R1} result, while identification of internal artefacts (e.g. different RI's/chemical composition) can provide I_{R2}, I_{R3}, I_{R4}, I_{RN} values w.r.t. time-delay (≡ probe-beam distance).

EMR transmission through the substrate to exit the posterior face, negates collection of single-pass I_T values unlike the TPI method. Unlike transmission analysis where RI can be found with knowledge of the substrates thickness, and thus a single-pass I_T value may: (1) Be considered an extraneous parameter, if (2) A successful RI approximation can be made from the proportion of the EMR reflected at I_{R1}.

Fresnel's amplitude reflection coefficients provide a mathematical model to predict the RI of a material with the division of the INTENSITY of incident light reflected & detected at the first point of interaction with the sample as the divisor of a gold-plated mirror reference; where $I_0 \approx I_R$.

3.5.2 Transmission system configuration

A conventional transmission system-configuration (is used for FD and TD transmission studies (*See Figure 24*). Measurements are recorded with the substrate braced to a sample holder (at the point of light divergence in *Figure 24*), and the compartment is then sealed and purged with N_2.and individually, all reference and sample TD waveforms are the mean results recorded from *900* pulses acquired at a resolution of $1.2\ cm^{-1}$.

Where FD transmission is used, the thickness of the substrates was recorded with a Mitutoyo sliding-type micrometre, offering scrutiny to ± 0.005 *mm*.

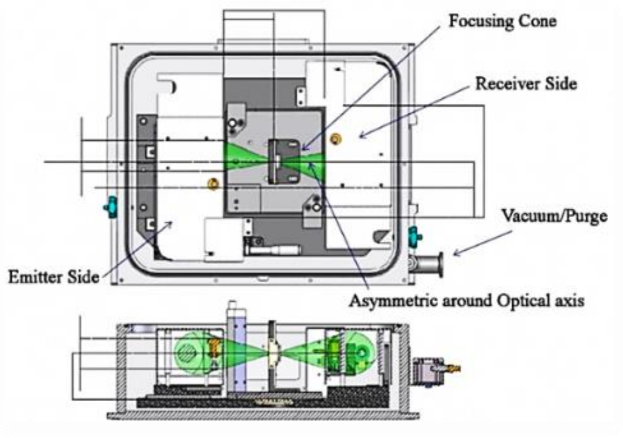

***Figure 24*: Schematic diagram of the transmission chamber. The top image represents looking into the chamber, and at the bottom, is a cross-sectional side-view. The laser footprint is shown in green to show OAP laser-divergence onto the sample.**

Purging the sample compartment with N_2 is essential in order to diminish absorption peaks characteristic of water-vapour present in standard atmospheric air. The duration of purging prior to measurement is readily judged by observing the minimisation of such H_2O peaks in the power spectrum. Purging was carried out at a pressure of 2 bar and a flow-rate of 20 *l/m.*

3.5.3 Reflection based system configuration

The TPI reflection based method utilises the Imaga1000™ module (TeraView, Cambridge, UK) as shown in *Figure 25*. The photograph '*A*' shows the *xy* rastor shifting gantry with an illustration of the off-axis parabollic mirror (OAP) module seated beneath the gantry in '*B'*.

The white insets shown in image *'A'* show the planes of movement in the *xy* directions. The *z* dimension (gantry height) is altered by the highlighted micrometre, allowing for focussing of the probe-beam to a plane with maximum reflection signal intensity. The OAP mirror module functions to direct and focus the probe beam (shown red) to intercept the substrate at an oblique angle of incidence.

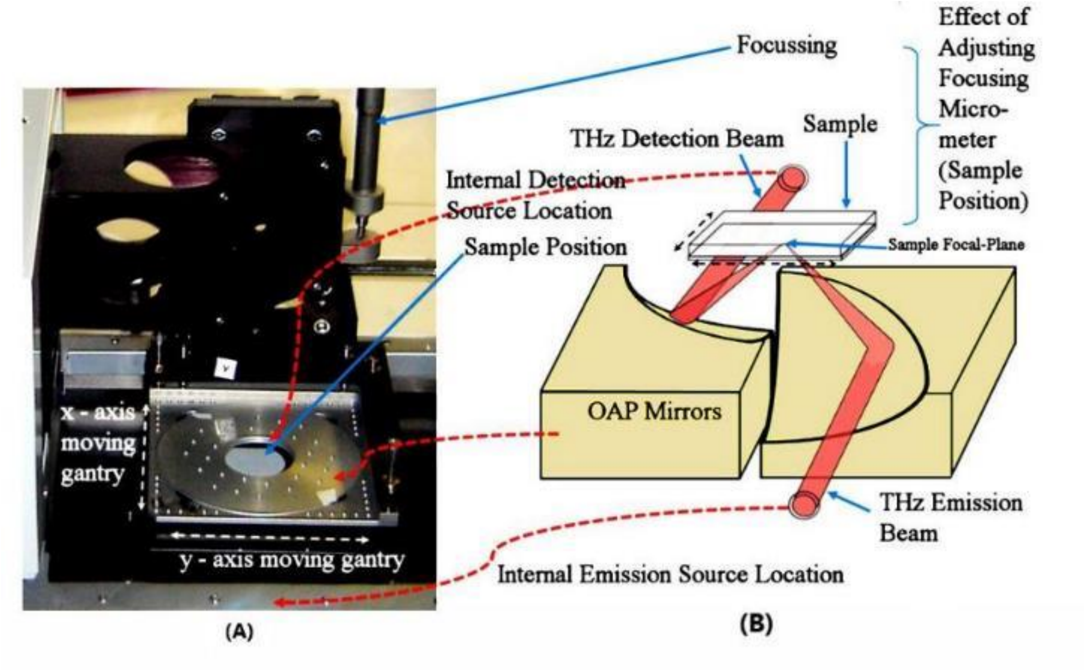

Figure 25: **Photographic and schematic illustrations of TPI. Shown LHS, *A* is TeraView's' Imaga1000™ module, and sketched *in 'B' is the* parabolic mirror assembly underneath the gantry.**

➢ Spot imaging

The majority of the recordings in TPI were taken at singular points at defined points upon the substrates surface. This differentiates acquisition of waveforms from 'spot imaging' and larger '3D' 'regional imaging'. The benefit of spot imaging largely concerns the quality of the TD waveforms: for instance, the any number of pulsed signals can be taken to form a mean waveform during spot imaging, allowing a mean profile to be recorded.

A number of substrate locations were then chosen and scanned with 100 pulses to form a mean waveform representative of exact locations using a gridded co-ordinate system controlled by the software in regard to *xy* positions.

- **3D imaging of a region of the sample**

Regional or full 3D imaging is useful to investigate larger portions of a material. However, the time to carry out this procedure is inversely proportional to the resolution of the image, and material size. Resolution can be defined in TPI imaging as the distance the substrate is moved in respect to the laser. For instance, one waveform could be recorded and later compiled after the gantry is moved 0.5 *mm* vs. 0.02 *mm*. Additionally, measuring a 4cm^2 surface would take substantially longer if the comparative number of scans acquired in spot imaging (100) from one spot, is multiplied by the number of *xy* waveform locations scanned (100 x stated resolution). The resolution quality of the image is thus influenced by the number of pulses and the rate of gantry movement, whereby the accepted resolution of the system is maximally rated at 20 microns. Combining a low number of scans (i.e. 2) with a high *xy* (i.e. 0.6) rate would result in waveforms that are both nosier and not optimising the full resolution offered by the TPS-3000.

Experimentally aquired *E-Field* waveforms collected to predict RI requires application of the Hilbert(*t*) transformation, in order to yield greater accuracies. Found by simulating the complex *H-Field* correctly and thus, converts $E^{max(or\ Min)}$-*Fields*(*t*) magnitudes into signal intensities I^{AUC} values. In regard to the magnitude of the E^{MAX}-*Field* plot. Then with knowledge of (a predicted) RI, the differental optical time-delays of the TD waveform can be used to estimate thickness if $E_t{}^1{}_r{}^1$ (See *Figure 26*) is known to be the posterior surface, and $\theta t°$.

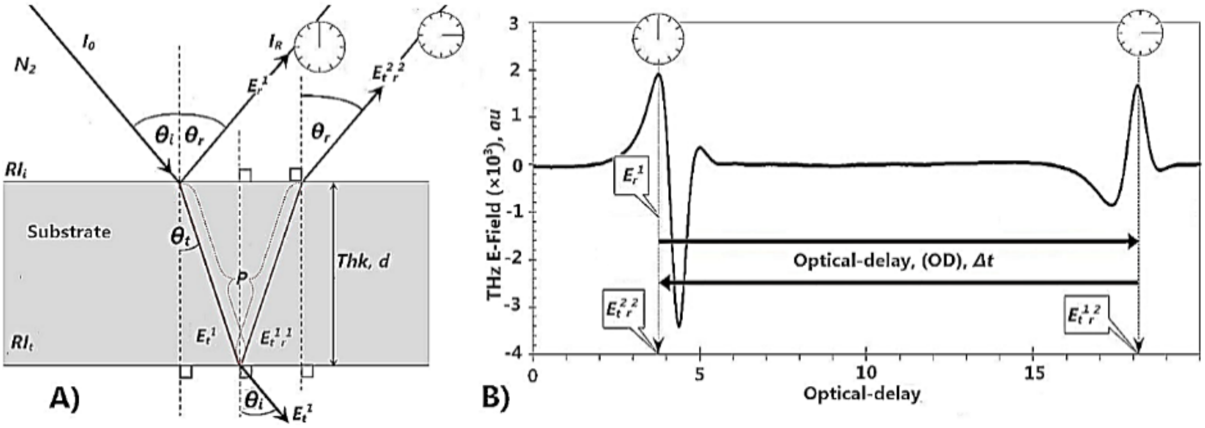

Figure 26: **Schematic (*A*) and a graphical overview, (*B*) of TPI thickness prediction method. The diagrams show typical plots for a slide of fused silica.**

3.5.4 Time-domain transmission (TDT) to predict thickness *or* RI with signal-delay and internal-delay measurements

The transmission method can be exploited to supply two optical time-delay values. One of these stages involves the E^{max}*-Field* (t) between the empty-system reference and that of the first E^{max}-*Field* occurring during singular passage. This sub-method results in a signal-delay (SD) time indicative of the substrates RI & path-length. The second sub-TDT method involves recording the time-delay of internally originating Fabry-Pérot resonations and because the time-delay originates from internal resonations this method is abbreviated to TDT-ID. This method does not require a reference measurement as does TDT-SD, and can be selectively used when the optical-delay window and the E^{2max}*-Field* are both sufficiently broad/sensitive, respectively. The accuracy of thickness predictions is in-turn, theoretically enhanced[13].

A graphical representation of material thickness determination by the *SD* & *ID* TDT methods is illustrated in *Figure 27*. *SD* values correspond to *Figure 27B* labelled as time at '*a*', and between the Emax-Fields peaks 1 and 2, and can only be used when the substrate is static and the corresponding reference time can be obtained. Further interpretation of the plots in *Figure 27* show that internally caused resonations are caused by multiple probe-beam passes inside the

---

[13] With understanding that the substrate is homogenous and θ°_t is minimal.

substrate (hence the attenuation of peak ‘3’ c.f. ‘2’).These peaks correspond with times denoted ‘2’ and ‘3’ and referred to as the E^{2Max}-*Field*. The SD measurement is presented in the combined equation shown inset as ‘*a*’ and ID, as ‘*b*’ to provide a value for path-length/thickness (naturally the equations can easily be re-arranged to provide RI if the thickness is known).

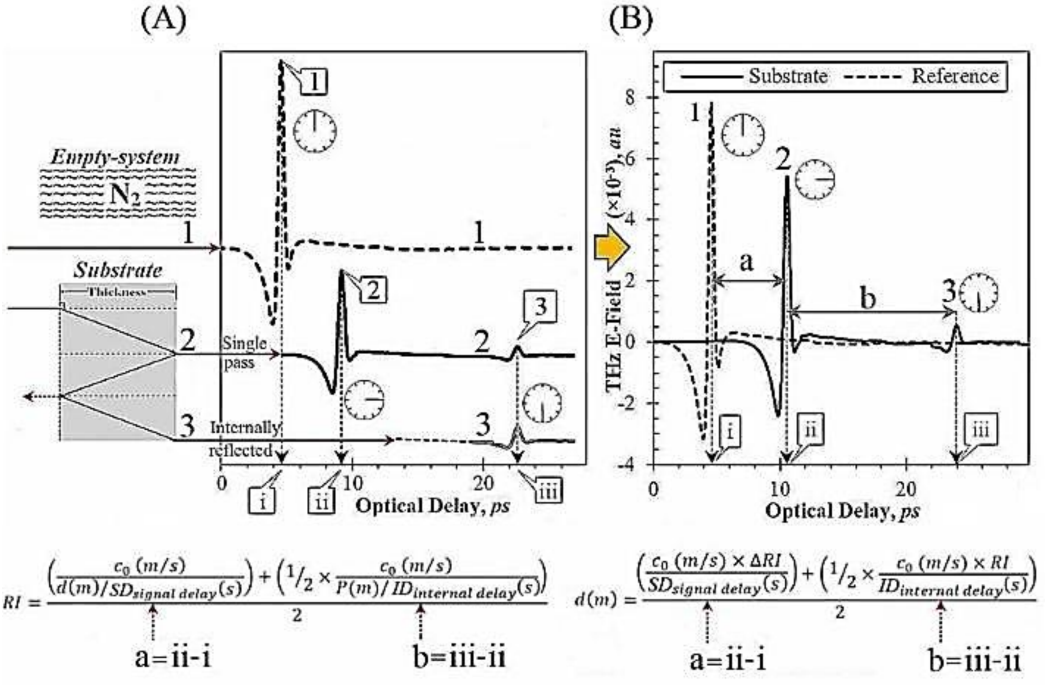

$$RI = \frac{\left(\frac{c_0\,(m/s)}{d(m)/SD_{signal\ delay}(s)}\right) + \left({}^{1}/_{2} \times \frac{c_0\,(m/s)}{P(m)/ID_{internal\ delay}(s)}\right)}{2}$$

$$d(m) = \frac{\left(\frac{c_0\,(m/s) \times \Delta RI}{SD_{signal\ delay}(s)}\right) + \left({}^{1}/_{2} \times \frac{c_0\,(m/s) \times RI}{ID_{internal\ delay}(s)}\right)}{2}$$

Figure 27: **Overview of the TDT method to determine thickness using the TPS-3000. Incorporating principles originating from SD and ID based measurements. The plots depict time-resolved waveforms for a sheet of fused silica glass.**

Attenuation of the magnitudes of maxima peaks (*See Figure 27* ‘*1*’) is further paralleled with peaks *2* and *3*. The *above* waveforms also illustrate that transmission analysis does not enable quantification of light reflected at the first interception, or lost to the LHS side of the sample (where no detector is present). The waveforms therefore shows the effect of the materials RI with equivalence to the intrinsic absorption coefficient of the substrate, and to the path-length traveled.

Additionally, extrapolation in *Figure 28* of the TDT waveform of silica at ‘*ii*’ and ‘*iii*’ (at approximately 17 *ps*) suggests that if an E^{max}-*Field* magnitude reading could have made of the internally reflected 1st echo (from the posterior), that by fitting a linear line of best fit through points *i*, *ii* and *iii* and noting the time, this time matches the halfway point between peaks ii and iii. This linearity indicates that the sample is homogenous in regard to RI (thus, chemical uniformity), thickness (from the perspective of optical time-delay) and planar in topology.

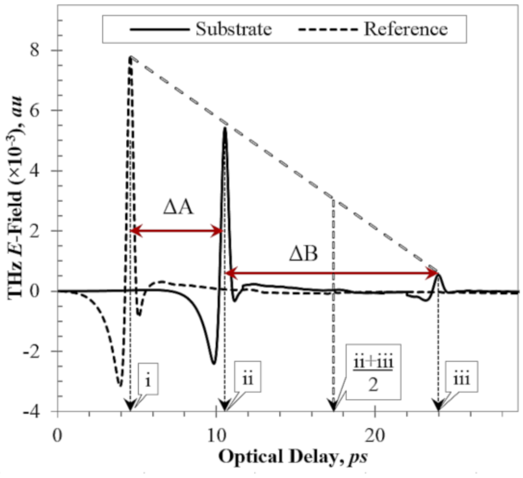

Figure 28: **Transmission TD spectral plot of the (homogenous) silica glass showing the linear dependent function of substrate thickness/path-length'.**

Transmission analysis of either spectral or TD data can only be considered currently as an off-line method (re) PAT application. This issue raises the point that in regard to real-time analysis, pharma compacts will not comply with a defined thickness nor RI. **Moreover, the knowledge of either of these parameter is essential for potential real-time usage**. For the reason to enable RI/density measurements (acquired rapidly), the principles of time-delay can be key in uniting the principle methodologies of reflection and refraction to independently provide a parameter of RI.

3.5.5 Extraction of RI from the TPI method

The TPI derived RI of a substance is an approximate value that follows from a number of data interpretational stages and calculations that require a comparative value (of the material under investigation) to form a reflection coefficient against a highly reflective gold plated mirror. These steps are addressed within this section. The first stage is to acquire TD profiles of the analytes and the mirror, with care taken to assure the pulsed signal's path-length (or *z*-distance) is identical in all cases. This is done by moving the gantry up or down to align the maxima *E-Fields* magnitudes to equal optical-path values(t), to place all analytes at equal focal planes. The acquired TD data is then passed through a standard Hilbert transformation routine (*defined in 3.5.6* to give amplitude profiles *See Figure 29E*) and then interpreted to find the area under the curve (AUC).This represents the initial interaction of the THz pulse with the analytes. This time region will be similar amongst all analytes due to successful focussing of the z-plane method step. To further enhance the AUC (therby the r_p). a low signal amplitude filter is then applied to both remove system/background and artefacts[14], while also providing information of which intensities are great enough to be considered for the calculation. The samples AUC is next divided by the mirrors AUC value (with the assumption that $I_{r0} = I_{r1}$, atleast systemically), providing a reflection coefficient (*Equation 5)* necessary to next predict RI.

$$r_p = \frac{AUC_{substrate}}{AUC_{reference}}$$

Equation 5

---

[14] The data correction techniques applied to the Hilbert *H(t)* profile are developed in *Experimental chapter 1 & Experimental chapter 2* to enhance the accuracy of any RI prediction.

With reference to *Figure 29*, *A* and *B* represent the physical origins of the experiment and the corresponding *E-Fields* (*t*) of *A*→*C* and *B*→*D*. Followed through in *E*, the Hilbert transformed profile of *C* and is compiled (giving *I*(*t*)) [102]. The next stage is to analyse the relevant data-bins of the time-intervals in regard to the time regions of the initial probe beam-substrate interaction (i.e. in *Figure 29* '*E*' these would be in the region of 0 to 5 *ps*) and of course, the heights of the amplitudes. With the optimal $\int r_p$'s interpreted and used in *Equation 5*, the substrates RI is readily calculated with the use of *Equation 6*:

$$RI_{substrate} = \frac{1 + r_p}{1 - r_p}$$

Equation 6

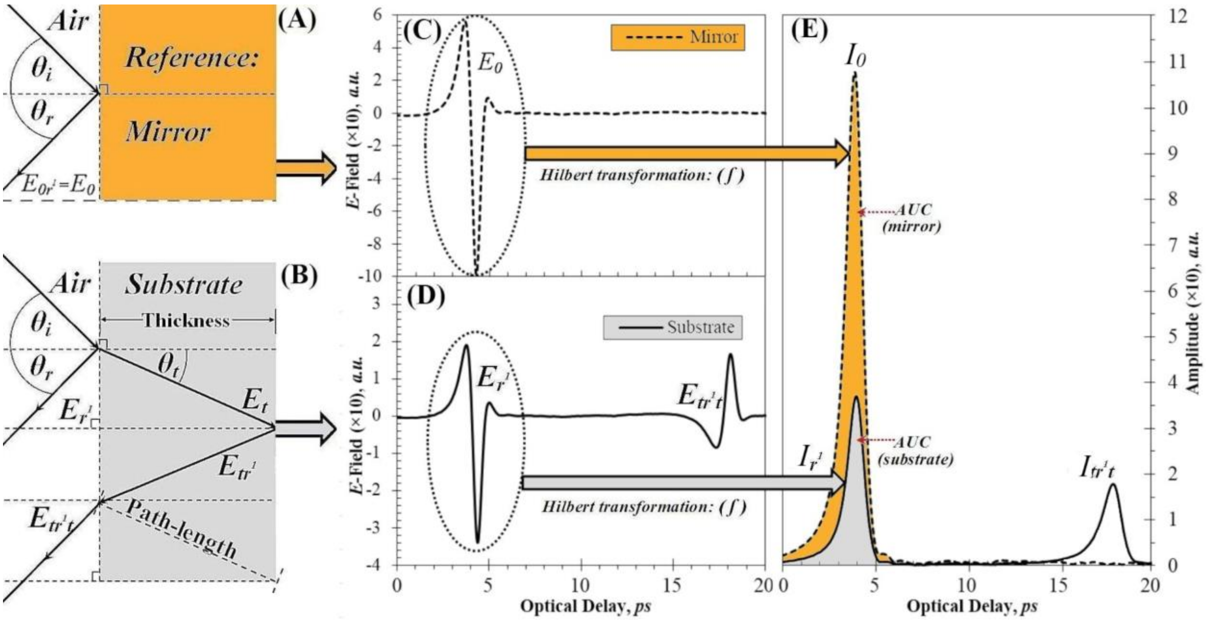

Figure 29: **Overview of TPI analysis to determine RI using the TPS-3000 using compiled TD waveforms and a compiled amplitude plot of silica glass.**

3.5.6 The Hilbert transformation

To predict accurate material RI values using TPI, the *E-Field* magnitudes of the conventional TD waveform (e.g. *Figure 29*, *C* and *D)* need to be transformed into amplitude values (signal intensity). This stage requires the use of a Hilbert transformation procedure, because the real component given in TD waveforms (the *E-Field*) is not wholly descriptive of the conductivity changes in the photoconductive antenna. This signal processing technique is commonly applied to TPI analysis for extraction of intensity/amplitude values [103], which can later be substituted into a simplified Fresnel amplitude reflection coefficient (*Section 3.5.7*).

A greater description of the mathematical transformation can be found in resource [104]. Yet in summary, as the reflection amplitude coefficient, r_p is needed to predicted RI, the time-resolved complex conjugate of the real-valued *E-Field* ± *E*(*t*) of *E* (where *I* (t) = *E* (t) × *E* *(t)) needs to be found. By using the transformation defined using the model given in *Equation 7*, the complex conjugate becomes the amplitude, *I* (t).

$$\bar{E}_{x,y}\,(t) = \; E_{x,y}\,(t) + \Im H\left(E_{x,y}\,(t)\right)$$

Equation 7

The resulting profile is modelled in the TD with an *envelope* of intensity values over a range of discrete time-bins. By then applying Pythagorean theory (*Equation 8*) to the results, real-valued amplitudes (*t*) can be constructed (*as illustrated in Figure 30*):

$$I\,(t) = \sqrt{E^2(t) + \bar{H}^2(t)} \Rightarrow I(t) = \sqrt{E^2 + \bar{H}^2}$$

Equation 8

The integral of the amplitude plot can readily be calculated, yet system noise and definition of peak areas at the specific interaction time of the area of interest for RI determination (witnessed in *Figure 30* between 15 – 23 *ps)* encourages the use of trapezoidal area under the curve (AUC) analysis for increasingly sensitive RI's rather than the integral value.

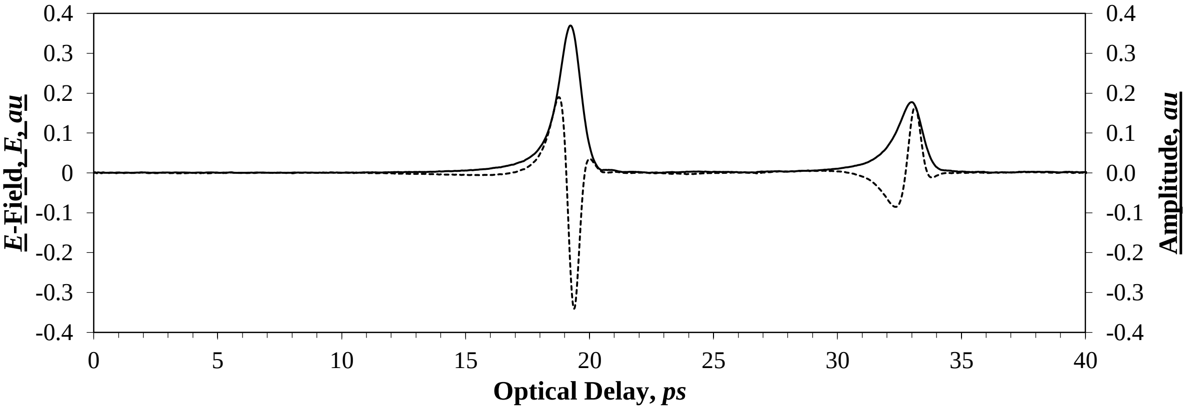

Figure 30: **A typical TD waveform (dashed line) of the *E-Field* (t) response of an Avicel® tablet with the signal modelled amplitude results from the profile of the Hilbert transformation (solid line).**

3.5.7 Fresnel's reflection amplitude coefficients

The origin of Fresnel's reflection amplitude coefficients stem from Maxwell's classical wave equations (*See Appendix Section 10.1.1*) and incorporate derivations that include Snell's law of reflection in order to predict either RI's of two mediums or the probe-EMR's angle of incidence to either medium.

The two general forms of Fresnel's parallel (||) and perpendicular (⊥) coefficients for amplitude **reflection** are given in *Equation 9*. The parameters denoted r_x, are the terms of the reflection (w.r.t. the plane of incidence), where ⊥ signifies the perpendicular component of an EMR signal and, || the parallel component. An overview of the concept of the positioning of the *E-Field* to both || and ⊥ to the incidence plane is shown in *Appendix Section10.1.2.1.*

$$r_{\parallel} \equiv \left(\frac{E_{0r^{\circ}}}{E_{0i}{}^{\circ}}\right)_{\parallel} = \frac{n_t\,cos(\theta_i{}^{\circ}) \;-\; n_i\,cos(\theta_t{}^{\circ})}{n_i\,cos(\theta_t{}^{\circ}) \;+\; n_t\,cos(\theta_i{}^{\circ})} \qquad r_{\perp} \equiv \left(\frac{E_{0r^{\circ}}}{E_{0i}{}^{\circ}}\right)_{\perp} = \frac{n_i\,cos(\theta_i{}^{\circ}) \;-\; n_t\,cos(\theta_t{}^{\circ})}{n_i\,cos(\theta_i{}^{\circ}) \;+\; n_t\,cos(\theta_t{}^{\circ})}$$

Equation 9

For brevity, the steps of the empirical derivation of the *above* equations to express r_x in respect to the angle of incidence only (*0*°) and then to an RI (of one r_p) are shown in the Appendix (*Section 10.1.2*), which yields *Equation 10*, and then simplified to give *Equation 11*:

$$r_{\parallel} \equiv \left(\frac{E_{0r}}{E_{0i}}\right)_{\parallel} = \frac{\sqrt{1^2} - n_t \times 1}{\sqrt{1^2} + n_t \times 1} = \frac{1 - n_t}{n_t + 1} \qquad r_{\perp} \equiv \left(\frac{E_{0r}}{E_{0i}}\right)_{\perp} = \frac{1 - \sqrt{n_t{}^2 - 0^{\circ}}}{1 + \sqrt{n_t{}^2 - 0^{\circ}}} = \frac{1 - n_t}{1 + n_t}$$

Equation 10

$$\Rightarrow \boldsymbol{n_t} = \frac{\boldsymbol{1 + r_p}}{\boldsymbol{1 - r_p}}$$

Equation 11

To produce a practical equation for RI determination *Equation 12* is further yielded from derivation given in Appendix Section And can be further simplified (*see Appendix Section 10.1.2.2*).

$$RI = \frac{1 + r_p}{1 - r_p}$$

Equation 12

3.5.8 Limitations and constraints of data treatment

Simplification of the Fresnel **amplitude** reflection coefficients assumes that the RI of the surrounding medium is *1* and the substrates are planar /specular. As the angle of incidence, θ_i°, increases from the normal line of incidence, θ_0°, the $r_{\perp}$ and $r_{\parallel}$'s diverge increasingly t for the $\perp$ and $\parallel$ components in a inversely proportional relationship as $\theta_i^{\circ} > 5°$ (*See Appendix Section 10.1.2.3, Figure 111*) yet, the two field-components can be traced from mathematical modelling to show the r_p (the mean value of the $\perp$ and $\parallel$ components), results in an r_p (predicted) discrepancy of 0.0009, equating to a discrepancy in RI of 0.005 (Silica's RI is 1.95).

Importantly, and the experimentally deduced r_p of the silica glass modelled here takes at angle of incidence from the norm. of $\theta_i^{\circ} = 30°$ The significance of this small error has a relatively low impact on the RI prediction, signalling that the simplified Fresnel equation can be used for a reasonable indicatory RI estimation in this field of work (e.g. well with 5% agreement of true RI).

3.5.9 TPI thickness determination following Fresnel/Hilbert and data interpretation techniques

To yield thickness from optical delay-times requires registration of the reflected proportion of the incident pulse from the substrates anterior surface (*Figure 31B* as E_r^1 *or '1'*), coupled with the OD time originating from reflection from the rear of the substrate ($E_r^2 t^2$ *or '2'*); providing a Δt value, '*P*'. Coupling knowledge of the materials RI, θ°_t and the OD derived path-length of *2-1* allows prediction of material thickness with the inset equation which incorporates trigonometric functions because the incidence angle of the probe-beam to the normal line is substantially greater (*30*°) than that used in the TDT method.

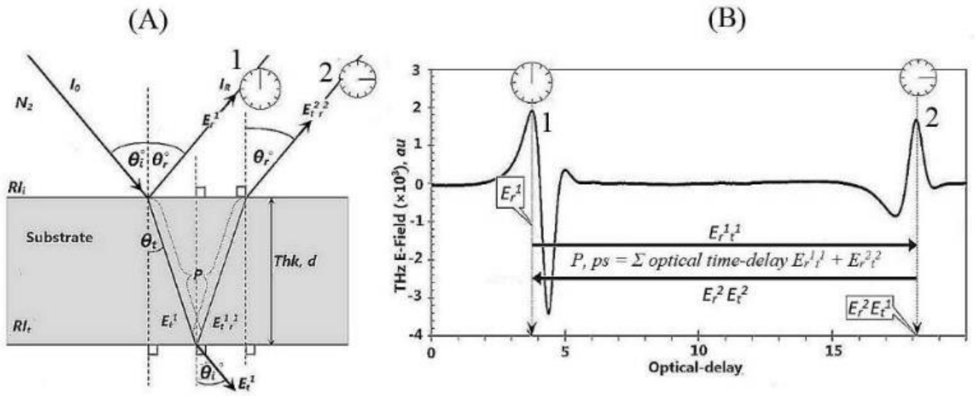

$$\theta_t^\circ = ArcSin\left(Sin\,\theta_i^\circ \times \frac{RI_i}{RI_t}\right) \Rightarrow Thk^n = \left(\frac{c_0(m/s)}{RI_t}\right) \times \tfrac{1}{2} P(m)\left(Cos\,\theta_t^\circ\right)$$

Figure 31: **Overview of TPI to determine material thickness with known RI. The diagram shows typical plots for a slide of fused silica glass.**

3.5.10 Conclusion of using reflection and light refraction to determine the RI of a material thickness or

Estimation of RI from principles of light reflection using the simplified ‘non-oblique’ Fresnel equation with TPI allows material RI to a high degree (-0.005) Using the true oblique angle of incidence to yield a practical mathematical solution of $r\perp$ and $r_{||}$ to yield absolute RI’s may not be fit-for-purpose. For instance: The benefits of inherently more accurate RI’s would necessitate greater computationally power (and thus time). Furthermore, consideration must be made of the necessity for highly accurate/absolute values of RI in a practical setting. For instance, if the discrepancy of the assumption provides RI’s with minimal errors, these would be both 1) Systematic, and a correction factor could be devised and, 2) TPI RI readings are there to predict density in a continuous setting. Importantly, uniformity assessment of any analyte would be relative to the current production run and not necessarily important for batch-to-batch comparison, particularly with different formulations. Finally the effect upon thickness determination is also relative, yet expected to be marginal. This will be assessed in method development of the TPI technique (vs. TDT) in the *Experimental Chapters.*

3.6 Experimental frequency-domain transmission with the TPS-3000

The FDT method provides the most precise method of measuring the bulk RI values with transmission through the entirety of the substrate, as a function of frequency. TD waveforms are subsequently limited to give absolute RI's waveform profiles are unable to readily indicate frequency. This method is solely included to serve as a comparative technique therefore to the two time-domain methods and like all transmission studies requires knowledge of either RI or material thickness to yield the other.

3.6.1 System setup

See Section 3.5.2.

3.6.2 Frequency-domain transmission (FDT) to predict material RI

Extraction of RI requires a time-resolved reference measurement in order to contrast the signal velocity against the retardation of *c* occurring with material propagation. A time-domain profile of a reference measurement (sample positioning and spectral analysis parameters are given in *Section 3.5.2*) is shown overlaid in *Figure 32A* (1) with an arbitrarily chosen Avicel® tablet; (labelled '*3' in Figure 32A*). In this method a routine fast-Fourier transformation of a conventional time-domain profile are calculated (via bulk software of the TPS-3000) to produce: 1) A frequency-domain power spectrum (*Labelled 'B' in Figure 32*) from the real component of the Euclidian data and the transmittance phase from the complex component (Giving a phase profile as seen in *Figure 32C*). The complex RI's are then calculated with usage of the inset equation in producing a RI plot as a function of frequency (*See Figure 32D*). The RI's reported from this method are taken as a mean RI value taken from the region of THz frequencies that plot the greatest plateau region, and if possible, bare a std. deviation of < 0.2.

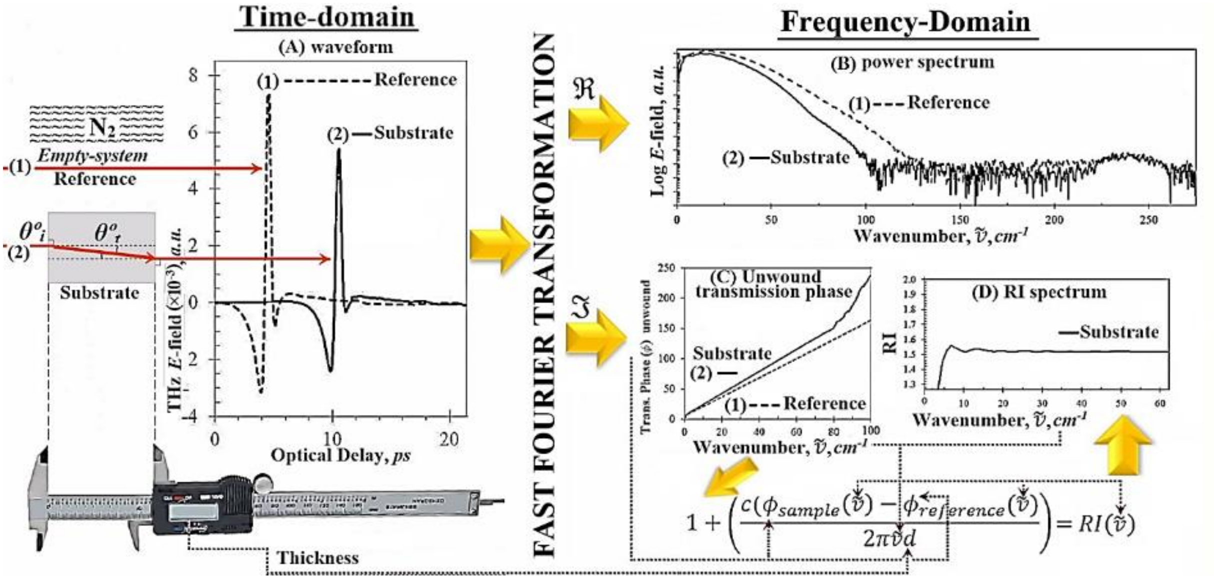

Figure 32: **The overview of FDT analysis to determine RI using the TPS-3000.**

3.7 Unique modes of material characterisation offered by TPS-3000

The ability to quantify the permeability of an optical emission having propagated through a material has been established with many spectroscopic tools. Studying the THz spectral band furthermore advances property characterisation to the existing optical tools.

The energy conveyed within pulses of THz EMR is non-ionising to non-conductive species, beneficial particularly to pharmaceutics. Illustrating this within the infra-red region a comparison is made in *Figure 33* between the sensitivity of a THz pulse against that of a 50 *fs* 800 *nm* optical source (NIR)[15]. A greater number of single-cycle oscillations of *E-Field* readings/ unit-time via femtosecond sensitivity obtained via THz than a more rapidly oscillating pulse-train; less readings than by NIRS. Although NIR spans a comparatively narrow EMR than THz. Direct measurement of the *E-Field* component samples a greater number of frequencies associated with discrete time-bins, not with-standing the greater resolution in regard to depth analysis.

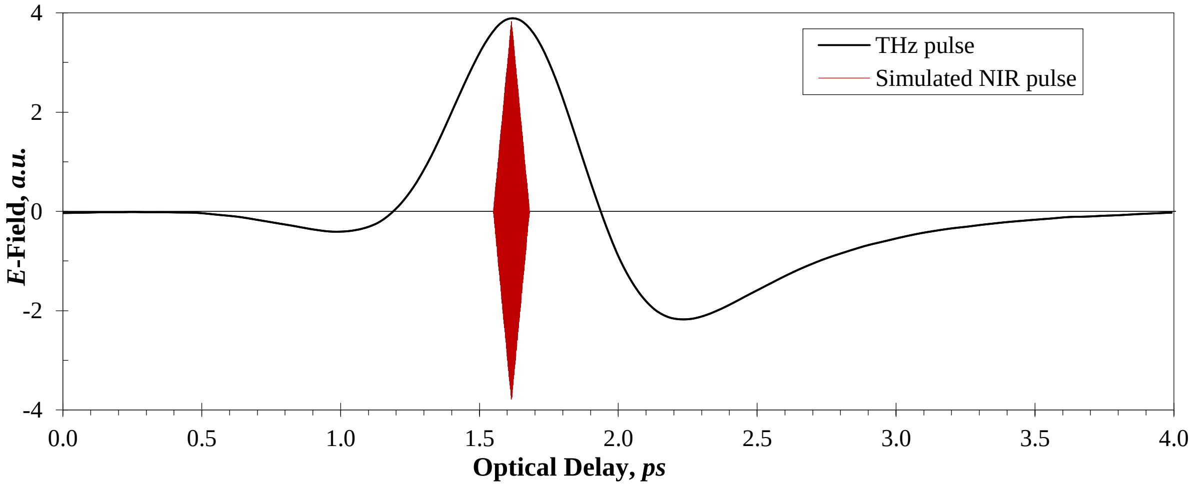

***Figure 33:* Time resolved *E-Field* of a typical THz pulse and a simulated field of a NIR pulse. Note the elongation of a greater scale of scrutiny with TPS.**

In summary TPS provides inherent ability to :

---

[15] Used herein to generate the THz pulse via photo-excitation

1. Coherently detect signal peak intensities (reported at several orders of magnitude with continuous wave IR devices provides a significantly higher SNR [105, 106]), with heightened temporal precision.
2. The E_v imparted over the THz range reduces photo-excitiation and potential damage to the substrate/API. The longer wavelengths of THz radiation are thus less prone to scattering effects, making it particular useful for imaging purposes [107].

3.7.1 Uptake of THz technology by the pharmaceutical industry

THz EMR has been trialled for pharma material characterisation. These include:

i. Spectroscopy for evaluating the degree of crystallinity/cataloguing the absorption coefficients and refractivity of molecules/materials.
ii. Polymorphism, and hydration character [107, 108].
iii. Imaging technologies for qualitative and quantitative characterisation of multi-layered substrates. For instance, peer-reviewed literature cover tablet coating uniformity/thickness, [40, 93, 109-112] and to correlate coating efficiency with dissolution profiles [113, 114].

3.7.2 Conventional solid state spectroscopy

Vibrations of non-covalent bonds at the intermolecular level and, around large molecular pendent units are the key microscopic effects influencing THz spectroscopy from photon absorption [107], the majority of solid-state THz transmission has focused on probing characteristic lattice vibrations of crystalline materials to extract unique behaviour and data including amplitude and phase of the pulse[16].

Analysis to evaluate and develop accurate RI readings from in-line TD configuration mode. The focus of spectral THz usage shall focus on the origin, definition and uses of refractivity ahead of the many spectroscopic tools the technique can provide, which are ostensibly made in-line to the process.

The RI is an important parameter for many pharmaceutical applications [116]. Traditionally measured using polarised light microscopy (PLM) at a wavelength of 598nm under STP, RI has been used to identify compounds, polymorphic nature [117], and for prediction of material properties including surface tension [118] and solubility [119]. In returning to RI, the accuracy of PLM is limited for many reasons, of which advancements in THz technology is now, including thickness measurements for semi-conductors, [120] polymers [121], glasses [106] and paints [122].

Successively, more simplistic methods of assessing TD waveforms for thicknesss and density have arisen [123-125] and discussed herein, qualify as tools to monitor chemical and bulk properties and conceive a potential method to monitor and control output properties in-line (i.e. roller-compaction).

Imaging is a more recent technological advancement employing the same principles of THz generation and detection that is applied in solid-state (transmission) spectroscopy. The majority of TPI research for PAT applications focus on monitoring coating thickness in solid dosage forms [40, 93, 99, 109, 110, 113, 114, 126-133]. Yet a small number of studies have evaluated TPI for tablet compression behaviour in time-domain applications [134].

---

[16] Acquisition of amplitude and phase directly relate to the absorption coefficient and the complex refractive index, as well as the complex permittivity 115. Schmuttenmaer, C.A., *Exploring Dynamics in the Far-Infrared with Terahertz Spectroscopy.* Chemical Review, 2004. **104**: p. 1759-1779..

3.7.3 Tablet coating thickness determination

Initial TPI usage as an at-line product assessment tool for thickness uniformity of the coating process is documented in [133]. Here a TPS-3000 and Imaga2000™ unit: a 6-pivot robotic arm assembly (TeraView, Cambridge, UK) scans the complete surface of tablets at a point spacing of 200 µm × 200 µm. With acquisition of waveforms (i.e. pixels) of thousands of single pulses, time-resolved reflection events are compiled, yielding 3D images of coating thickness to correlate with comparison to destructive dissection and SEM imaging [93]. An example of a single waveform made from one spot measurement is shown in *Figure 34*, courtesy of TeraView [135].

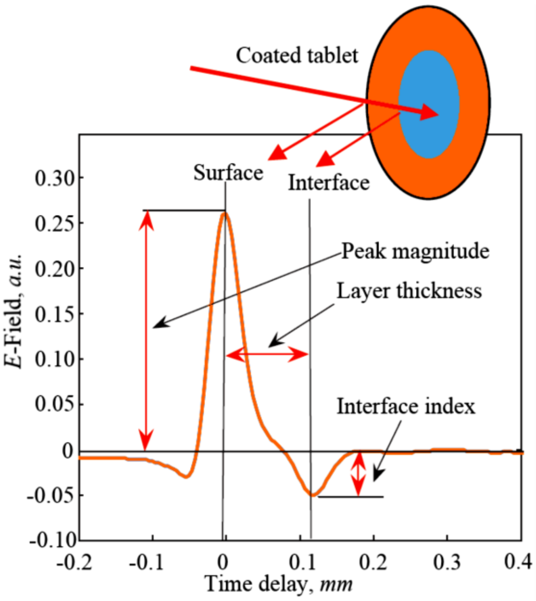

Figure 34: **A typical THz waveform of a single-layer coated tablet. The coating thickness is calculated as the OD (t) between the surface reflection and interface reflection (using the RI of the coating). The insert shows schematically how THz pulses were reflected from the surface and the interface of a tablet. Image readapted from source [99].**

TPI product inspection is of course time-consuming and thus, cannot be representative of entire batches. Quantitative and rapid transitions of THz technologies are emerging in coating analysis whilst gaining increasing attention with product and process understanding over the past decade (2012) [107]. Where repeated and individual reflectance readings are acquired during coating to profile the mean coating thickness. The potential benefits are then of a real-time data acquisition system, supported by a knowledge-based database of defined quality parameters to ultimately motion the endpoint of the process. Unlike at-line analysis, singular THz pulses recorded in this manner are therefore representative of random spatial points at the substrates surface while mean thickness profiling samples more of the batch. The scale of scrutiny (or the entirety of the information of coating distribution per dosage form) is subsequently reduced, but so too is measurement acquisition time (lessening from ~30 minutes to ~50 *ms*). Further demonstrations of quasi in-line capabilities of CQA monitoring and CPP control of the coating process (situated in early stages of drug development) are reported in these recent sources [107, 132, 133], and an illustration of THz probes situated around a perforated coating drum are shown *Figure 35*. Advantageously, TPI is not significantly affected by coating residue on the antennae units (which can be an issue in NIR PAT) because the coating material is invariably semi-transparent to THz radiation, and that the focal-point of the laser-footprint can be adjusted, beyond the lens. To the detriment of coating analysis assessment with optical methods, relatively narrow coatings may prove insufficient to allow distinction of laminar layering due to the time-resolution of the instruments' wavelength [107], thicker coatings suffer less from this issue.

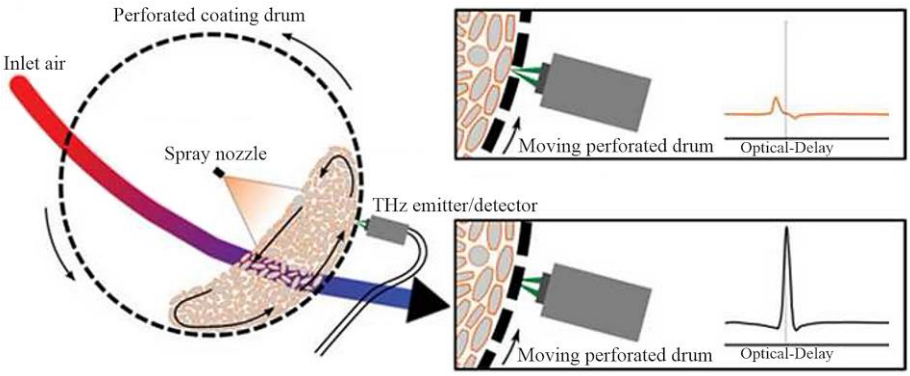

Figure 35: **Schematic diagram of a pan coater with a fitted terahertz coating sensor. Re-adapted from source [135].**

3.7.4 Tablet compression behaviour

Palermo [134] studied the attenuation of maxima *E-Field* magnitudes as a function of compaction-force. A non-linear correlation between pulse attenuation and compact density was observed (R^2 = 94.8%). Also found was that RI's were sensitive to density with a R^2 of 93.7%. The compaction forces used by Palermo [134] to press disks (or pellets) was aligned to pressures used in manufacturing-scale tableting. The author also observed that THz absorption spectra were not significantly sensitive to the density of the compacts and concluded that there the advantages to using FD absorption analysis is best suited for chemical uniformity, but time-domain and RI's were optimal techniques for density analysis.

3.8 Usage and constraints of alternative spectral techniques to provide tensile strength predictions

A literature search reveals non-destructive mechanical-rigidity testing has been undertook with the light based spectroscopic tools of NIR and Raman spectroscopy. With knowledge that mechanical-dynamics are understandably linked to the intra/inter-molecular bonding within a material, and not necessarily with density. THz analysis may be indicative as a PAT/quality test solution for the prediction of mechanical strength from RI assessment (equivalent to density and thus solid-fraction and compressibility) of same-batch products. A brief summary follows of the research (*Sections 3.8.1* & *3.8.2)*

3.8.1 NIR spectroscopy

The procedure is based on absorption to create overtones of intra-molecular bond vibrations, NIR has been proven as a versatile optical method in the fields of drug uniformity and 'finger-printing'. Similar to THz spectroscopy, NIR spectra can be acquired within seconds, and comparative work can require little preparation as long as sufficient knowledge of a materials' spectral features are already characterised [36, 75, 76]. In evolving NIR to NIR-CT, the long established technique has recently been evaluated for predicting tablet hardness.

The two parameters of hardness and strength is frequently measured and are subtlety different in there definitions. Accepted widely is that the strength is a materials ability of resist deformation and hardness is seen as the ability to resist localised indentations, wear and abrasion.

Correlating NIR spectroscopic [17] observations to mechanical rigidity, researchers have evaluated tablet hardness to compaction; yet, to varying degrees of success [75, 79, 81-83]. NIR spectral λ for instance, does not alter with tablet hardness but the baseline and thus intensity (*See Figure 36*) indirectly indicates hardness where an upward (baseline) shift ($\text{Log}_{10}1/R$; *Figure 36*) is used to which fit a line of best-fit.

NIR/CT techniques require computational routines (generally used to convert raw data with principle component analysis (PCA) and routine use of least square analysis to further probe tablet hardness; the full method can be found in source [75]. Given in reference to *Figure 36*, the aforementioned wavelength similarities in both ‘a’ and ‘b’ (with regard to spectral peaks) is common in NIR due to intra-molecular vibrations. Tablets (*Figure 36a*) and ‘b’ are compressed at increased forces and demonstrated is that fitting of best-fit lines over the data sets produced increased systematic changes to the gradients, despite the manner of trending spectra like this [80].

---

[17] Which ostensibly originate from inter-molecular bonds.

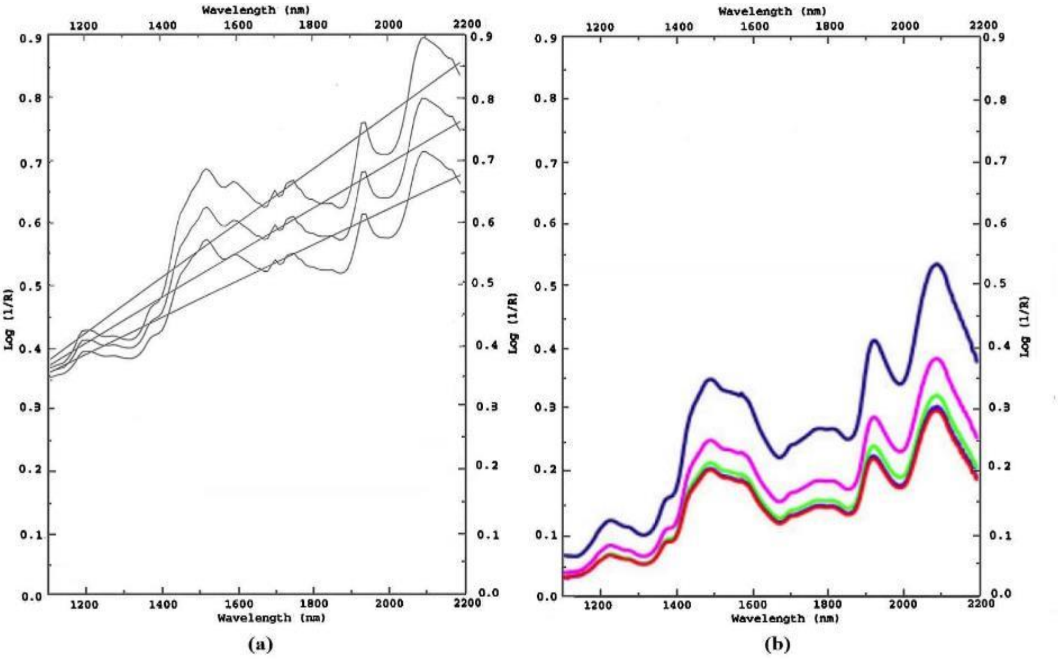

(a)

(b)

Figure 36: **NIR spectra of 20% (w/w) cimetidine tablets (*a*), with diametric hardness between 1.5 and 6.5 KP, fitted with a best-fit line through each spectrum. The increase of gradient in the lines of best-fit do correlate increasing tablet hardness. Shown in 'b', Avicel roller-compacts produced with increasing force again show an upward shift if best fit lines are envisaged. The images have been adopted from sources (*a*: [75], and *b*:[34]).**

Donoso *et. al.* however proposes that the resultant hardness values given by NIR are chiefly influenced by the smoothness of the tablet or compact rather than the mechanical properties. This implies that the gradients (as seen in *Figure 36*) are resultant of the compactional-force creating a s more specular surface, thus affecting reflection and, in-turn absorption nature [79]. A further limitation for hardness testing using NIR is that in practice a new calibration is required to be developed each time an individual product is run, requires extensive testing of multivariate models with PCA [75].

3.8.2 Raman spectroscopy

Research using Raman spectroscopy as a method technique for predicting the mechanical strength of intact tablets [39], also infers that diffuse reflectance increases with a substantial rise of signal intensity with increasingly compact tablets. As with NIR, Raman spectroscopy is has a degree of sensitivity that can be attributed in-directly to a compacts mechanical strength. Virtanen also trialled compressed compacts consolidated at abnormally high compression-forces, to indicate that the Raman signal intensity is $\propto$ to a tablets density [42]. Virtanen and Johansson support the conclusion with demonstrating that a plateau of the interpreting method of hardness prediction prior to the materials true density is reached [42, 85]. In this instance mechanical strength would increase until the material can no longer be consolidated.

To surmise; the sensitivity of Raman spectroscopy is largely the effect of the substrates surface smoothness [85], and neither Raman nor NIR spectroscopy recordings are wholly sensitive to tablet compaction-force and strength [84].Method/materials and tablet preparation regime.

3.9 Current gap in the knowledge.

The gap in the knowledge can be broken down to these factors:

1. Regional SF and thk^n of RC ribbons are key CQA's of the RC process [20]. In reference to *Table 15* the multi-faceted nature of RC is explored from factors requiring enhanced PP control of in-line unit processing, ensuring optimal product performance. On the other hand balancing system settings, system design, the mechanical properties of the compact and material variance [87, 134].
2. Currently robust and practical PAT methods for evaluating local variation of regions of density remains a technological challenge to enhance further regulation of RC PP's
3. Uniform density distribution is acknowledged as an important product attribute which is directly linked to the mechanical properties of a compact. Consequently consolidation is key to product quality and TPI is promoted here as a solution to the gap left by technologies listed in *Table* 15.

The technological limitations to quantify density and thickness with conventional tools is summarised in *Table* 15.

Table 15: **Relevant and recent analytical techniques and their significant disadvantages to rapid density measurements/in-line process compatibility during manufacture.**

Non-appliance in a real-time environment.	Gas pycnometry, NIR-CT, THz TPI.
Destructive techniques that in-turn, can only be applied to a small sample population.	Physical destructive testing (i.e. diametric hardness/ dissolution/ friability etc.)
May contribute to material degradation mechanisms.	Ionising χ-ray CT
High sensitivity to formulations and conditions, and thus require a high degree of user interaction and re-calibration.	NIR-CT, Raman techniques.
Quantification of a comparable density value.	Transducer contour mapping.
Insensitivity to measure local density variation.	RC's that indirectly calculate geometric density from the granule bulk produced (mass) and from the combined roll-gap/circumference and RPM.
Safety of operators.	Ionising radiation sources.

In summary, much literature surrounds reflection analysis for coating thickness evaluation [40, 93, 109, 110, 113, 114, 126-128, 131] and off-line FD analysis to correlate density and compaction-force [92, 115, 123, 125, 134, 136]. Yet there are no published online PAT methodologies to harness the non-evasive, non-destructive characterisation that TPI can be used to monitor and then developed to control the critical process parameters of roller-compaction [92, 110]. The gap can be distilled to 3 THz methods herein for either thickness and/or RI determination. As a benchmark, FDT spectroscopy is used herein to validate parameters involved with evolving the TD methods to potentially indicate routes to improve the uniformity of the properties of thk^n and RI in RC.

- Conventional transmission system configuration using orthogonal pulse/substrate interaction is practised in TDT and FDT methods (See *Figure 37* ‘*a’*).
- The first TD method studied uses principles of optical-delay (OD) to determine material thickness with illumination of glass substrates by THz radiation (synonymised with TDT).
- The second THz TD method incorporates the ability to measure both the OD values of EMR resonance and TPI reflection behaviour with non-orthogonal substrate illumination. For convenience, the reflection method will be abbreviated to TPI with the suffixes of OD and RI for distinguishing optical-delay and surface RI modes.

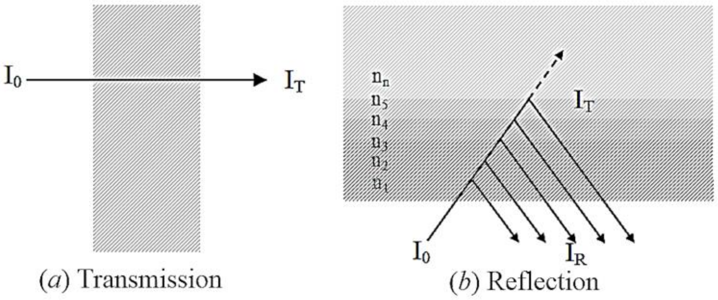

Figure 37: **Pencil ray-diagram of light propagation during (*a*) transmission and (*b*) reflection (TPI) mode analysis.**

Finally, there remains an issue with characterising the density/porosity of pharma products which does not involve off-line only investigation or simple methods of geometric volume and mass accounting. Examples of off-line porosity include gas pycnometry (which gas be insensitive in penetrating tight pores). Similarly X-ray techniques are off-line and can be difficult to quantify, while technology found in some RC's enable rough estimation of bulk density (on a large scale of stock). This system takes the mass of the powder blend and asserts a volume value based on the ribbons assuming uniform thickness and rectangular shape and length derived from the roll-wheels RPM. This method is of course flawed for local uniformity and issues suchas powder leakage.

The conclusion is THz RI measurement may stand as a suitable proxy measure (a unified one) suitable to measure solid-to-air fraction ratios (SF's), applicable to rapid, ultra-fast spot measurements to best offer a large sampling rate for uniformity.

3.9.1 How THz is applicable practically

In *Experimental chapter 1* RI's are provided by literature values measured by Naftaly and Miles' (2007) [137]. *Experimental chapter 1* aims to establish preliminary routines to precisely measure thickness in homogenous glass substrates, and to evaluate TPI as a means to measure RI independently from conventional transmission routes of optical time-delay registration. The use of known standards, stands to gauge whether an accuracy (e.g. within 5% agreement to the literature [137]) can be made with TPI-RI use, and then the OD (t) principles must be galvanised with TDT and then adapted and tested against known parameters (thickness, RI proportional to thickness) with the support of literature to justify a hypothesis to use TPI measured RI's to TPI-OD in-order to validate our methods.

In *Experimental chapter 2* and *Experimental chapter 4*, the work will be extended and re-evaluated with appreciation that the results evaluated on homogenous substrates may need modifying to provide insightful analysis of model substrates comprised of compacted powder (*Experimental chapter 2*). *Experimental chapter 4* meanwhile takes the R&D of the conclusions and modifications to show the effectiveness when applied to ribbons.

This global aim can be concisely depicted in terms of method stages in *Figure 38*, which are in entwined with the material attributes, the design of the specific RC machine system settings to yield ribbons of desirable CQA's (See *Figure 39*).

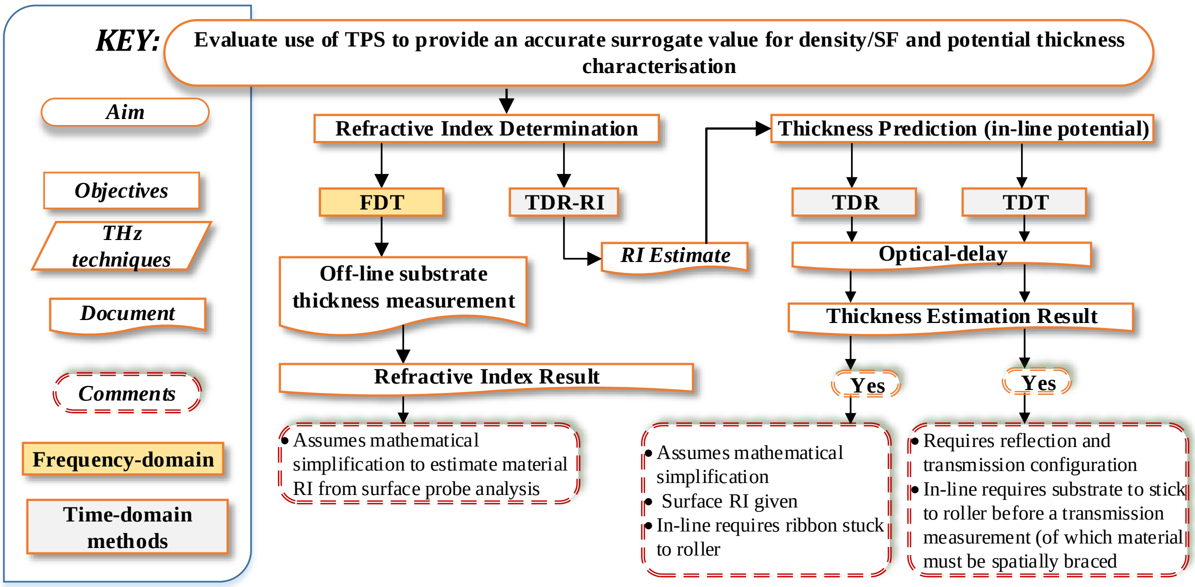

Figure 38: **Flow diagram of the aforementioned THz techniques with suggestive benefits and limitations of the methods.**

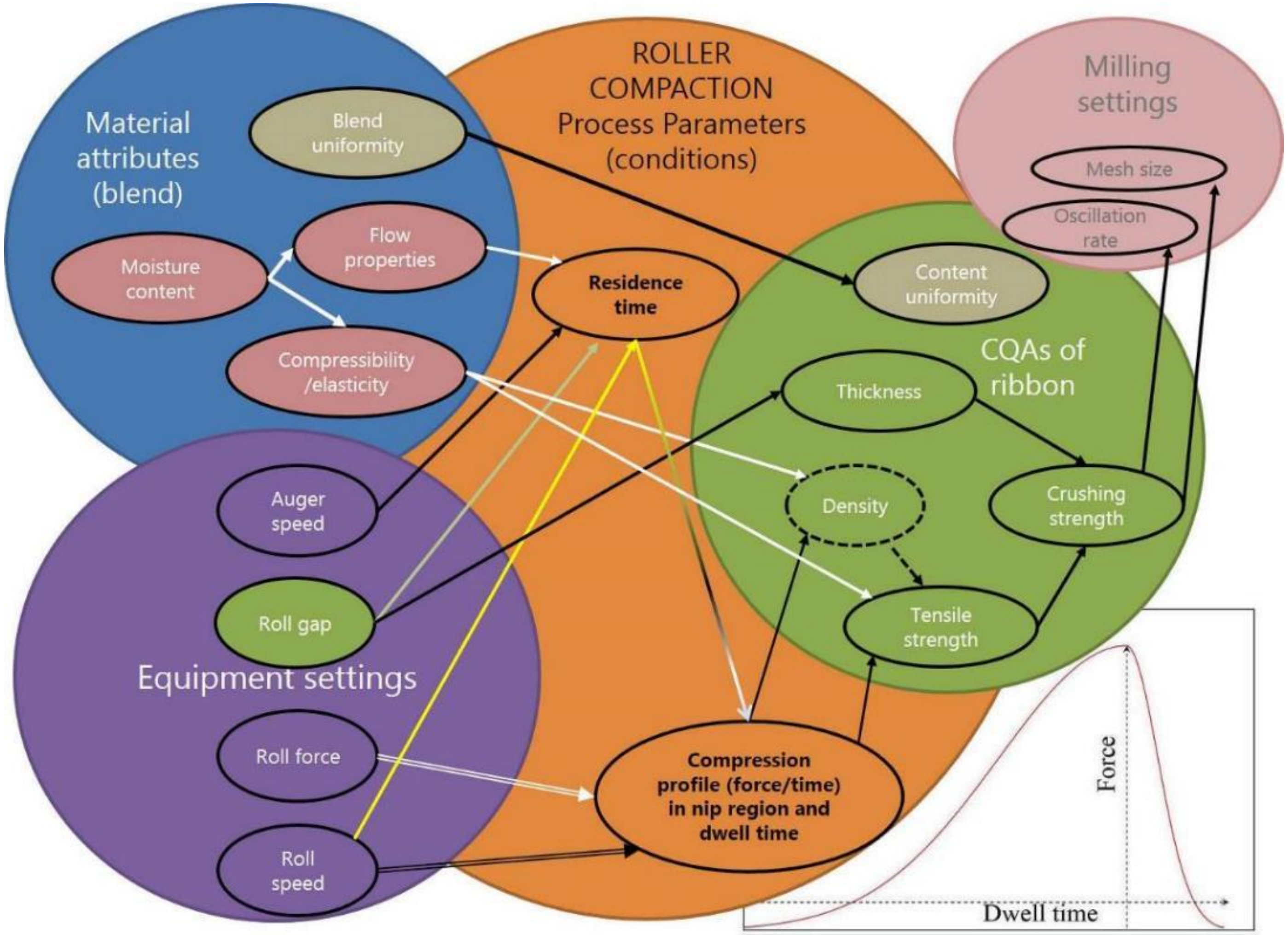

Figure 39: **Schematic representation of the main interactions encountered during the RC unit process. The ribbons CQAs can be largely controlled by the CPPs (or equipment settings) in direct response to variations of the MA's through matching the RC's process conditions to ensure the blends mass flow rate is precisely in tune with the compressional rate (at the roll-wheel) per unit time (as depicted in the inset plot). The use of THz spectroscopy as a potentially secondary PAT tools in industrial manufacturing, if RTS determination using TPS can provide a reliable and potential method to non-destructively test 100% of a production batch of tablets.**

3.10 Summary of TPS analytical methods.

Surmising the methods used herein, exemplar plots are given below and also, the critical parameters needed for characterisation and the main limitations and constraints of the methods.

Time-domain transmission (TDT) analysis

This transmission method can incorporate an etalon detection routine (internal-delay) to complement the experimental accuracy of an OD measurement, (a method referred to as 'signal-delay') recorded between the ref. (empty system) & the 1st signal interaction with the substrates' surface (= Δ *OD*, denoted '*A*'). Denoted '*B*', the internal reflected peak (assumed to originate from the rear surface) provides the Δ *OD* to support measurement '*A*'.

Limitations

Measurement requires the substrate to be:

i. Spatially located in the exact position continuously (between the THz antennae).
ii. Pre-characterised for thickness.

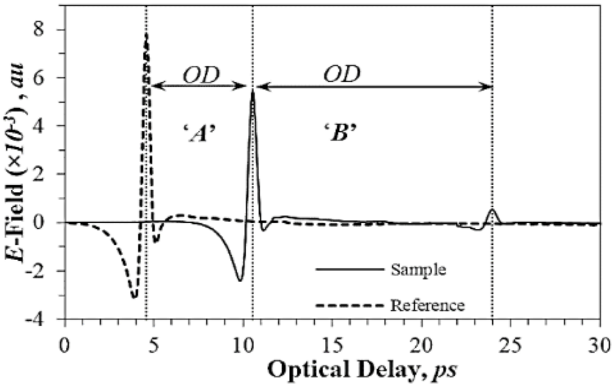

Time-domain reflection (TDR-OD) interpretation

The resultant *OD* value between the substrates front and rear emanating peaks is used with the RI result of method 2 (TDR-RI) to give a thickness measurement.

Limitations

Measurement requires the substrate to be:

i) Of sufficient thickness &/or RI to allow registration of the rear etalon peak to provide a Δ *OD* value. Of note, the increased breadth of the time-window in reflection mode (c.f. with the limitation of method 3's TDT internal-delay) allows thicker/denser analysis.

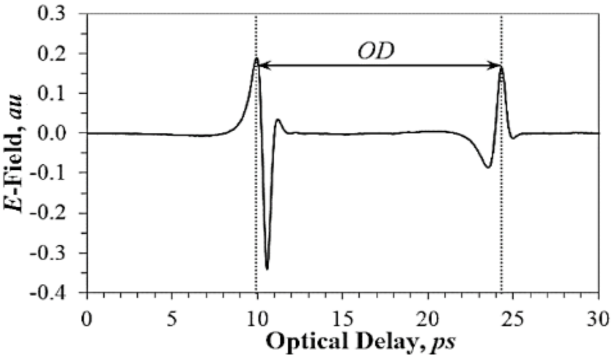

Frequency-domain transmission (FDT) spectroscopy

Shown is a RI plot as a function of frequency whereby a FFT routine compares a required reference measurement to the substrate The quoted nominal range of the TPS is between 0.1 – 3 THz.

Limitations

Measurement requires the substrate to be:

i. Pre-characterised for thickness.
ii. Exactly and continuously positioned between the THz antennae.

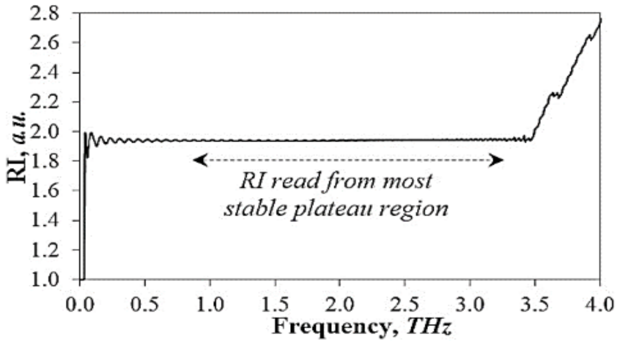

Time-domain reflection analysis with Hilbert transformation (TDR-RI)

The integral of the amplitude (not shown) is interpreted from the initial signal interaction from the substrates surface and contrasted with a reference area (not shown) to form an amplitude coefficient (r_p) for use in a variant Fresnel equation to provide RI.

Limitations

Measurement requires the substrate to be:

i. Exactly and continuously positioned between the THz antennae.
ii. The Fresnel equation requires simplification and is thus subject to a small degree of error in RI determination.

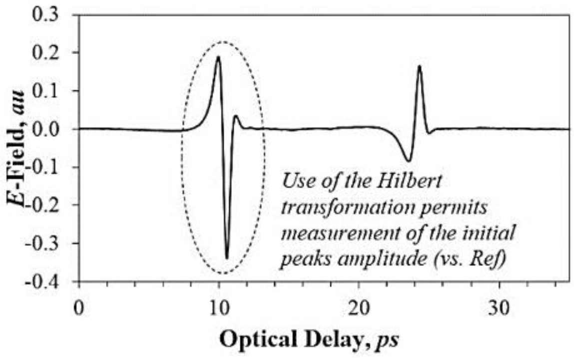

Part II

4 Experimental chapter 1

To establish two terahertz time-domain (THz-TD) methods to reliably measure the thickness of three glass samples by evaluating and developing robust measurement system of optical time-delay differences. Using one method requiring a 'free-space' reference time of *c* (within the system) and knowledge of the intrinsic property of the OEM refractive indices (RI), combination and refinement of the methodologies test the ability to find material thickness and RI independently.

Scope of chapter

The two time-domain methods of transmission and TPI are assessed in order to correlate *E-Field* (*t*) events with material properties (e.g. RI and known thickness). The methods of time-domain (TD) transmission and reflection are abbreviated to TDT and TPI, respectively. The Transmission acquired waveforms are first analysed and interpreted because, 1) refractive index (RI) values are required for optical time-delay analysis; here supplied by literature results of the OEM glass standards made by Naftaly and Mile's [150]. Secondly, as TPT is preferred over TPI at this initial stage because of EMR phenomena including orthogonal interception of the probe-beam with the substrate at the normal angle of incidence (as examined in *Section 3.5.5*). Objectives include establishing the correct steps to predict thickness to a degree of accuracy (>95%) from the optical delay-time from the *E-Field* waveform (w.r.t. time) whilst relying on literature based RI's to necessarily validate the equations to achieve rapport of RI and thickness.

The objective is to then infer the principles of OD analysis (of the transmission method) to reflection imaging (TPI). The system configuration between the methods warrants a complex mathematical model than TDT to derive the parameters (as described in detail through *Sections 3.5* and *3.5.5*). It is the purpose of the comparator literature to help steer development through issues of oblique incidence, and interpretation steps to derive an accurate thickness prediction OD-time. This stage again focuses on the ΔOD time events of waveforms that are common to both methods.

The final stages of development explored lie in evaluating the amalgamation of TDT-OD and TPI reflection principles for thickness prediction exclusively from the TPI method to acceptable limits (with 5% agreement to the literatures RI [150]). Notably, THz RI readings from the literature are instrumentally and mathematically comparable, despite literature values being derived from a routine fast Fourier technique to provide frequency-dependent (FD) values from TD waveforms.

The advantages of Naftaly and Miles's [150] use of FFT to derive conventional spectroscopic data and the disadvantages of their approach shall be explained as the study develops of THZ-TD methods for PAT application.

The chief objective is to therefore gauge the correct method to predict a materials' thickness from to within 5% agreement of the literature which includes correct usage of a viable RI extraction method from TPI [150]. The TPI-RI stages thus stands central and is therefore open to interpretational verification (e.g. trigonometric factors which would alter the direction of the propagated pulse internally due to refractivity) to ensure valid comparison to frequency-RI's

4.1 Objectives and tasks

1. Establish a reliable thickness measurement method with TDT.

➢ Acquire waveform profiles of the three OEM glass substrates.

➢ Evaluate artefacts within the waveforms relevant to time-delay to achieve a thickness accurate to ± 5% actual thickness, given known RI values with measurement from a Vernier calliper.

2. Establish the TPI method to measure the RI and thickness of the glass slides.
    ➢ Where necessity prevails, develop data interpretation techniques to improve the accuracy of interpreting AUC values for an accurate RI method (essential for thickness estimation) to closely approach values given in the literature [150].

- Evaluate the waveform characteristics, in the aim of predicting a thickness value accurate to ± 5% and express any trigonometric factors that influence this method in regard to path-length/.
- Report the and thickness values predicted and deviation/error limits of the method

3. Using RI values calculated from the reflection amplitude coefficient (found from the properties of the first time-resolved waveform), calculate the thickness values of the TPI method from the optical time-delay.

- Evaluate TPI for accurate RI prediction to a degree within agreement ± 5% of the literature.

4.2 Introduction

The specular and planar nature of the glass slides make them ideal substrates for reproducible testing and foundational development This is because they have an (assumed) chemical uniformity, and also planar and uniform thickness given their molten/liquid production. Key to initial OD-time evaluation, thicknesses can readily be verified with a slide micrometre (accurate to ± 0.005 *mm*). The chemical and thickness uniformity is hypothesised to deliver a near (if not equal) density distribution, both in regard to material bulk and its' surface (specular) topology. This is especially significant if one considers that pharmaceutical compacts are the product of mechanical consolidation where regions of differing densities and thickness maybe envisaged. For instance, compacts may potentially display laminar banding owing to the blend's ability to rearrange prior to compaction, variable compression because of retention of the blend on the roll-wheel, dispersion of pressure to each region equally, demixing of powder composites (regionally or locally) and the potential of elastic recovery of the least deformed/bound particles; potentially at the edges.

4.3 Method/materials and ribbon/wafer preparation regime

4.3.1 Materials

The glass slides were acquired from ESCO Products (New Jersey, NY, USA) and are equal to those studied by Naftaly and Miles' [150].

4.4 Product specifications

Glass slides serve as suitable substrates for principle RI and thickness investigation because of density, chemical, thickness, specular nature and chemical composition. Properties specific to the glasses are listed in *Table 16.*

***Table 16*: Specification of the glass slides.**

Glass Properties			
Physical Characteristics			
	Silica	Pyrex	BK7
Thickness ‡, *mm* (uncertainty)	1.08 (± 0.005)	1.73 (± 0.005)	1.01 (± 0.005)
Literature RI † @ 0.1-2.5 *THz*	1.95 (± 0.05)	2.10 (± 0.1)	2.50 (± 0.1)
Geometric density ‡,m g/mm^3 (uncertainty)	2.19 (± 0.5%)	2.18 (± 0.3%)	2.52 (± 0.5%)
Chemical Composition †, *Mol %*			
SiO_2	100	83.0	74.0
B_2O_3	-	11.5	10.0
Na_2O	-	4.0	10.0
Al_2O_3	-	1.5	-
BaO	-	-	1.0
K_2O	-	-	5.0

†: Naftaly and Miles' (2005) *A new tool for the study of glasses in the FIR*. J. Non-Crystalline Solids, **351**, pp. 3341-3346.

‡ = Thickness precision available with a Vernier calliper.

The addition of ionic modifying agents to glass production has commercial applications in order to manipulate the glass strength and chemical suitability as vessels and in the electronic industries (i.e. touch-sensitive screens). The glasses RI's investigated have ionic composition with increased proportions of modifying agents (*Table 16* and *Figure 40*) than with those which do not. The broad RI ranges warrants a brief review of glass engineering in appreciation of the benefits offered by adding various oxides. The essential intra-molecular structure required to form a glass relies on *network formers*, which include SiO_2 and B_2O_3. Alone these form glasses as singularly pure molecular composites [138]. *Network Intermediates* such as aluminium oxide species (as included in Pyrex) are used to improve molecular order (i.e. packing assemblage), thus effecting the macro-scale rigidity. Such intermediaries cannot form a conventional glass structure alone. *Network Modifiers* are included into the network formers for more specific applications. For instance, Na_2O, BaO and K_2O (alkaloid oxides) serve as *Ionic Modifiers*, and in the case of BK7 are necessary in recent touch-screen technologies for the purpose of charge conductance. The inclusion of increased levels of network and modifying agents (i.e. Pyrex and BK7) is shown in *Figure 40* to increase RI (independent of both thickness and density disproportionality).

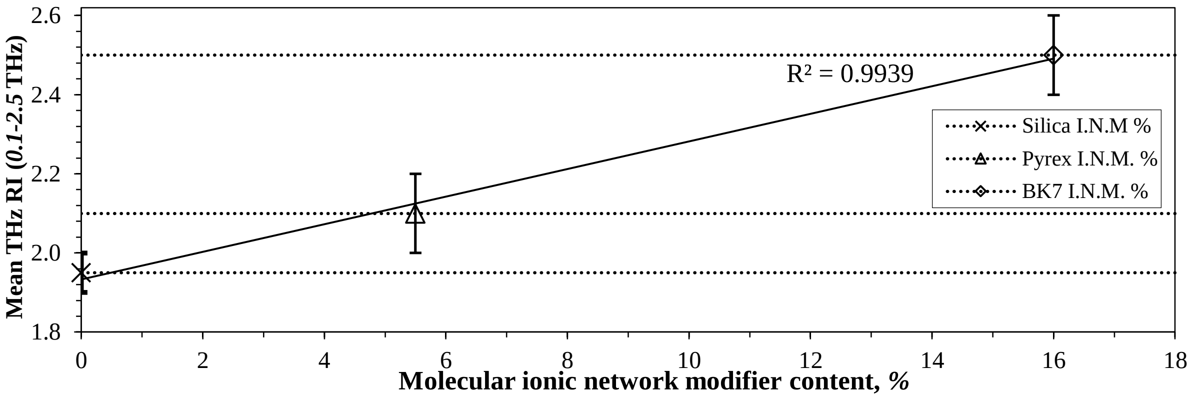

Figure 40: **The contribution of ionic network modifiers to the RI of the glass slides. RI's from source [150].**

Naftaly and Miles' [150] investigated the absorption coefficients of the modified glasses (not shown here) and concluded that the absorption coefficients of BK7 and Pyrex is greater with ionic network modifiers because alkali oxides increase a materials polarisabilty.

4.5 Analytical equipment and methodologies

Detailed in *Section 3.5.2* is the configuration of the spectrometer, and the method of operation for TDT, TPI are described in *Section 3.5.2* and *Section 3.5.3*, respectively.

4.6 Analytical equipment and methodologies

4.6.1 TDT for predicting material thickness using the two optical time-delay routines of signal and internal-delay

See Section 3.5.4.

4.6.2 TPI for prediction of physical thickness

See Section 3.5.9.

4.6.3 TPI peak intensity for prediction material RI

See Section 3.5.5.

4.7 Results and discussion

The first objective is to position TDT as a reliable means to yield material thickness by interpreting properties of *E-Field* waveforms at markers, specifically at *E-Fields* maximums' corresponding to the greatest phase-shifts of the *E-Fields*. Secondly, TPI is used to record E^{MAX}-*Field* resonations to quantify thickness of any propagated portion of the probe-beam which is registered at both anterior and posterior surfaces. TPI features oblique incidence and therefore needs attention to recalculate thickness from a path-length of the refracted signals' OD (*t*), of which is effectively the hypotenuse travel path-path and not the *adjacent* form signifying thickness with trigonmetrical operators. Using the TD methods with OEM glasses provides known RI's, and thus a practical comparative value to avoid deconvolution of RI and path-length in OD (*t*) recognition and TPI-RI following Fresnel-Snell usage and Hilbert transformation. The intensity of light reflected at the anterior surface in TPI aims to bridge independent RI reflection analysis and thus fed into reliable OD thickness prediction.

4.7.1 Objective 1: TDT-SD method development

The basic methodology and system setup are given in *Section 3.5.4.* The transmission waveforms of Silica, Pyrex and BK7 are displayed against the reference in *Figure 41*, alongside RI's supplied by the literature [150]. All off-line thickness predictions subsequently are c.f. actual thicknesses recorded with a Vernier calliper. Multiple OD (*t*) responses from unprocessed TDT waveforms (not shown), consistently report a travel-time taking *301.932 ps* for an empty-system; due too to the additional path-length of the probe beam vs. the pump beam. For convenience, the time-resolved *E-Field* readings are shifted by deducting 301.932 *ps* to create an equal time-baseline for comparing E^{max}-*Field* values. The effect (*see Figure 41*) demonstrates that the SD times (labelled to the LHS side of *Figure 41*) increase, i) By the same time values as the E^{max}-*Field* events labelled RHS of *Figure 41* (relative to the reference) and that, ii) that the increase correlates with material RI/unit of distance. This effect agrees with the findings of Pupeza [139], that the magnitudes of the E^{max}-*Fields* decrease with increased RI. The absence of an obstruction is unsurprisingly given by the empty-system resulting in the greatest magnitude measurement. This allows the *E-Field* EMR to propagate through free-space to bias the detector with minimal absorption (which would lead to attenuation).

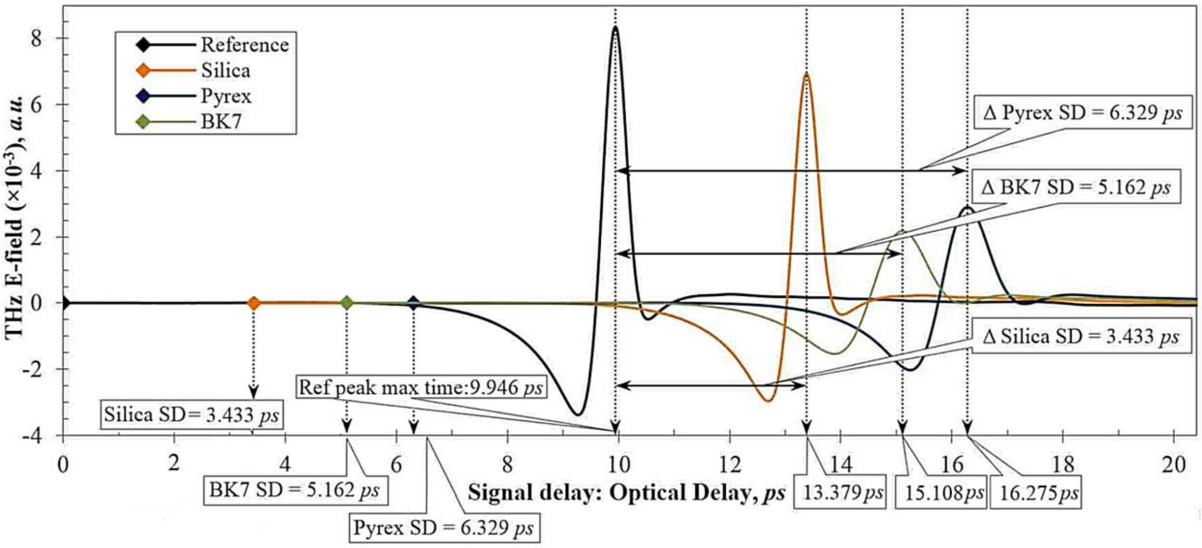

Figure 41: **The TD *E-Field* transmission waveforms of Silica, Pyrex and BK7 against the reference response used during SD. The inset time labels (*LHS*) are the delay-times of an *E-Field* response (at first detection) with corresponding E^{Max}-*Fields* (*RHS*). Being identical, the calculation of SD values can be calculated from E^{max}-*Field* comparisons aswell.**

The SD (*t*) delay-time of a probe-beam passing through the entirety (bulk) of a material can be mathematically modelled with *Equation 13* to give a method for predicting thickness [124], where c_0 is the empty-system measure (*m/s*), and *Δ*RI is the substrates RI - 1.

$$d(m) = \frac{c_0\ (m/s) \times OD_{SD}(s)}{\Delta RI}$$

Equation 13

The significant values inset in *Figure 41* are displayed in *Table 17*.

Table 17: **TDT waveform interpretation to determine thickness. Method: Signal-Delay.**

The first detected optical-delay time of the reference signal, *ps*			301.932
n recordings =	10	10	10
Substrate =	Silica	Pyrex	BK7
Mean Δ OD time, *ps* (uncertainty)	3.43 (± 0.0 %)	6.33 (± 0.0%)	5.16 (± 0.0 %)
Literature RI † (uncertainty)	1.95 (± 2.6 %)	2.10 (± 4.7 %)	2.50 (± 4.0 %)
Actual thickness ‡, *mm* (uncertainty)	1.08 (± 0.5 %)	1.73 (± 0.3 %)	1.03 (± 0.5 %)
Predicted thickness, *mm* (uncertainty)	1.08 (± 3.1 %)	1.72 (± 5.0 %)	1.05 (± 4.5 %)
Discrepancy of thk^{n} with mean RI's and 3 s.f.'s calliper readings	-0.4 %	0.9 %	-0.5 %
Possible thk^{n} range derived from RI/thk^{n} uncertainty, *mm*	1.05 – 1.11	1.63 - 1.65	1.03 – 1.07

†: Naftaly and Miles' (2005) *A new tool for the study of glasses in the FIR*. J. Non-Crystalline Solids, **351**, pp. 3341-46.

‡ = Thickness precision available with a Vernier calliper.

The thickness values derived from the TDT-SD method shows promising results with the mean literature RI values of the substrates compared with calliper derived thicknesses to produce errors of < 1% at 1.08 *mm* for silica as an example:

$$Thickness, d\ (mm) = \left(\frac{c_0(m/s)\ \times OD_{SD}(s)}{\Delta RI}\right) \times 10^3 \Rightarrow \left(\frac{2.997 \times 10^8(m/s) \times 3.43\ \times 10^{-12}(s)}{1.95 - 1}\right) \times 10^3 = 1.08\ mm$$

Equation 14

The descrepancies reported for each substrate and the reference measurement show no variation above 5 s.f.'s with repeated meaurements of 10 taken. The origins of the reported uncertainities can majoritively be attributed to the ± 0.005 *mm* incremental sensitivity of the calliper readings and added to the broad RI margins reported in the literature [150]. Deviation from the mean RI's accounts for the greatest deviation from the actual thickness readings to the predicted thicknesses, while uncertainity accountable to the Vernier calliper are less detremental with errors reported to a maximum deviation of ± 0.5 %. It is not surprisinging that Pyrex and BK7 display greater degrees of uncertainity with reflection of the compostion of the glass-slides, due too the addition of *network formers* and greater proportions of ionic species.

Discounting relatively minor discrepancies causal of the Vernier calliper, and the deterimental effect of additional ionic species. The results displayed in *1*, (especially for silica) at this point, indicate that the TD-SD times assigned to the *E^{max}-Field* magnitudes are viable points to indicate interaction of the THz signal at the substrates interfaces.

4.7.2 Objective 1: TDT-ID method development

Further characterisation is yielded in instances when F-P resonations are measurable. Quantification of FP resonations requires the substrate to possess, a sufficient path-length; (either too narrow, so that the *E-Field* peaks can be differentiated, or the returned THz-signal probe-beam is not attenuated below the level of system sensitivity and finally, the width of the time-rail may be inadequate. The transmission waveforms of Silica, Pyrex and BK7 are displayed in *Figure 42*. Visually apparent is that the SD result (*Figure 41*) omits a reference measurement, and also that ID plots can be (*Figure 42*) displayed over a broader delay-rail/time-window. A broader window is available increasing convenience because the substrates time-axis can be shifted to the region (the maxima *E-Field* values) of interest.

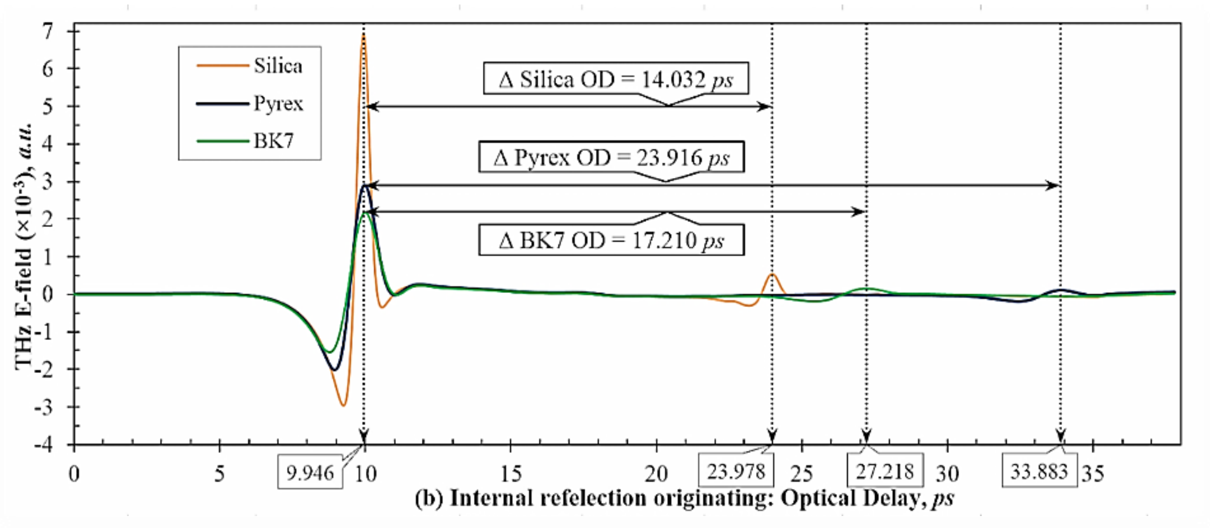

***Figure 42*: ID OD (*t*) *E-Field* transmission waveforms of Silica, Pyrex and BK7. The E^{Max}*-Field* responses are normalised to equal optical delay-times. The insets show *Δ* OD's of THz *singular* probe-beam propagation and the event time of the FP reflections detected on the *x*-axis.**

The additional path-length resulting from ID based F-P resonations requires modification of *Equation 14* to determine thickness as given in *Equation 15*. The term '*P*' = 2*d (m)* f.

$$P\ (mm) = \left(\frac{c_0(m/s)\ \times OD_{ID(s)}}{RI}\right) \times 10^3 \Rightarrow d\ (mm) = {}^{1}\!/_{2}\left(\frac{2.997 \times 10^8 (m/s) \times 14.03 \times 10^{-12} (s)}{1.95}\right) \times 10^3 = 1.08\ mm$$

Equation 15

Using the optical time-delays of the E^{2max}*-Fields minus* E^{max}*-Fields*, these values are reported in *Table 18*.

Table 18**: The interpretation of the TDT-ID waveform.**

Initial max magnitudes shifted to, *ps* =			9.946
n recordings =	10	10	10
Substrate =	Silica	Pyrex	BK7
Mean *Δ*OD time, *ps* (uncertainty)	14.03 (± 0.0 %)	23.92 (± 0.0 %)	17.21 (± 0.0 %)
Literature RI † (uncertainty)	1.95 (± 2. 6 %)	2.10 (± 4.7 %)	2.50 (± 4.0 %)
Additional path-length factor	× 2	× 2	× 2
Actual thickness ‡, *mm* (uncertainty)	1.08 (± 0.5 %)	1.73 (± 0.3 %)	1.03 (± 0.5 %)
Predicted thickness, *mm* (uncertainty)	1.08 (± 3.0 %)	1.71 (± 5.0 %)	1.03 (± 4.5 %)
Discrepancy of thk^n with mean RI's and 3 s.f.'s calliper readings	0.2 %	1.4 %	-0.2 %
Possible thk^n range derived from RI/thk^n uncertainty, *mm*	1.05 – 1.11	1.63 - 1.79	1.03 – 1.07

†: Naftaly and Miles' (2005) *A new tool for the study of glasses in the FIR*. J. Non-Crystalline Solids, **351**, pp. 3341-3346.

‡ = Thickness precision available with a Vernier calliper.

Beneficially, the ID OD (*t*) method removes the need for an empty-system measurement; yet, still requires knowledge of material RI. The increased mean errors for Pyrex and BK7 (bottom row) indicate that the method is less accurate in this comparative test to OEM glasses because c.f. with SD, the broad frequency RI margins in the literature and thickness uncertainty with the Vernier calliper. The combined transmission SD and ID methods improve the statistical uncertainty of the thicknesses. The results are exemplified in *Equation 16*.

$$d(m) = \frac{\left(\frac{c_0\ (m/s) \times OD_{signal\ delay}(s)}{\Delta RI}\right) + \left({}^{1}\!/_{2} \times \left(\frac{c_0\ (m/s) \times OD_{internal}(s)}{RI}\right)\right)}{2}$$

Equation 16

Accordingly, the SD and ID results are displayed in *Table 19*, and demonstrate that thickness predictions are in greater agreement to the physically measured values and in-turn, greater agreement with the literature (including the uncertainties aforementioned).

Table 19: **Combination of SD and ID originating waveform (max) peaks to predict thickness.**

TD transmission using signal-delayed and internally-delayed OD times to predict thickness.			
n recordings =	10	10	10
Substrate =	Silica	Pyrex	BK7
Literature RI † (uncertainty)	1.95 (± 2.6 %)	2.10 (± 4.7 %)	2.50 (± 4.0 %)
SD: Predicted thickness, *mm* (uncertainty)	1.08 (± 3.1 %)	1.72 (± 5.0 %)	1.05 (± 4.5 %)
ID: Predicted thickness, *mm* (uncertainty)	1.08 (± 3.0 %)	1.71 (± 5.0 %)	1.03 (± 4.5 %)
Predicted thickness, *mm* (uncertainty)	1.08 (± 3.0 %)	1.72 (± 5.1 %)	1.03 (± 4.5 %)
Actual thickness ‡, *mm* (uncertainty)	1.08 (± 0.5 %)	1.73 (± 0.3 %)	1.03 (± 0.5 %)
Discrepancy of thk^n with the mean RI's (no error margins) and 3 s.f.'s from callipers	**± 0.44 %**	**± 2.20 %**	**± 2.03 %**

†: Naftaly and Miles' (2005) *A new tool for the study of glasses in the FIR*. J. Non-Crystalline Solids, **351**, pp. 3341-3346.

‡: Thickness precision available with a Vernier calliper. (3 significant figures adopted).

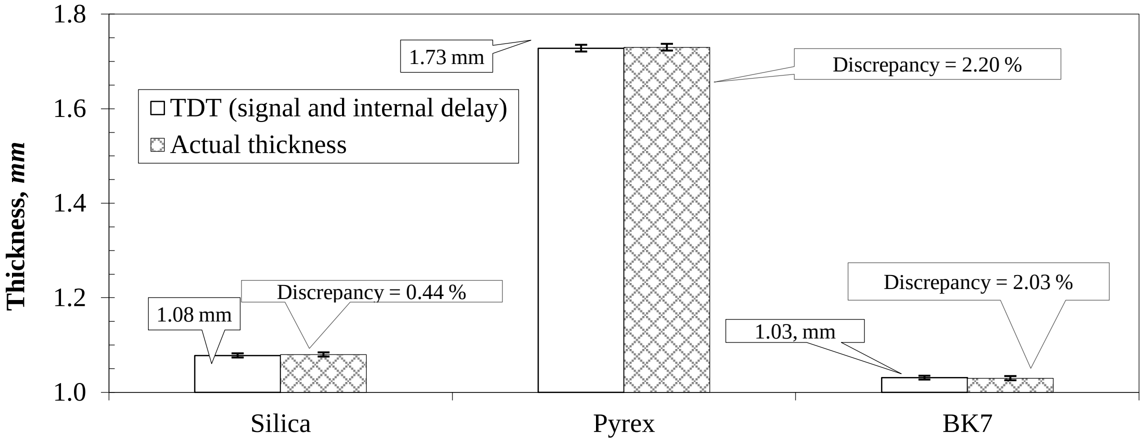

Figure 43: **Plotted comparison of the combined TDT methods (signal-delay & internal-delay) in contrast to the thickness calculated from the mean RI literature values.**

4.7.2.1 Objective 1 summary

The combined transmission methods indicate reliable RI's can be recorded for glassy substrates with provision of a THz RI measurement. Showing sufficiently accuracy (<5% discrepancies for thickness predictions) using the mean RI's provided by Naftaly and Mile's [150][18], further evaluation of accuracy cannot be quantified due to Vernier callipers insensitivity which effects the prediction by a maximum mean error of 1.6%.

Importantly, the principle of using the impeded velocity of the signal propagation are shown to correlate with path-length because of the relatively close RI's of silica and Pyrex.

---

[18] Solid ratification of the methods due to absence of a comparable level of precision in regard to RI, the impact of the broad RI ranges to the predictions are consequently discounted in validating thickness predictions. Instead, the statistical mean is taken as the comparator and benchmark RI against the experimental predictions, because TD analysis cannot return RI's as a function of frequency.

4.7.3 Objective 2: TPI method development for RI prediction

Using principles of THz OD (t) in the previous section, the objective here is to evaluate TPI as a method of light reflection to provide RI's of the glass slides to ultimately yield one of the two parameters required in OD (t) for thickness. In turn this method could be proposed as a PAT tool in RC uniformity assessment.

Like TDT waveforms are essential for OD (t) readings aligned with thickness, the probe-beam is positioned at oblique substrate incidence to the normal which has the effect of enabling the quantification of the portion of the emitted signal that is reflected from the anterior. Importantly he anterior reflection can be used to indicate RI in many scenarios and so to the internally transmitted (and posterior reflection) may act as the trigonometric function to derive OD (t).

Starting with the knowledge that non-orthogonal 'striking-pulses' have practically be shown herein to produce an RI error margin of 0.5% (*See Section 3.5.8*) c.f. FDT/TDT, the mechanisms that follow to turn the anterior reflection (vs. a mirror) are addressed in order to enhance any values yielded from AUC amplitude plots as treated with the Hilbert transformation (*See Section3.5.6*) by methods that attempt to systematically provide a TPI r_p acquisition method that is valid and robust. Naturally the RI's obtained from TPI will be cross-correlated with the literature [150], and hence-worth can serve to steer the trigonmetery factors of oblique illumination for accurate OEM glass slide thicknesses.

The TD window returned by the transformation of the *E-Field →I-Field*[19] is broader than conventional TDT windows (w.r.t. time), and makes it necessary to reduce any adverse artefacts outside of the investigative region occupied by the anterior reflection peak. This enables work to scrutinise only the minimal and relevant area to deduce an AUC, then a r_p, and then a RI.

---

[19] Generation of intensity profiles as a function of time are computed over 2,050 data-points.

Following Hilbert transformation it becomes necessary to limit low-level amplitude readings, *I* (*t*) of arbitrary system/background noise (dB). Consequently, finding region of *I-Fields* (*t*) substantial in amplitude to indicate reflection, also serves to provide the OD (*t*)'s. Thus AUC calculations, in turn become simplified by allowing use of a simple trapezoidal area modelling equation.

Once a method to successfully apply boundary conditions to time and intensity areas (*See Section 4.7.3.1*), an assessment of signal smoothing techniques (*See Section 4.7.3.2*) are trialled on the waveforms (prior to Hilbert transformation) and the transform is performed and assessed. Following development of accurate boundaries and signal smoothing techniques (which will proceed the transformation in subsequent work) to reach accurate literature RI's. The thicknesses of the correlation coefficient derived RI will then be tested.

4.7.3.1 Limiting artefacts in regions of AUC envelopes to yield r_p*'s* and more accurate RI's

1) Establishing a low-level amplitude response filter (parallel with the *x-axis*)

The reason to apply a low-level, I (*t*) threshold made after consideration that singular reflection events should manifest at one instance of time only. To illustrate this case two Hilbert transformed profiles (OriginLab 9.0) are shown in *Figure 44*, and evident in the magnified plot *Figure 44b* (*post 22 ps*) are artefacts along the full delay-rail for a fully-reflective mirror.

However, signal responses occurring before and after the significant reflection event are indicative of either system design (i.e. minute misalignment off the OAP mirrors/frustrated reflections resonating from within the sample chamber) or alternatively from the presence of conductive species, such as water vapour, or from background blackbody radiation. This. The detected 'artefacts' at low-level intensities are especially and would consequently produce erroneous area predictions.

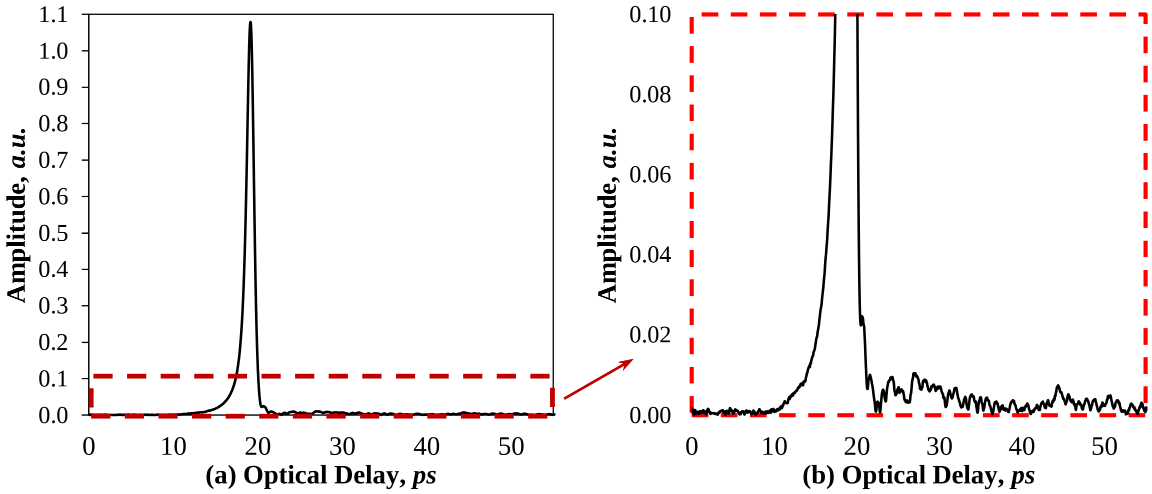

Figure 44: **The transformed amplitude plots taken from the gold plated mirror. The inset region presented, plot (a) is magnified to show arbitrary low-amplitude readings recorded across the full delay-rail (b).**

The first attempt to reduce unwanted amplitude spikes took a baseline measurement without the presence of the reflectance mirror and w/o to account for regular/periodic transmitted blackbody EMR. In the absence and then presence of the reflective mirror, the reduction of such artefacts (*Figure 44* ‘*b*’) had little or no consistency of amplitude values, perhaps indicating the irregularity of profiles were likely caused originating from an irregular environmental-background source or from a SNR issue. Thus, low-level amplitude baseline was proposed.

The step involved assessing the data sets of ten transformed reference plots (with the mirror in place) and accessing the intensity values reported over the full delay rail in order to hypothesise a general baseline. Illustrated in *Figure 45*, an amplitude value of 0.0035 was yielded from the means where significant reflection peaks were absent. The effectiveness of a low-amplitude threshold filter proved mathematically viable in order to discount adverse artefacts; yet, also provided a beneficial routine to enable automatic detection of the onset and demise times of the significant reflection events. For instance over a data set of 2,050 time-resolved amplitude values, values of I *(t)* < 0.0035 can be immediately discarded.

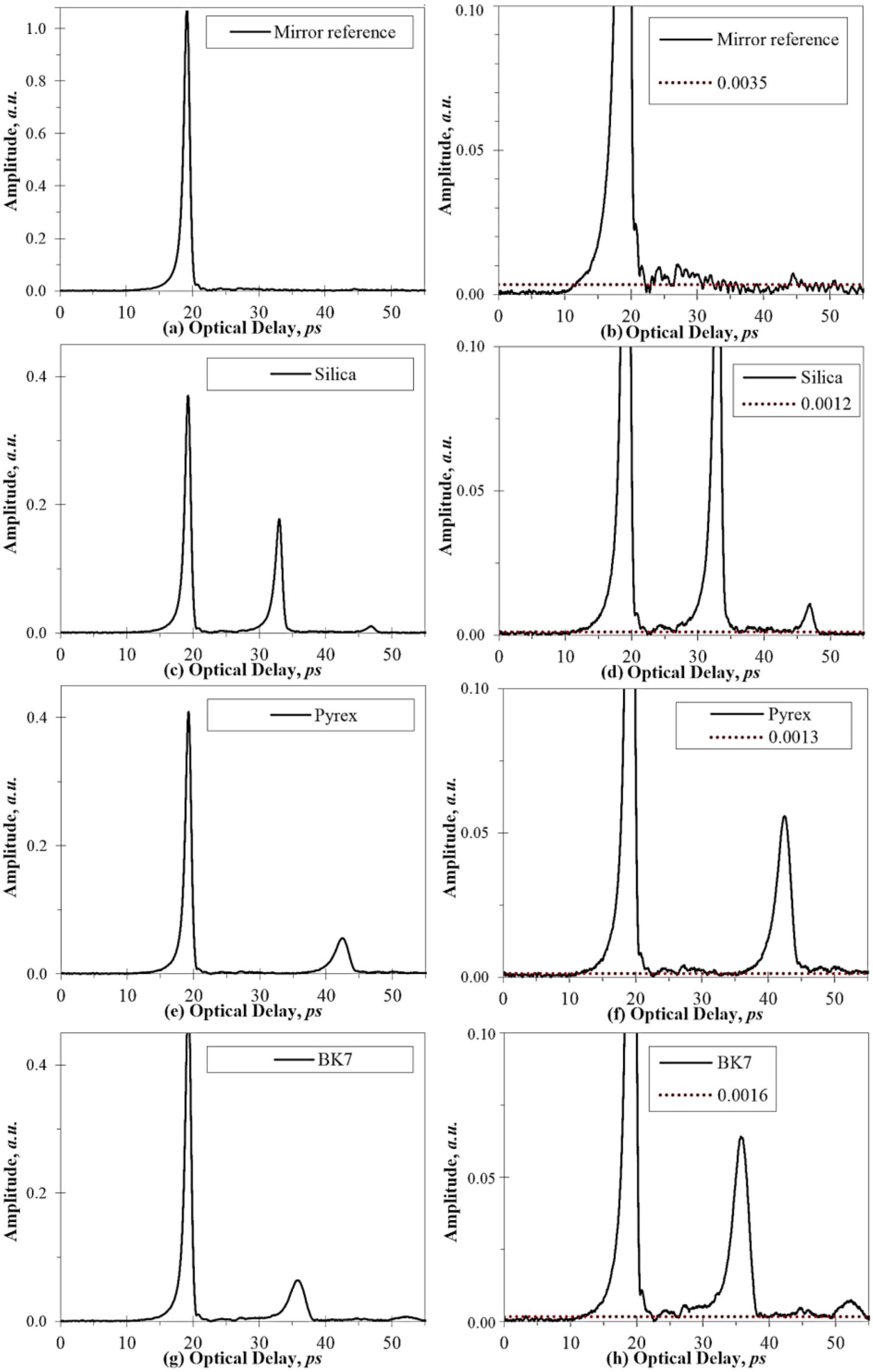

Figure 45: **Graphical illustration of applying a general limit of 0.0035 to reduce low-amplitude artefacts across the series of substrates.**

2) Constraining the time-region

The reduced I^{Max}*-Fields* of each substrate (which in-turn, are then accessed relative to the *constrained* reference) must therefore be considered further for a number of reasons (observation is made is made in Figure 45; *c-h, of event broadening*) to return valid RI values.

Firstly, the baseline of 0.0035 cannot be applied for each substrate indiscriminately because the proportion of the I^{Max}-*Field* event reduces with RI, effectively *squashing* the y-axis/ amplitude. For instance, if the I^{Max}-*Field* of the reference is 1 and BK7 is 0.5 then the integral of the peak of BK7 will be effected because the constrained amplitudes of the time-region period is not proportional to the reference. Secondly, the onset and peak demise times would adversely discount valid (chiefly, the onset time) and consequentially the resultant integral/envelope of area will be under estimated. In order to remedy underestimation of RI's due to amplitude thresholds, a stage of development is to accept the presence of SNR/environmental artefacts yet, proportionally reduce the threshold caused by reflectivity by division of the ratios of the individual substrates I^{Max}-*Field* relative to the reference I^{Max}-*Field* value to reduce the statistical bias implied by a threshold of 0.0035. And thirdly, the position of the substrate in relation to the emitting and detecting antennae can skew the time-delay of the reflection to an extent.

Using the three above points to maximise accuracy, evident in *Figure 46* whereby the inset lines displayed vertically are imposed at optical time-delay's corresponding to amplitudes > 0.0012 (for the first reflection peak; see the area shaded grey) to aid trapezoidal AUC calculation.

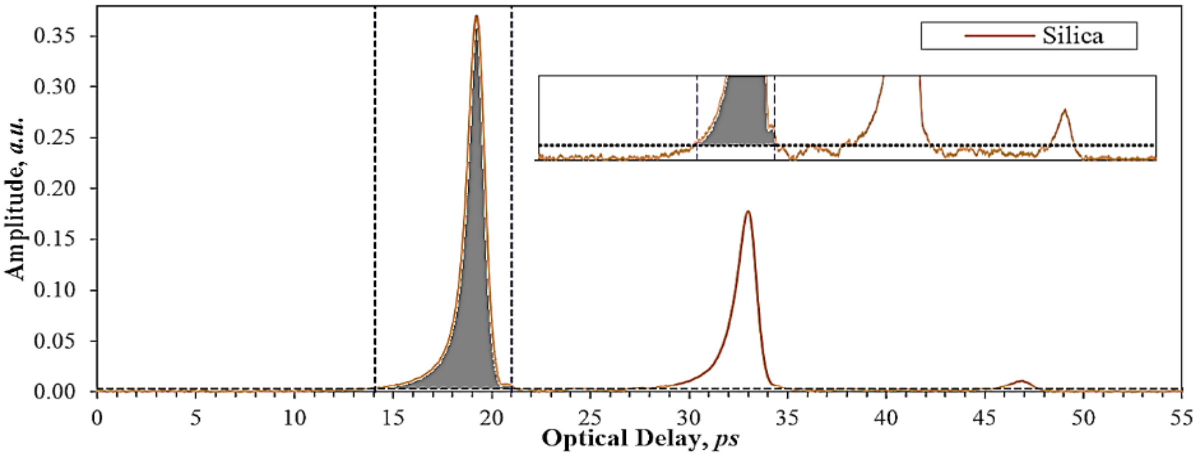

Figure 46: **An amplitude plot originating from a TPI measure of silica. The magnified inset highlights the baseline (0.0012). This low-level amplitude threshold, in-turn aids a procedure of constraining the time-region, OD (*t*). Amplitudes therefore > 0.0012 become the shaded AUC over the lowest event peak (*14-21 ps*).**

Plots for the glass slides and the reference mirror (*Figure 47*) are shown alongside secondary plots labelled with both the peak onset and demise times. The times are calculated at the intersection of the proposed baseline for omitting low-amplitudes.

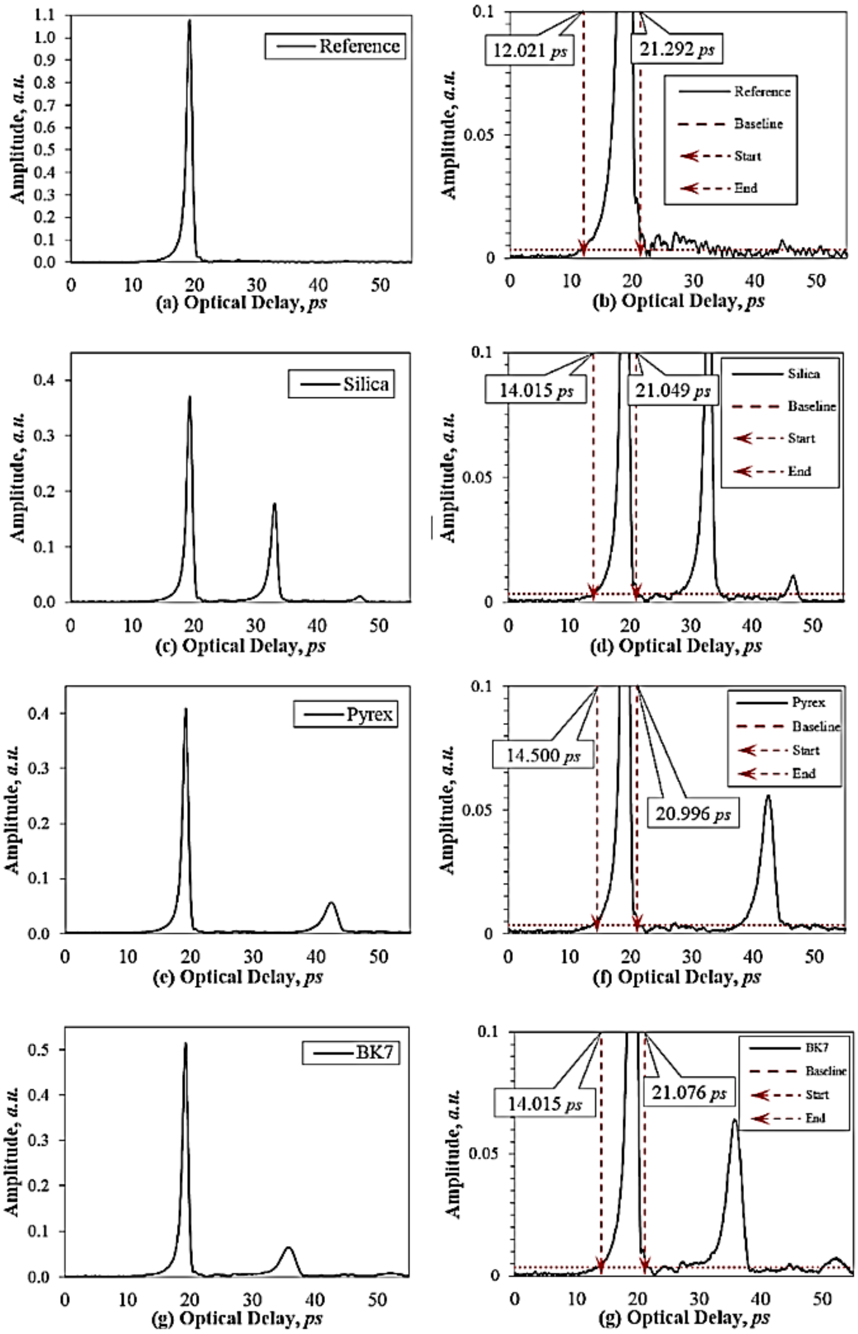

Figure 47: **Graphical illustration of applying amplitude limits to reduce low-amplitude artefacts across the series of glass substrates. This in-turn, dictates the placement of the vertical boundaries. Inset labelling is included to shows the peak on-set and demise boundaries.**

The low-amplitude threshold limit has accordingly been set at 0.0035 for the mirror and the substrates are limited by an amplitude threshold which is the ratio of the max peak height (*I*) divided by the reference max (*I*) and now allows systematic identification of the onset and demise of the relevant reflection peak to be studied. The Δ limits are substrate specific, and account for the broader bases (thus more low amplitude data) for plots of greater intensity.

4.7.3.2 Application of signal smoothing

The constraints described previously to the time region are applied to allow comparative assessment in both *Table 21* and *Table 22*. Signal smoothing is required for the Hilbert transformation to reduce the periodic (π/2) adjustments to the saw-tooth patterned phase changes plus minor spikes introduced by simulation of the *H-Field* (parodied to the conjugate complex of the *E-Field*) and therefore must be assessed concurrently with signal smoothing techniques.

Changing the length of the pump beam to bias the detecting antennae leads to 2,050 discrete data-bins/profile as a mean of 100 pulses, which corresponding to ~0.022 *ps* per data point. While the SNR ratio of the instrument is low, signal smoothing techniques are evaluated and assessed before applying an effective technique. Of the techniques explored in *Table 20*, the many results of each practice is not shown for brevity. Eventually adopted was a five-cell adjacent median cell smoothing technique in order to return the median of 5 *E-Field* values (i.e. 410 blocks of 5 equal *E-Field* values) which is applied before the Hilbert transformation. The other listed techniques given were shown to effect the reflection envelope's shape unfavourably, and thus not developed further.

***Table 20:* Signal processing, smoothing and filtering techniques attempted.**

Signal filtering and smoothing techniques	Parameters evaluated	Comments
Savitzky-Golay filtering	Polynomial orders of 2 & 3	A smoothing technique to increase the signal to noise ratio by removing 'system-spikes' by smoothing otherwise linear adjoined discrete points discrete points or a polynomial curve of the 2nd or 3rd order. The result was that while low intensity values were effectively smoothed, that the maxima peaks were visibly effected.
Percentile Filtering	50% - 75%	Percentile filtering operates in a similar manner to adjacent cell median filtering, thereby taking generally 'noisy data sets' and taking a median value for the x adjacent values. Although this method is principally the same as taking median values of a number of adjacent y-axis points a balanced medium could not be found to both reduce low amplitude SNR and the visible peak shape of the initial reflection peak.
Adjacent cell	5 adjacent median	Much like Percentile filtering, the median value of a number of y-axis values is retuned over a defined number x-axis 'blocks'. The effect is that the number of unique *E-Field* (*t*) values is reduced from 2050 to 410 (with a 5-cell adjacent filter) yet occupies the original 2050 time points; hence a plot is returned of 2050 x-axis points and median *E-Field* (*t*) values. This method was adopted herein because of the apparent reduction of SNR spikes without apparent alteration of the max peak of interest.
FFT filters	Low-pass	Blocks all high frequency responses beyond a defined point.
	High-pass	Blocks all low frequency responses beyond a defined point.
	Band-pass	Specifically defines the area between low and high pass frequencies.
	Band-block	Band block subsequently blocks frequencies between the low and high.
	Threshold	Threshold filtering removes frequencies below a defined value.
	Neither forms of FFT filtering were preformed because the limits had to be initially found and manipulation of the TD data into the FD was a routine delineating from the aim of maximal use of TD analysis.	

The 5 cell median filtering technique (i.e. smoothed or not smoothed) are assessed in *Table 22*, indicating that use of the filtering technique improves the predicted RI's in comparison to the literature to less than 5%. Successively greater agreement is observed with increasing RI of the substrate from 2% (Silica) 2.6% (Pyrex) and 4.4% for BK7, whilst the discrepancies for the set decreases with smoothing. The peak widths displayed are generally equal at ~7% and therefore the theoretical time-ranges imposed, suggest that the onset and demise times have minimal or no contribution to skew the reported RI's in regard to the AUC values (particularly with observation of similar RI improvements seen in *Table 20* where a threshold is imposed. The discrepancy limits given in the final rows or both tables are calculated with calculation of the experimental results to the margins given by Naftaly and Mile's [150].

Table 21: **RI's measured between peak onset and the reflection demise (as a function of the routine returning a baseline of 0.0035) with no limitation opposed on low-level amplitude readings (i.e. 0).**

Substrate =	Reference	Silica	Pyrex	BK7
n recordings =	10	10	10	10
Baseline derived time-period of surface reflection peak: on-set and demise				
Values				
Baseline derived value for peak on-set:	12.021 (± 0.0 %)	14.015 (± 0.0 %)	14.500 (± 0.0 %)	14.015 (± 0.0 %)
Baseline derived value for peak demise:	21.292 (± 0.0 %)	21.049 (± 0.0 %)	20.996 (± 0.0 %)	21.076 (± 0.0 %)
Peak width, *ps*:	9.271	7.034	6.496	7.061
Predicted RI (UNSMOOTHED):	-	2.07	2.26	2.87
Predicted RI (SMOOTHED):	-	2.03	2.20	2.75
Literature RI † (uncertainty):	1.00	1.95 (± 0.05)	2.1 (± 0.1)	2.6 (± 0.1)
Discrepancy of unsmoothed RI's with literature %, (uncertainty %):	-	**5.9 % (± 6.0%)**	**7.4% (± 7.7%)**	**10.2% (± 10.4%)**
Discrepancy of smoothed RI's with literature % (uncertainty %):	-	**3.9 % (± 4.0%)**	**4.8% (± 5.0%)**	**5.8% (± 6.0%)**

The final results of application of the three waveform refinement techniques are displayed in *Table 22*. The reported RI values are within agreement of the comparator and fall further to within a 5 % tolerance limit (even with inclusion of the literatures' RI margins) for the TPI-RI method. Of note, the inclusion of ionic modifying agents correlate with increased RI deviation, this is likely to be a consequence of the increasing polarisabilty between silica (0) to Pyrex and BK7.

Table 22: **RI's measured between peak onset and the reflection demise (as a function of the routine returning a baseline of 0.0035) with AUCs omitting amplitudes below 0.0035.**

Substrate =	Reference	Silica	Pyrex	BK7
n recordings =	10	10	10	10
Baseline derived time-period of surface reflection peak: on-set and demise				
Literature RI † (uncertainty):	~ 1.00	1.95 (± 2. 6 %)	2.10 (± 4.7 %)	2.50 (± 4.0 %)
Baseline derived value for peak on-set:	12.021 (± 0.0 %)	14.015 (± 0.0 %)	14.500 (± 0.0 %)	14.015 (± 0.0 %)
Peak width, ps:	9.271	7.034	6.496	7.061
Baseline derived value for peak demise, *ps:*	21.292 (± 0.0 %)	21.049 (± 0.0 %)	20.996 (± 0.0 %)	21.076 (± 0.0 %)
Predicted RI (UNSMOOTHED):	-	2.03	2.20	2.75
Predicted RI (SMOOTHED):	-	1.95	2.13	2.54
Literature RI † (uncertainty):	1.00	1.95 (± 0.05)	2.1 (± 0.1)	2.6 (± 0.1)
Discrepancy of unsmoothed RI's with lit. %, (uncertainty %):	-	**4.1% (± 4.2%)**	**4.8% (± 5.0%)**	**5.8% (± 5.9%)**
Discrepancy of smoothed RI's with lit. % (uncertainty %):	-	**0.0% (± 0.1%)**	**1.4% (± 1.7%)**	**-2.3% (± 2.2%)**

4.7.3.3 TPI restraining and method summary

Good agreement to the literature (Ref. [150]) was found from the TPI reflection method. The applied techniques of boundary constraints and signal filtering further enhance the accuracy of RI's by ~6 - 10% to a level well within the range of <5% discrepancy. This is despite the experiment limitation of performing reflection analysis at an angle of incidence oblique to the normal line, as discussed in *Section 3.5.5* and the findings of Pupeza *et. al.* (2007)[20]. There are a number of further conditions for yielding accurate reflection coefficients and these are given in *Appendix Section 10.2.2.*

It is worthwhile at this point to highlight that using a RI determination method with known inaccuracies, must be balanced with its intended use to monitor RI's relative to values found in a fixed system. Absolute RI determination is on one-hand, useful for quantifying SF's off-line in a transmission configuration where the thicknesses of different ribbons (of differing formulations and batches) can be measured, yet not necessary for monitoring local variations in ribbons per production cycle.

4.7.4 Time-domain Reflection: Material thickness predictions (TPI-OD)

The final objective of this chapter, warrants the accurate prediction of thickness with innovative use of TD analysis. Despite 'ideal' substrate uses of glasses herein, primary validation of the equipment, interpretational factors, development routines were probed and; now, finally requires the coupling of the fundamental optical-physics of EMR propagation in regards to velocity impedance (see *Table 23*) and reflection principles to deliver a measurement based on delay-time (thickness) between the E^{Max}*-Fields* and/or $E2^{Max}$*-Fields*. Time-delay is achieved with *Equation 17* and *Equation 18*, to yield path-length[21]:

$$\frac{Sin\theta_i°}{Sin\theta_t°} = \frac{RI_{samp}}{RI_{air}} \Rightarrow \frac{Sin(30°)}{1.950}$$

---

[20] Material RI prediction using the simplified variant of Fresnel's amplitude coefficient at angles exceeding 5° reduces accuracy accordingly.

[21] This example uses pre-defined knowledge the silica's RI (1.95) to find the transmitted path-length.

$$\theta_t{}^{\circ} = ArcSin\left(\frac{Sin30^{\circ}}{1.950}\right) \Rightarrow \theta_t{}^{\circ} = 14.8572$$

Equation 17

$$d(m) = {}^{1}\!/_{2}\left(\frac{c_0(m/s)}{RI_t}\right) \times \left(OD(s) \times Cos\theta_t^{\circ}\right)$$

Equation 18

Table 23: **Method and interpretational differences between transmission and reflection time-delay analysis.**

○	The oblique angle of incidence (*30º*) with the substrate will cause a greater trigonometric shift for thickness determination from the actual vector path-length compared with orthogonal incidence (*0º*).
○	The instruments optical-delay window can be made broader with reflection mode measurements than capable with the transmission method. This results in an increased ability to detect a phase inversion of the signal, signifying reflection from the rear of the substrate following transmittance.
○	The TPI technique allows the user to manually alter the position of the substrate in the *z* dimension in order to enhance focus to the specific focal point of interest. Generally, focusing the instrument to the initial signal/substrate interception is practiced for surface RI determination, yet can be altered.

A TPI waveform of a silica slide is illustrated in *Figure 48*). The presence of the anterior phase-induced (*E^{Max}-Fields* ~ 18 *ps*) and the posterior surface: ~ 34 *ps* reflection peak. Unlike intensity studies, the *E^{Max}-Fields* and/or *E2^{Max}-Fields* are required for *Δ* time-resolution, permitting extraction between the event peaks with inclusion of the substrates inherent RI.

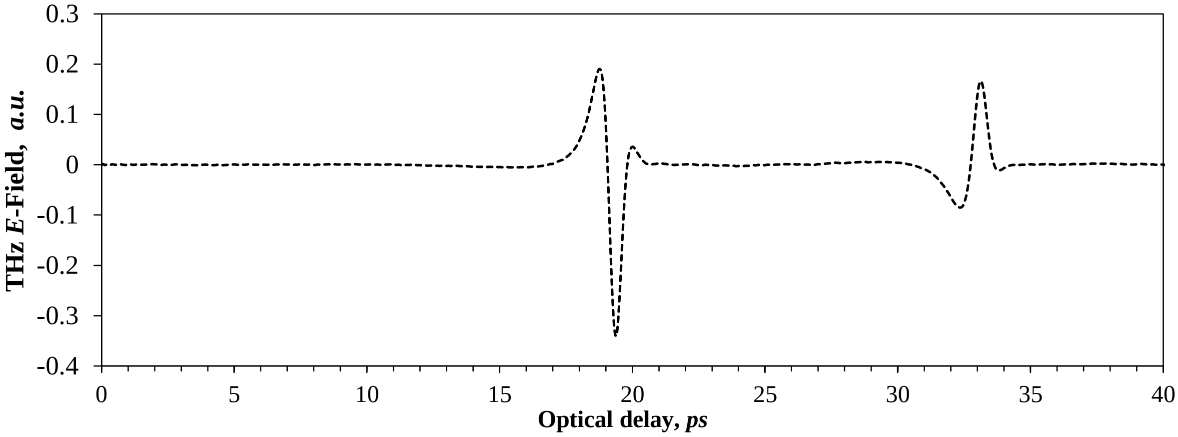

Figure 48: **The *E-Field* (*t*) waveform of fused silica acquired from TPI imaging combining the stages of development evaluated within this chapter.**

Table 24: **Thickness results from using the optimised TPI-RI method and OD**

Substrate	**Silica**	**Pyrex**	**BK7**
n recordings (of substrate and thicknesses measured with callipers)	10	10	10

Baseline derived time-period of surface reflection peak: on-set and demise			
Literature RI † (uncertainty)	1.95 (± 2.6 %)	2.10 (± 4.7 %)	2.50 (± 4.0 %)
RI results derived from TPI-RI of smoothed and constrained (threshold and time-region) values.	1.95	2.13	2.54
Optical-Delay (P), *ps*	14.365	24.203	17.600
Angle of internal transmission, θ_t°	14.857	13.576	11.353
Angle of incidence from the normal line, θ_i °	30	30	30
calliper thickness, *mm* (uncertainty range, *mm*)	1.08 (± 0.005)	1.73 (± 0.005)	1.01 (± 0.005)
Thickness estimate from TPI-RI (uncertainty, %)	**1.07 (± 2.2%)**	**1.70 (± 1.5%)**	**1.04 (± 2.8%)**

The error margins are expectedly greater with the reflection method as can be witnessed in *Figure 49*. The inclusion of ionic modifying agents is believed to contribute to the increasing inaccuracy from the literature for Pyrex and BK7; respectively, because of the influence upon the materials permittivity and subsequently increased polarisation of the THz probe–beam. It is proposed that simplification of Fresnel's amplitude reflection coefficients provides an increased degree of accuracy when fewer compositional forms of molecular species are present, than for example silica.

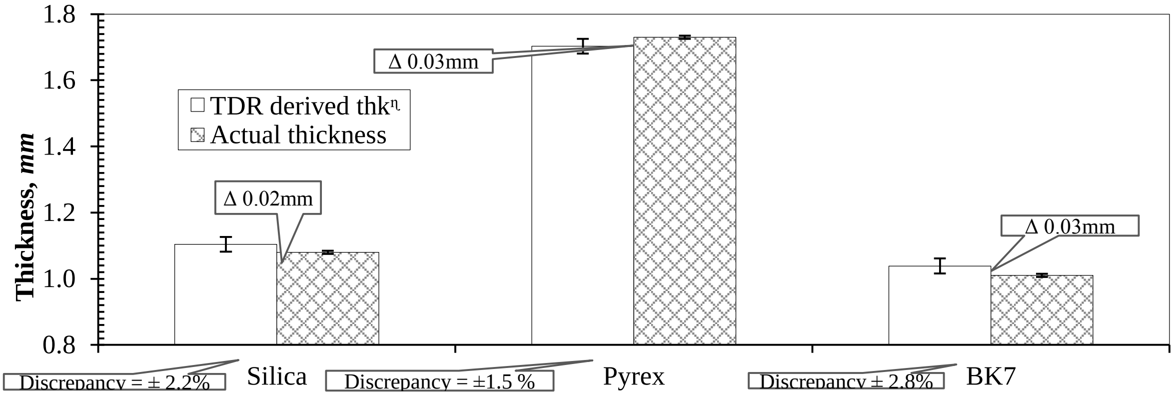

Figure 49: **Relative comparison of the two TD methods assessed against FD derived results of Naftaly and Mile's [150].**

4.8 Conclusions

The results of the TD methods for thickness determination are in agreement with actual physical readings, and the TPI-RI method is within 5% agreement to FD literature values [150]. Of considerable note, transmission/OD (*t*) methods require an RI to be given (or predicted).in-order to predict material thickness.

4.8.1 Objective 1: TDT ID and SD

The thickness values derived from the TDT-SD method shows promising results as all thicknesses were within 1% of the actual thickness readings. This value covers all three glass substrates and, as most of the studies suggest, the glasses of greater capacity to ionise (as a consequence of network modifiers) deviate further than silica alone. The individual ID results possess a accurate prediction for thk^n to with mean discrepancies ranging from ±0.4% to 1.2%.

The less complex TDT-ID method cannot be said to be greater than SD because the ID method requires every scan of a substrate to be in exact dimensional alignment (as opposed to a SD measurement where repeated reference measures can be taken. In unison, the TDT techniques were marginally more accurate for deriving either of the two parameters than TPI. The combination of TD transmission methods (SD + ID) is shown to improve the accuracy of thickness prediction and surpass TPI (of which a greater amount of method development has been extended at this stage). With accuracy limits of the procedures demanding at least a > 95% agreement [150], the TD methods will be tested further for thickness prediction.

4.8.2 Objective 2: TPI method development

Unlike the TDT method, TPI fails to sample the entirety of the substrate. With consideration of the reflected EMR, the substrates outermost surface is alone responsible for the indicative RI measurement. The bulk properties of the substrate analysed with TDT have the apparent effect of retarding the THz pulse as the gross function of the mean RI of the material. If density and chemical composition is homogenous then bulk RI is highly indicative of the RI at any point within the substrate. However, if presented with a heterogeneous substrate, or particularly one in which the surface is denser than central regions, the RI will be misreported, and can no longer be considered an absolute RI.

This judgement signifies that using TPI methods to quantify the intrinsic RI of a material is more likely (w.r.t. accuracy) for materials of fewer chemical constituents, particularly for ionic species; so in-turn, the method is best suited to provide values for RI in a relative *like-for-like* manner. Therefore *true* or *absolute* RI's using TPI may not form the reference RI following consolidation, rather that PAT assessment adopts a rule of systematic errors providing relative RI's comparisons for measurements of the consistency in varying pharmaceutical formulations while (to alike materials in alike environments) may arguably provide useful indicatory material attributes in a PAT application.

Of final note, the internally refracted probe-beam *bends* towards the normal, orthogonal line within the investigative material, consequently reducing error of the TPI method. With the error indicated above for a material of 1.95 for RI, this value is also in similar in regard common for most pharmaceutical compacts (as will be seen).

5 Experimental chapter 2

To test whether the density and thickness properties of Avicel® tablets can be successfully predicted with the two THz time-domain methods. TPI is first used to generate RI values as a surrogate parameter of density and then this value is then used to calculate tablet thickness using the principles of optical time-delay.

Continuing development from the previous *Experimental chapter* the aim stands to assess densification of MCC tablets (as models to ribbons) to evidence that RI is sufficient as a surrogate parameter for density/SF. Previous accuracy of the thicknesses exceeded 95% (the mean error of the 3 slides being 1.27%, excluding uncertainties) to that of the impeded velocity of THz light through the characterised standards (known as RI). This was done with transmission TD spectroscopy and method 2 (TPI) via surface reflectance and analogous to TDT enables an OD reading to provide thickness was successful in predict RI. Literature RI values (provided by Naftaly and Miles [150]) served as a development tool to methods especially to validate TPI readings involving linear integration of THz pulses using the Hilbert transformation function, as well as noise reduction and signal filtering techniques. The data treatment methods developed in *Experimental chapter 1* are next assessed on a more complex series of multi-variant substrates, comprising of pure MCC.

Here, MCC tablets will be produced under specific conditions to ascertain continued TPI validity. In the first instance, a comparator FD technique is established to ensure that instrumental and mathematical derivation of RI's is in agreement to the results of Naftaly and Mile's [150] for silica glass (1.95).This method is then applied for the purpose of measuring RI's of MCC tablets. Thus MCC model substrates are manufactured for the aim of correlating RI to density (SF) and to study proportionality of SF and thickness. Compared to OEM glasses, MCC tablets differ in at least two crucial ways.

1) The chemical composition of tablets is not assumed to be as homogenous (as glass) because the degree of porosity/density in compacts is presumed to be less with incorporation of air, because of a greater degree of freedom in the powder-blend. Subsequently, RI as a bulk (and average) measurement may differ from surface-derived RI's due to how the powder blend is consolidated.
2) Compacted Avicel tablets and glass slides may differ in regard to diffuse and specular surface light reflection.

The target specifically attempts to assess how compaction force effects RI in consolidation routines, again with similarities reaching across tablet production and RC. In experiment one, tablets of various RI's shall be analysed with FDT, TDT (SD & ID) and TPI. With an equal target mass, a range of compaction loads are applied over the batch. The optical thickness (i.e. the signals path-length) shall remain equal, while application of variable forces results in density ranges, to model porosity and in-turn, RI and S/F understanding. In experiment two, tablets of uniform volume and thickness, but different mass and compaction force are manufactured and tested with the three THz methods. With alteration of fill weights across the batch, variable densities can be achieved and readily measured physically using a calliper.

5.1 Objectives and tasks

- Objectives/tasks

1. Present a frequency-domain THZ method to report RI’s of manufactured materials that cannot be sourced from the literature. With the thickness/RI studies of *Experimental chapter 1,* the TPS-300 can be readily verified and as a precaution used again to measure silica glass.
2. Validate the use of RI’s as a suitable surrogate value, highly indicative of SF in heterogeneous tablets.
    - Manufacture tablets with a variable range of densities and thickness. In order to isolate the effect of path-length from RI, the DoE is to be designed to have tablets of equal volume yet variable density and also a contrasting batch of tablets with fixed fill-weights produced under fixed compaction forces.
3. Reassess the TD methods for continued and viable methods to yield RI/thickness giving:
    1. Bulk RI accuracy predictions are within 5% agreement to the FDT standard.
    2. Knowledge of whether surface-derived RI’s can also provide accurate predictions within 5% agreement to the FDT standard (using TPI).

5.2 Introduction

There are no literature/reference values (*as in Section Experimental chapter 1*) to contrast, verify and develop TPI RI predictions because the compacted substrates are inherently unique. The RI values reported for the glass slides by Naftaly and Mile's [150] were *bulk* measurements; the mean RI's of the substrate, with probe-beam analysis after passage through the entirety of the material. A bulk measurement is therefore insensitive to lateral density changes/laminar banding (e.g. higher surface densities than the core). In contrast to bulk measures, surface reflection from the anterior interface provides the origin of RI's during TPI method.

Re-evaluation of the predicted RI values (as predicted by transmission and reflection based methods) is a necessary requisite because:

i. Compacts are assumed to possess a marginally less planar air/surface interface than the glass slides.
ii. Potential issues regarding variable regions of laminar densification (e.g. surface hardness) verses internal *core* consolidation.

5.3 Method/materials and tablet preparation regime

5.3.1 Materials and tablet preparation

Samples of Avicel® PH-101 (FMC BioPolymer, Belgium) were weighed to target fill-weights and transferred to a 13 *mm* diameter die and tapped with a spatula to allow the Avicel® to settle inside of the die and then were compacted into flat, cylindrical tablets.

***Table 25*: The true density of MCC.**

Excipient	g/cm^3	Source(s)
(MCC*) Avicel® PH-101	1.51-1.67 g/cm^3	Handbook of Pharmaceutical Excipients, Ed. 6, 2009 (1 of 4)

Note: The true density of specific brands of MCC are inconsistently reported between sources, and thus listed are the approximate ranges researched

5.3.2 Modelling production of tablet to mimic key RC CPP's

Illustrated in *Figure 50*, the CPP's common between tableting and RC can be envisaged (i.e. feed-rate and compaction-force) of both unit processes. The tablet press provides a relatively narrow range of compaction forces (up to 500 *kg*). The DoE (See *Table 30* and to be successfully produced for TPS measurements to reveal waveform features sensitive to RI and thickness. For instance the first batch of tablets featured equal volume (and hence thickness) with variable densities, and the second batch were manufactured to produce MCC compacts with equal fill weights and increasing compaction forces.

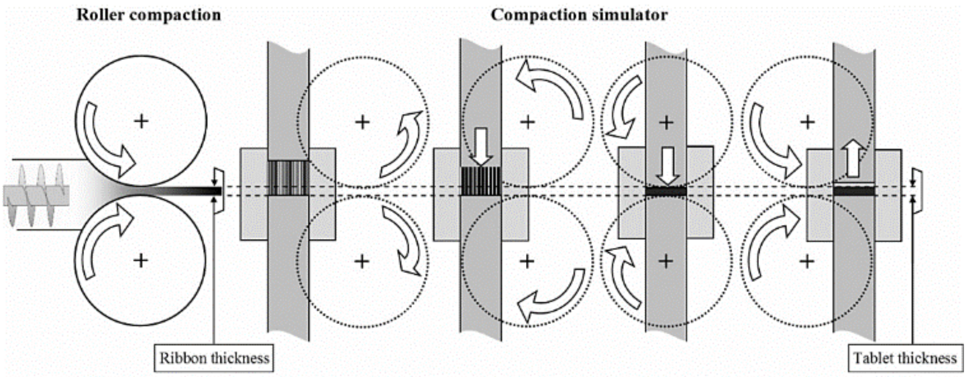

***Figure 50:* A schematic diagram comparing the similarities between roller-compaction and uniaxial tablet pressing. The processes occur (w.r.t. time), Left → Right, resulting in particle rearrangement, and consolidation principles of the powder into solid compacts.**

5.4 Tablet production with the PCT

Tablets were manufactured using a modified compaction force tester (originally a CT5), adapted to produce individual tablets to a high degree of precision (*See Figure 51*). The modified instrument originally has been renamed a precision compaction tester (PCT, Gamlen Tableting, Nottingham, UK). To ensure controlled conditions of pressure and tablet thickness, the precision provided by the PCT is deemed essential in-order to validate and ensure spectral/TD effects follow from a more interactive device (c.f. a RC).

Figure 51: **Precision compaction tester (PCT).**

The critical control parameters (CPP's) and feedback information of the PCT are detailed in *Table 26*, while a schematic diagram shows the compression procedure of the tablet press (*Figure 52*). The bridge holding the punch is fitted with a force transducer and is capable of vertical movement at rates between 2-75 *mm/min*, definable also to the distance of travel. During tablet production a target-weight of powder is placed in the die, tapped repeatedly to level the powder ('*a*'), the target compression-force or punch travel (~ tablet thk^{n}) and rate of punch movement is set and the process is started ('*b*'). Offering no option to set dwell-time, once the load or punch-travel is met retraction proceeds at 75 *mm/min* ('*c*')

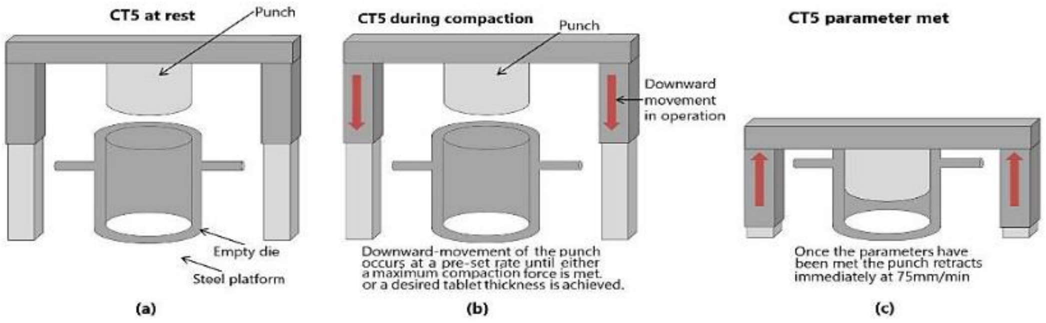

***Figure 52*: Illustrations of the actions of the PCT.**

***Table 26*: Control parameters of the PCT.**

Variant	**Specifications/Description**
Diameter of the corresponding punch and die sets.	The inter-changeable sets determine the diameter of cylindrical tablet.
Compaction force/compression load delivered by vertical movement of the punch.	There is no limit of the lowest compaction force that can be exerted onto a powder blend contained within the die. The force can be adjusted by the operator up to a maximum of 500 *kg*. Pressure transducers report this value.
Punch distance from its retracted default position	This enables tablets to be manufactured with fixed thickness, whilst the compaction force is reported in achieving the level of compaction (< 500 *kg*).
The compaction rate	The lower limit of the instrument can be manually tuned to travel between 1mm/minute to 75 *mm/minute* .
Dwell time. Invariable	Once the target force is met, the punch retracts immediately at 75 *mm/min*. The production thus, precludes a dwell time setting, whereby the punch would remain stationary at the target compaction force or height.

5.4.1 Product specifications

Twenty-six Avicel® PH-101 tablets were manufactured over 4 batches with PP's to explore the effects of both density and path-length (tablet thickness) independently. The production thus, precludes a dwell time setting, whereby the punch would remain stationary at the target compaction force/height. *Table 27:* Specifications of variable density MCC tablets whilst controlling thickness.

***Table 28:* Specifications of variable density MCC tablets whilst controlling thickness.**

Compaction Load, *kg*	Fill-weight, *mg*	Thickness, *mm*	Volume, mm^3	Density, g/cm^3
77.6 (± 0.05)	359.1	4.62 (± 0.005)	613.2 (± 2.271)	0.586 (± 0.001)
138.9 (± 0.05)	404.9	4.62 (± 0.005)	613.2 (± 2.271)	0.660 (± 0.001)
190.2 (± 0.05)	424.0	4.62 (± 0.005)	613.2 (± 2.271)	0.691 (± 0.001)
203.0 (± 0.05)	436.3	4.62 (± 0.005)	613.2 (± 2.271)	0.712 (± 0.001)
264.7 (± 0.05)	463.6	4.61 (± 0.005)	611.9 (± 2.269)	0.758 (± 0.001)
312.9 (± 0.05)	482.1	4.62 (± 0.005)	613.2 (± 2.271)	0.786 (± 0.001)
349.7 (± 0.05)	502.0	4.63 (± 0.005)	614.6 (± 2.273)	0.817 (± 0.002)
420.9 (± 0.05)	525.4	4.62 (± 0.005)	613.2 (± 2.271)	0.857 (± 0.002)
462.8 (± 0.05)	550.3	4.64 (± 0.005)	615.9 (± 2.275)	0.894 (± 0.002)
497.1 (± 0.05)	572.0	4.65 (± 0.005)	617.2 (± 2.277)	0.927 (± 0.002)

- **Correlating equal power masses (hence implied OD) with RI**

With an incremental decrease in compaction force, 16 equally weighted (± 0.1 *mg*) MCC tablets with varying thickness and densities serve to mimic equal powder-feeding in RC manufacture (*See Table 29*). The densities are calculated geometrically with a calliper and mass readings.

Table 29: **Specifications of fixed-fill weight MCC tablets.**

Compaction Load, *kg*	Fill-weight, *mg*	Thk^n, *mm*	Diameter, *mm*	Volume, *mm*^{3}	Density, *g/cm*^{3}
486.4 (± 0.05)	145.3	1.10 (± 0.005)	13.0 (± 0.005)	146.0 (± 1.289)	0.995 (± 0.005)
479.2 (± 0.05)	146.2	1.12 (± 0.005)	13.0 (± 0.005)	148.7 (± 1.285)	0.983 (± 0.005)
474.4 (± 0.05)	146.2	1.15 (± 0.005)	13.0 (± 0.005)	152.6 (± 1.280)	0.958 (± 0.005)
465.3 (± 0.05)	145.1	1.15 (± 0.005)	13.0 (± 0.005)	152.6 (± 1.280)	0.951 (± 0.005)
453.1 (± 0.05)	146.6	1.16 (± 0.005)	13.0 (± 0.005)	154.0 (± 1.279)	0.952 (± 0.005)
439.8 (± 0.05)	145.7	1.19 (± 0.005)	13.0 (± 0.005)	158.0 (± 1.274)	0.922 (± 0.005)
399.0 (± 0.05)	146.6	1.22 (± 0.005)	13.0 (± 0.005)	161.9 (± 1.269)	0.905 (± 0.004)
382.8 (± 0.05)	147.0	1.21 (± 0.005)	13.0 (± 0.005)	160.6 (± 1.270)	0.915 (± 0.004)
341.9 (± 0.05)	145.8	1.24 (± 0.005)	13.0 (± 0.005)	164.6 (± 1.265)	0.886 (± 0.004)
315.1 (± 0.05)	145.4	1.26 (± 0.005)	13.0 (± 0.005)	167.2 (± 1.262)	0.869 (± 0.004)
290.0 (± 0.05)	145.3	1.33 (± 0.005)	13.0 (± 0.005)	176.5 (± 1.251)	0.823 (± 0.004)
268.2 (± 0.05)	145.4	1.35 (± 0.005)	13.0 (± 0.005)	179.2 (± 1.248)	0.811 (± 0.004)
248.6 (± 0.05)	145.3	1.37 (± 0.005)	13.0 (± 0.005)	181.8 (± 1.244)	0.799 (± 0.004)
214.9 (± 0.05)	146.5	1.42 (± 0.005)	13.0 (± 0.005)	188.5 (± 1.237)	0.777 (± 0.003)
194.3 (± 0.05)	146.0	1.51 (± 0.005)	13.0 (± 0.005)	200.4 (± 1.223)	0.728 (± 0.003)
175.0 (± 0.05)	146.1	1.52 (± 0.005)	13.0 (± 0.005)	201.8 (± 1.221)	0.724 (± 0.003)

5.5 Analytical equipment and methodologies

Detailed in *Section 3.5.2* is the configuration of the spectrometer, and the method of operation for FDT in *Section 3.6.* While descriptions of the configurations and the method of operation for TDT, TPI are described in *Section 3.5.2* and *Section 3.5.3*, respectively.

5.5.1 FDT for comparative measurement of material RI's

The *TD* waveforms were transformed with a standard FFT routine to provide comparator frequency-domain results to establish the TDT and TPI methods. The system configuration and method principles used are described in *Section 3.6.*

5.5.2 TPI for prediction of material RI and then thickness

The method for predicting tablet RI's can be found in *Section 3.5.5*, and subsequent thickness prediction information is found in *See Section 3.5.5.*

5.5.3 TDT to predict material thickness/RI

See Section 3.5.4.

5.5.4 Physical profiles

The physical profiles of the two batches of tablets are evident in *Figure 53* to illustrate the CPP's of the tablet manufacturing process.

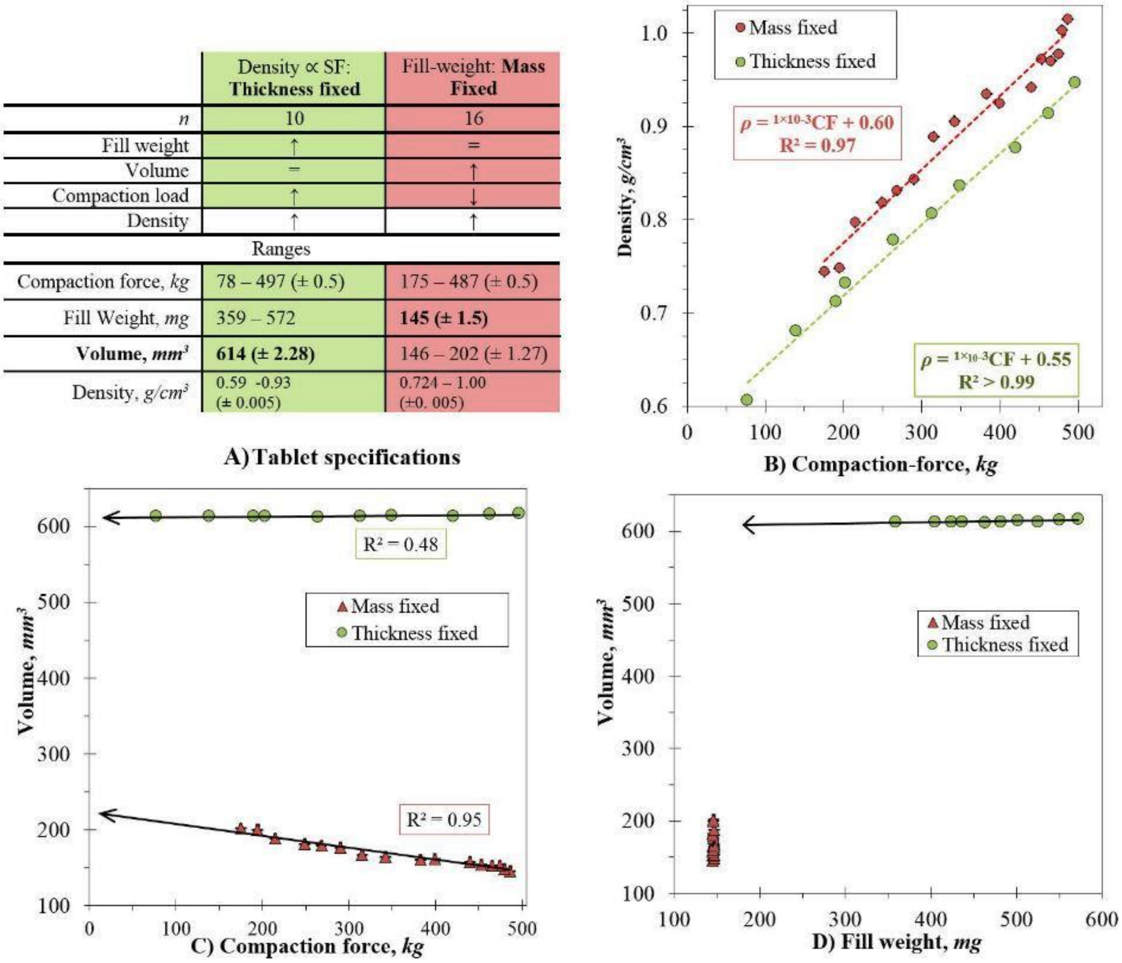

	Density ∝ SF: **Thickness fixed**	Fill-weight: **Mass Fixed**
n	10	16
Fill weight	↑	=
Volume	=	↑
Compaction load	↑	↓
Density	↑	↑
Ranges		
Compaction force, *kg*	78 – 497 (± 0.5)	175 – 487 (± 0.5)
Fill Weight, *mg*	359 – 572	**145 (± 1.5)**
Volume, *mm³*	**614 (± 2.28)**	146 – 202 (± 1.27)
Density, *g/cm³*	0.59 -0.93 (± 0.005)	0.724 – 1.00 (±0. 005)

A) Tablet specifications

B) Compaction-force, *kg*

C) Compaction force, *kg*

D) Fill weight, *mg*

***Figure 53:* The physical properties of batches 1 and 2. Clockwise: (A) The specifications of tablets used in the DoE, (B) Tablet density (geometrically measured) as a function of increased compaction force. (C) Tablet volume as a function of compaction force, and (D) the tablets volume as a function of compaction load. * The densities are calculated geometrically with a calliper and mass readings.**

5.6 Results and discussion

5.6.1 Objective 1: Present a frequency-domain THZ method to report RI's of manufactured materials

Experimental chapter 1 demonstrated encouraging use of TD methods to successfully predict material thickness by concurrently interpreting optical delay-times and indirectly from reflectance data. The combination of these principal techniques highlights the inherent parameter of a material refractivity to impede the velocity of light, and the bulk RI is ∝ material path-length. In developing this study to report RI's as a surrogate value to SF/density (and in-turn, the uniformity in ribbons) is supported by FD assessment to acquire RI because of the absence of comparator literature data to verify TD results. Despite its use as the 'gold-standard' of frequency based measurements FDT cannot alone be used to give RI values for the same reason that OD (*t*) transmission requires a pre-requisite knowledge of a unknown parameter in RC. Of further detriment, FDT requires the thickness parameter and thus, is incompatible to feed data into the TPI method.

The ease at which measurement of tablet thicknesses and density can be made to validate the results of TDT, FDT and TPI-RI→TPI-OD, illuminates differences between bulk (transmission) results and surface derived RI's. Brief comparison of RI values derived from FD analysis performed on the silica glass can be seen with reference to *Figure 54*. The *LHS* plot illustrates the frequency-dependent results from the TPS-3000 and the *RHS* plot originates from the studies carried out by Naftaly and Miles's [150]. Along-side correlations (> 95%) in *Experimental chapter 1*, equivalence of the TPS to literature knowledge is verified with re-measurement of the silica slide. The TPS-3000 produces a mean RI of 1.94 between 0.75 – 2.4 THz (*Figure 54*) with a standard deviation of 0.17 and RI margins of ± 0.005 over this range. The RI margins from Naftaly and Mile's [150] are ± 0.1; yet, can be readily be ascribed to the broader frequency range (*0.1 – 1.5/3.3 THz*) of which the margins are reported.

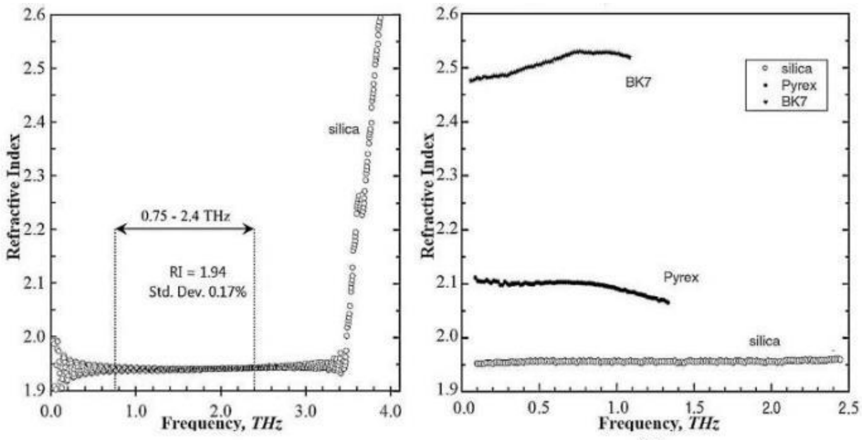

(A) (B)

***Figure 54*: Comparison of experimental results from the TPS-3000 (operating in spectral FD-RI mode) of RI index plots. In '*A*' the TPS shows the RI profiles of silica, Pyrex and BK7 as does '*B*', but of Naftaly and Miles.**

5.6.2 Objective 2: RI as a surrogate value to density/SF off MCC tablets

Here binary composites are characterised with TPS giving mean RI's that increase with the geometric density as shown in *Figure 55.* The numerical specifics of the substrates with equal volume and increased mass are given in *Appendix Section 10.3.* Plotting the changes of SF/density against RI (*see Figure 55*), the apparent trend of increasing RI's in line with density allows a linear line of best-fit to be applied to the data over a compactional range of 78 -500 *kg* at 0.75 – 1.25 THz. Providing a correlation coefficient of 1 supports the hypothesis that density alone can be quantify, measured and serve as a surrogate measure of binary mixes at least between compactional forces of 0.586 to 0.927 g/cm^3. Confidence of the linearity over this data range is then tested (*see Figure 55b*) with extrapolation to a density of zero. This results in a 1.01 RI.

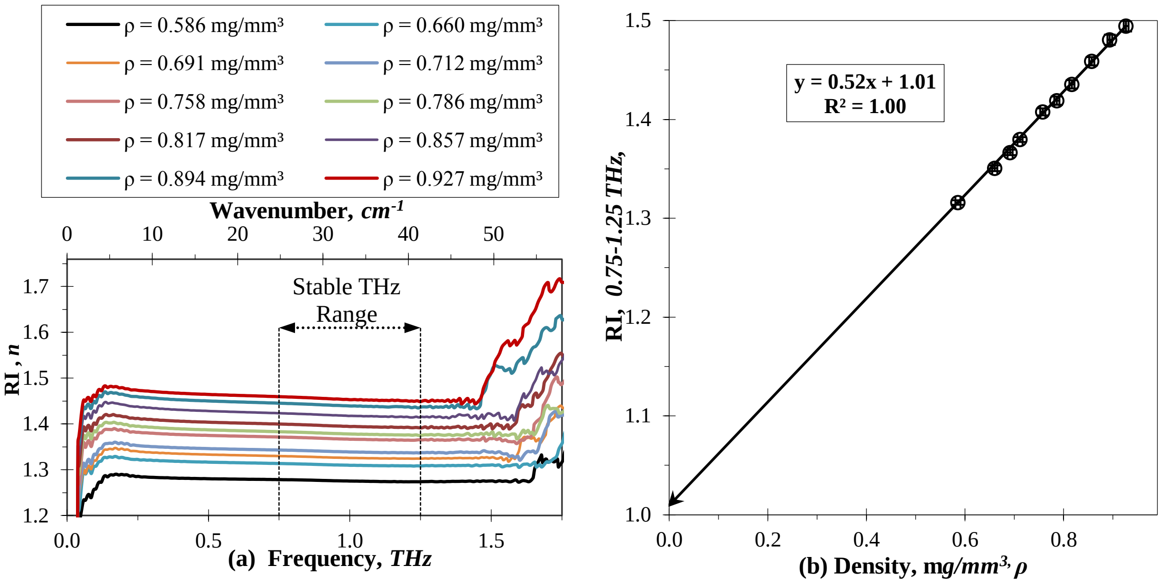

***Figure 55*: Plots of a range (10) ↕ρ MCC tablets with RI measurements by FDTS as a function of '*a*', freq., and '*b*' as a function of ρ. The inset range '*a'* interested reflection RI's where taken to deduce a *x* and the distribution is marked by the error bars in (*b*).**

5.6.3 Objective 2: Tablets of equal fill-weights with inversely proportional thickness and densities

Using compressional forces between *100–500 kg* in producing tablets of comparable fill-weights (and in all cases produced sufficiently durable compacts in respect to handling), increasing consolidation within the process in a confined punch-die environment is shown to have the same influence upon RI as tablets of equal thickness (*tabulated in Appendix Section 10.2.1/Table 52. and graphically in Figure 56*). In both simulations SF's correlate with RI's as would be expected with a reduction of the solid-to-air ratio. Described by Palermo [134], the gradient of compression profiles of MCC typically trend towards a plateau as the materials true density is approached[22]. The true density of Avicel® PH-101 is stated as 1.51-1.67 mg/mm^3 in Guy's Handbook of Pharmaceutical Excipients: 6th edition [140], although broader ranges exist within the literature for different variants of MCC.

---

[22] As if the material was in a truly homogenous de-aerated state.

The unsurprising proportionality demonstrated in *Figure 56* to account for the linearity described by fitting a line of best-fit is again, expected of the compaction forces used for the inherent RI of (2) materials and the path-length propagated by the probe-beam is again suitable. It is extrapolated to a near index of 1 for zero density, while extrapolation to higher densities to achieve compressional forces required to remove substantial proportions of inter-particular voids (i.e. a compact free from air) believed to produce the quoted true density of MCC were unobtainable with the PCT. In accordance with the true density values reported by Palermo [140] for Avicel®, additional insets are displayed in *Figure 56b.* THz RI's values are supposed to lie within the regions of ~1.86–1.95 if the relationship with density (0.724–0.995 g/cm^3) was extrapolated further, however the stages of consolidation (including, particle rearrangement, mechanical inter-locking with particle fragmentation and bond formation) would be expected to inflect from linear line fitted. To aide later work involving greater stresses (CPP's) of compression achievable with RC, lines of best-fit are forward extrapolated by the mean values as inset solid black (*Figure 56b*) and the uncertainties of measurements and standard deviation over the n=10 readings/tablet are inset as dashed lines.

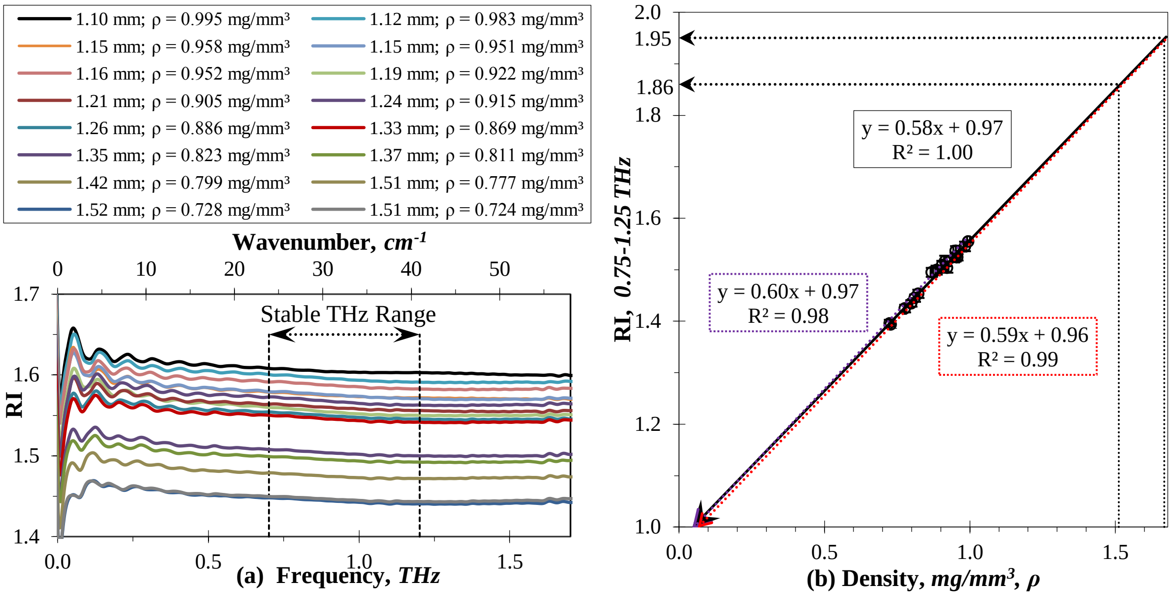

***Figure 56:* Two plots of 16 MCC tablets featuring '=' masses under ↑ forces. The RI profile '*a*' indicates *a* steady mean with low distribution (showing as error bars in '*b*' between *0.75 – 1.25 THz*.**

5.6.4 Objective 3: Variable density tablets to yield RI using TDT

Using TD technology at its most raw state of *E-Field* (*t*) waveform interpretation (*see Figure 57*) of MCC tablets of equal volume/differing mass quickly illustrates how the E^{Max}-*Field* (±) are attenuated with increased density (*0* g/cm^3 = *reference*). As a bulk transmission measurement, attenuation of the probe-beam is chiefly influenced by surface reflection at the anterior surface, with further lessening being due to absorption and potential scattering phenomena. Highlighted also, is that despite shifting the time-delay axis to accommodate the reference probe-beam, that further shifting of the *x*-axis (*not shown)* prevents the FP resonations (E^{2Max}-*Field* event) of the higher density/SF to be distinguished with certainty, either because of the limited breadth of the delay-rail or the quantifiable magnitude of the E^{2Max}-*Field(s)* [23]For instance with a material with a RI of 1.5 and path-length >4.65 *mm* a TDT-ID is unlikely to be quantifiable unless a delay-rail of 65 *ps* is used.

---

[23] The *Emax*-Field events shown graphically are exclusively from TDT SD registration contrasted against the time-delay from the reference E^{max}. The absence of internally-delayed data was not possible with TDT on this set of tablets

The decrement of ± E^{max}*-Fields* events with a polynomial line of best fit (to the order of 2) to give a correlation coefficient of 1 with extrapolation back to reference signal with density = 0 is shown in *Figure 57*. This correlation is also shown as an inset diagram in *Figure 58*, alongside the effect of density with time-delay. Notably, a linear line of best-fit closely follows the points; yet a curved line was embedded with inclusion of the reference line to improve the R^2 values. Thus either fitting routines can arguably be seen to approach a linear decay function.

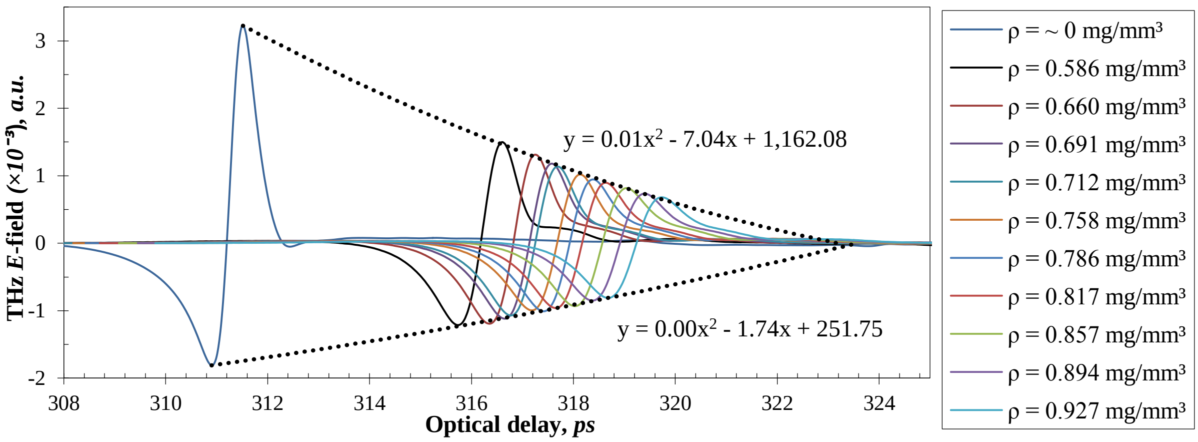

Figure 57: **↕ ρ MCC tablets (n=10) compiled TD transmission waveforms with equal path-lengths.**

The effect of increasing density indicates attenuation of the E^{max}*-Field* peak alone, without effecting its breadth. The increased density impedes the velocity of light to a linear degree resulting in detection of the signal, evidenced by an increased optical delay-time. Using an arbitrarily chosen optical-delay value to align E^{max}*-Fields* (*Figure 58*), E^{max} peak height is attenuated by 46% with a 63% increase in density across the range (Δ 0.34 g/cm^3).

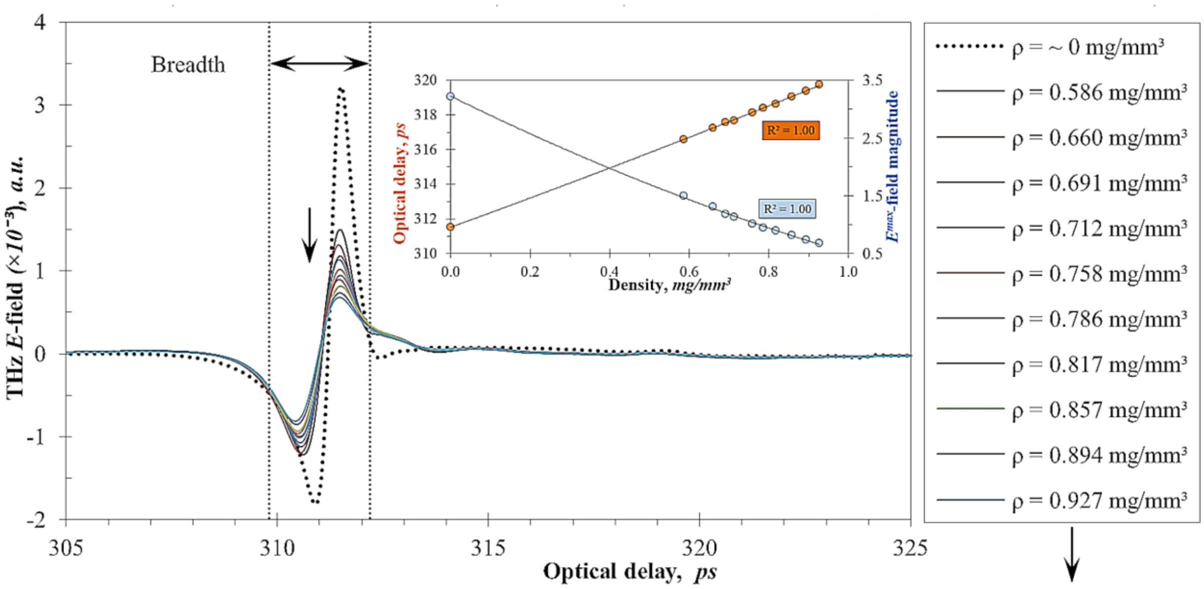

***Figure 58*: Plot of the E^{max}-*Fields* against times of ↕ ρ/= vol MCC (10) shifted to equal time-delays (w.r.t. E^{max}). The inset plot meanwhile shows density c.f. curved responses to E^{max} and 0 time-delay.**

- **Fixed fill-weight tablet analysis with TDT SD/ID**

Assessing the E^{max}-*Fields* of substrates where density/SF are directly propagation to the path-length (i.e. signal propagation through an equal matrix of air/MCC in *Figure 59*) the equal magnitudes of the E^{max}-*Fields* indicate (conversely to *Figure 58*) that fixed density is not solely responsible for the TD waveform effect with full probe-beam propagation. Rather that the variable material density and thickness influence the E^{max}-*Field* magnitudes as physical thickness, and consequently the ratio of MCC/air is responsible. Unlike the broader range of tablets studies (*Section 5.6.2*, *Figure 58*) of ~4.65 *mm* tablets, the reduced fill-weight of this tablet set allow FP reflections to be. Furthermore, the E^{Max}-*Field* events recorded on the TPS as is evident in the graphical inset (*Figure 59*) report a constant (if not marginally differing) peak breadth (by the dotted inset lines).

The TDT SD and ID values found to yield RI's reported above are reported in *Table 47* in *Appendix Section 10.3*.

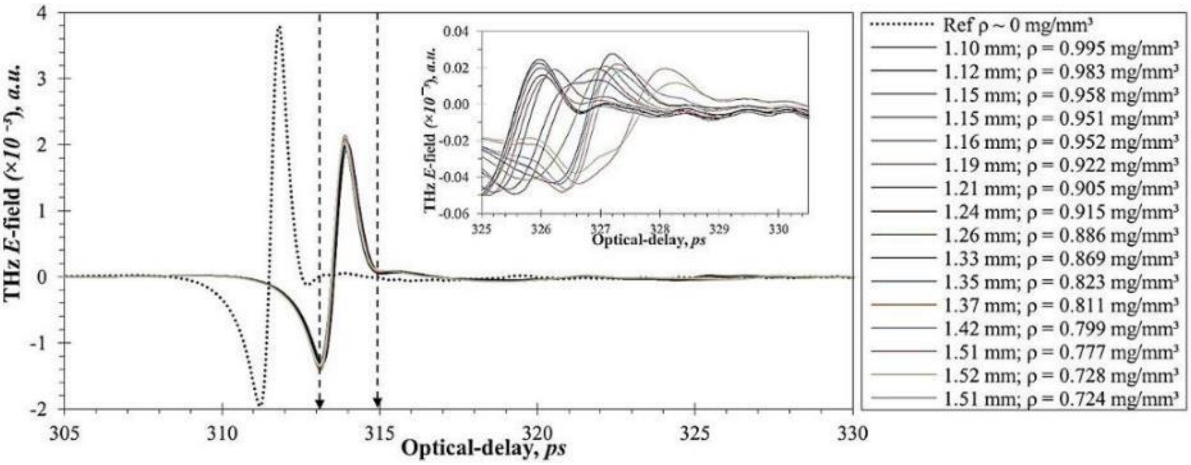

***Figure 59*: Plot of the non-shifted E^{max}-*Field responses* against the delay-time of ↕ 16 MCC tablets with fixed target fill-wgt and non ∝ proportional ρ and thk^{n}. Inset are the vertically dashed lines.**

5.6.5 Objective 3: Variable density tablets tested with TPI

The methodology outlined for TPI-RI/TPI is re-evaluated on both sets of batches for provision of RI. To meet the objective of accurate RI thickness predictions must be indicative for both tablet sets.

1) Equal conveyance meets the target of roller-compacting in regard to compressional force with floating thickness. (the ten tablets) and,
2) Scenarios in which thickness and compressional feed led to consistency (the 16 tablets).

The following data has been subjected to the 5-cell median smoothing technique, Hilbert transformation and constraints familiar to *Experimental chapter 1*. The amplitudes are shown for variable density tablets in *Figure 60* alongside tablet specifications and inset graphically, magnification in the broader dash region. The many amplitudes of the equal time-resolved points had a mean measurement taken from 10 recordings of each substrate and the mean reference amplitude; comprised of 20 measurements both before (10) and after (10) the measurements of the tablets.

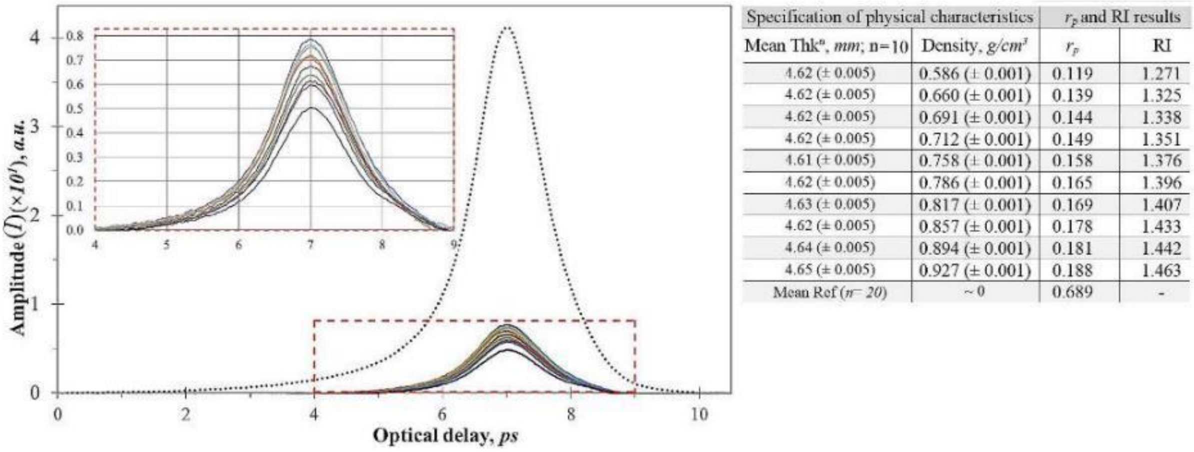

Specification of physical characteristics		r_p and RI results	
Mean Thkⁿ, *mm*; n=10	Density, *g/cm³*	r_p	RI
4.62 (± 0.005)	0.586 (± 0.001)	0.119	1.271
4.62 (± 0.005)	0.660 (± 0.001)	0.139	1.325
4.62 (± 0.005)	0.691 (± 0.001)	0.144	1.338
4.62 (± 0.005)	0.712 (± 0.001)	0.149	1.351
4.61 (± 0.005)	0.758 (± 0.001)	0.158	1.376
4.62 (± 0.005)	0.786 (± 0.001)	0.165	1.396
4.63 (± 0.005)	0.817 (± 0.001)	0.169	1.407
4.62 (± 0.005)	0.857 (± 0.001)	0.178	1.433
4.64 (± 0.005)	0.894 (± 0.001)	0.181	1.442
4.65 (± 0.005)	0.927 (± 0.001)	0.188	1.463
Mean Ref (*n*= *20*)	~ 0	0.689	-

***Figure 60*: Plot and data summary of *I*-Field amplitudes against optical time-delay of ten MCC tablets of variable density/SF and equal volumes.**

- **TPI: Fixed fill-weight tablets**

The amplitudes are shown for variable density/ thickness tablets in *Figure 61* alongside tablet specifications and inset graphically, magnification in the broader dash region. The many amplitudes of the equal time-resolved points had a mean measurement taken from 10 recordings of each substrate and the mean reference amplitude; comprised of 20 measurements both before (10) and after (10) the measurements of the tablets.

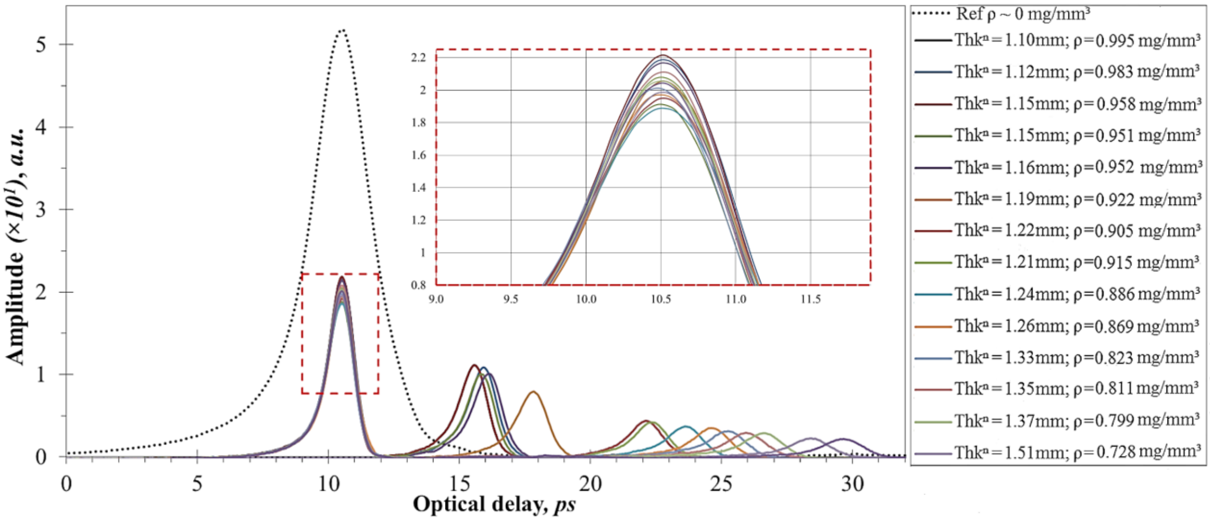

***Figure 61*: Plot and data summary of the *I-Field* against optical time-delay of 16 MCC tablets of fixed fill-weight tablets.**

The RI results from the three techniques (one frequency), *Figure 62* indicate reflectance measurements are skewed systematically to produce lower surface density than with a bulk density (RI being a surrogate value) from the entire cross section of the compact. The method and particularly the interpretation and calculation of RI with Fresnel's coefficients may predominately produce a lower than expected RI.

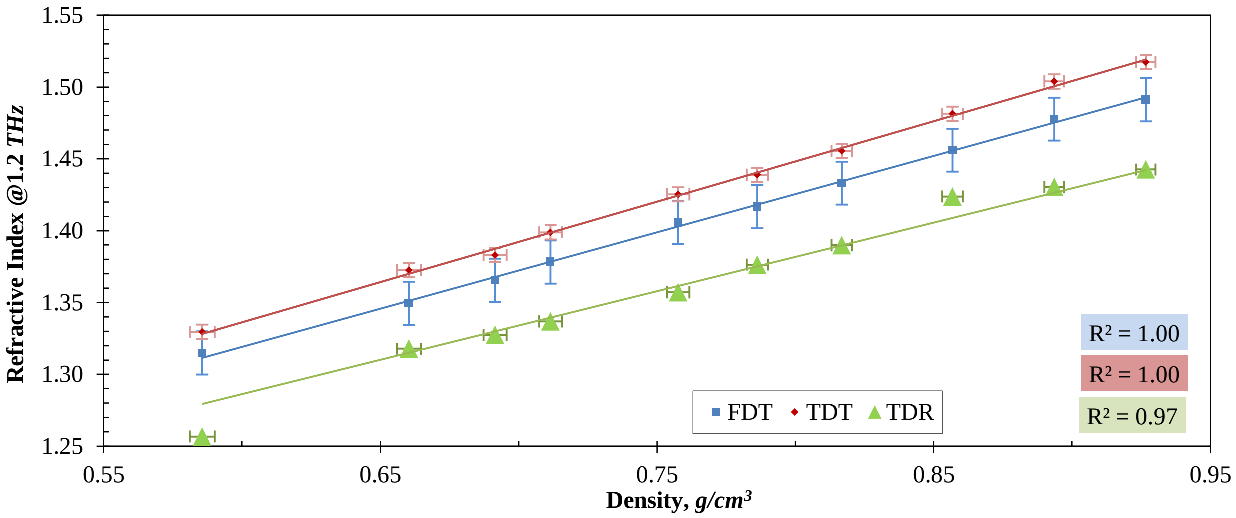

***Figure 62*: RI results from the three techniques**.

This may be a factor covering a number of issues:

1) **Water loss:** Water is known to have a RI of 1.5 and evaporation from the tablets surface may marginally lower the expected RI when in competition with bulk measurements. With a moisture content quoted at <5% [140], the bulk measurements may therefore include any residual moisture within the inside of the tablets. Furthermore, loss of surface moisture may impart a de-consolidation role given time and consequently reverse any deformation associated with water acting as a binding agent.
2) **Elastic recovery:** The surface particles shrouding the tablets may have a greater propensity to elastically recover than internally bound Avicel for the simple reason that internal particles are interlocked/binded within a three dimensional space. In contrast the surface particles are only capable of cohesion with lateral neighbouring particles

laterally and to particle beneath only. This may result in decreased deformation and the existence of a greater number of air voids.

3) **Diffuse planar nature:** A further consequence of elastic recovery and possibly water loss, is that the THz probe- beam will strike the surface of the tablet but the reflection of the beam to meet the detector is liable to be less than the reference comparator.
4) **Mathematical error:** Simplification of the Fresnel reflection amplitude coefficient is a certain source of a degree of error. The systematic trend of TPI in comparison to FDT is notably a systematic trend of altering gradients.

5.7 Conclusions

5.7.1 Objective 1: Present a frequency-domain THZ method

The TPS-3000 is able to record RI’s to an equivalent accuracy to the previous *Experimental chapters’* comparator. The ability to access specific frequencies with the TPS enhances our capability to reduce error margins by simply reducing the delay-window. The lower standard deviation (0.17) gave an RI of 1.947, c.f. Nataly’s 1.95 ±0.1.

5.7.2 Objective 2: Validity of RI’s as a suitable surrogate value

A good degree of sensitivity is found between SF and adoption of RI as a surrogate parameter resulting in a correlation coefficient of 1 once a linear line of best fit was chosen to correlation the trend. Including the second batch of FD RI’s to SF. With both tablet sets displaying consistently high R^2 (>0.985), in-process application would provide confident assessment of SF; yet, practically the method and thickness determination (chiefly laterally) provide adverse issues.

Demonstrated also, the time delay difference between the single travel pulse and the secondary travel pulse may be considered for compacts given a known thickness and of equal material composition. The use of the TDT was only been possible because of the mathematically complex FFT derived THz RI values obtained from FDT. Notwithstanding, the technically less complex TDT method has been shown to be within at least 2 % agreement. To TDT's limitation, reflection echoes pass beyond the limit of detection for samples with greater thickness and RI values as witnessed in *Figure 63* (i.e. with a thickness greater than 2.27 *mm* and density greater than 1 g/cm^3).

5.7.3 Objective 3: Reassess the TD methods for MCC

The RI results from the three techniques (one frequency), indicate reflectance measurements are skewed systematically to produce lower surface density than with a bulk density (RI being a surrogate value) from the entire cross section of the compact. The method and particularly the interpretation and calculation of RI with Fresnel's coefficients may predominately produce a lower than expected RI

The accuracy warranted underpins the success of the two TD measures Shown in *Figure 63* is a flow diagram depicting the aim of using THz technology to quantify a parameter equivalent to SF and the materials thickness. Represented by parellelagrams are the 2 TD and 1 FD techniques and within diamonds are the questions posed or answered. Skewed to question whether TPI could be a successful method for RI prediction as FDT the stage of an independent thickness measurement is encountered for the transmission methods as the first task prior to interpretation/generation of the *E-Field* data. During transmission the presence of a second reflection peak (questioned by the lowest diamond shaped field in *Figure 63*) results in either a prediction based on the signal time of the THz signal alone or whether the time delay value can be statisically enhanced with observation in the time-domain of a second internal reflection. This derives a calibration curve when thickness is known displaying RI as a function of RI (proposed surrogate to density/SF). Converging to a now established correlation of density/SF to RI is a key success in yielding a universal parameter, the convergence of the TPI method and TPI is the answer of our aim.

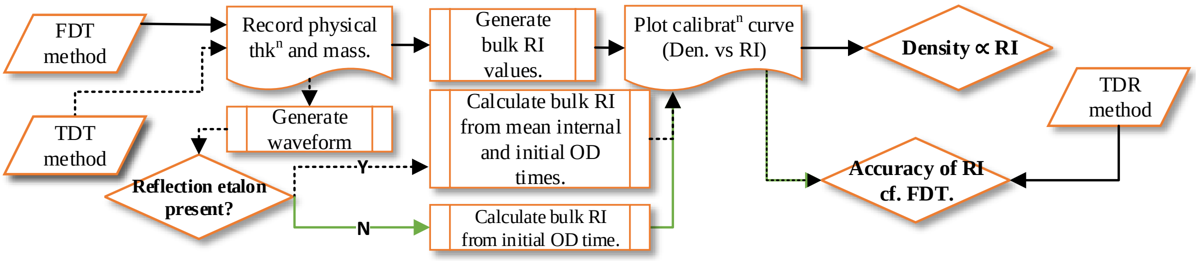

Figure 63: **Flow diagram depicting the aim of using THz technology to quantify a parameter equivalent to SF and the materials thickness.**

Importantly, the sytematic errors of the two TD methods for RI (see *Figure 62*) if FDT is considered ‘the gold standard’ method and therefore *Figure 63* highlights RI inaccuracies are present depending on the method. However, the two methods are a highly indicative tool to predict RI and for TPI RI and thickness. It must be stressed that without an independent measurement of thickness TPI remains the most viable method to predict density and thickness.

It is hypothesised that a reflection method would be more practical in an industrial environments and consequently, TPI is the main focus further developed with scrutiny of the procedural methods and interpretation routines. Advantageously, in an off-line system use of TPI-OD (e.g. measured from the estimated TPI derived RI) can be compared to actual off-line thickness readings Reflectance TPI measurements are likely to be the most practical solution for testing in our move forwards to in-line RC density uniformity measurements. The main merits for the technique remain: (1) A reduced need for physical thickness determination, and (2), rapid data acquisition rates can be achieved (<50 ms/waveform). This is illustrated in *Figure 64*

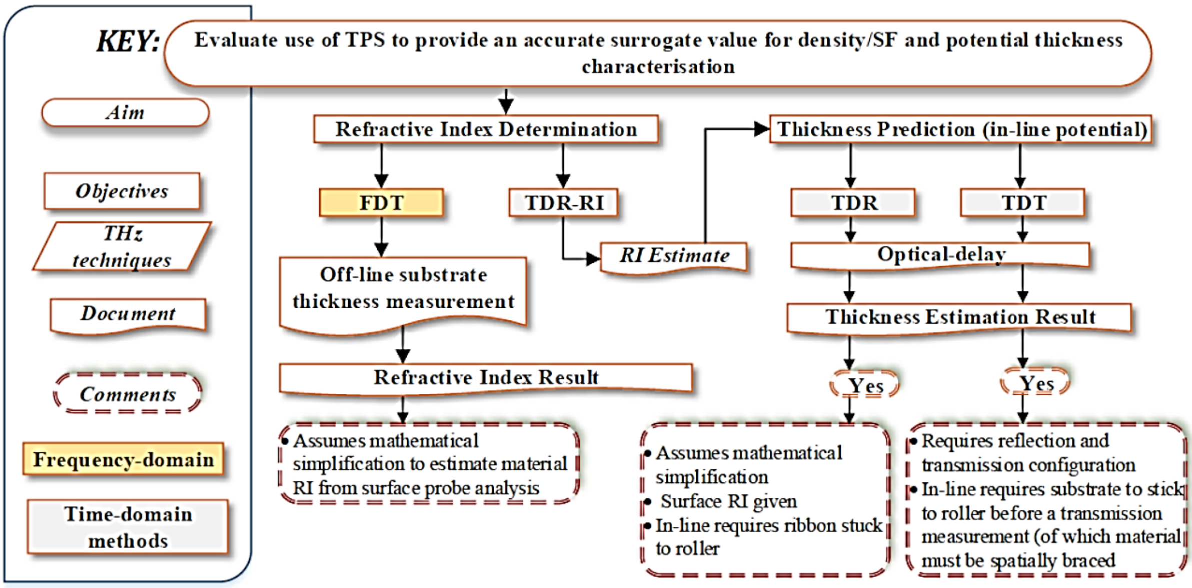

***Figure 64*: Flow diagram of the aforementioned THz techniques with suggestive benefits and limitations of the methods.**

Also observed is a highly correlated sensitivity between THz derived RI measurements to bulk density. Given greater compaction duress, material density is suspected to enter an irreversible deformation consolidation state whereby linearity witnessed linearity may not be apparent.

6 Experimental chapter 3

Evaluation of using terahertz frequency-domain spectroscopy to predict the radial tensile strength of microcrystalline cellulose tablets with refractive index measurements

Scope of chapter

Compendial testing of mechanical strength (in terms of friability and crushing force) are mandatory in assuring that tablets can withstand packing, transportation and consumer handling and because mechanical strength has an obvious bearing on the disintegration process and dissolution rate and hence the bioavailability of the drug [149]. In-line measurements of RTS might therefore lend itself to the development of the control strategy. In this Chapter, terahertz spectroscopy is examined for links between the parameters of resistance to diametric crushing force Radial Tensile Strength (RTS) and THz frequency estimates for RI of Avicel® tablets, as determined by the method of FDT.

The design space of the objectives is arranged to illustrate the effects of controlling two critical tableting parameters: fill-weight (and thus the effect of volume change within the sample with alteration of compression force to RI) and compression force with known thicknesses in order to profile density and possible deformation behaviour. First, two individual tablet batches of constant masses are produced of altering compaction-forces to map the RI profile over a range between ~0.8 - 1.1 g/cm^3. The expectation is to better understand the deformation character of Avicel® (PH-101), and to then monitor the resistance to diameteric crushing, be measuring and inturn, the RTS of this first set of tablets explored. The hypothesise challenges that if two compacts (of comparable density), yet differing thicknesses are diametrically crushed, that the thinner substrate should be less ‘strong’ than the other (before normalisation for thickness by RTS). The premise is that greater compressional load-time (or *residence time*) with the more massive tablets, while being greater, increases propensity for particle re-orientation. The dissipation of force through a greater volume/number of particles is thought to create a more temporary *deformed product*, where the core of the tablets and the edges would feature a broader distribution of density (ρ). In other words, the extent of transition between elastic to plastic consolidation in a more massive tablet may be less and proportional to the number of particles co-operating.

Reduction of the particle volume conversely may demonstrate that equal compression-forces between two batches would show a narrower distribution of consolidation mechanisms. For instance, force is conveyed to lesser numbers of particles but the gross effect would favour more permanent deformation compared with the higher fill-weight (HFW) tablets to elastically recover.

***Table 30*: DoE of tablets manufactured. The green solid coloured fields show controlled tableting constants, and yellow to grey gradient fills relate to max to min PP variation.**

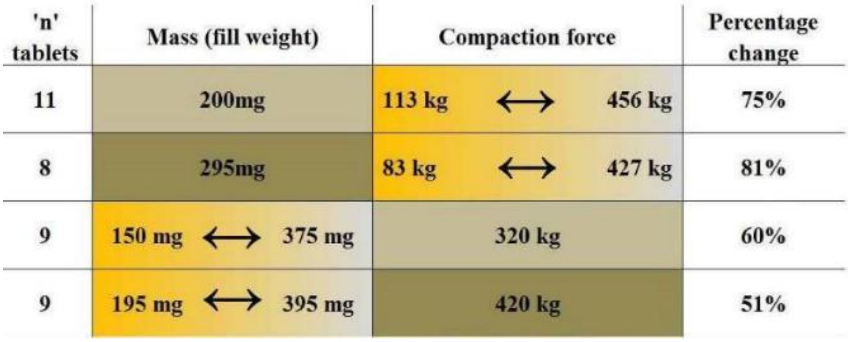

'n' tablets	Mass (fill weight)	Compaction force	Percentage change
11	200mg	113 kg ⟷ 456 kg	75%
8	295mg	83 kg ⟷ 427 kg	81%
9	150 mg ⟷ 375 mg	320 kg	60%
9	195 mg ⟷ 395 mg	420 kg	51%

In summary, the hypothesis demands a constant conveyance of the blend to the nip-region gap $\propto$ compaction-force to avoid the effects of volume change and density variation. The importance of consistent mechanical-strength is **crucial** to the physiological profiles of the delivery device [87].

6.1 Objectives and tasks

1. Produce 2 sets of Avicel PH-101™ tablets with fixed masses (200 mg, 295 mg), increasing force. (Thus density & thk^n ↓).
    - Contrasting the RI results of the density ranges of the two batches, a view to monitor the deformation behaviour of different masses of powders will be securitised
2. Produce 2 sets of Avicel PH-101™ tablets with fixed forces (320 Kg, 420 Kg), with increasing mass. (Thus $\rho \sim$ equal as a comparator for the first two batches).
    - The reversal of fixed fill-weight and fixed compaction force is likely to affect readings of crushing-force substantially, while the effect on RTS may further elucidate mechanical dynamics and behaviour to resistive forces.
    - Produce calibration curves of the RI FDT data and *crushing force* and RTS results
    - Appreciate any semblance adjoining the properties of tablet thickness, density, to the diametric resistance to crushing force and RTS by:
        - Assessing the diametric crushing force data and relationships to RTS, while explaining the dependency of tablet compaction forces and fill-weight between the RTS and RI.
        - To conclude and comment of the applicability during large scale manufacture.
        - Consider whether there is a secondary function of THz spectroscopy to match the critical process parameters (CPP's) of tableting, to the applicable CPP's of roller-compaction.
3. To consider the consolidation mechanism occurring between the tablet batches as a function of compaction-force and fill-weight.
    - The validity of diametric crushing force and any relationship to RTS
    - To emphasise any matches of the CPP's of tableting to the related CPP's of RC.

6.2 Introduction

The RTS is an important parameter indicating the inherent ability of integral tablet failure following an off-line test of resistance to crushing [141]. Mechanical strength determination, either by *crushing strength* or calculation of the RTS requires an off-line measurement, typically done by a diameteric tablet hardness tester. The term *crushing strength* is frequently used erroneously with diametric testing, for it is '*the force to fracture a tablet'* which is realistically measured [142]. The test requires the tablet to be placed upon a moving plate which then moves towards a fixed surface (the largest shaded static regions in *Figure 66*). The plane of the moving plate is fitted with a force transducer to detect the the maximal force (the breaking force) following the differentational induction force prior to zero resistance. The resistive force that accompanies all manners of solid dosage forms (i.e. varying geometry/thickness/diameter) can be entered into a mathematical expression (*See Equation 19*) to provide an RTS value.

$$RTS\ (MPa) = \frac{2p\ (N)}{\pi d(m) l(m)}$$

Equation 19

Where RTS is twice the crushing force, *p, d* as multiplied by the compacts diameter and *l*, the compacts thickness. Adversly this method of testing is destructive while taking a finite time to execute off-line. Highlighting that off-line testing obviates a real-time response to the compaction-stage and also, reduces detection of ocassional product failure criteria [27].

Sought is a quantitative reading of the degree of a materials densification/SF, while avoiding geometric density testing (in which limits determination of irregular shaped compacts) and both, gas pycnometry (which is an apparent reading; not accounting for impermeable void regions) or radiation based techniques towards the χ end of the EMR.

By producing samples of mixed density tablets with floating volume over a broad compaction forces, there presents a possibility of linking mechanical strength and THz RI data. Tableting is done with one excipient in order to reduce the parameters between tableting and RC (typically multi-component blends using fewer PP's and parameter conditions (e.g. our THz acquisition methods for predicting accurate values of density/SF independently of thickness however, the two attributes do not assure mechanical friability.

The DoE's attempt to evaluate any manifestation of different consolidation mechanisms to the tableting process. Additionally, tableting in experiment equal thickness tablets are ostensibly analogous to roller-compaction where the powder-blend maybe insufficient drawn into the nip region regardless of the roller-force.

Conversely, tableting in the experiment with batches of floating fill-weights and increased loads' are ostensibly analogous to roller-compaction where the powder-blend maybe consistent yet the roller-gap is momentarily unable to impart the correct roll-force.

6.3 Usage and constraints of alternative spectral techniques to provide tensile strength predictions

A literature search has uncovered non-destructive mechanical-rigidity testing has almost exclusively been undertook the light based spectroscopic tools of MIR/NIR /Raman spectroscopy and χ-ray techniques. Mechanical-dynamics of materials are understandably linked to intra/inter-molecular bonding mechanisms within, while not necessarily attributed directly to agglomeration/packing. Whilst indicative in regard to granulation and specifically sensitive to void fraction in (transparent) blends, THz RI registration is hypothesised to correlate to mechanical interlocking/short-range bonds as proposed by Parrot and Bindhumadhavan [58] [2], in DG/RC. These align with the unique features of THz. Analysis will be conducted against current reviews of the aforementioned techniques summarised below w.r.t. mechanical characterisation. A brief summary follows of the research (*Sections 6.3.11* & *3.8.1.2)*

6.3.1 NIR spectroscopy

Based on absorption of NIR, overtones of intra-molecular bond vibrations, invariably proceed.

NIR has been shown as a versatile optical method in the fields of drug uniformity and 'finger-printing' and is seeing advances in CT applications. Respective to THz spectroscopy, NIR spectra can be acquired within seconds from a prepared sample, as long as sufficient knowledge of a materials' spectral features are known [39, 82, 151]. In evolving the long established technique of NIR to NIR-CT is being researched for predicting the hardness of pharma preparations. The differences between the two parameters of hardness and strength are subtle and both can be measured in various ways. In differentiating strength and hardness, strength is a materials ability of resist deformation while hardness is seen as the ability of the material to resist localised indentations, wear and abrasion. Correlating NIR features (which ostensibly originate from inter-molecular bonds) with hardness, researchers have achieved varying degrees of success [75, 79, 81-83]. The character of NIR spectra is noted to not alter with tablet hardness, yet the baseline indirectly supplies a methodology for determination. The method monitors baseline shifts and uses these as a training set of standards through which a line of best fit is drawn for hardness prediction (*See Figure 65*). PCA is then generally used to convert the data into a principle component routine (PCR) and least-square analysis is applied for calibration (provided by the training set). The full method can be found in source [75]. With reference to the lines of best fit as seen in *Figure 65*, the spectra for prediction is representative of the intra-molecular vibrations of the sample (thus is composed of many peaks). Unconventionally this means these linear-lines are applied over plots providing hardness estimations from the linear gradients [80]. An upward shift of '*m*' is reported to be due to compaction-force, increasing the amplitude from shorter to longer wavelengths, increasing the amplitude from shorter to longer wavelengths [110]. This is evident in *Figure 65* with the diametric hardness between 1.5 and 6.5 kP, fitted with a best-fit line through each spectrum. The increasing gradient in the best-fit lines do correlate increasing tablet hardness. Pure MCC is tested for the hardness of a RC ribbon (*b*).

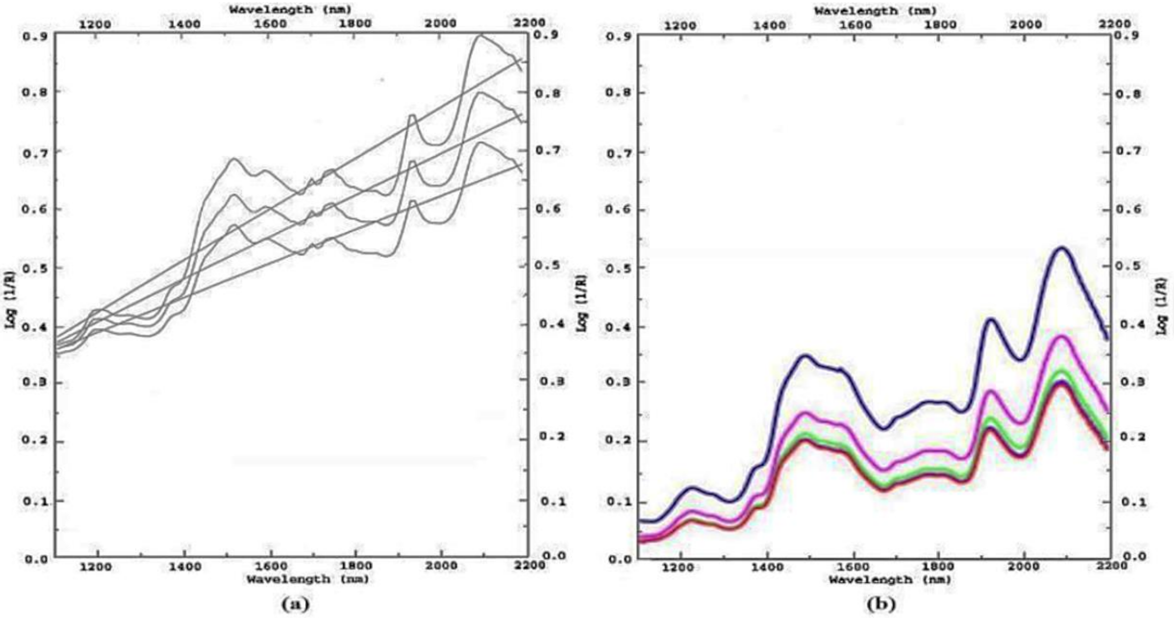

Figure 65: NIR spectra of 20% (w/w) cimetidine tablets (*a*). Pure MCC is tested for the hardness of a RC ribbon (*b*) The images have been adopted from sources (*a* [110]), and (*b* [34]).

Donoso [79] proposed that the resultant hardness values given by NIR are chiefly influenced by the smoothness of the tablet or compact, and the product of less diffuse reflection [79]. A further limitation for hardness testing is that the performance of these approaches is generally tested by using multivariate models of PCA and PCR, so that in practice a new calibration is required each time a new product is run.

6.3.2 Raman spectroscopy

Raman spectroscopy has also been researched as a surrogate measurement for predicting the *mechanical strength* of intact tablets [39]. Similar to Donoso *et. al.* conclusion of NIR research has indicated that diffuse reflectance increases with a substantial rise of (Raman) signal intensity (from the tablet's surface) of more greatly compressed tablets and thus, in-direct relation to a tablets mechanical strength [79]. Virtanen also trialled highly compressed compacts, thus further indicating that the Raman signal intensity is ∝ to a tablets' density (as a consequence of compaction-force). However this may be an indirect consequence because the signal trended towards a constant intensity with increasing CF, trended to an almost homogeneous result. Notably, this observation is not repeated to coincide with materials true density.

Furthermore, in relation to consolidation and mechanical strength, Johansson noted that no significant effect upon the Raman signal is found in relation to the compaction process that is insensitive to the effects of strength with unreproducible results for accurate hardness predictions [84]. Supported also by Wang, to surmise; the sensitivity of Raman spectroscopy is largely the effect of a substrates surface smoothness [85], and not sensitive to tablet CF and strength; Raman spectroscopy [85].

The use of X-ray diffraction techniques are regarded as very powerful tools for elucidating the atomic distribution of density in materials [87, 143, 144]. The X-ray based techniques do naturally suffer from the issues of ionising radiation and the unviable rapid quantification of in-line monitoring**.**

6.4 Production/formulation and material properties

Samples of Avicel® PH-101 (FMC BioPolymer, Belgium) were weighed, transferred to a 10 *mm* diameter die and tapped to allow the Avicel® to settle inside of the die and then were compacted into flat, cylindrical tablets.

Table 31**: The true density of MCC. Note: The true density of specific brands of MCC are inconsistently reported between sources, and thus listed are the approximate ranges researched**

Excipient	g/cm^3	Source(s)
(MCC*) Avicel PH-101	1.51-1.67 g/cm^3	Handbook of Pharmaceutical Excipients, Ed. 6, 2009 (1 of 4)

6.5 Tablet production with the PCT

Using the PCT (as detailed in *Section 5.4*) the four batches of tablets were manufactured to the specifications listed in *Table 32* following the method given in *Section 5.4*. The two sub sets of different, but equal tablet masses were compacted with increasing force to permit elucidation of whether the mechanisms of bonding are dependent on the number of particles in the die to interlock and bind. Thus, increasing duration in reorientation and consolidate posed is whether an increased ‘powder population’ is likely to increase orientation/binding capability and so deform.

The two process parameters (i.e. tablets which retain their form post-compaction to the ‘hardest’) under control were chosen to reflect a range of mechanical properties and densities ranges, where the instrumented tablet press is capable to compact up to a maximum of 500 *kg*.

.

6.5.1 Product specifications

Thirty-seven Avicel® PH-101 tablets manufactured over 4 batches with PP’s to explore the effects of both resistance to crushing force and RTS testing. The production thus, precludes a dwell time setting, whereby the punch would remain stationary at the target compaction force/height. Post compaction possible elastic recovery/relaxation was behaviour was expected and the tablets were then placed into sealed sample bags and stored in a desiccator for 48 hours at a RH of 30% at standard room temperature and pressure conditions (STP). A summary of the tablet specifications are given in *Table 32*.

Table 32: **Specification for 4 batches of Avicel PH-101® tablets.**

Batch *i*, ●			**Batch *ii*, O**			**Batch *iii*, ▲**			**Batch *iii*, Δ**		
200 mg ± 2, n=11			**295 mg ± 2, n=8**			**320 Kg ± 2, n = 9**			**420 Kg ± 2 n = 9**		
Density, *g/cm^3*	CF, *Kg*	Thk^n, *mm*	Density, *g/cm^3*	CF, *Kg*	Thk^n, *mm*	Density, *g/cm^3*	Fill-weight, *mg*	Thk^n, *mm*	Density, *g/cm^3*	Fill-weight, *mg*	Thk^n, *mm*
0.73	113.5	3.57	0.84	82.5	4.33	0.831	375.52	4.89	1.063	393.9	4.60
0.90	226.6	2.87	0.91	208.5	4.08	0.897	349.99	4.53	1.051	371.71	4.79
0.96	285.5	2.68	0.96	274.4	3.94	0.961	325.9	4.22	1.054	346.7	4.20
1.00	325.9	2.53	0.99	320.8	3.81	1.035	303.62	3.92	1.037	322.8	3.97
1.03	355.7	2.52	1.00	351.6	3.73	1.136	277.31	3.57	1.047	295.8	3.59
1.04	376.7	2.46	1.02	373.4	3.70	1.254	249.84	3.23	1.033	272.4	3.34
1.07	376.7	2.39	1.03	391.7	3.62	1.396	22825	2.91	1.051	244.3	2.94
1.08	393.0	2.37	1.04	427.0	3.53	1.598	200.73	2.55	1.047	223.23	2.70
1.09	407.8	2.35				1.012	153.33	1.93	1.029	196.95	2.36
1.11	418.8	2.31									
1.12	456.0	2.28									

6.6 Analytical equipment and methodologies

6.6.1 PharmaTest PTB 311E

The force required to break the tablets between two parallel plates was measured with use of a PharmaTest PTB 311E. The principle action is shown in *Figure 66*.

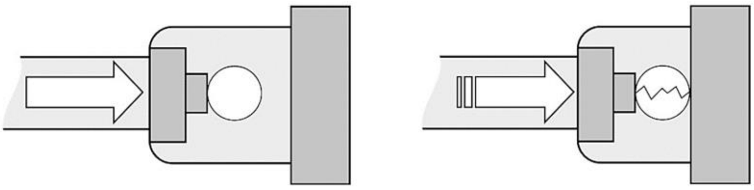

Figure 66: **Schematic representation the determination of diametric crushing strength. The fracture originates from a defect in the internal bonding and propagates along weak regions.**

6.6.2 FDT for measurement of material RI's

The *TD* waveforms were transformed with a standard fast-Fourier routine to provide comparator frequency-domain results of tablet RI's. The system configuration and method principles used are described in *Section 3.6.*

6.7 Results and discussion

6.7.1 Objective 1: Produce 2 sets of Avicel PH-101™ tablets with fixed masses (200 mg, 295 mg) to assess links between compaction-force and tablet thickness/SF

Unsurprisingly the compaction-force and the thickness of equal volumes of powder clearly shows a reduction of thickness with increased compaction-force in both batches. A notable observation in reference to *Figure 67*, is that a linear line of best-fit can be drawn over the compaction-force and thicknesses of 295 *mg* tablets (over the range of compaction-forces between 90 – 450 *Kg*, generating a correlation co-efficient of 0.99). Although, over a comparably broad range of compaction-forces, the thickness data associated with the 200 *mg* tablets cannot be fitted with a continuous linear line of best-fit (linear correlation coefficient of 0.94 but, a polynomial line is instead fitted for the illustrative purpose to show divergence). One explanation for this general trend may stem from the ability of a greater powder mass to initially contort by a greater extent (with cumulated additional forces applied by a greater residence time of punch on contact with the Avicel). However being more massive the particles may permit rearrangement and collectively dissipate the force over a broader number of particles (hence more voids), yet at the expense of resisting a more permanent deformed state because of retention of elastic forces. With the tablets of lesser mass, less material is effectively consolidated into an irreversible deformation state with increased transition of an elastic to brittle/plastic behaviour.

This explanation follows from the principles of densification where the energy initially imparted during compaction (via the punch) causes reorientation and a reduction of voids with air displacement within the blend. Creating a more closely packed structure, the materials' inherent deformation nature then largely influences the compacts' resultant mechanism to retain the effect of strain, where MCC is reported to consolidate both elastically and plastically prior to fragmentation of particles (generally leading to fresh binding sites and further void reduction through creation of fines) [67].

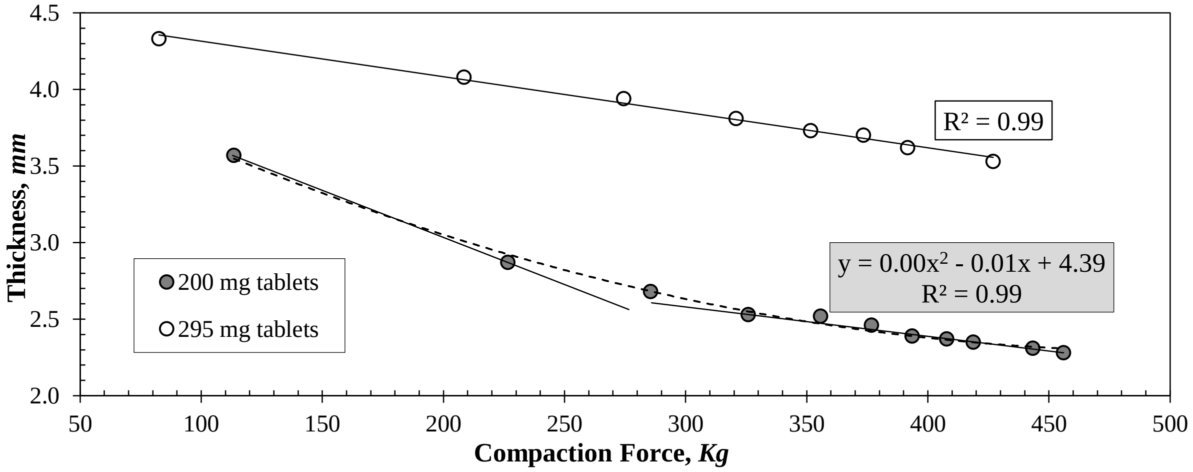

Figure 67: **The effect of increasing compaction forces to the thickness of two batches of Avicel PH-101 tablets of differing fill weights.**

The relationship between compaction-force and geometrical measured density, ρ, of the two tablet batches is illustrated in *Figure 68*. An apparent linear trend observed for the 295 *mg* tablets with the inclusion of a line of best-fit fitted over the compaction-force and density. Providing a correlation coefficient of > 0.99, the consistent inability to draw a linear best-fit line is again true for the 200 *mg* tablets with a polynomial line of best-fit, being more appropriate (with an R^2 1). The observation of the apparent linearity of the higher-fill weight tablets (HFW), and the divergence of the lower fill-weight (LFW) tablets is similar to that as seen with compaction-force versus thickness (*Figure 67*). Comparing the two sets reveals a near equally spaced out set of lines of the linear trends at higher ranges of pressure (between 300 – 450 *kg*). It would seem permanent deformation are in common and approximately linear, to both masses. This near parallel observation is marked in *Figure 67*, however divergence as pressure decrease is further indicative that higher fill weight tablets are more likely to relax or are more resilient to lower pressure permanent deformation.

Prior to a compaction-force of ~295 *Kg*, the tablets with the greatest mass have a greater ρ than the least heavy tablets. Post-convergence, the density of the lesser fill-weight tablets is greater. The differing gradients of the systems come with consideration of the initial mass of the tablets. Indicated is that the 295 *mg* tablets represents a system with an increased degree of efficiency in dissipating the energy imparted during compaction. Given an equal compression rate (in both populations of tablets) below this threshold of approximately 295 *kg*, the greater number of particles present within the die may permit the powder-mass to rearrange more effectively to form an '*early-stage*' consolidation method and permit ↑ reversible consolidation (*See Figure 82*). Past the threshold of 290 *kg*, consolidation in both systems has undergone greater rearrangement in the powder-mass and that further compaction and ρ increments is inclusive of irreversible deformation (i.e. plastic and potential new bonding site creation with particle fragmentation).

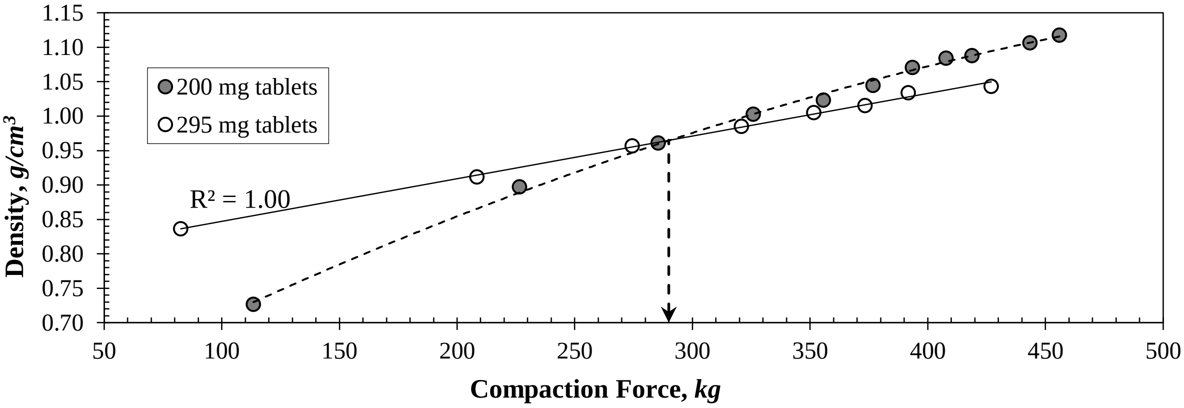

***Figure 68*: The effect of compaction force on tablet density. The inset vertical line indicates a compaction-force of 290 *kg*.**

6.7.1.1 Quantitative summary: of material consolidation dynamics including the additional punch movement

The larger powder blends occupy a greater volume in the tablet die than would lighter masses and in-turn, the punch will travel at a fixed rate and apply an equal pressure onto both sets (comparing between batches). The overall time that the punch is in contact with the powder blends will therefore be different and it is suggested that the ratio of elastic to plastic deformation in the thinner tablets is greater than within the thicker tablets (as illustrated in *Figure 69*).

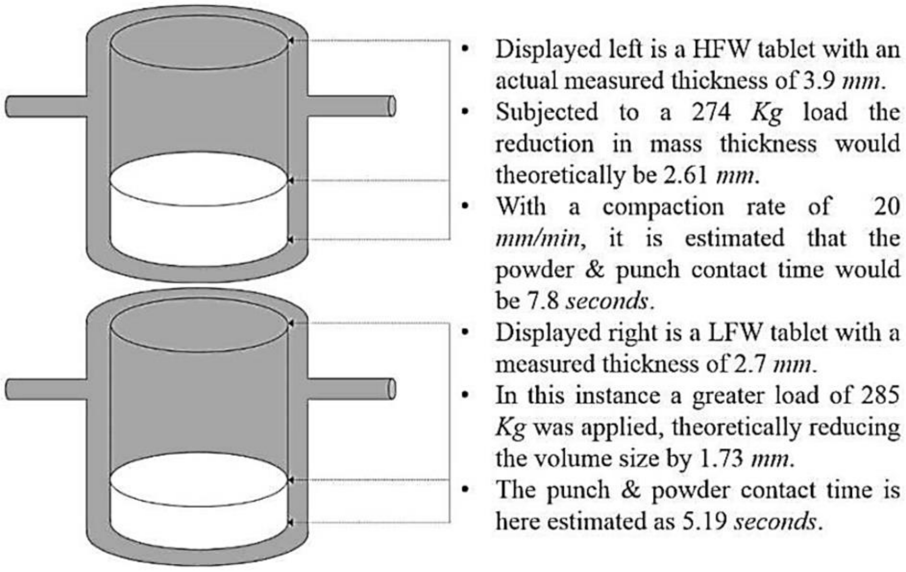

- Displayed left is a HFW tablet with an actual measured thickness of 3.9 *mm*.
- Subjected to a 274 *Kg* load the reduction in mass thickness would theoretically be 2.61 *mm*.
- With a compaction rate of 20 *mm/min*, it is estimated that the powder & punch contact time would be 7.8 *seconds*.
- Displayed right is a LFW tablet with a measured thickness of 2.7 *mm*.
- In this instance a greater load of 285 *Kg* was applied, theoretically reducing the volume size by 1.73 *mm*.
- The punch & powder contact time is here estimated as 5.19 *seconds*.

***Figure 69*: Examples of a 10mm die containing, *above* 295 *mg* of material; and *below*, 200 *mg* of Avicel.**

6.7.2 Objective 2: Produce 2 sets of Avicel® PH-101 tablets with fixed forces (320 Kg, 420 Kg)

Relating diametrical-resistance to fracture and RI with tablets of variable mass/ fixed compaction-force (*Figure 70*; Δ) are broadly linear with fitting of lines of best-fit. Denoted by the Δ points, it is unsurprising because the diametrical-resistance to fracture is logically influenced by the thickness of the tablet. It is believed that similar deformation mechanisms are internally formed (inherent to create internal-cohesion). The differing horizontal trends with the *Δ* tablets support this and previous discussion of fundamental compaction behaviour to consolidation (and thus the surrogate RI values). The negative gradient is more appreciable with 320 *mg* tablets however. It is indicated expected that this trend (temporary binding follows increased thickness) is causal of the compression with appreciation that equal compaction rates in production are repeated. Thus, less powder less powder in contact is of a lesser proportion.

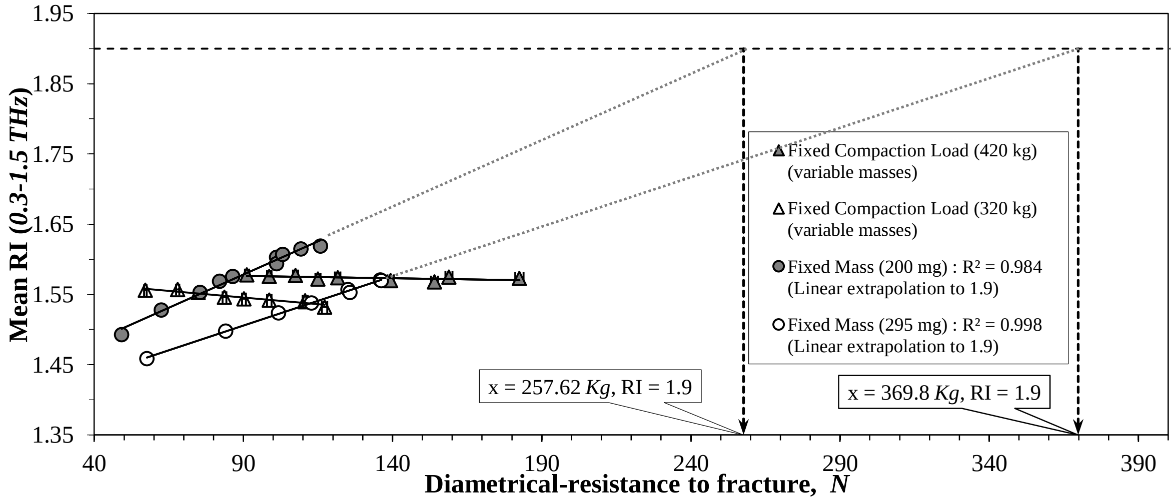

Figure 70: **Plot coupling THz derived RI's of 4 Avicel® PH-101 tablet batches and the *resistance to diametric crushing force* (i.e. crushing strength). Linear extrapolation is inset to all tablets to a RI of 1.9 to give a theoretical crushing strength if linearity is assumed.**

The relationship coupling the two tablet batches of fixed mass (○) with *crushing force* and RI can be traced with linear best-fit lines over the actual ranges (40-140 *N*) can be assigned straight line equations (200 *mg*: $y = 0.0019x + 1.4$, and 295 mg: $y = 0.0014x + 1.38$). Extrapolation to an RI of 1.9 from the experimental data with linear derivation of true density at this value indicates again that:

- ↑ Compaction, ↓ thickness and ↑ consolidation (and thus our RI surrogate measurement) in a near proportional manner (R_2 = 0.984 & 0.998 with respect to 200 *mg* masses and 295 *mg*.
- The gradient operators do however differ (Δ= 0.0005) and indicate that diametrical-resistance to fracture would exptrapolate 200 *mg* and 295 *mg* tablets to 258 and 370 *kg*, respectively. Although linearity is expected to lessen as the true density value is apprached (proposed previously as 1.9), the gradients over the tested ranges, suggest the mechanisms of deformation are dissimiliar and here that the tablets of lesser mass are densified more effectively with respect to RI.

Relationship between radial tensile strength and RI

The relationship between RI and material density (*Figure 83*) is broadly linear (with a correlation coefficient of > 0.99). This is expected given that consolidation during the compaction process, results in particle rearrangement and an increase in the solid to air fraction in a confined punch-die environment. The line of best fit ($y = 0.59x + 0.98$) extrapolates to a value of ~1 which is expected given the fact that the refractive index of N_2 is ~ 1[22]. The compaction forces used in this study are between 82 – 456 kg, and in all cases produced sufficiently durable compacts in respect to handling. Extrapolation of the line of best fit to the true density of MCC (1.512-1.668 g/cm_3; $\bar{x}$ = 1.59 [148]) provides an estimate of the THz RI for the pure material (in this case $RI_{100\%MMC}$ = 1.90). The uncertainty in this estimate may be derived also, based on the root mean squared error (RMSE) from the line of best fit, whereby the lower limit is defined by $RI_{100\%MMC}$ – RMSE (= 1.899) and the upper limit is defined by $RI_{100\%MMC}$ + RMSE (= 1.901). Extrapolating of the line of best fit to find the RI at zero density provides an estimate (in this case RI = 0.966). The uncertainty based on the RMSE from the line of best fit in this estimate for the lower limit is defined by RI_{N2}– RMSE (= 0.996) and the upper limit is defined by RI_{N2} + RMSE (= 0.997). Given that the RI estimate for N_2

is slightly lower than one might expect (marginally > 1) it might then be concluded that the RI estimates of the pure MCC may also be slightly higher than they are in reality. The extrapolated RI for pure MCC may be even lower if the line of best fit has indicated regions of broad linearity and the work of [134, 145] show inflexions and plateauing at density ranges/solid-fractions outside of our compaction window.

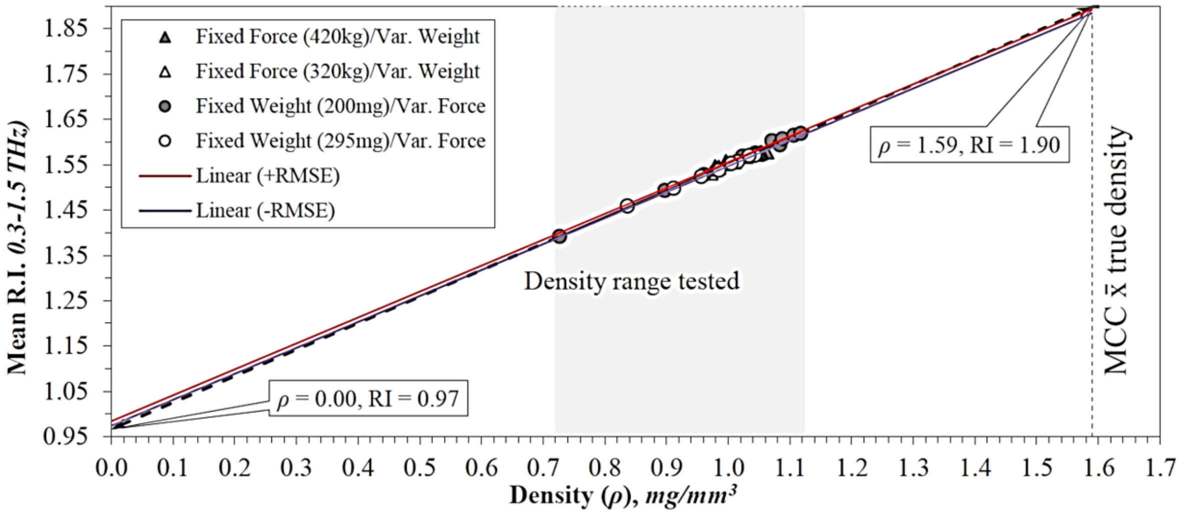

***Figure 71:* The effect of increasing density/porosity to the THz derived RI of all four batches of MCC (Avicel®). The linear correlation coefficient (R_2) is 99.6% is achieved with the inclusion of all batches.**

Palermo [134] examined the correlation between THz RI and compaction-force (on MCC tablets), to report that use of compaction-forces > 900 *kg*, that the stress yield of MCC lessens and densification becomes non-linear, plateauing at a range ~ 3600 *kg*. Unfortunately, the upper force limit of the tablet-press prevents accurate production above 500 *kg* (*See Figure 77*) used by Palermo [137]; who suggests that it is the saturation of binding sites in MCC beyond plastic and possible fragmentation deformation. This theory adequately explains that under greater compaction, that brittle fragmentation would create 'fresh' binding sites and evacuation of air voids, necessary to approach a true density value (*shown inset 'maximum applicable pressure' Figure 77*).

The compaction forces used herein are between 82 – 456 kg during manufacture of Avicel® PH-101 tablets. Recording the mean THz RI the relationship between RI and compaction force is shown to be broadly linear over the CPPs (*See Figure 86*) where correlation coefficient's of the tablets of the 200 and 295 *mg* tablets are 99.4% and 99.8% within our compaction range, respectively. Extrapolation of the lines of best fit from the used compaction range to postulate an RI of Avicel® true density using a line of best fit of a supposed linear model does not satisfactorily describe the relationship compaction outside of the compaction range used here following the description provided by Palermo [137] Reasons for this are speculated because:

- At low forces observed more clearly in Section *6.5.1*, lesser mass tablets are indicated to form different consolidation mechanisms.
- At greater compaction forces where deformation proceeds (suggestively from plastic and further mechanical interlocking via fragmentation) to reduce the proportional relationship of densification with increased force in obtaining an eventual true density (See *Figure 91*). Approximate plateauing of Avicel® being met at ~ 1600 kg [137].
- The linear extrapolation displayed in *Figure 72* indicates a true density could be achieved with the same material as a bearing of fill-weight. For instance 200 – 295 kg fill weight blends would likely delineate above the compaction window to reach the predicted RI (1.9) at true density at similar forces. This result is erroneous as true density of a single material is intrinsic to its molecular character (predominately inter-particulate nature). Therefore, 200 mg tablets would reach (an assumed) true density at 870 kg (RMSE ± 0.38) and for 295 mg tablets would reach (an assumed) true density at 1358 kg (RMSE ± 0.42).

Indicated by *Figure 72*, the assumption that the true density of Avicel® ($\bar{x}$ *1.59* [148]) corresponds to a THz RI *1.90 ± 0.01* is used to support Palermo's [137] findings (i.e. linearity is lost). Displayed in *Figure 72*, linear extrapolation indicates that true density would be met at dramatically different compaction forces resultant of tablet the fill-weight.

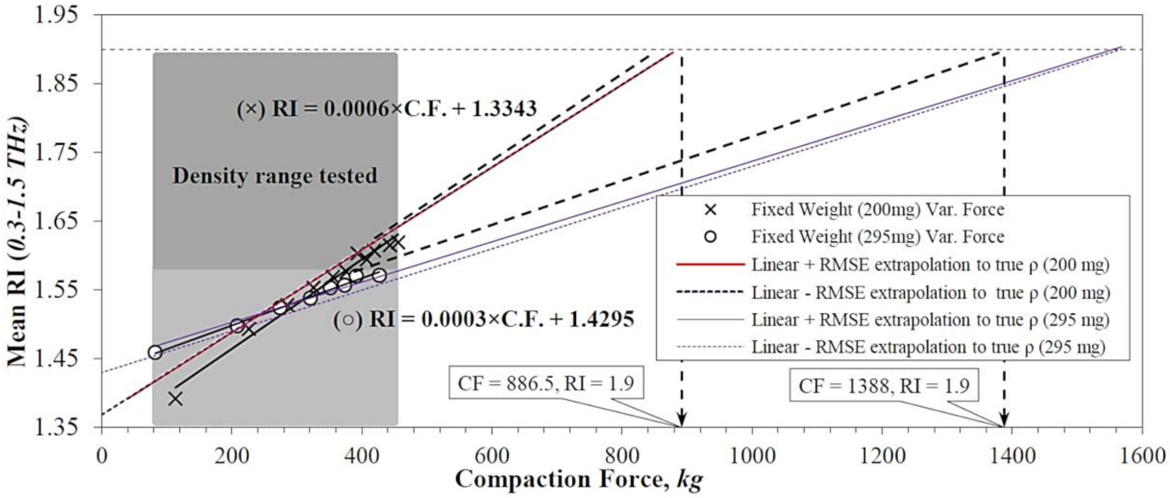

Figure 72: **The effect of compaction force on the THz derived RI of Avicel® PH-101. The linear correlation coefficient of the tablets of 200 mg (R2) is 99.4% is achieved over the compaction range of 113 – 456 kg. The linear correlation coefficient of the tablets of 295 mg (R2) is 99.8% over the compaction range of 82 - 427 kg.**

The relationship of RTS, (as a unified value indicative of mechanical strength) and RI, the tablets of 295 *Kg* are broadly linear with over-laying a line of best-fit (R2 = 0.992) and the lesser mass tablets are approximately linear, yet best fitted with a polynomial line of fit (*See* ***Error! Reference source not found.****)* The trend of a non-linear relationship with lower masses may again be explainable with differing proportions of mechanical inter-locking and elastic/plastic deformation.

The tablets of greater mass were approximately 50% thicker than the low mass tablets, so greater compaction forces was used during compaction in order to reach similar densities/RI (than the low fill-weight tablets). It may be suggested that the tablets of greater mass are able to undergo both elastic and plastic consolidation during compaction, in contrast to the tablets of lower masses. With reduced interfacial-contact between particles would, for instance would influence the proportions of mechanisms responsible for consolidation. Convergence of the extrapolated lines, both populations may predominately deform irreversibly. Therefore at lower compaction forces, the ability of lesser weight tablets to elastically recover is proportionally hindered (resulting in differing gradients at ‘low’ compaction forces). With a greater presence of irreversible binding in either systems this may result in internal flaws to the integrity of the tablet forming and therefore explain the reduced parallel profile of RTS.

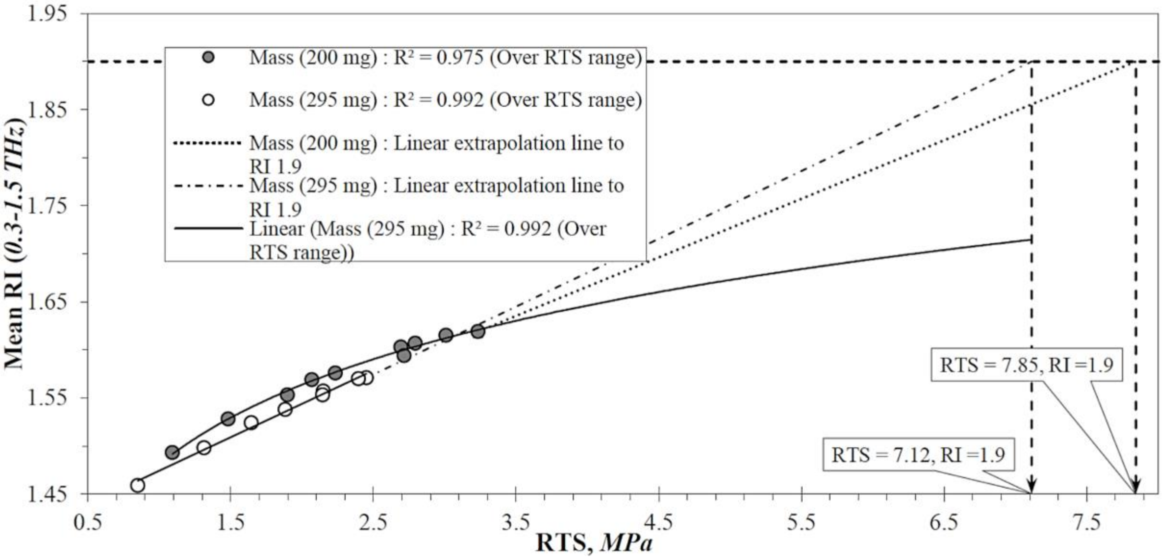

Figure 73: **The relationship coupling the RTS of 2 MCC Avicel® PH-101 tablet batches produced under variable compaction forces) and the mean measured THz RI**.

With observation of the two batches of tablets of masses 200 and 295 *mg* and compressed with variable forces (*See* ***Error! Reference source not found.***). The fit-lines appear to converge at the point of 1.63 RI / 3.5 *δ* / density 1.1 *g/cm*$_3$. The error bars are applied in order to compensate for possible volume inaccuracy in reading the thickness of each tablet with a micrometre and for tablets that where not completely flat.

Summary

Tablets compacted at fixed forces (*See Figure 74*) cover a much narrower RTS and RI range as expected. The increased gradient associated with the tablets compacted at 420 kg indicate that while RI remains generally equal, that RTS is less so than with the tablets of a lower compaction specification. The tablets compacted at 320 *kg* feature a broader density range which would be expected for lower compaction forces and lower force appliance for consolidation. The varying gradients between the two batches surmises the observations of Avicel's® deformation behaviour, because of influences of increased compaction forces to initially repack the particles (i.e. at low stresses) and following inter-particle reorientation, elastic and irreversible plastic deformation may predominate. Elastic deformation is therefore more likely to be evidenced in density profiles before the point of inflexion (w.r.t. compaction force) from linear behaviour where additional compaction forces are required to overcome particle fracture and possible intra-molecular repulsion in creation of new binding sites attributed to void removal through the stages of elastic and plastic deformation.

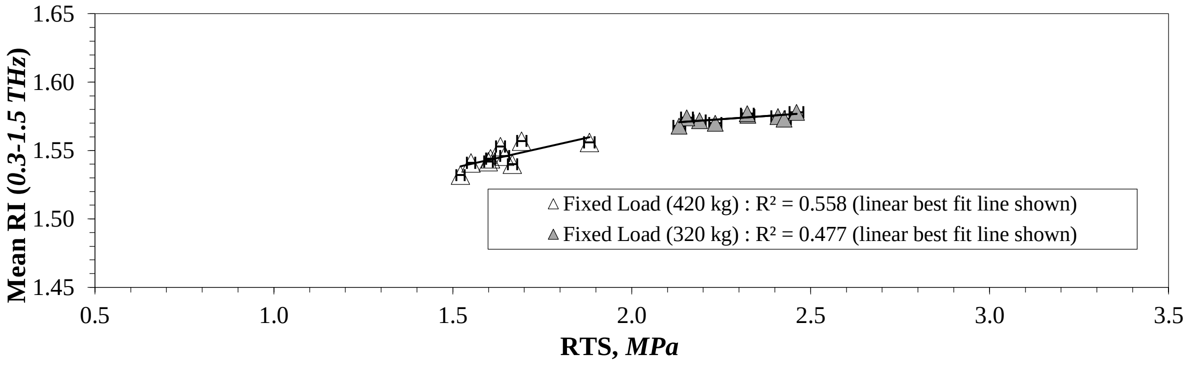

Figure 74: **The relationship coupling the radial tensile strength of 2 Avicel® PH-101 tablet batches (made of different fill weights) and the measured mean THz RI.**

The production of fines during compaction is additionally heightened at greater pressures because of brittle fragmentation and here would produce fines and account for increased ρ with the filling of empty voids. The greater mass tablets on the other hand may possess sufficient combined particle-particle freedom to predominately undergo less abrasive consolidation processes (including a greater degree of reversible compaction) under greater pressures in compaction, both populations were exposed to full compaction. It is postulated that particle-particle binding mechanisms, at a lesser compressional force and greater tablet size give rise to a greater ability for a tablet to elastically recover post compaction, either immediately or over time, which would function the effect of resistive forces exerted by the die-wall. When the punch is released, pressure exerted by the tablet onto the die walls will decrease; however some residual die-wall pressure may still exists [146], and addresses, that in practise thicker tablets need a greater ejection force.

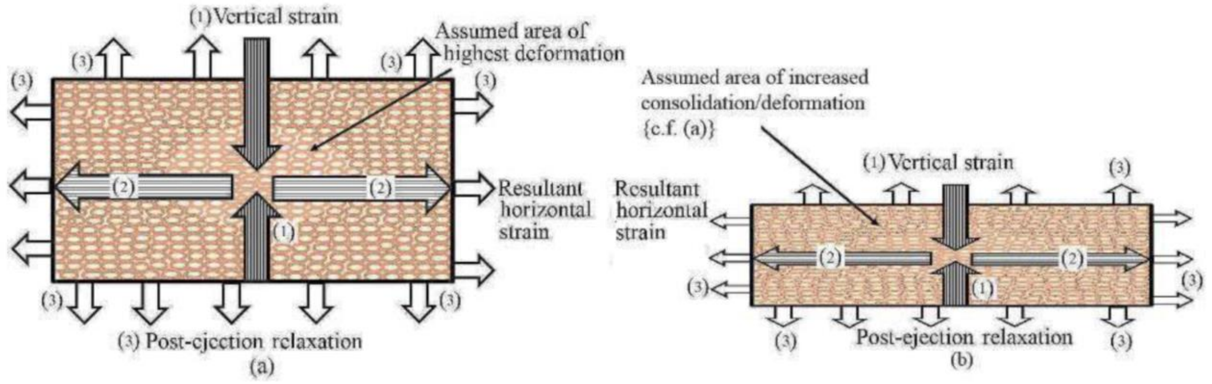

Figure 75: **Schematic illustration of two HFW and LFW tablets during compaction and the dissipation of force which may occur.**

6.7.3 Objective 3: Consolidation mechanisms and dynamics of residence-time and mass-flow

Transposing all four batches of tablets onto the same plot (*See Figure 76*) and with addition of a line of best fit, a relationship is demonstrated which approaches linearity. Producing a root mean square error (RMSE) of 11.1 *MPa* and a correlation coefficient of 90% this method of analysing compacts of mixed densities (as a consequence of equal fill-weight and increasing compaction force) as well as for differences in fill-weights does not seem sufficiently accurate

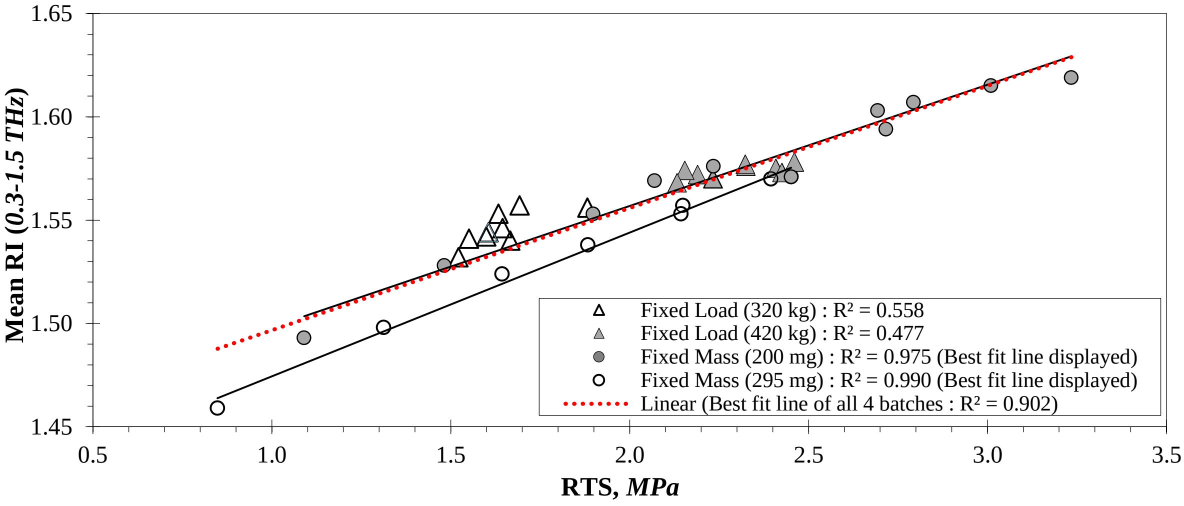

Figure 76: **The correlation between RTS and terahertz derived mean refractive indices over the four batches of manufactured Avicel® PH-101 tablets.**

It is thought that if compressional forces were much greater (1000's *Kg*) that consolidation by fragmentation may predominate (*See both illustrations of Figure 77*) and particle interlocking by the weak forces associated with brittle fracture would cause a positive upswing in trend evident with a period of plateauing (as seen RHS in *Figure 77*) between compaction force and density.

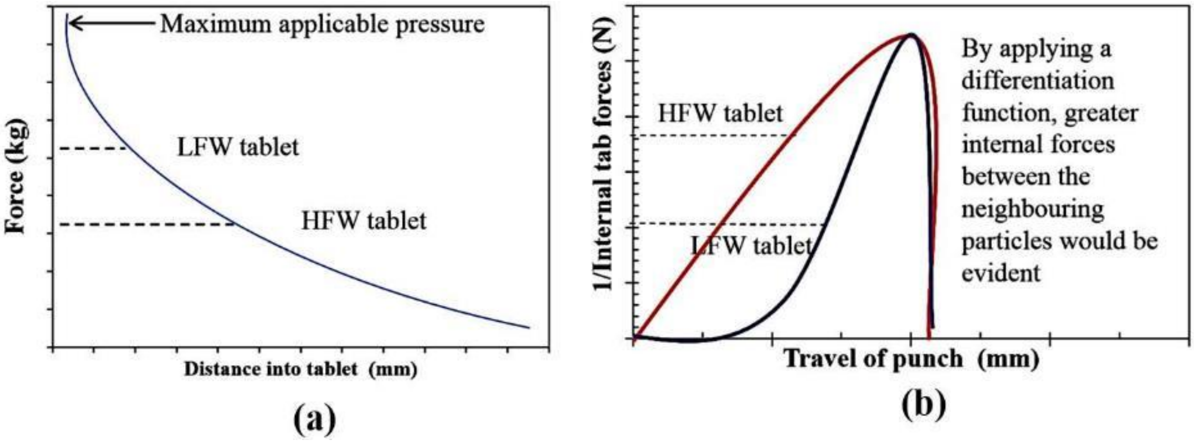

Figure 77: **Associated with tableting is that porosity and force is typically non-linear over a broad-range of force, eventually plateauing at ↑ CF's. Inset to exemplify the two previous sections of low fill-weight (LFW) and high fill-weight (HFW) tablets, the gradient of the profile could be viewed as more linear for HFW than LFW; yet the perspective of scale must be appreciated. Image adopted from a MCC tablet compression paper [147].**

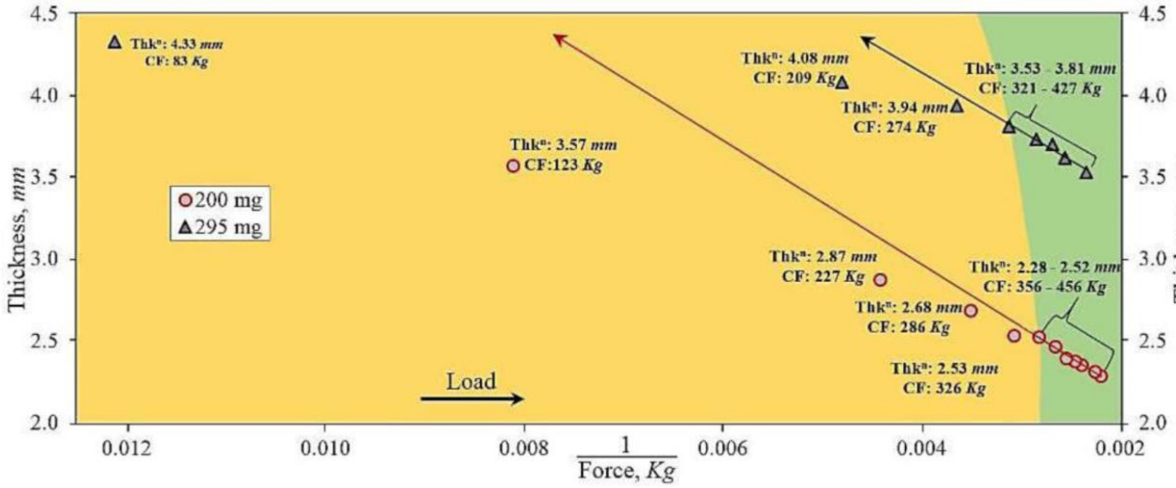

Figure 78: **The operating windows indicative of compaction force and thickness of two tablet masses of Avicel® PH-101 tablets. Differentiation by colour divides the linearity of the supposed bonding mechanisms acting for both tablet masses.**

6.8 Conclusions

6.8.1 Objectives 1 & 2: Produce 2 sets of Avicel PH-101

We have demonstrated that the relationship between compaction force and the surrogate value for/and density appears to follow a linear trend below a certain threshold of force. Under greater duress particle movement becomes compromised and the void fraction between powder particles and expelled air reduces with the introduction of further consolidation. The proportion of consolidation models, albeit, reversible (elastic) and irreversible (plastic) for the material studied, is suspected to be variable in respect to tablet fill-weight.

The deformation mechanism of the thinner (200 *mg*) tablets is observably more consistent over the compression-forces used. The resistive response to consolidation promotes a greater linear trend than with the HFW tablets. With the thickness divergence from linearity of the LFW tablets, a shaded region has been added (which corresponds with ~ 285 *kg in Figure 72*) to represent a probable change in the resistive and responsive dynamics of consolidation in the blends dynamics. Furthermore a reduction in punch residence time may be a contributing factor in the progression of elastic deformation to an irreversibly plastic nature. The mechanism of axial to radial stress transmission is also likely to account in this observation. During tablet compaction, the continued axial movement of the punch onto the confined powder mass will predominately increase the pressure exerted at right angles to the path of the punch with increased tablet weight and compaction force (presented in *Figure 69*). This will create greater radial pressure at the die-wall as the force is increased [18]. Thus a reduction in compaction time may be one contributing factor in the progression of elastic deformation to an irreversibly plastic nature.

The relationship between compaction-force and geometrical measured density, showed an apparent linear trend for HFW tablets. This yielded a correlation coefficient of > 0.99. However with the LFW tablets, a polynomial line of best fit was needed to express the profile, indicating greater particle volume effects the manner in which the bulk blend agglomerated. Analysed through bulk transmission measurements, it can be argued that the mean of the tablets RI's are effected by inter-particulate binding than laminar banding. This is because the two batches of tablets were analysed, and neither equal volumes nor equal fill-weights (vs. density) gave inner-batch inconsistencies. Thus lateral effects associated with laminar banding is suspected to have little or no effect when 'cracked' diametrically.

6.8.2 Objective 3: To consider the consolidation mechanism occurring between the tablet batches as a function of compaction-force and fill-weight

Revealed by approximately parallel lines of best fit (even with extrapolation) the linear lines of HFW tablets suggest that compaction is meet by an equivalent resistive response at all pressures. This is in contrast to LFW tablets where a threshold is apparent, at which point the SF (RI) diverges from linearity at specific points. Whereafter the SF is greater after sufficient stress; interestingly, the trajectory of the extrapolated lines of LFW tablets indicates a linear response to consolidation is maintained with greater forces, and also at much lower forces. It seems highly probable that the inflexion seen in LFW tablets (at mid range compaction forces) correlates strongly with the packing structure achieved, and importantly maintained. For instance MCC possesses elastic/brittle and plastic character, and so must have transitional (or strain thresholds) whereby the relatively highly porous (yet crystalline) structure undergoes brittle fracturing adding to the number of shear faces/clefts, enabling enhanced mechanical interlocking and/or additional binding.

Conversely, equally high compaction forces conveyed to HFW tablets did not apply sufficient stress to overcome a modicum of consolidation and consistent levels of mechanical interlocking yet, the force may not have been sufficient to cause further breaking of the MCC's structure and thus failed to interlock and form additional bonds to deform as significantly. Having alluded to the elastic/plastic character of MCC it is also possible to hypothesise that insufficient force imparted (to the HFW's) was dissipated from axial pressure to radial pressure due to,

(1) Greater number of particles to deform (which, in-turn have elastic tendencies).

(2) Materials with an elastic component (including MCC) demonstrate the least residual die-wall pressure, and during de-compaction and ejection show the greatest elastic recovery [148]. With pressure (and thickness) the gross effects of the resistive forces acting axially and radially have a high elastic recovery potential. With ejection more surface area may loosen anterior particles, especially if one considers that the increased number of particles reduces the radial pressure (permitting increased elastic recovery) which is envisaged to be far greater in LFW tablets in regard to axial and radial pressure. (3) Larger powder blends occupy a greater volume in the tablet die than would lighter masses and in-turn, the punch will travel at a fixed rate and apply an equal pressure onto both sets (comparing between batches). The overall time that the punch is in contact with the powder blends will therefore be different and it is suggested that the ratio of elastic to plastic deformation in the thinner tablets is greater than within the thicker tablets.

7 Experimental chapter 4

Interrogation of a multi-variant sets of ribbons with TPI to evaluate the success, limitations, constraints and practical implications of a PAT technique to eventually monitor and control the roller-compaction process for increased efficacy.

Scope

Continuing development from *Experimental chapters 1* and *2,* TPI is chiefly used to monitor the consistency of consolidation across regions of a multi-variant sets. Firstly, comparator RI's (as a function of λ) are taken from wafers (rectangular slugged compacted with identical punch markings and composition of their 'sister' ribbons), supplied courtesy from Bristol-Myers Squibb (BMS) substrates for FDT and TPI evaluation.

The wafers formulation and gas pycnometry SF ratio values match the properties of the ribbons. Allowing the apparent SF and density, ρ, to be contrasted to FDT and TPI RI's of acceptable TPI consistency, while also introducing greatly diffuse substrates resultant of knurling (a system parameter), and enable gas pycnometry SF's. Despite the readily quantifiable manner in which the volume and density of wafers can be recorded (compared with ribbons, *see Figure 88* for morphological differences), the singular latticed surface of the wafers introduce the potential issues of diffusive light reflection (as described later).

The next stage is to evaluate 'ideal' ribbons from the perspectives of system setup (e.g. smooth vs. knurled rolls) roll-force/roll-gap and formulations. By admission of Gururajan, Hsu, Li, Meyer, roll-force is the most critical parameter (while the roll-gap only becomes an important and influential parameter when significant changes in the roll-gap occur (e.g. > 1.5 mm) [4]. Step by step, RC-ribbons are then produced to cross-analyse parameters/settings to observe any THz responses, and report any limitations and constraints encountered.

Matching the DoE's of roll-force and roll-gap, plus formulation and system differences is objectively studied here. Using current feedback-controlled RC's to interrogate the causality of MA's (the case in continuous roller-compaction); rather the methodologies of defining a surrogate density/SF parameter

.

7.1 Objectives and tasks

1) Establish a guideline to elucidate method issues which could be detrimental to TPI analysis and access resolutions.
    a. Analyse popular forms of ribbons and wafers. Wafer are rectangular pressed compacts sued in early stage development and crucial for pycnometry measurements Being rectangular and supplied with gas pycnometry values gives a basis to correlate not only THz RI with SF, but also match apparent gas displacement figures. This may require FDT and TPI methods (i.e. wafer and BMS ribbons are knurled on one surface which may influence physical thickness recording and importantly, reduce the ability to both distinguish the probe-beams optical delay-time, and the prediction of the RI owing to the principles of reflection (with surface based TPI), and the intensity of the probe-beam/surface with FDT. Both methods may therefore suffer diffusion owing to $\theta i \neq \theta r$.
    b. Resolve any problems influencing the calibration of RI, ρ, (and report if necessary) and highlight further limitations of both measurements (TPI & TDT) and whether these can be abated to tolerable levels or completely addressed.
2. Further test the TPI method on ‘ideal’ roller compacted ribbons.
    a. Devise a DoE to allow sensitive evaluation of THz results and thus manufacture ribbons of controlled, key CPP’s including:
        - Compaction force, roll-gap.
        - Three formulations to address for varying material attributes.

b. Produce c-sectional images of the ribbons laterally and longitudinally to quantify TPI derived RI’s to predict ribbon thickness. Thus validate the accuracy of the method by comparing the calliper based thicknesses and the combined TPI-OD and TPI-ODT methods.

c. Produce regional ribbon scans and interpret the TPI *E-Fields* at points defined by a 25 point matrix (per ribbon) to construct topological and RI/thickness distribution plots; indicative of uniformity

d. Purport any further constraints, limitations and proposed methods to construct a viable, valid, and practical use of THz technologies as a PAT tool. Notably, continuous manufacture and continuous monitoring and control of the process for enhanced operational efficiency, as too greater assurance demanded with QbD principles[24].

3. Purport any further constraints limitations and proposed methods to engineer a viable RC featuring RC probes

---

[24] **This serves to evaluate and validate previous work in regard to analytical methods necessary for greater achievement of the CQA's. The proposal of sensitive and rapid data boundaries defined into an in-line PAT system is acceptably trivial, however optimal control of DG/RC challenges, whether and how PP's can be made to respond and importantly whether uniform blend conveyance is a system design element and/or a dynamic process parameter.**

.

7.2 Introduction

The impact of conditions during roller-compaction including material attributes, equipment settings on the critical quality attributes (CQAs) of the ribbon is explored through a DoE in order to minimise the risk of undesirable/out of specification (oos) CQAs. The attributes for a ribbon include content uniformity and thickness/density at the heart of its mechanical strength. Specific issues that arise during the feeding/compaction stage (i.e. hopper → auger(s) → uniform de-aeration → slip →nip regions) include flowability and multiple causes such as flowability, de-aeration, and cohesion can affect the blends distribution before pressing at the nip- zone.

A labelled photograph of the graphical-user interface (GUI) of a the Gerteis PolyGran™ is shown in Figure 93, in order to introduce the dynamic feed-back mechanism which is invariably featured on modern DG/RC's such as those produced by AlexanderWerk (AW) and Gerteis to assist compliance with the user defined parameters. Typically the lower roller-wheel is held in a fixed position and is so, inactive with regard to torque registration. Generally, the top roller is mounted on an axle containing force inducers and has two-way movement to control the roll-force. In reference to Figure 93 the main process parameters (PP's) set by the user are those highlighted by the yellow fields and the corresponding white fields are the real-time system responses. Here, the roller-force is set at 5 kN/cm and the roller-gap at 4 mm. The auger speed is fully-automated and operates independently at a rate which will deliver the PPs of compaction force, roll-gap and roll-speed sufficient to draw powder into the slip region to meet these two PP's. As uniform conveyance of the powder is therefore critical to be able to control the roll-force and roll-gap. The roller-speed is another parameter set by the user however, is not considered be a highly critical PP, but it does have two functions'. 1) The user is able to control the throughput of ribbons, while controlling the duration of the compaction time (analogous to dwell time in tableting), and 2) reduces the potential for the powder backing-up' in the auger (affecting particle rearrangement/pressures greatly) and thereby to assist the flow rate through the system. However, a suitable PAT will maintain the roll-force and the roll-gap even when insufficient powder stock cannot be delivered by the augers functionality.

Figure 79: **Labelled photograph of the Gerteis PolyGran GUI. The yellow fields are set by the user and the corresponding white fields are the real-time system responses.**

Including all the attributes associated with the blends MAs, equipment settings (PP’s) and the systems parameters (e.g. the conditions experienced during the process), the key conditions inter-relating to successful densification centre on the mass flow-rate through to the nip region and the force (and the duration of the stress). The CQAs are responsive to a large extent to the equipment’s setup/design and the dynamic response of the CPP’s in reaction to the MA’s. The system design therefore plays a synergistic role to match hopper design and the blends path-way to compaction, control of the PP’s, stemming again from dynamic treatment of the MA’s.

The correlation of system/PP’s and MA’s is illustrated in *Figure 94* and shows the key roles of user defined PP’s (shown in yellow) and the logic bridging the absolute necessity of consistent blend deposition at the rolls in order to achieve optimal CQAs within ribbons. The definable PP’s are acknowledged with direct interaction with the MA’s and also to the instruments capabilities and limitations. For example roll-speed is noted as a less critical PP because the through-put of the blend is user-defined and not reactionary to the uniform conveyance from hopper to the ejection. The roll-speed is therefore a factor more analogous to the dwell-time of the tableting process linked to sufficient tensile strength.

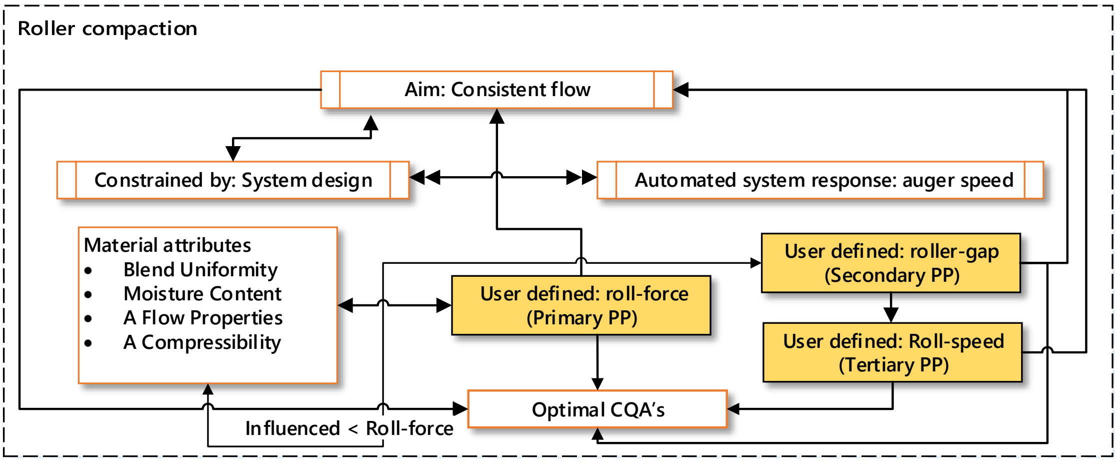

Figure 80: **Overview of the inter-relationships in RC particularly with emphasise of MA's ↔ system design ↔ CPP's.**

In considering the current issues of DG/RC, the real-time roll-gap reading (*see Figure 93*) could serve to supply part of the coupled/convolved parameters of RI (with path-length). However, the problem with this solution is that. (1) The reported separation of the rolls provides the gap of the axle distance between the rolls (minus one diameter) analogous to giving a *parallel* value. The reported RC roll-gap would be indicative of the maximum separation distance, therefore insensitive to lateral ribbon thicknesses at local positions, and (2) Any possible relaxation of the ribbon may be unequal either laterally or longitudinally post-ejection.

In order to address these 2 issues increased localised scanning is proposed (*see Figure 95*), whereby in-line 50 *ms* probe-beam scans could be used with correct probe alignment to monitor lateral and longitudinal differences (e.g. multiple implementation of additional augers, depositing at the slip zone by smart design[25] , or incorporate a mechanism of run-off to waste inadequate ribbons.

---

[25] Smart design in this instance is suggested by the author to counteract sinusoidal conveyance of powder to the nip region (as seen in the work of Simon and Guigon) and design to counteract adhesion to the side cheeks (creating greater flow of powder to the central region of the ribbon).

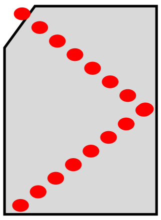

***Figure 81*: Schematic diagram of an ejected ribbon and a potential THz sampling pattern (red dots) envisaged for real-time THz monitoring.Method/materials and ribbon/wafer preparation regime**

7.2.1 Production/formulation and material properties: A DoE summary

Of 49 samples of ribbons and wafers:

1) Three analytes of are regular-shaped wafers (with a SF ratio between 63 – 90 %), where the SF's of 2 of these 3 sets of wafers (courtesy of Stuart Charlton of Bristol Meyers-Squibb, BMS) correspond to the irregular shaped knurled RC ribbons.
2) Produced on a Gerteis PolyGran at the University of Bonn, two formulations were prepared. Eight ribbons were made of Vivapur® (following Avicel® produced tablets investigated in the previous chapters), with PP's focusing on roll-force and roll-gap at a roll-speed of 3 RPM and 16 smooth faced ribbons attempted at 1, 5 10 and 15 *kN/cm* at 4 (*1-4 mm*) thickness again at a roll-speed of 3 *RPM*. A summary is given in *Table 33*.

Table 33: **Summary of the substrate ribbon and wafers analysed**

Produced	RC's	Composition (w/w %)	Wafers	Character	Immediate Problems/Issues
BMS	15 samples -1 CPP changed (Roll-force)	• Avicel® PH-102 (*78.6 %*) • Anhydrous lactose (*19.4 %*) • Croscarmellose sodium (*1.5%*) • Magnesium stearate (*0.25%*)	10 samples -1 CPP changed (Compaction-force) - Compressed at 4.79 – 6.79 *kN/cm.* -Roll-gap of 2.2 *mm* during production	Ribbon SF's / Mean thickness: • 63 *%* / 2.78 *mm* • 76 *%* / 2.68 *mm* • 83 *%* / 2.82 *mm* Wafer SF's / Thickness • 63 *%* / 2.32 *mm* • 83 *%* / 2.27 *mm* • 90 *%* / 2.28 *mm*	• Diffuse light scattering: • Knurled face prevents specular reflection from lattice face, or • Posterior time-delay is imprecise
University of Bonn	16 samples • Roller-force • Roller-gap •	• Vivapur 102 (*78.0 %*) • Anhydrous lactose (*18.25 %*) • Croscarmellose sodium (3.0 *%*) • SiO$_2$: Supernat 160 (*½ %*) • Magnesium stearate (*¼ %*)		Roller-force: • 1/5/10/15 kN/cm Roller-gap: • 1/2/3/4 mm **Roller-speed: 3 *mm***	
	8 samples • Formulation	• Vivapur 102		Roller-force: • 1/5/10/15 *kN/cm* Roller-gap: • 2/4 *mm* **Roller-speed: 3 *mm***	

The BMS wafers are investigated first for the objective to tie the measured density, apparent gas pycnometry and THz FDT (+FFT). Expectedly, the diffuse knurled compacts presented problems with RI estimation or thickness approximation, because of the topology raising potential issues of incomplete reflection and thus the lessening of the probes beams intensity. However, the knurled features were removed with abrasion to allow the three parameters to be correlated. Notably this is the first time in this study (or in the known literature) that apparent gas pycnometry and geometric density have been coupled. Beyond regular shaped wafers, the true geometric density and apparent gas pycnometry with ribbons cannot be matched empirically with ribbons.

7.2.1.1 Material true densities

Table 34**: The true densities of the materials used within this section. Note: The true density of specific brands of MCC are inconsistently reported between sources, and thus listed are the approximate ranges researched.**

BMS wafers and ribbons		
Excipient	*g/cm^3*	Source(s)
(MCC*) Avicel® PH-102	~1.51–1.71 g/cm^3	Handbook of Pharmaceutical Excipients, Ed. 6, 2009 (1 of 4)
Anhydrous lactose	1.589 *g/cm^3*	Handbook of Pharmaceutical Excipients, Ed. 6, 2009
Croscarmellose sodium (Ac-Di-Sol)	1.543 *g/cm^3*	Handbook of Pharmaceutical Excipients, Ed. 6, 2009

Magnesium Stearate	1.092 g/cm^3	Handbook of Pharmaceutical Excipients, Ed. 6, 2009
Gerteis Ribbons/Tablets		
Excipient	g/cm^3	Source(s)
(MCC*) Avicel® PH-101	1.51-1.67 g/cm^3	Handbook of Pharmaceutical Excipients, Ed. 6, 2009 (1 of 4)
(MCC*) Vivapur 102	1.42-1.46 g/cm^3	[140, 149]
Anhydrous lactose	1.589 g/cm^3	Handbook of Pharmaceutical Excipients, Ed. 6, 2009
Croscarmellose sodium (Ac-Di-Sol)	1.543 g/cm^3	Handbook of Pharmaceutical Excipients, Ed. 6, 2009
Silica Dioxide: 160 Sipernat	2.0-2.1 g/cm^3	Functional Fillers for plastics, edited by Marino Xanthos
Magnesium stearate	1.092 g/cm^3	Handbook of Pharmaceutical Excipients, Ed. 6, 2009

**The various types of producers and grades offer have varying/sometimes contradicting values over many literature sources*

7.2.2 BMS wafer lattice nature, production and mounting for FDT analysis

The ribbons and wafers supplied by BMS feature approximately 12 indentations (lattice squares) per cm^2 and pressed with a uni-axial punch imparting a lattice-geometry matching the lattice roll-wheel of the RC roll-wheel to the composition and character given in *Table 33*. The first FDT test of a lattice wafer was immediately apparent when mounted horizontally in the sealed sample holder (e.g. diffuse light interception; highlighted previously in the problems/issues, *see Table 33*) when mounted in the TPS-3000 using clips for static positioning (*see Figure 82*).

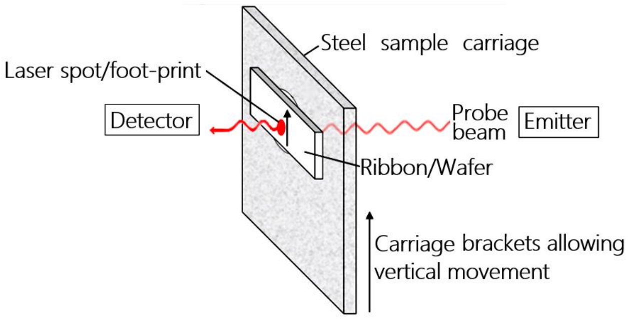

***Figure 82*: Illustration of ribbon/wafer configuration for transmission analysis[26].**

---

[26] The laser spot size or *foot-print* cannot be readily quantified because of the broad frequency-ranges produced by the TPS-3000 (0.1 THz-300 GHz). However, the converging beam has an approximate diameter of 1 *mm* at ~ 1 THz (TeraView).

7.2.3 BMS wafer mounting for TPI analysis

The wafers were next analysed with TPI on the Imaga1000™ stage to acquire multiple **spot images** (i.e. an array of *E-Fields*) in the lateral and longitudinal dimensions at increments of 0.2 *mm* between scan acquisitions. This creates 40 waveforms of the mean of 25 *E-Field* (*t*) waveforms, necessary to reduce background radiation/abnormal responses.

7.2.4 Gerteis ribbon production

The powder-blend (*Detailed in Table 35*) was mixed for 2 minutes with a Turbula blender to follow a more extensive CPP than the BMS ribbons and wafers and using a Gerteis system with a DoE in accordance to the CPP's listed in *Table 38* at thicknesses of 1, 2, 3 and 4 *mm* for the multi-component blend (mimicking the BMS formulation), and also to 2 and 4 *mm* ribbons for comparison to previous experimental factors used in tablet production.

***Table 35*: Composition of the multi-component Gerteis ribbons.**

Composition of Blend	
MCC (Vivapur 102)	*78.00 %*
Anhydrous lactose	*18.25 %*
Croscarmellose sodium	*3.0 %*
Silica Dioxide: 160 Supernat	*0.5 %*
Magnesium stearate	*0.25 %*

7.3 Product specifications

7.3.1 BMS wafer specifications

In order to achieve (near) specular light reflection necessary for both uncomprised RI's and thickness results, a low grit sand-paper (2400 grade) was used to remove the visible lattice protrusions whilst additionally allowing a consistent lateral and longitudinal thickness across the chosen wafers from each SF supplied as samples from the many BMS wafers. Post sanding the new dimensions of the wafers are reported in *Table 38* and visual shown below:

Table 36: **Dimensional and helium pycnometry derived values of the sanded wafers. The displayed dimensions were measured ~14 days after manufacture.**

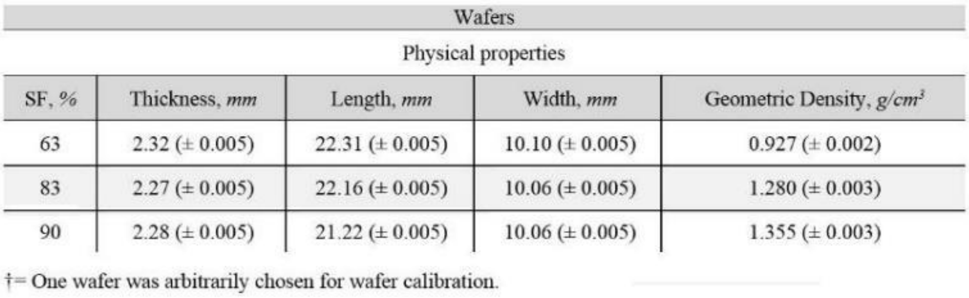

Wafers				
Physical properties				
SF, %	Thickness, *mm*	Length, *mm*	Width, *mm*	Geometric Density, *g/cm³*
63	2.32 (± 0.005)	22.31 (± 0.005)	10.10 (± 0.005)	0.927 (± 0.002)
83	2.27 (± 0.005)	22.16 (± 0.005)	10.06 (± 0.005)	1.280 (± 0.003)
90	2.28 (± 0.005)	21.22 (± 0.005)	10.06 (± 0.005)	1.355 (± 0.003)

†= One wafer was arbitrarily chosen for wafer calibration.

Photographs of the supplied wafers after removal of the visible lattice knurls.

7.3.2 BMS ribbon specifications

Alteration of the PP (#1) of roll-force (between 4.79 – 6.79 *kN/cm*) gives one three ribbons with density variance; yet, comparable thicknesses and composition identical to the wafers, (*see Table 33*). Produced at a PP of 3*RPM* (analogous to dwell-time) provides lattice compacts SF with parameters of 63, 83 and 90 %. The ribbons were produced at a roll-gap of 2.2 *mm* and evidently (*see Table 37*) have elastically recovered with inclusion, still featuring knurls, produced on 10 *cm* diameter rolls (one being knurled) with a width of 4 *cm*.

***Table 37*: Physical character of the BMS AW ribbons.**

Physical properties: Knurls retained		
Solid Fraction, *%*	Thickness during processing (roll-gap), *mm*	Mean Thickness after processing (~ 14 days), *mm*
63	2.20	2.78
76	2.20	2.68
83	2.20	2.82

7.3.3 Gerteis ribbon specifications

The ribbons were analysed with TPI on the Imaga1000™ stage to acquire multiple **spot images** (i.e. an array of *E-Fields*) in the lateral and longitudinal dimensions at increments of 0.2 *mm* between scan acquisitions. This creates 40 waveforms of the mean of 25 *E-Field* (*t*) waveforms, necessary to reduce background radiation/abnormal responses. The wafers were secured on the gantry by use of several fastening clips.

***Table 38*: CPP's used during production with the Gerteis PolyGran.**

Roller-gap, *mm*:		**1**	**2**	**3**	**4**
Roller-speed: 3 *mm*					
Press Force, *kN/cm*	1	†	†	†	†
	5	✓	✓	✓	✓
	10	✓	✓	✓	✓
	15	✓	✓	✓	✓
MCC (Vivapur 102)					
Roller-gap, *mm*:		**2**		**4**	
Press Force, *kN/cm*	1	†		†	
	5	✓		✓	
	10	✓		✓	
	15	✓		✓	

† Production at 1mm resulted in unviable and fragile ribbons.

7.4 RC equipment used

Three DG/RC instruments are utilised or referred to in this chapter. Depicted in *Figure 83* are AW WP-120 '*A*', Gerteis's PolyGran *'B'* and the Macro-Pactor '*C*'. The AW press was operated by BMS for producing ribbons and wafers investigated in *Section 7.6.1.2,* and the Gerteis PolyGran were used for producing the ribbons (*Section* ***Error! Reference source not found.***). The Macro-Pactor is used primarily used during pilot/clinical/full scale production so while it was not used in this study, it is included because its intended use in large scale production and dimensionally capable of housing the current THz probes.

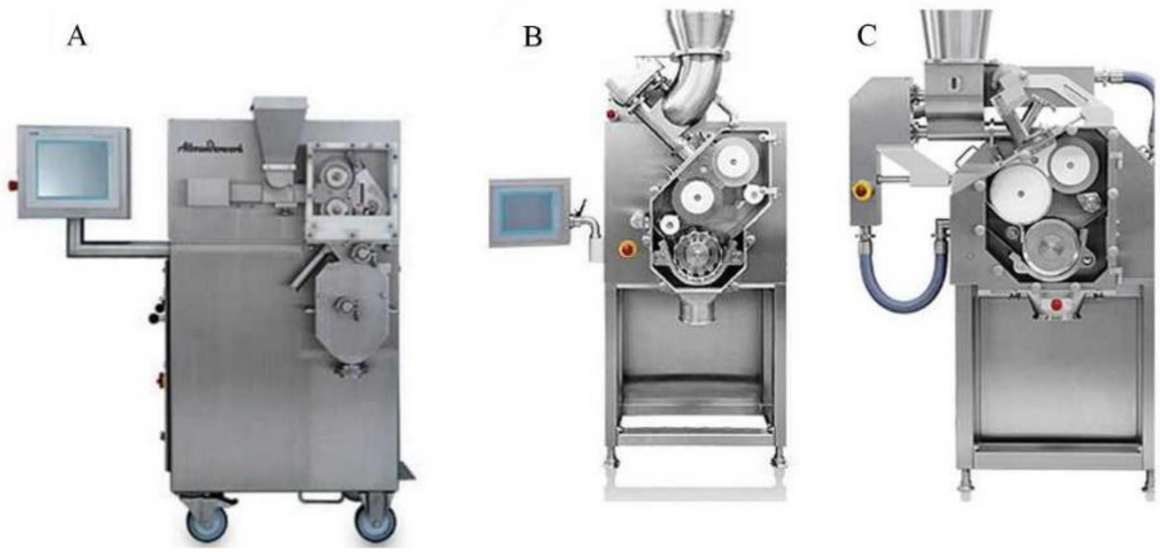

***Figure 83*: Photographs of the automated roller-compactors used or proposed for use in this study. : The AW WP-120® (‘*A*’), The PolyGran® (‘*B’*) and the Macro-Pactor® (‘*C’*).**

The WP-120 is generally used during R&D and small-scale production, and provide a throughput of 8-40 *kg* of powder/hour; further specifications of the equipment are given in *Appendix Section 10.4.1* (*Table 56*). Additionally, the WP-120 features a horizontally mounted single auger from the hopper to the slip, nip and release regions in contrast to the schematic of the Gerteis machines featured in *Figure 85*.

7.4.1 General relationship of roller-compaction parameters

The frequently observed consequences of altering CPP’s in RC’s is illustrated briefly in *Table 39*. Consistent variables (denoted ‘=’) can be maintained with adjustment of alternate parameters (↑↓). For instance to achieve a steady roll-gap and roll-force (regarded as the two chief CPP’s [1, 3, 4]), the feed-rate must be increased to convey greater blend to, 1) Force the rolls apart to the defined gap and, 2) The extent to allow the target roll-force to be met. Such logic can be seen in *Table 39*, for instance, reduction of the feed-rate effectively ‘bottle-necks’ the cycle in reducing the roller-rate whilst maintaining a constant force, gap.

***Table 39*: General relationship of roller-compaction parameters.**

FEED-RATE	ROLL-FORCE	ROLL-RATE	ROLLER-GAP
=	=	↑	↓
=	↑	=	↓
↑	=	=	↑
↓	=	↓	=

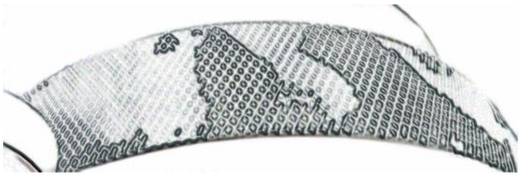

***Figure 84:* Enhanced photograph of a knurled roll-wheel following ~20 minutes of operation of a Gerteis PolyGran with a multi-component placebo ‘typical blend’[27].**

7.4.2 The Gerteis PolyGran™

The PolyGran™ is a smaller unit than the Macro-Pactor and is generally used in R&D and small scale environments with a throughput of ½ - 200 *kg* of powder/hour; further specifications are given in *Appendix Section 10.4.1* (*Table 57*). In addition to the schematic of the instrument, the possible process and control parameters in automated RC’s is inset in *Figure 85* with the indicative consequences, particularly in regard to producing uniform ribbons. The PolyGran™ also contains a paddle in the hopper (*See Figure 86*) for improved agitation of the blend prior to auger-led conveyance.

---

[27] Anhydrous lactose, MCC, a glidant and a small level of lubricant.

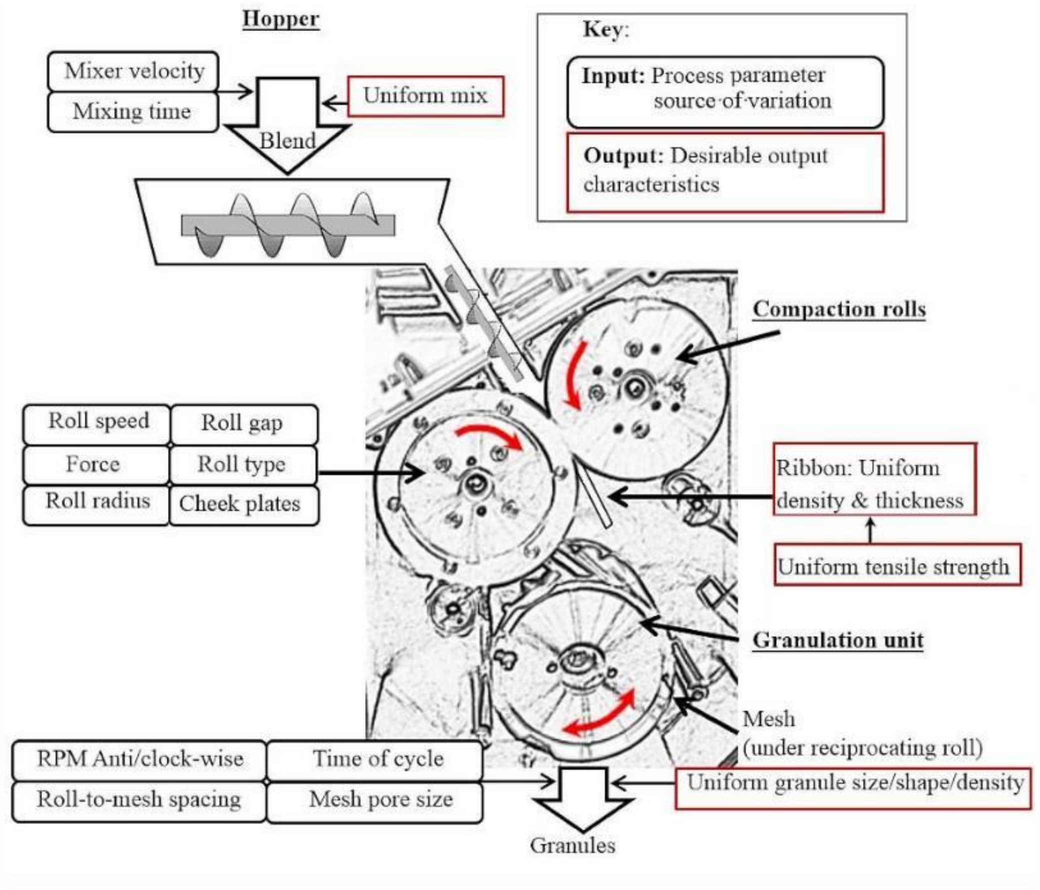

***Figure 85*: Scaled representation of a Gerteis UltraGran (roll-wheels with Ø 10 *cm*), superimposed with annotations of input and output factors and feed-augers and an ejected ribbon. Notably the proximity of the granulating-wheel and the real size of the sealable *DG/RC* would not accommodate current TeraView fibre-optic probes for TPI of transmission analysis (technology current to TeraView and Gerteis in 2014).**

7.4.3 Equipment conceived for use: The Gerteis Macro-Pactor™

In full-scale production, it is common to see a Macro-Pactor™ in DG/RC operation, capable of operating at *0.1 - 400 kg* of powder-stock/hour. Additional specifications of the Macro-Pactor™ can be found in *Appendix Section 10.4.1* (*Table 58*).

Figure 86: **Aerial photograph of the agitation paddle in the PolyGrans' hopper.**

7.5 Analytical equipment and methodologies

Detailed in *Section 3.5.2* is the configuration of the spectrometer, and the method of operation for FDT in *Section 3.6.* While descriptions of the configurations and the method of operation for TDT, TPI are described in *Section 3.5.2* and *Section 3.5.3,* respectively.

7.5.1 FDT for comparative measurement of material RI's

The *TD* waveforms were transformed with a standard FFT frequency-domain transformation to establish the accuracy of TPI methods. The system configuration and method principles used are described in *Section 3.6.*

7.5.2 TPI for prediction of material RI and then thickness

The method for predicting compacts RI's can be found in *Section 3.5.5*, and subsequent thickness prediction information is found in *See Section 3.5.5.*

7.5.3 TDT to predict material thickness/RI

See Section 3.5.4.

7.5.4 Interpretation of A, B, C-Scan images

In a full TPI image of thousands of compiled *E-Field* (*t*) waveforms used in TPS TPI, '*B*- scans' and '*C*-scans' (with use of TeraView software) are compiled to give *z-axis* time-scale of a substrate. Illustrated in *Figure 87*, the familiar *E-Field* (*t*) is shown '*B*' for a *xy* position on the material. The substrate here is a 28 sheet pad of paper. *The B-Scan* (*see Figure 87;* '*a*' and '*e*') is a cross-sectional image corresponding to the green planes within illustration '*f*' and the horizontal lines seen in ‘*c*’ and ‘*d*’. Inset as a blue vertical-line at ~ 17 *ps* to time-delay depth slices of the planar *xy* images, ‘*d*’ and, ‘*e*’, as a function of time is shown. The E^{MAX}-*Field* peaks (of ‘*b*’) thus translate into the striations of the sheets within the pad separated by air. In summary, B and C-scans are the product of assigning colour variants dependent on the *E-Field* magnitudes (of the *A-Scan*) following compilation of all the waveforms acquired by raster scanning on a small gantry. The recorded optical time-delay can later be approximated as a physical thickness once the RI of the sample is known.

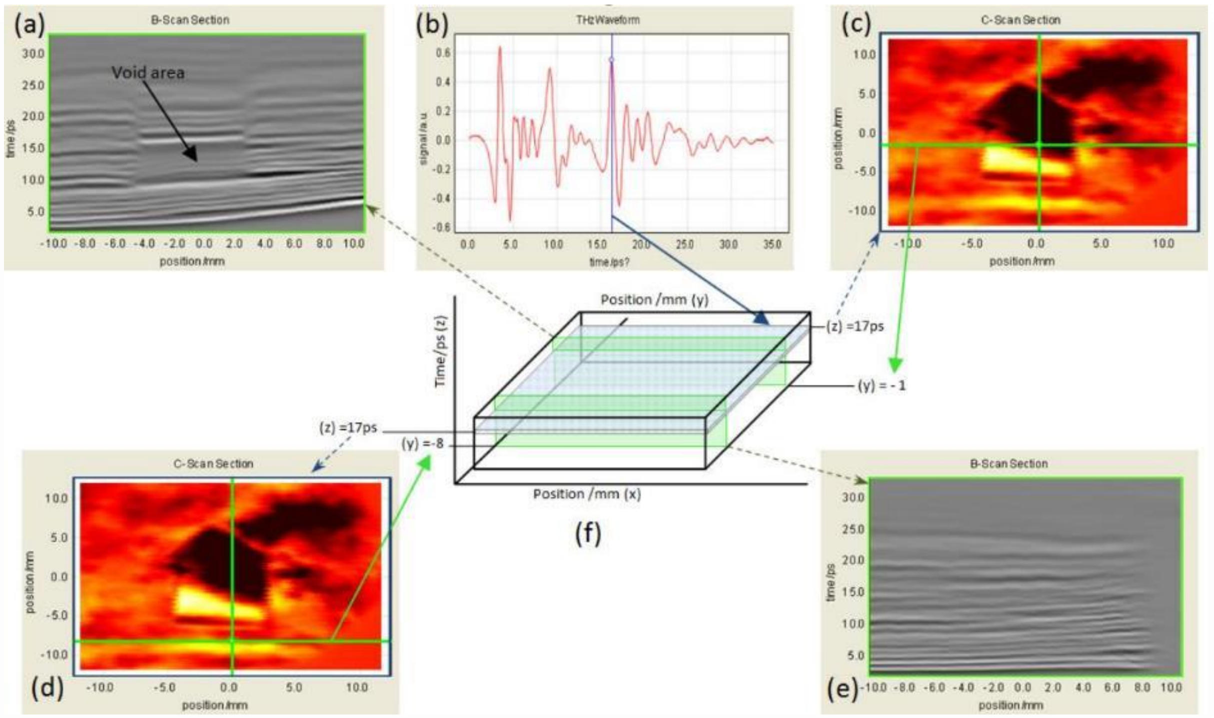

Figure 87**: Views of various A, B and C-scans used in full TPI of a pad of paper featuring a hollow internal region (‘*f*’).**

7.6 Results and discussion

7.6.1 Objective 1: Establish a guideline to elucidate method issues which could be detrimental to TPI analysis and access resolutions

7.6.1.1 The effect of knurling

Knurled rolls are frequently used in the industry as a requirement helping drawing-in raw powders into the nip region. Although knurled (or briquetted) rolls are not absolutely essential, there use often either improves conveyance and also, can reduce R&D resources for compensating against poor flowing materials (e.g. a stage to balance the maximum use of glidants and lubricant excipients.) The use of a singular knurled punch/roll was used in the production of the BMS's wafer/ribbon samples (*see Figure 88*)

Figure 88: **Photographs of an 85% *SF* Ribbon composed of 78.6 % MCC, 19.4 % Lactose anhydrate, 1½ croscarmellose and ¼ % Mg St.**

Knurling is first feasibility tested in because of a high potential risk of failure for spectral/THz characterisation tools. This is apparent when studied usage of Snell's law of reflection.

To simplify proceeding TDT analysis is first used on account of orthogonal light incidence and a rough knowledge of the wafers and ribbons thickness. Having recorded the geometric density of a regular shaped wafer, indicated to be of an 83% solid-to-air ration of a multi-composite formulation. 3 scans were made (n=10) while in three distinct spatial positions to the laser-footprint. With observation of *Figure 89*, plot a shows an apparent single-passage waveform whereby the maxima *E-Field* beam was emitting and focused onto the rear/flat surface, whilst the contrasting profile is a profile taken from the reverse side. Plot B was constructed to see the effect of the signal if the wafer was moved by approximately 2 mm in a random direction.

The effect of knurling (*Figure 89a*) is dramatic. Plot 'A' reports a typical phase change on entry with a respectable degree of material passage with little attenuation. Issues arise when OD (*t*) readings are needed of signal-delay times via either FP resonations or positional anterior time information if analysing the front. The attenuations observed for the lattice intercepted profiles signify that in comparison to the first 'specular' transmission, that a large proportion of the orthogonal pulse-probe is unable to penetrate the wafer; a consequence of reflected EMR is scattered in an unknown direction due to diffusion. Focusing on plot 'A' it also apparent that the red peak is elongated upon entry, while the black pulse returns an impracticable echoed value for thickness determination. Elongation here indicates that the surface is either highly textured and thus polarises the EMR to planes inaccessible with TD analysis, highly absorptive or most likely, scattering reflected light in a 'frustrated' manner (*See Figure 90b*) .Not Shown here, material thickness could be possibly to predict from the black pulse in 'A', yet thickness is required (thing is an awkward method even with callipers). It in-turn follows that a more diffuse surface is likely to diminish the propagation/transmission of any probe-beam in this configuration.

For information to be harnessed from a one sided knurled ribbon, requires the reflectance TPI technique. This method will atleast provide an RI value of established accuracy for relative spot measurements if SF uniformity is of prime interest. The wafer was again analysed by THz spec from the latticed side and the planar side (*See Figure 90*). Viewing the cross-sectional scans (where the y axis is depth in time) the possibility of extracting a reflection coefficient is probable in A. Contrasted against B, this is not the case and provides no further means to judge the distance (time) of the posterior surface.

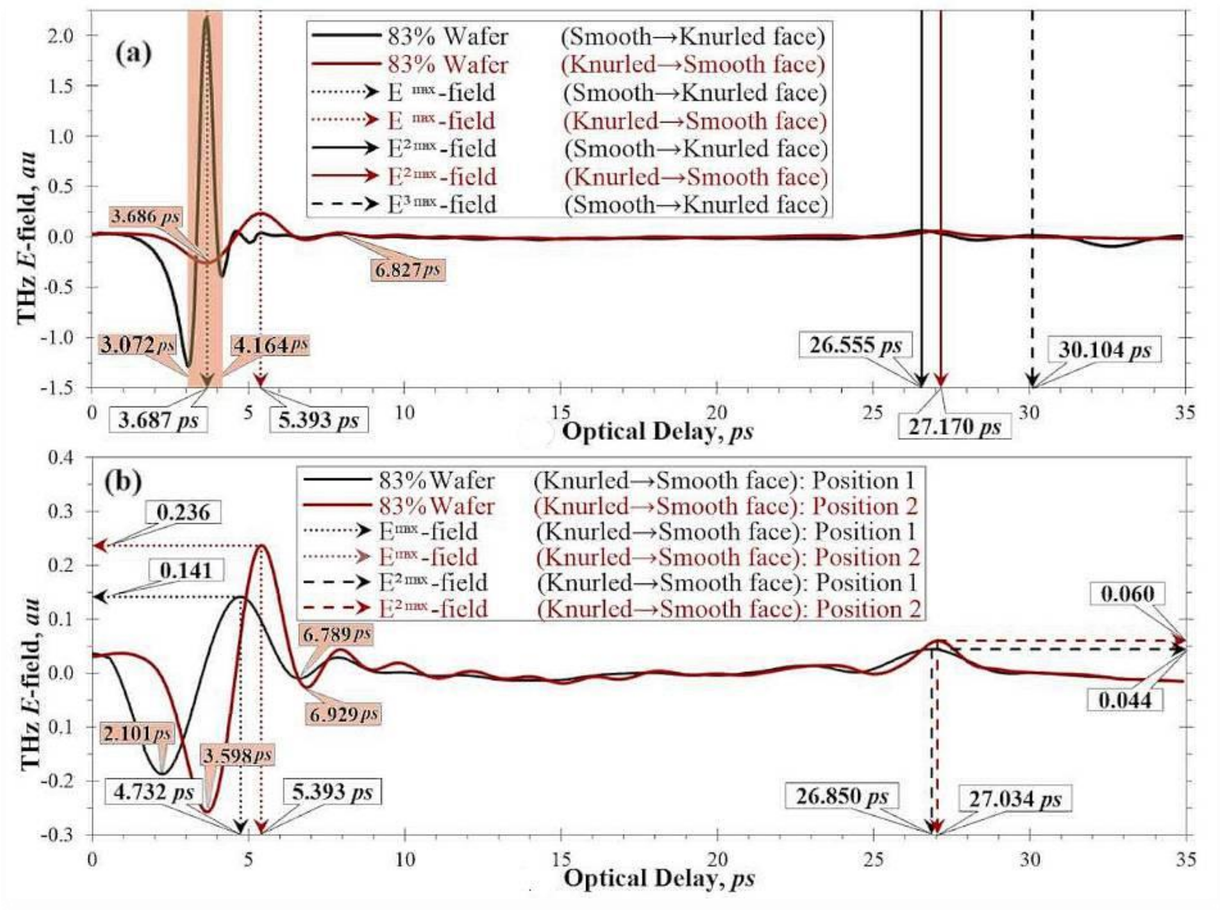

***Figure 89*: Transmission waveforms displayed over two time-resolved *E-Field* plots: Pictured top *(a)* the wafer of *83%* SF is scanned through both smooth/knurled orientations in regard to the propagating pulse source and, bottom *(b)* the same waveform of the knurled facing ribbon (coloured red in *'a'*) is scanned from a second position following vertical movement by 2 *mm* vertically. The wafer is composed of 78.6 % Avicel® PH-102, 19.4 % Lactose anhydrate, 1½ croscarmellose and ¼ % Mg St.**

In constrast, figure (*Figure 90b*) represents TPI reflections at $E^{MAX}1$ that are unlikely to reflect at an angle to the incidence of *30°*, and thus are unregistered, whilst scattering of the probe-beam may account for the internal ripples witnessed between 5 and 15 *ps* with reduced magnitudes and optically delayed-times from the diffuse surface as seen.

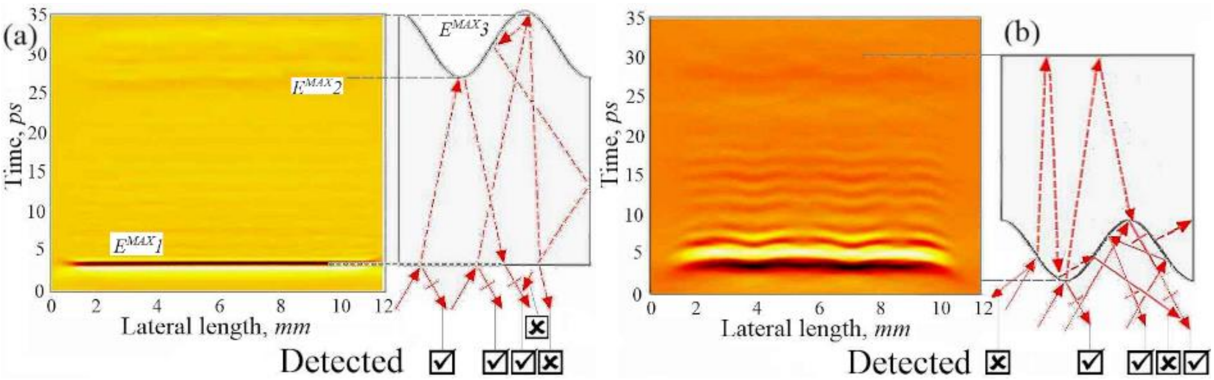

***Figure 90*: A cross sectional image (*a*) taken from the smooth face of the wafer and schematic representations *(b)* of the studied 83 % SF wafer taken with the TPS-3000 + Imaga1000™ from either side. Image '*a'* is the product of scanning through the smooth face and '*b'* from the knurled face. Inset on the schematics are possible passages of THz pulses and indicate why the signals reflection reduces in diffuse circumstances.**

In developing ideas of surface to probe-beam interaction in regard to the E^{Max}-*Field* magnitudes observed in *Figure 89a*, the E^{max}-*Fields* of smooth surface interception vs. the knurled differ by 1.92: 3.687 *ps* (smooth), and 5.393 *ps* (knurled). The apparent depth of a lattice intrusion (the exact spot size of the probe-beam is estimated as 1 *mm*; yet, is still a broadband signal with a range of crest heights) which cannot be easily aligned to a specific point on the substrate. The 1.7 *ps* difference indicates a 'depth' of ~0.25 *mm* with moderate movement of the wafer in-order to pit the footprint within the lattice feature. Furthermore, plot *Figure 89* include an inset of optical time-delays at $E^{Max/Min}$ –*Fields*, indicating pulse breadths. These are readily found by finding the *E-Field* inflexions at ± values (i.e. $\frac{dy}{dx}$). The shaded region in plot '*a*' contrasting the smooth and knurled surfaces provide a relative difference of 288%, (equivalent to 3.141 *ps*), and from the two separate regions of the knurled interaction (see *Figure 89b*), a relative difference of 192% and a depth difference of 0.19 *mm* is observed.

➢ Summary

In summary of lattice wafers disparity between the optical delay-times of E^{max}-*Field* events imply that lattice /knurled/grooved substrates cannot be exposed to THz analysis for reliable material RI prediction. Although RI's are unlikely to be detrimentally impaired if analysed from smooth/planar surfaces. Prediction of thickness from TDT/FDT/TPI delay-times however, become unreliable without viewing precise and distinctive posterior reflections (seen also in *Figure 114a* between *25-35 ps*).

- **Summary**

The confidence implied by the correlation characteristics between RI, SF and density over the tested SF range (of smooth de-knurled wafers) leads next to the re-evaluation of the wafers with the TPI method and consequently prediction of wafer thickness also.

7.6.1.2 Alteration of roller-gap and force with the use of smooth rolls on a Gerteis PolyGran for uniformity assessment

To establish initially whether the Gerteis ribbons had a planar or bowed nature to enable reliable prediction and determination of RI uniformity from reflection measurements was to carry out lateral and longitudinal scans of their dimensions. Cross-sectional B-scan images were acquired of the Vivapr-102 ribbons and 3 of the blended ribbons (*see Figure 92*) to conclude that the smooth rolls or the equipment importantly produced ribbons indicative of that have substantially less or no bowing. Both the images (*Figure 104* and *Figure 105*) are representative of all the five scans acquired in regard to a planar or near planar nature. Additionally, this enhances the secondary objective to predict and monitor the ribbons thickness with greater certainty from reflectance RI/density derivation.

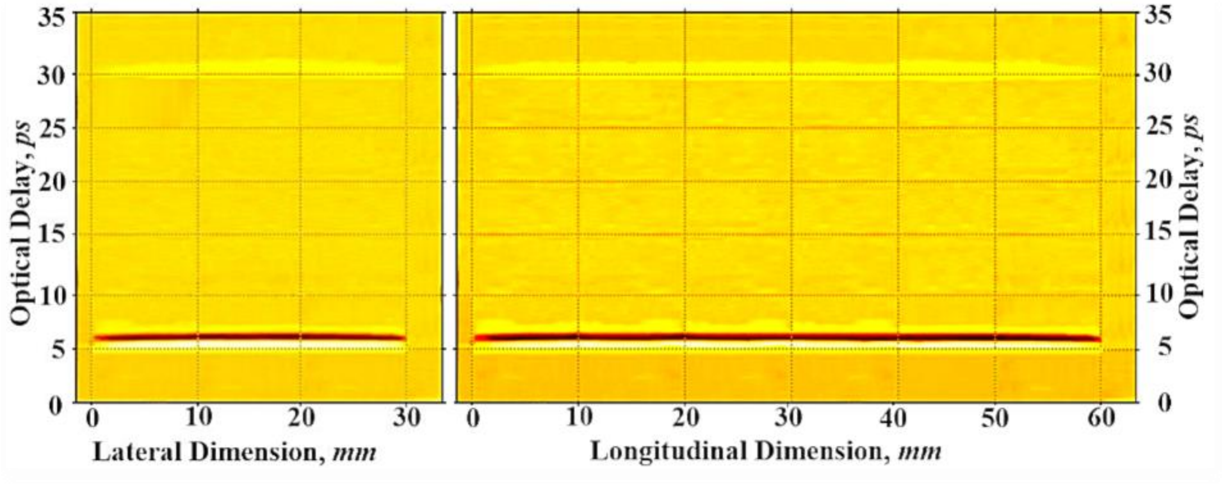

***Figure 91*: *15 kN/cm, 2 mm* MCC cross-sectional lateral scan from a Gerteis PolyGran (feat. Smooth rolls).**

Reflectance spot imaging was used to gather 40 data points for the 18 sets of smooth ribbons in order to; 1), chiefly quantify the uniformity of surface derived RI/density and, 2) assess thickness uniformity. The ribbons are 3 *cm* in width and at least 6 *cm* in length and allowed waveforms to be acquired in a matrix configuration where lateral scans were made systematically, forming 8 data sets points and longitudinally, 5 points (every 1 *cm* in length) were acquired. This is best illustrated with reference to *Figure 92*.

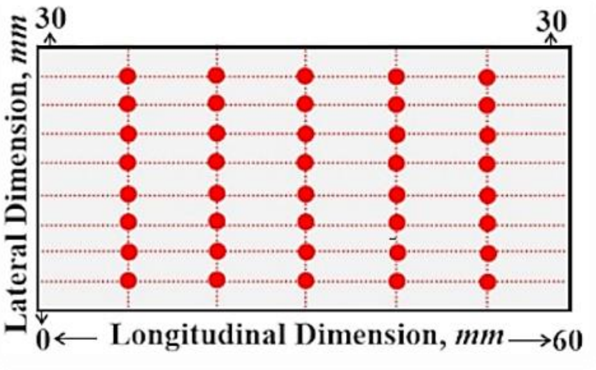

***Figure 92*: Schematic diagram illustrating the acquisition of up to 40 THz data points of the ribbons surface with reflectance imaging.**

7.6.1.2.1 Effect of Roll Force and thickness

The excipients present in used in the blended ribbon are listed in Table 40 , giving material true densities are the ratios present(Ref [140, 149]).

***Table 40*: Excipient specifications.**

Excipient	Density	Proportion (*w/w %)*
Vivapur-102	1.42-1.48 g/cm^2 (True)	78 %
Lactose-β anhydrate	1.589 g/cm^2 (True)	18.25 %
Croscarmellose Sodium	0.589 g/cm^2 (Bulk)	3.0 %
Silica Dioxide	1.234 g/cm^2 (True)	0.5 %
Magnesium Stearate	1.092 g/cm^2 (True)	0.25 %

With reference to *Figure 93* -

Figure 95, observation of the histograms of the ribbons principally shows an increase in RI's (and thus density/SF) with greater compaction force. Unsurprisingly, this corresponds with previous explanations that RI is a good indicator of density/SF because RI describes the ratio of an effective two phase medium of particles and air in bulk measurements and the effective surface hardness obtained under increased pressure as with reflection studies.

The Blend 1 ribbons were prepared with differing thicknesses and compactional forces for surface derived density/RI contour mapping for lateral and longitudinal uniformity (see *Figure 93* -

Figure 95).

The inclusion of crystalline components are well evidenced in solid-state THz literature to produce strong absorption bands in the frequency-domain, believed to result from vibrational motions of crystalline structures and possible movement within porous solid media [77, 100, 150]. The relation of strong spectral peaks in the frequency-domain were shown to have an apparent impact of the THz-TD profile by varying degrees. For instance, water absorption lines shown (in the water diagram someplace) do little to attenuate or broaden the THz-TD waveform profile, present little concern for the accuracy of registering the *E-Field* (*t*) magnitudes or OD's; yet, with a study made on various composites of MCC (only marginally crystalline) loaded with greater ratios of crystalline lactose monohydrate (LMH) for the purpose of an assay methodology, (see the poster presentation: *Appendix 10.5.6*). The principle observations are the increasing magnitude of spectral peaks corresponding to LMH loading and the intensity of ripples and the THz-TDS profile. The quantification of meaningful data (either temporal or spectral) of amorphous and crystalline blends may seem problematic yet using PCA transformation of the orthogonal of the input data found similarities in the dataset, eliminating regions in the spectra where equal values are found [100, 110, 150]. The differences however are amplified and regressed over the whole LMH range. The results of the study were statistically equivalent, although the PCA approach us restricted to identification and provide qualitative results.

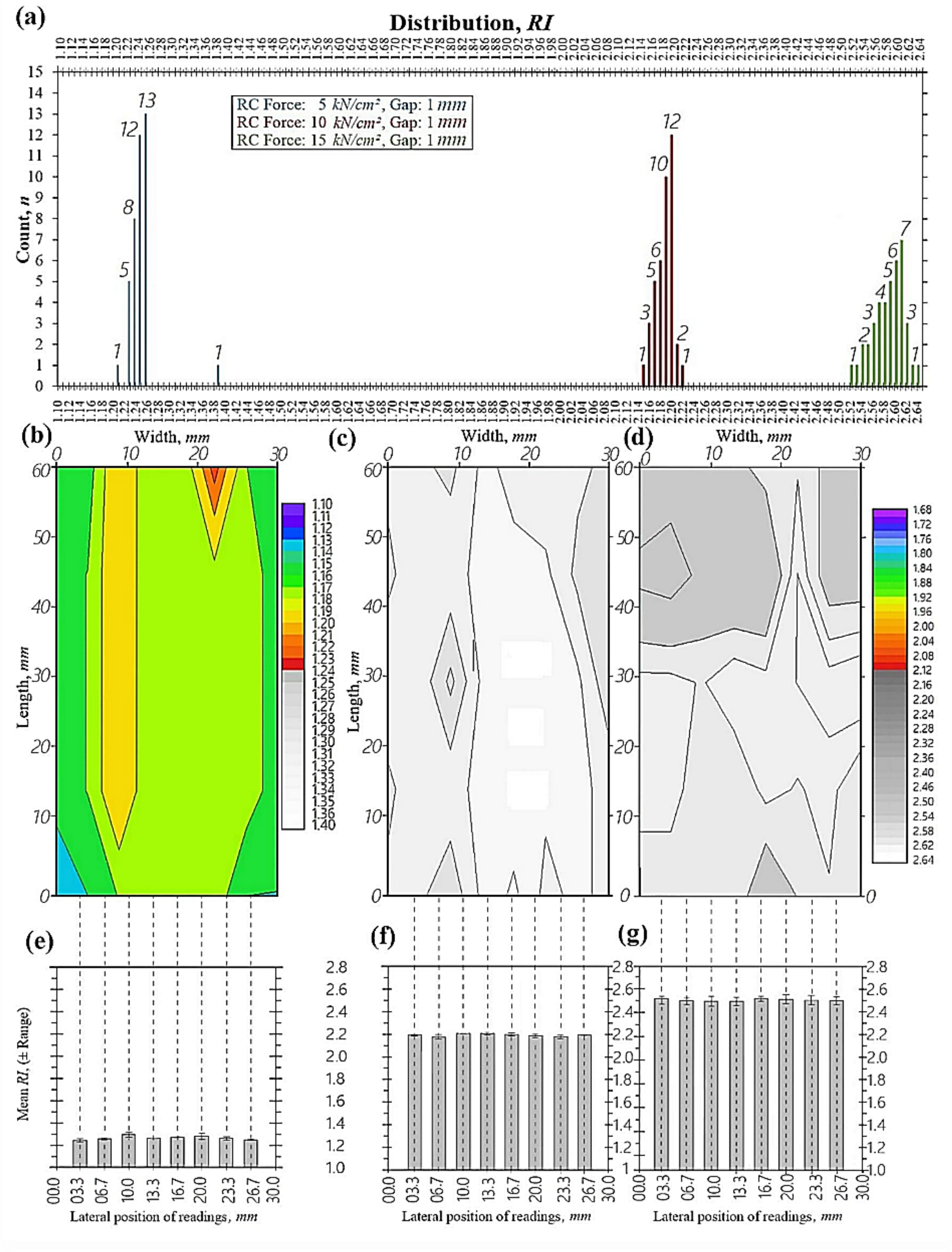

Figure 93: **Surface RI analysis. The histogram, (*a*) displays the distribution of the all the ribbons (points analysed/ribbon = 40), while individual contour images are shown (*5 kN/cm*: '*b'*, 10 *kN/cm*: '*c*', and 15 *5 kN/cm*: '*d*'). In '*e*', the mean lateral I distributions are plotted, with error bars for the minimum to maximum RI's along the ribbons' length.**

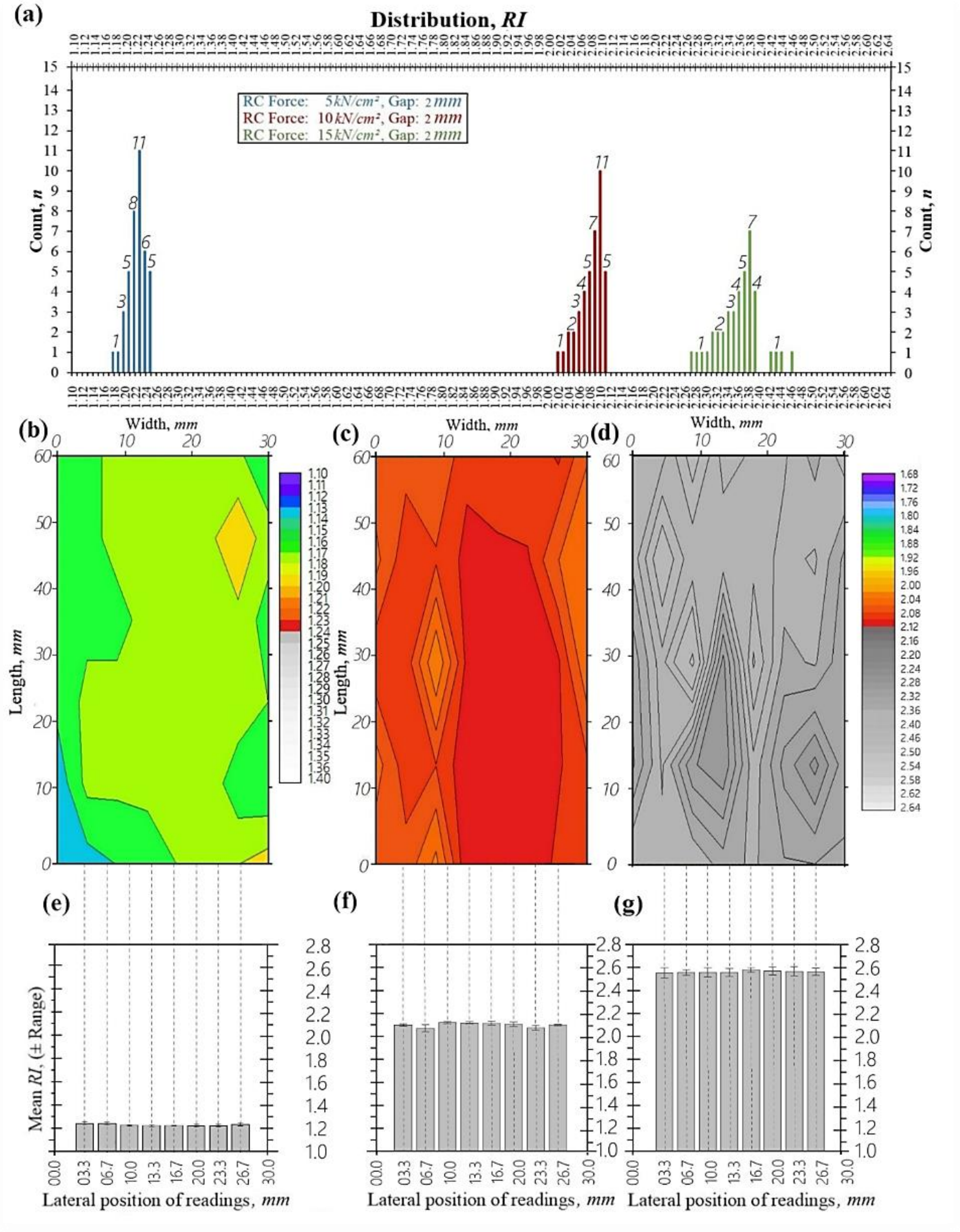

***Figure 94:* Surface RI analysis of the blended ribbons with a pre-defined roller-gap of 2 *mm*. The histogram, (*a*) displays the distribution of the all the ribbons (points analysed/ribbon = 40), while individual contour**

images are shown (5 *kN/cm*: ‘*b’*, 10 *kN/cm*: ‘*c*’, and 15 *kN/cm*: ‘*d*’). In ‘*e*’, the mean lateral I distributions are plotted, with error bars for the minimum to maximum RI’s along the ribbons’ length.

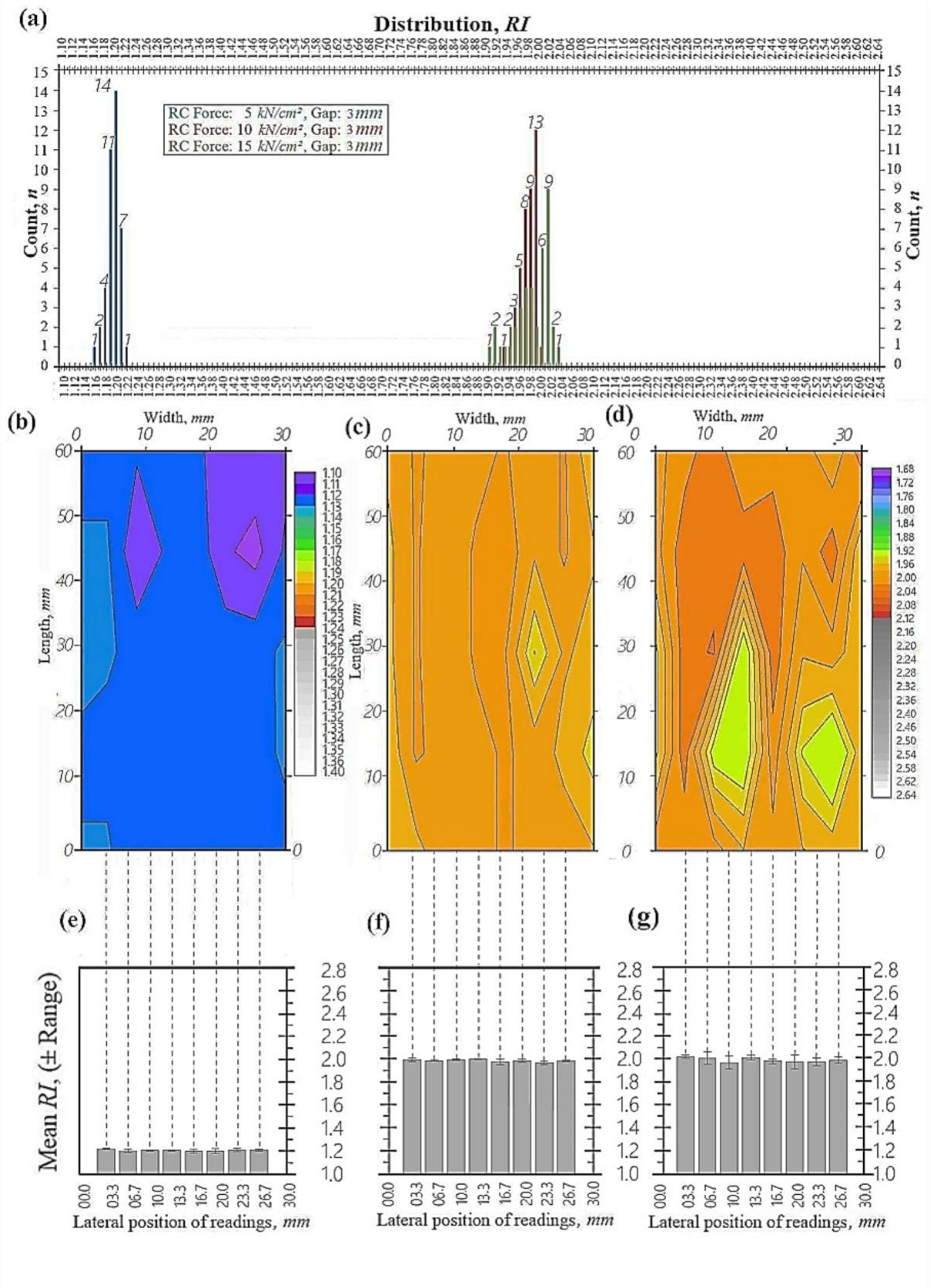

Figure 95: **Surface RI analysis of blended ribbons with a pre-defined roller-gap of 3 *mm*. The histogram, (*a*) displays the distribution of the all the ribbons (points analysed/ribbon = 40), while individual contour images are shown (*5 kN/cm*: '*b'*, 10 *kN/cm*: '*c*', and 15 *kN/cm*: '*d*'). In '*e*', the mean lateral distributions are plotted, with error bars for the minimum to maximum RI's along the ribbons' length.**

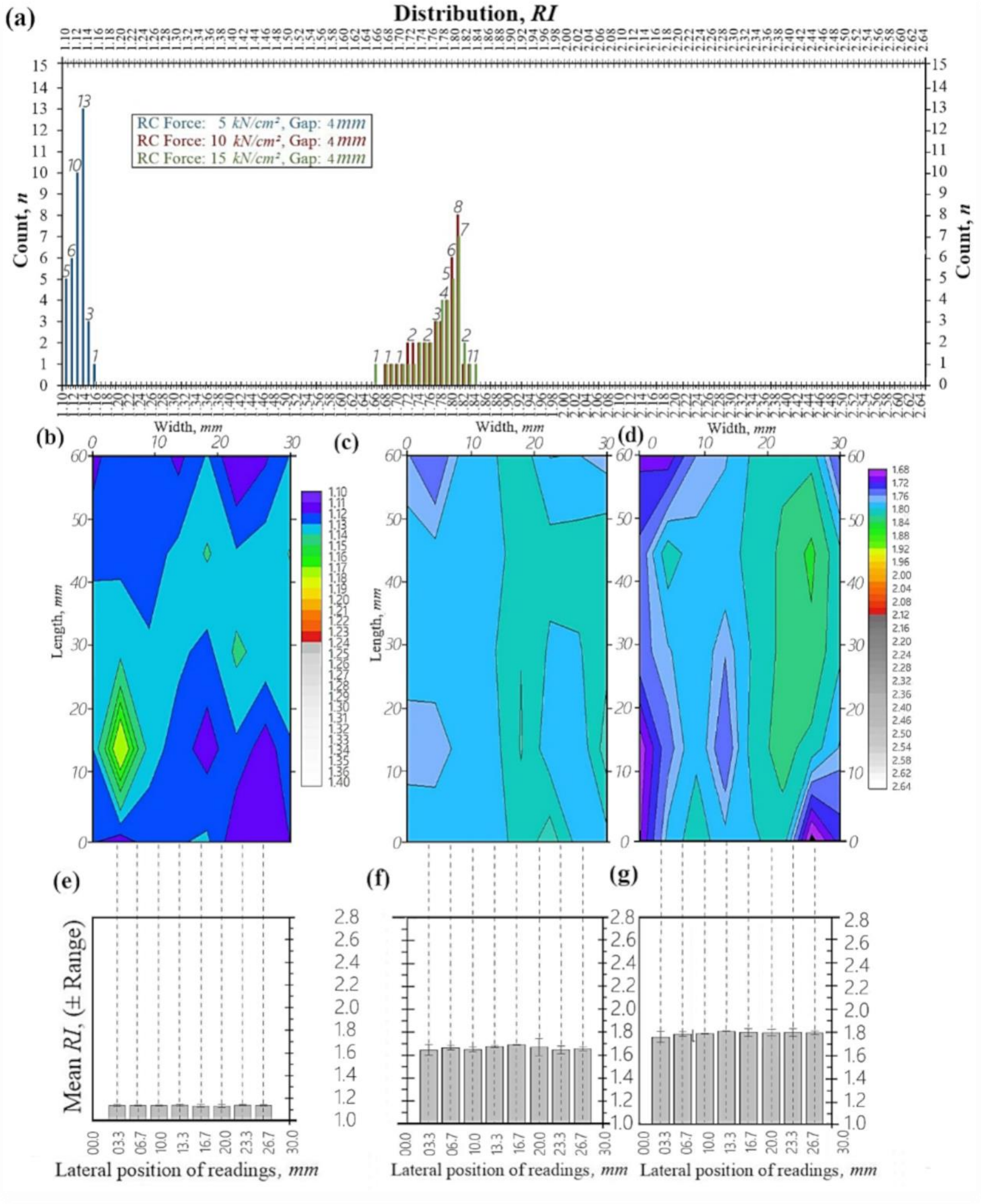

Figure 96: Surface RI analysis of the blended ribbons with a pre-defined roller-gap of 4 *mm*. The histogram, (*a*) displays the distribution of the all the ribbons (points analysed/ribbon = 40), while individual contour images are shown (*5 kN/cm*: '*b'*, 10 *kN/cm*: '*c*', and 15 *kN/cm*: '*d*'). In '*e*', the mean lateral distributions are plotted, with error bars for the minimum to maximum RI's along the ribbons' length.

The smooth rolls/Gerteis instrument has importantly shown that the detrimental effects of lateral and longitudinal bowing has been appreciably reduced in contrast to previously encountered bowing of ribbons. The effect is that the ribbons manufactured have a greater planar surface, beneficial to accurate reflectance RI/density approximation, additionally this aids the secondary objective to predict and monitor thickness with greater certainty.

The compaction to RI/density profile (*see Figure 97*) does show a general linear relation at lower forces (i.e. 5 to 🕓 8 *kN/cm*); yet, the degree of material consolidation lessens as the true densities of the materials are approached, resulting in a plateauing effect on compaction profiles (*see Figure 97*).

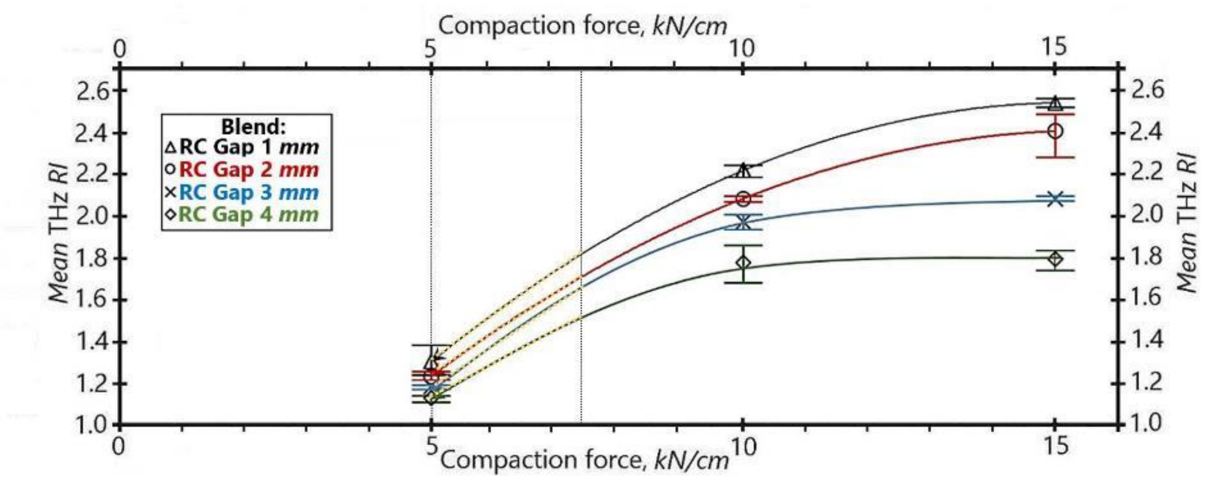

Figure 97: **The RI of Blend 1 ribbons against greater compaction forces. The inset error bars indicate the distribution of the surface RI's across 18 ribbons (points analysed/ribbon = 40).**

7.6.1.2.2 Density uniformity of the MCC ribbons

The brittle fracture and the ability of the particles to mechanically interlock in the current state or through creation of new clefts/bonding sites are the primary cause of consolidation during dry granulation. Permitted by the PCT in *Experimental chapter 1 and Experimental chapter 2* with the 13↓ *mm* single-punch press and compaction forces capped at 500 *kg* (equivalent to 🕓6.5 *kN/cm*), a linear trend of RI and density (as a function of void reduction) was apparent with the ability to add linear lines of best-fit. The compaction to RI/density profile (*see Figure 98*) does show a general linear relation at lower forces (i.e. 5 *kN/cm* to 🕔 8 *kN/cm*), however, consistent with literature studies [3, 67, 151, 152] the degree of material consolidation lessens as the true density of the material (Vivapur 102: 1.42-1.46 *g/cm*^{2} [140, 149] is met with a plateauing effect on compaction profiles (*see*: 🕔 8 *kN/cm* to 15 🕔 8 *kN/cm*).

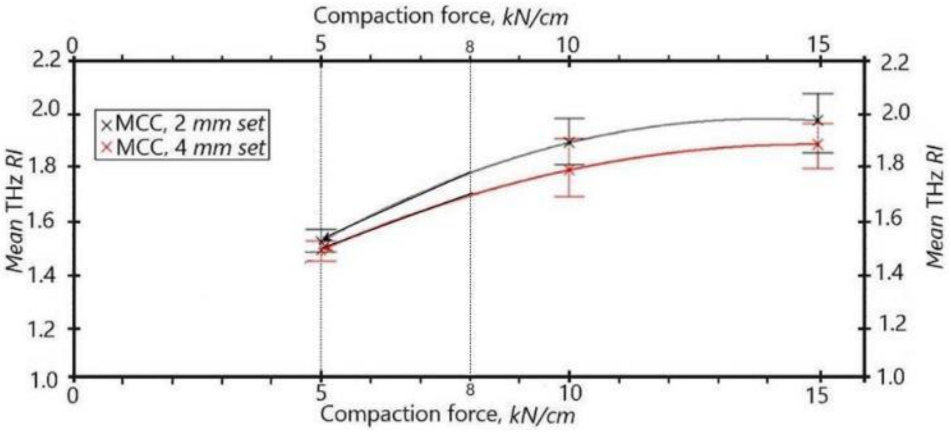

Figure 98: **The RI of MCC ribbons against greater compaction forces. The inset error bars indicate the distribution of the surface RI's across 6 ribbons (n = 40).**

The histograms (*See Figure 99 - Figure 100*) generally show a broader distribution of RI's across ribbons made at greater compactional forces. The distribution of RI's generally have a more symmetrical distribution than with the ribbons of Blend with the exception of the 2 *mm* ribbon produced at 15 *kN/cm*. The additional compaction forces exerted upon the powder blends is generally seen to be greater with more narrow ribbons with reference to the average RI's of the six MCC sets (*see Table 41*). Unlike compaction within a single-pinch press previously observed, is it presumed that the increased area existing within a roller-compactor, specifically with addition of a twisting paddle in the hopper and additional regions for powder consolidation to occur (e.g. the auger conveyance systems and the increased period of time prior to final consolidation at the nip region) permits enhanced powder re-orientation; coupled with greater compressional forces. Furthermore, the application of force deviates from compaction and RI linearity witnessed with the single-punch press and is consistent with literature studies [3] describing the lessening of consolidation as the true density of the material is met (MCC 1.630: Ref). This observation is highlighted more clearly with *Figure 99.*

Table 41: **Average RI's of smooth MCC ribbons.**

MCC Ribbon Character	***Mean reflectance RI (40 points)***
2 mm 5 kN/cm	*1.521*
2 mm 10 kN/cm	*1.889*
2 mm 15 kN/cm	*1.973*
4 mm 5 kN/cm	*1.480*
4 mm 5 kN/cm	*1.785*
4 mm 5 kN/cm	*1.883*
1	

		4 mm 10 kN/cm		*5 kN/cm*	
RANGE, ±	Relative Difference	RANGE, ±	Relative Difference	RANGE, ±	Relative Difference
0.029	0.05%	0.082	-0.8151%	0.021	-0.41%
0.046	0.20%	0.030	-3.2270%	0.022	1.16%
0.056	-2.27%	0.015	-2.6402%	0.027	-0.20%
0.013	-2.28%	0.031	-1.4038%	0.031	0.54%
0.024	0.72%	0.009	1.0847%	0.024	0.37%
0.013	1.192%	0.021	2.0430%	0.033	-1.157%
0.035	2.40%	0.019	2.6851%	0.025	0.257
0.027	-0.016%	0.066	2.2733%	0.026	-0.56%

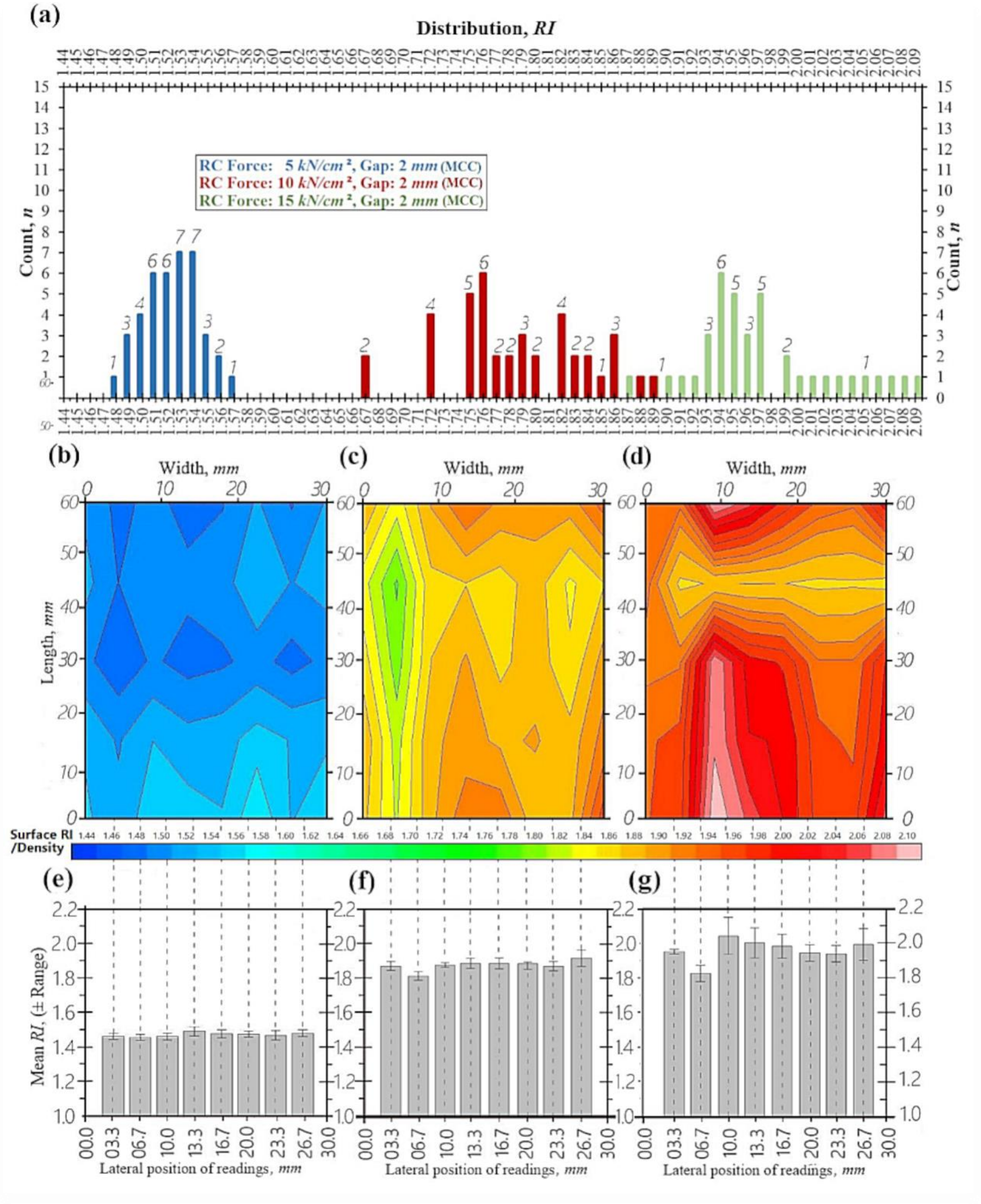

Figure 99: **Surface RI analysis of MCC ribbons with a pre-defined roller-gap of 2 *mm*. The histogram, (*a*) displays the distribution of the all the ribbons (points analysed/ribbon = 40), while individual contour images are shown (*5 kN/cm*: ‘*b’*, 10 *kN/cm*: ‘*c*’, and 15 *kN/cm*: ‘*d*’). In ‘*e*’, the mean lateral distributions are plotted, with error bars for the minimum to maximum RI’s along the ribbons’ length.**

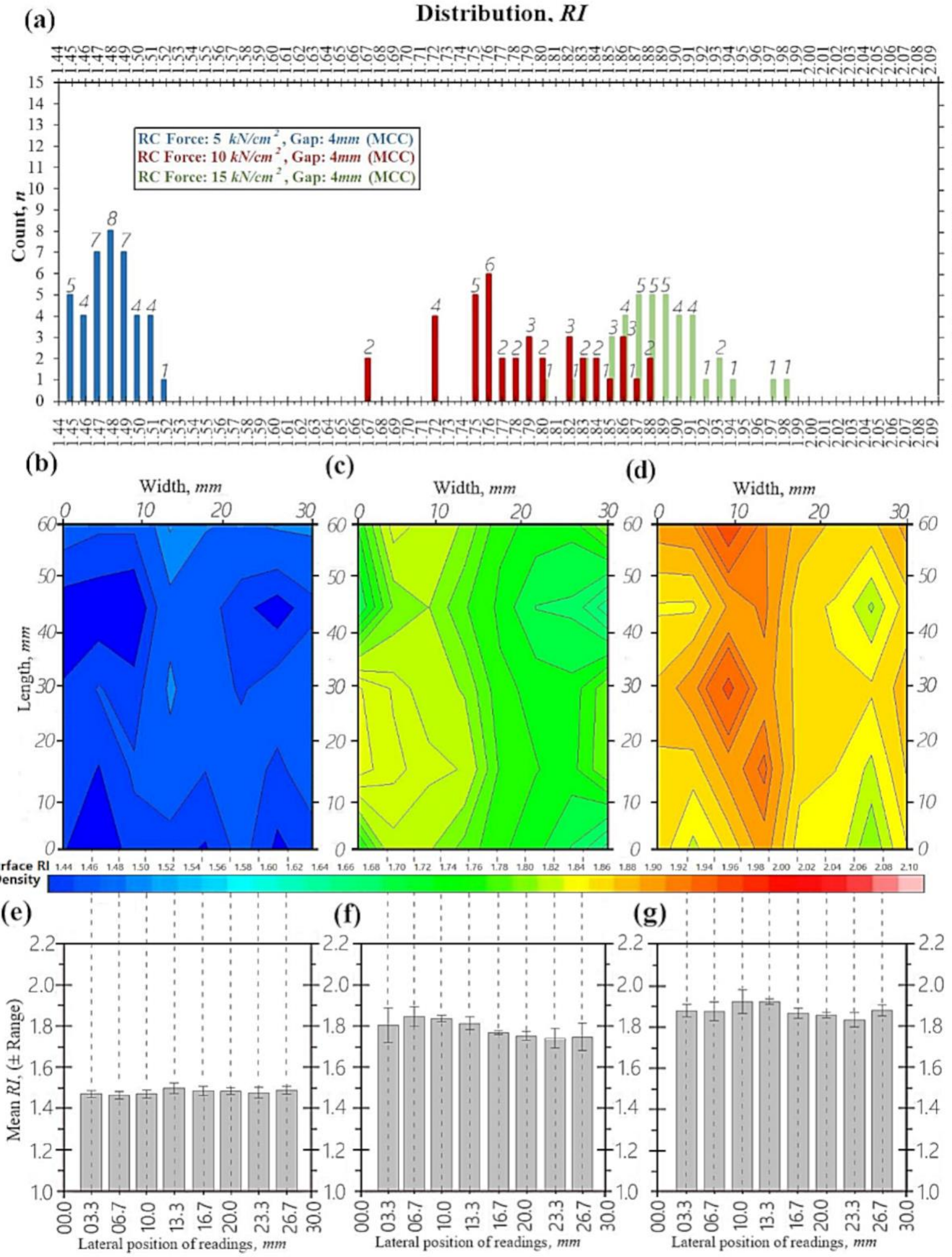

Figure 100: **Surface RI analysis of MCC ribbons with a pre-defined roller-gap of 4 *mm*. The histogram, (*a*) displays the distribution of the all the ribbons (points analysed/ribbon = 40), while individual contour images are shown (*5 kN/cm*: '*b'*, 10 *kN/cm*: '*c*', and 15 *kN/cm*: '*d*'). In '*e*', the mean lateral distributions are plotted, with error bars for the minimum to maximum RI's along the ribbons' length.**

7.6.2 Objective 2: Test the TPI method on 'ideal' roller compacted ribbons

7.6.2.1 Calibration with FDT

To capitalise on the BMS wafers in order to correlate physical density, apparent gas pycnometry SF's and THz derived RI's, four solutions are proposed in *Table 59* (*Appendix Section 10.4.2*) to reduce the effect of the physical knurling on the wafers. Here the selected wafers were placed within a vice and using a very high grain glass-paper (2400 grain), minimal abrasive force were used to remove visible lattice protrusions while concurrent calliper readings were taken to ensure equal lateral and longitudinal thicknesses.

The apparent SF/density are plotted on opposing *x-axes* against RI of 6 wafers at 3 SF ratios, n=5 (*see Figure 101*. Further extrapolation of SF and density both to a value of 1 for RI produces a range of 1.01 – 0.99, while error bars are added (*see Figure 101*) to account for calliper insensitivity and for minimal RI differences within the range of 0.75 – 1.25 THz frequency range.

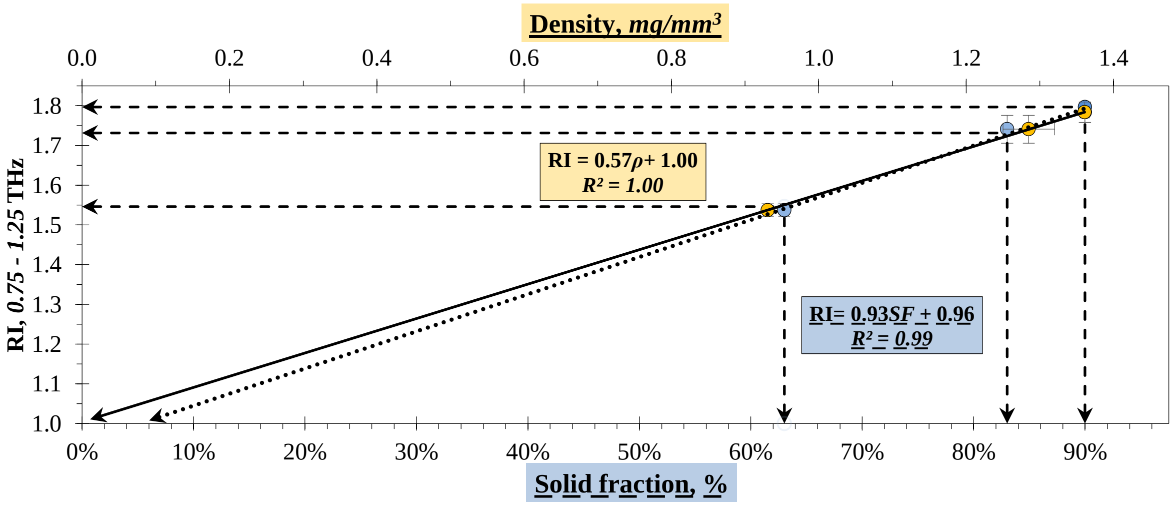

Figure 101: **Frequency-domain plot of 6 wafers compacted at 63 – 90% SF fractions. Relating geometric density and frequency-domain determined RI (FDT). The wafers are composed of 78% PH-102, 19% Lactose anhydrate, 1½% croscarmellose and ¼% Mg St.**

The RMSE errors associated with *Figure 101's* calibration curve are displayed in *Table 42* indicated by the equations linked to the apparent linear lines of best-fit (*inset Figure 101*), FDT derived RI values of smooth faced wafers are shown to be highly indicative of the apparent solid-fractions and densities of these models over this density range. Between THz FDT derived

RI’s and SF’s range from 1.6 to – 1.4% (averaging 1.22%) and FDT RI’s to density range from -1 to -0.3% (averaging 0.2 %).

Table 42: **RMSE statistics of the calibration curve.**

FDT RI	SF	Geometric Density,	SF RMSE, *%*	Geometric Density, RMSE, *%*
Mean *0.75-1.25 THz*	*%*	*mg/mm*^{3}		
1.538	63 *%*	0.931 (± 0.002)	1.40 *%*	-0.30% (± 0.002)
1.741	83 *%*	1.285 (± 0.003	-1.21 *%*	-0.10% (± 0.003)
1.784	90 *%*	1.361 (± 0.003)	1.57 *%*	-0.20% (± 0.003)
		RMSE Error:	1.22 *%*	0.20 %

7.6.2.2 Time-domain reflectance imaging (TPI) to predict wafer RI and thickness parameters

In order to test the ability to accurately measure RI with TPI and establish whether regional/local differences for the parameter of SF and substrate thickness can be compared relative to values over multi- compositional, still equal compacts. Using full imaging (as opposed to the more rapid ‘spot imaging’), TPI is applied to the sanded, planar wafers of varying SF’s ~140 waveforms in the lateral dimension and ~400 points acquired in the longitudinal dimension

A large number of *E-Field* (*t*) waveforms were consequently collected during imaging of each of the 6 wafers. Illustrated in *Figure 102*, the inset dots represent the waveforms interpreted to compile lateral and longitudinal data to qualify the method for, 1) accuracy, and 2) whether relative RI/thickness measurements are sufficiently reliable and precise.

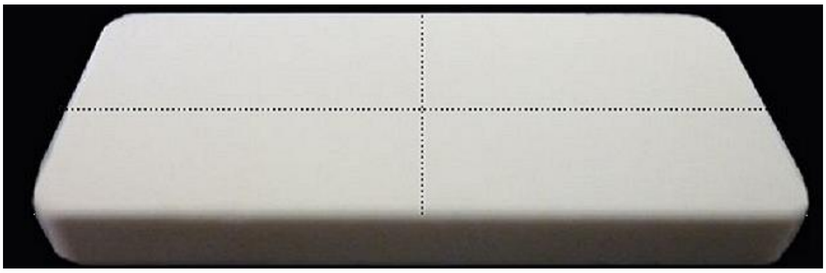

Figure 102: **Photograph of a 90% SF wafer (smooth on both faces) inset with lines illustrating the origin of *E-Field* (*t*)profile acquired by TPI acquired waveforms used in the following images (to follow).**

Three of the six wafers were scanned at equal resolutions (0.2) to compile plots (*see Figure 103; a-f*). The two prominent E^{MAX}-*fields* of the TD waveforms are displayed inset as black lines. E^{MAX}1-*Fields* signify anterior TPI reflection events (at approx. 2 *ps*), and the posterior (generally above 25 *ps*). The inset dotted lines are the predictions of thickness derived from RI's yielded from each waveform using the simplified Fresnel's reflection amplitude coefficients (not shown; yet in accordance to the method developed in

Experimental chapter 2, with the smoothing and amplitude/time constraining techniques). The data illustrated in *Figure 103; a-f* is tabulated in in *Appendix Section 10.4 , Table 55*.

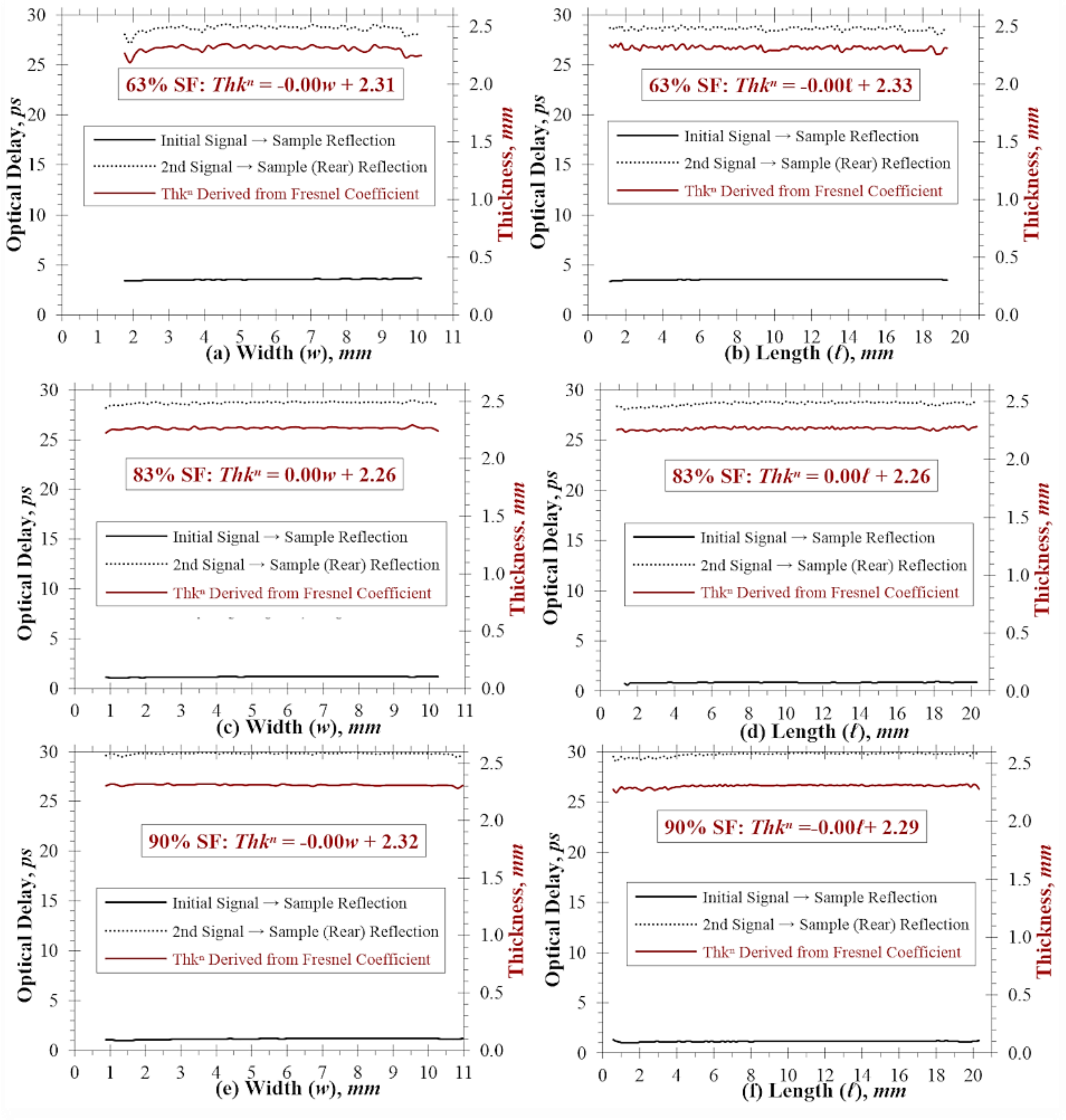

Figure 103: **TPI reflection time-domain waveforms of lateral and longitudinal scanned wafers of variable SF's. Displayed are the optical-delay events associated with E^{MAX} and $E^{2nd\ MAX}$-fields and the predicted thicknesses, *mm* (in red, corresponding to 2nd y-axis). The wafer is composed of 78% PH-102, 19% Lactose anhydrate, 1½% croscarmellose and ¼% Mg St.**

7.6.2.3 The BMS ribbons

Next, the irregular shaped ribbons of BMS (equal chemical compositions) were analysed in the same manner with TPI imaging, with signal-substrate interaction being focused onto the smooth surface of the 63% ribbons (see *Figure 104* and *Figure 105*). Lateral and length-wise images indicate that despite level mounting of the ribbons (following a sufficient duration of rest, allowing for elastic recovery) the lateral cross-section display an arced appearance to the smooth roll (estimated at 2.8° between the central width and the edges). Lighter regions depicted at the ribbons interfaces are shown to be relatively comparable to the central 'core' regions (see *Figure 104a/b, and Figure 105*), with denser regions indicated ~0.2 -0.4 *mm* into the air/substrate interfaces. While it may be postulated that the powder blend is subjected to greater compressional forces imparted to the ribbon faces this may not be evident in the images and possibly due too:

1. The extremities may have a greater propensity to *elastically recover* given the duration between production and analysis because the number of particle-to-particle forces are suggestively fewer than marginally deeper particles, and thus fail to permanently deform as effectively. For instance, surface particles may form bonds with vertically neighbouring particles and particles below, however as depth increases particles have an increased number of particles to interact with (i.e. effective 3D bonding is available at greater depths than on the surface; analogous to water evaporation from the air interface).
2. Also, it may be hypothesized that the extent of moisture exposed to the air interfaces permits water absorption, thus lowering the RI (i.e. the RI of water is ~1.5).

Furthermore it is important to consider that the bowing of a ribbon would give rise to a greater degree of reflection (generally at the center of the images where the peak or trough of the scan is orientated) in light of the fact that the differential curve is or closely approaches zero and consequently representative of greater specular reflection. The effect of bowing would however have an effect on the degree of the incident radiation that is reflected (e.g. as the specular/diffuse work has so far illustrated). The position of the red lines at the base of the images was decided in consideration that the plane of initial interception was met and pertains a greater differential in regard to longitudinal or lateral dimensions to zero, however the *E^{max}2 Fields* have been added with consideration of the known width the ribbon (recorded manually off-line) and with observation that the demise of the greatest *E^{max}2 Fields* (particularly apparent on the second plots 'b') signify a high degree of density/RI change. Corel Paintshop Pro X6 was used to re-render the cross sectional images to better enable subtle alterations to be emphasised.

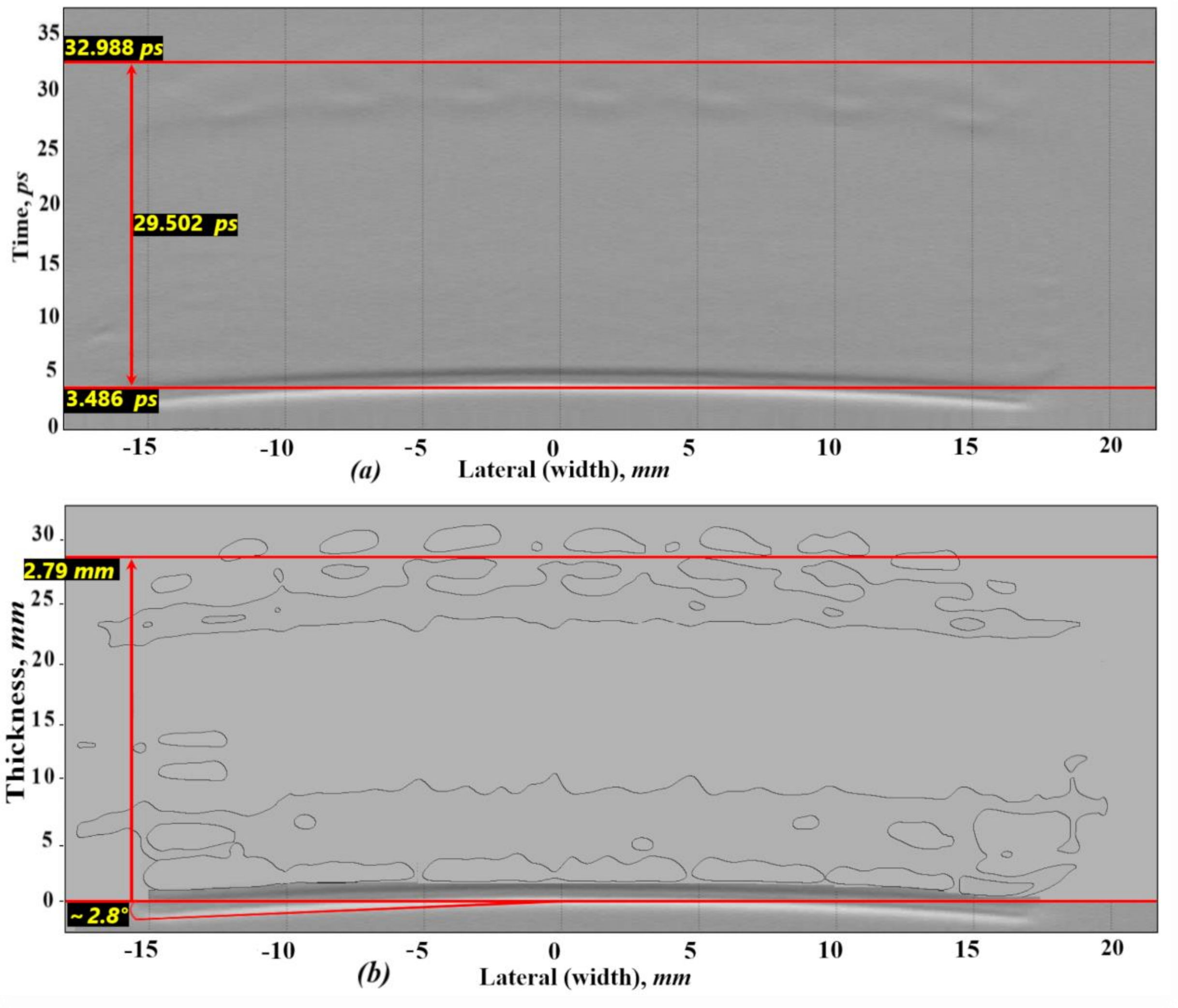

Figure 104: **(*a*) TPI lateral cross-sectional scan of one BMS 63% SF ribbon. Also displayed (*b*), is a contour interpretation of image (*a*) highlighting increased regions of RI (shown darker).**

The cross sectional and contour routine was repeated over the length-wise longitude (*Figure 105*).

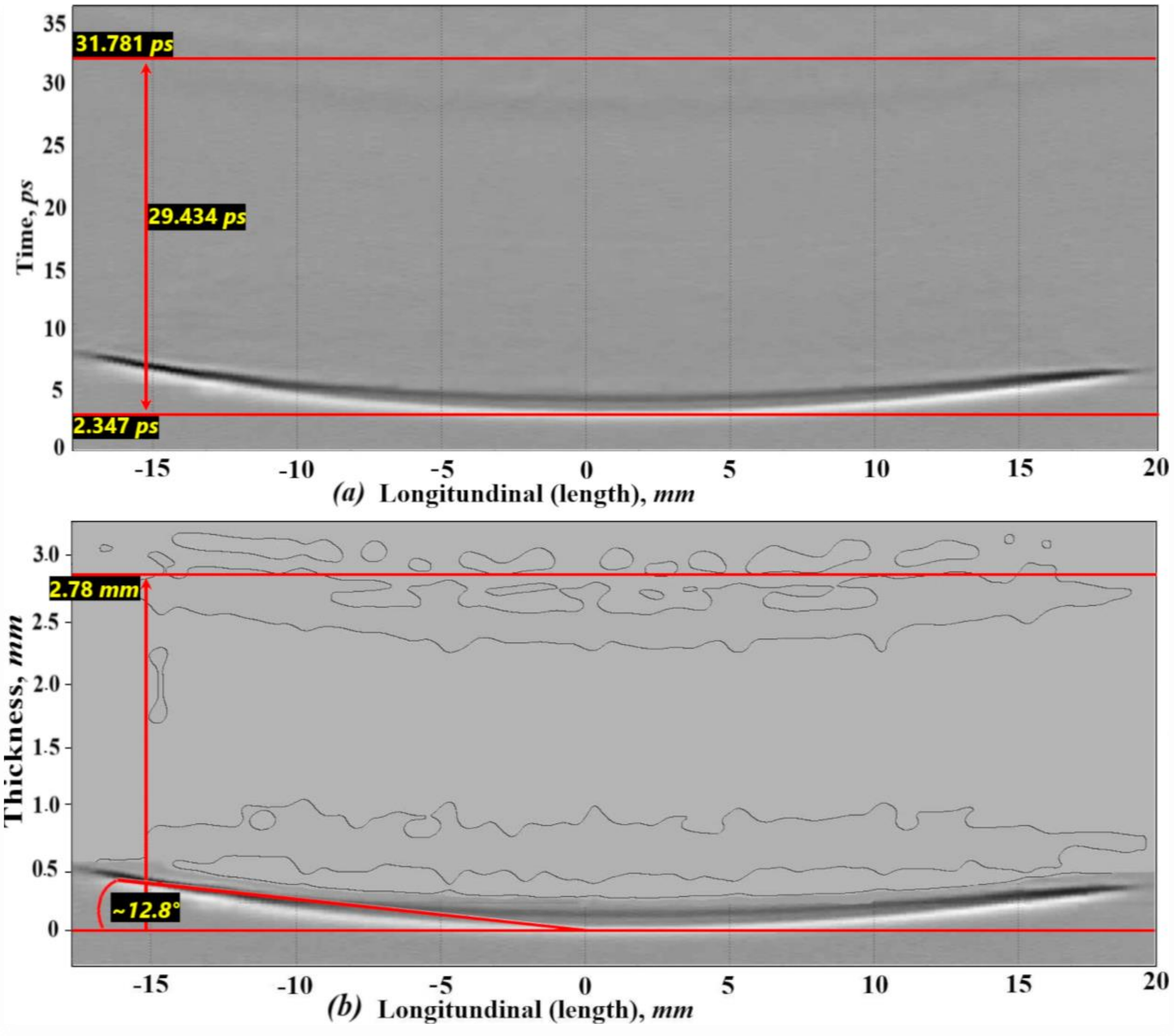

***Figure 105*: (*a*) TPI longitudinal cross-sectional scan of one BMS 63% SF ribbon. Also displayed (*b*), is a contour interpretation of image (*a*) highlighting increased regions of RI (shown darker).**

7.6.2.4 Thickness determination accuracy

The secondary interest of utilising reflection imaging for density monitoring is the ability to approximate the thickness of the ribbon immediately post-ejection. The density of the ribbon to the downstream granulation process has been indicated as a high priority for enhanced CQA's of the granulation. Sufficiently covered in this project is the influence that RI and the materials path-length have to the optical delay. The influence of roll-gap has been observed to marginally lower the RI of ribbons compacted with equal compressive forces.

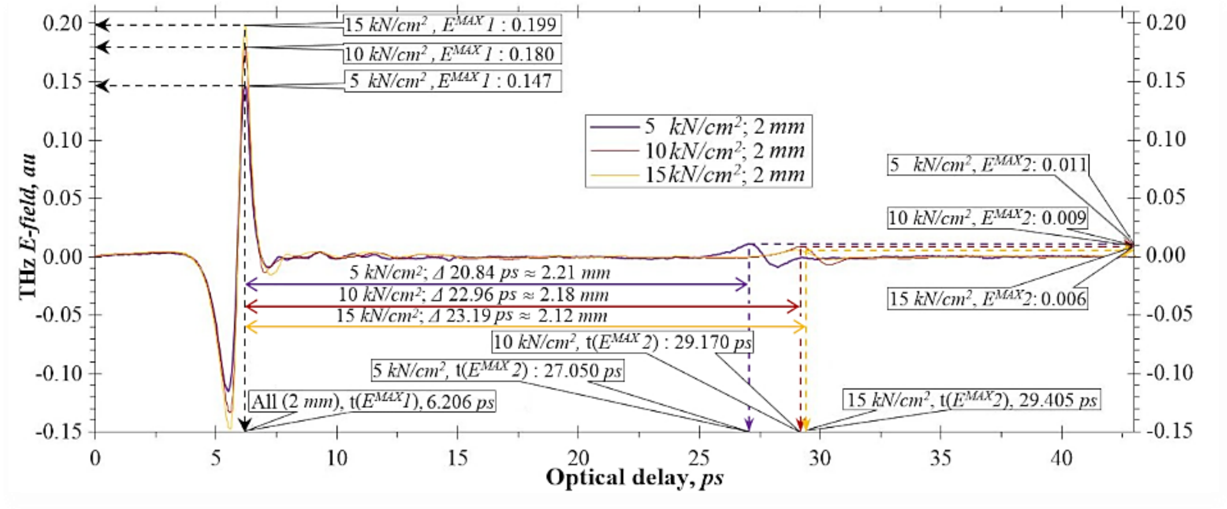

Figure 106: Reflection waveform of 2 *mm* thick MCC ribbons compacted under greater forces. Inset are the THz E^{MAX}-field magnitudes at 1: initial interaction and, 2: suggested rear-surface originating reflection (TPI derived RI is used to approximate thickness).

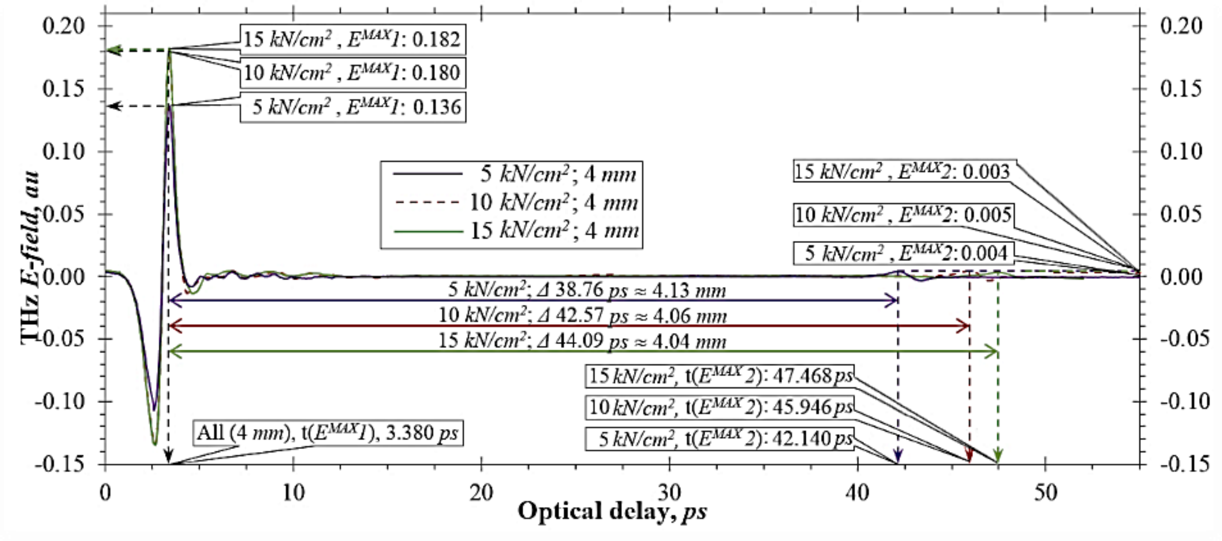

Figure 107: TPI waveform of 4 *mm* MCC ribbon. Inset are the THz E^{MAX}-field magnitudes at 1: initial interaction and, 2: suggested rear-surface originating reflection (TPI derived RI is used to approximate thickness).

The specifications of the thicknesses determined pre/post manufacture by reflectance imaging (calculations not shown) are given in *Table 43*. Immediate observation of *Table 43* in regard to the increased thicknesses of the BMS ribbons (measured with a Vernier calliper) between and post production and the reduction of these values with increased compaction force is apparent. Proportional similarities are relatively less, suggestive of the increased compaction ranges used (this a greater proportion of permanent deformation). Additionally, the indicative correlation of density and THz RI's (measured with the single punch press, *see Experimental chapter 2*) conforms less to linear trending with compaction force.

Table 43: **Specifications and analysis of 100% Vivapur 102 ~ Avicel® PH-102)**

Ribbons			
2 *mm* Avicel 101 Ribbons			
kN/cm	Thickness parameter displayed during processing (roll-gap), *mm*	Mean Thickness after processing (~ 14 days), *mm*	TPI-RI
5	2.00	2.21	1.326
10	2.00	2.18	1.511
15	2.00	2.12	1.580
4 *mm* Avicel 101 Ribbons			
5	4.00	4.17	1.299
10	4.00	4.12	1.481
15	4.00	4.09	1.548

7.6.3 Objective 3: Purport any further constraints/merits/limitations and proposed methods to engineer a viable RC featuring RC probes

Currently (2015) fiber-optic THz probes are available and would be absolutely necessary to advance any form of THz analysis into an industrial setting. Advantageously the angular ranges are flexible and so (going back to the Fresnel caveats) could be used in a conventional transmission alignment or at 5° for the angle of incidence to obtain absolute (non-simplified) predictions for RI. Although this would require very powerful THz signal-pulse generation and detection to keep the probes from clashing.

Worthy of note, the nature of THz EMR is well equipped to function in industrial climates for the need to continuously clean the probe/detector has been shown to out-perform NIRS for imaging applications. The unique gating system used in most photoconductive machines allows the focal point of the laser foot-print to be lengthened significantly meaning that collection of dust on protected lens effects acquisition minimally, and can be 'viewed-through' owing to the transparency of most pharmaceutics [129].

Operating the system for the use of TD analysis is a very simple procedure to do and requires very little reorientation or altering. Having spoken about the need for dry air herein, this requirement is absolutely necessary in spectral analysis for ionisable species will occupy three frequency regions, but 'water-spikes' are very marginal in TD spectroscopy. For instance, peak to peak analysis would not be effected and reflection analysis with the TPI module, as witnessed herein is not a sealed unit and functions in the ambient.

There remains two challenges however for implementation in DG/RC and these include augmentation into a RC device that can actuate the readily interpretable data that is produced by such systems. Spot scans can be taken in for instance at just 50 m/s (1 pixel) and also can 3D raster scan at high a resolution at approximately 1hr/15cm^2. Hence rapid to in-depth monitoring can be made, rather what features can be made to RC to action slight ribbon leanness here and there. With that implementation, of a bracing device would be required of a RC in order to continue monitoring the same focal plane from a machine operating at pico-second wave pulses.

7.7 Conclusions

7.7.1 Objective 1: Establish a guideline to elucidate method issues which could be detrimental to TPI analysis and access resolutions

Careful choice of the roll wheel is necessary for adequate readings with optic probes. Shown succinctly, a unit-process with a knurled roll limits the PAT potential by allowing only relative RI/SF measures to be acquired. This would not be possible on a dual knurled machine and except for off-line imaging of density uniformity. Hence plane rolls are recommended. Plane rollers do not just prevent lattice imprints from distorting vector light propagation, but also avoid potential creation of ribbons that are non-planar. A knurled ribbon is seen in an example of which it is slightly bowed and so loses (a close to) planar surface. Bowing in longitudinal or lateral directions does not pose such a detraction than knurls, yet, as measurements are microscopic, a sample that is several degrees arced will slip forwards and backwards to the laser focal plane and thus loose intensity.

7.7.2 Objective 2: Use of the TPS with RC ribbons and wafers

7.7.2.1 THz RI's further serve to as a surrogate measure to gas displacement pycnometry

After removal of lattice protrusions from a rectangular shaped wafer it was possible to extended FDT RI as a proxy measure for both density/chemical permittivity and pycnometry values. With three samples ranging from 63 to 90% solid/pore ratio, RI's found to be linearly correlating with a R^2 of 1 providing a RMSE error margin of 1.22% ± 0.2%. It is further believed from the success of previous work and the error margins in which the industry is allowed (100% ± 5%) that without a frequency based measurement that a rapid and in-line use of TDR would perform well within specification.

7.7.2.2 TPI to predict wafer RI and thickness parameters

Starting with the smoothed wafers, approximately 550 TPI spot scans were made laterally and longitudinally. Such work was time consuming on non-specialist software yet capturing the full length and breadth was important to see whether any non-uniformity in SF or thickness could be captured. Again 3 wafers of 63, 83 an 90% SF where fully analysed from random sides as to not misreport results originating from recently sanded faces to that of a pressed face. The TPI method reported that the RI discrepancies were between the mean of values-2.3%, 2.2% and -3.4% respectively, from the FDT data. Knowing the angle of internal transmission, the thickness were then yielded and reported on the axis using the OD (*t*) equation resulting in thickness discrepancies of ±0.2 mm over the three wafers, averaging the consistently shaped plots seen previously.

TPI to predict RI parameter of the BMS ribbons and an approximation of thickness

Supplied with the wafers from BMS were near equal SF ribbons which were C-scanned in across the breath and width. Immediately it became apparent that the most planar samples used were not as flat as one hoped. For this reason extensive interpretation was not carried out other than to demonstrate a key caveat of TPI imaging; that planar substrates are very important for accurate RI prediction. As can be seen the knurled face was the posterior surface and many of the pixel waveforms were disregarded for either the posterior was too blurred or to broad (indicating frustrated reflections). A number of reading where found where the focal plane matched the reference mirror and a distinguished posterior FB resonation was spotted. This enabled a handful of 4-6% discrepancy errors to be found of the thickness while applicable RI's were consistent with ±3% of TDT studies undertook

7.7.2.3 The four planar ribbons deduction of RI

The TPI lead RI prediction of the four variant planar ribbons was very successful the number of data points taken of each ribbon numbered fourth leading to a great deal of numbers RI's and thickness predictions. Accessing each ribbon for RI uniformity indicates that the compacts made at 10kN surpassed the 5 and 15kN ribbons with a narrow RI range of 0.023 RI over the 4 widths with smaller relative spreads of thicknesses. Next the 15kN mean ribbons had the leanest RI spread of 0.032 over the 4 thickness a marginally less uniform distribution than the 15kN ribbons. Unsurprisingly the two widths of MCC ribbons had similar RI profiles with the narrowest 2mm ribbon being more consolidated and the 4mm ribbon

Part III

8 Final conclusions

The measurement of the process conditions and formulation compositions (to characterise glasses, tablets and RC ribbons) was evaluated in positioning TPI as a potential pharmaceutical PAT application. The study of time-domain reflection has revealed that

1. The prediction of material RI's and thicknesses by the various TD methods are highly indicative of material density, solid-fraction, and chemical composition in the instance of glass slides.
2. Prediction of RC RI's is ostensibly a relative measurement (best suited for TPI) for monitoring density/SF, as opposed to an absolute RI measurement. It is thus suggested that the uniformity within a compaction run is of a greater importance to maintain than the accuracy of the dimensional properties (i.e. the constituents of the ribbons/thickness are may not give true RI's, rather than all the ribbon samples are compared on a like for like RI).
3. Different formulations would therefore require individual assessments to be made because of the inherent RI differences of constituent components and, the quality of these excipients.
4. Comparison of AW and Gerteis RC's using TPI assessment suggests that Gerteis ribbons are generally produced with greater compliance to the user-defined CPP's and thus; demonstrate favourable quality attributes.
5. Exclusive use of optical-delay measurements used in the TDT method is of lesser utility than TPI for material predictions of RI or thickness largely because prior knowledge of either parameter is needed. Without the combination achieved by coupling reflection and TDT-SD and/or TDT-ID, an in-line monitoring system using a transmission system, must therefore address:
    a. The apparent physical limitation of affixing two THz probes adjacent to each other.
    b. Thickness estimations taken from a secondary PAT tool, which could include;

- Using the RC unit’s instrumented roll-gap measurement that would require evaluation of adding additional augers to supply lateral regions of the ribbon at the point of the nip zone.
- Although SD and ID TDT methods are complementary, a major advantage is provided by the ID OD measurement because a reference of either an empty-system or a reflective surface is negated. However, internally resonating FP events can be difficult to distinguish when the substrate has a sufficiently high absorption coefficient and/or path-length.

6. The density of compacted pharmaceuticals is proportional to mechanical strength. Radial tensile strength (RTS) determination is a highly indicative parameter particularly with factoring of density and the tablets geometry.
7. In all instances (TPI or transmission configuration applications the probe-beams path length is crucial to give time-resolved result of either *I* or *E-Fields* (*t*). It would be necessary to consider the need to brace/guide the output ribbons into a scanning area because experimentally, samples must be placed in the holder at identical spatial positions.
8. Both transmission and reflectance methods would require bracing of the ribbon in a static position post ejection for the roll-wheels. For a transmission method to be successful the divergence of the probe-beam must be exact on each occasion, similarly TPI shows sensitivity to angular positioning and the probe-beam length from the emitting antenna. Therefore it is anticipated that integration of the unit-process and the spectroscopic device would necessitate some degree of re-engineering.
9. Fabry-Pérot reflections decrease proportionally with substrate RI and thickness. This is pertinent because the visible time-window is narrower with transmission measurements than

with reflection measurements[28]. Noted as a complementary technique to transmission TD spectroscopy, signal delay measurements cover a broader window (as the initial interception peak is substantially detected/focused at a lower optical-time) yet are highly sensitive to substrate positioning in relation to the THz emitter and detecting antennae; thus require a reference measurement. TPI also requires a reference measure; however a transmission-type configuration is proposed to offer less practicality in an in-line system with regard to antenna positioning in an active RC

10. Transmission measurements as a bulk measurement run the potential to deviate from TPI RI results because of the simple act of segregation of fine particles during RC. In this instance the fine particles are likely to fill voids and machine specifics could also the fine to fall to the bottom of a blend. TPI thus may be more to de-mixed fines than the bulk measurement in transmission work.

---

[28] The software developed by TeraView offers a time-window spanning 40 ps in transmissions, whilst a window of approximately 100 ps can be accurate obtained in reflection mode analysis.

9 Further work

The technological progress of THz capabilities, has allowed numerous of companies of various industries to build on the established reputation of THz EMR region exploitation. Previously used almost exclusively in spectral analysis Haddad, *et. al.* (*2013*) [97]. The varieties of THz applications have unsurprisingly grown around imaging for several reasons that include the ability of THz to penetrate many substances in a non-evasive manner with safe levels of black-body radiation[29]. This low level of energy is perceived to be harmless and is used to assess sensitive pharmaceutical API's (including bio-pharmaceuticals plus, semi-conductor technologies and also in the field of medical diagnosis [153]).

A number of obstacles have been seen/demonstrated in this study that would make industrial commitment tentative at this stage, particularly in regard to exacting protocols of PAT, QbD applications. However many issues associated with current DG/RC maybe developed further, having elucidated both benefits and issues as they currently stand before in-line consideration. There exists a number of key design and conceptual factors to consider however in *Table 44:* Advantages of perusing THz implications (THz probe-beams to be placed in larger DG/RC systems to enable continuous monitoring) and also obstacles met and developed for resolution.

Table 44: **Advantages of perusing THz implications (THz probe-beams to be placed in larger DG/RC systems to enable continuous monitoring) and also obstacles met and developed for resolution.**

Advantages of further development identified:	Issues to be resolved with engineering/software development:
Current probe units can tolerate moderate levels of powder deposition on the lens w/o significantly attenuating the probe-beam. Technically this is possible because the *z*-focal plane would advance focus onto the ribbon, invariably separated from the probe unit. Practically, deposition could reduce the beams intensity over time, as rapid measurements	The necessary simplification of Fresnel's equations to avoid computationally complex algorithms may very well be an issue to address. Withstanding the mathematical aptitude which exceeds the scope of this investigation. RI prediction by TPI stands as a relative measurement method; not for absolute RI knowledge. The result is that all

---

[29] THz absorption in solids are known to introduce low level of frequency vibrations in molecules. These vibrations do not effect singular atoms rather the rigid molecule structure itself, and are fully insensitive to amorphous items.

assessed in a relative nature (i.e. the lateral dimension of 1 meter ribbons as opposed to first and end ribbon properties of a long continuous cycle.	formulations must be assessed individually because RI's are intrinsic parameters of chemical composition.
In cased within the RC unit, THz probes could benefit from the insertion of inert N_2. This property would be less beneficial for TD optical time-delay readings but crucial for spectral analysis if a second PAT application or even chemical distribution was used to determine ribbon thickness.	Probe Design: The THz probes currently available from TeraView have been assessed to fit within a several current Gerteis systems. Unfortunately, the PolyGran is unable to house the probes at current sizes, yet the dimensions of the Ultra (full-production) unit would permit this (*See Figure 108*. Subsequently the process scale up procedure would require attention.
This study has demonstrated the RC ribbons are variably dense/thick. Successful implementation to assess local regions of ribbon in-line at rapid rates (currently one TPI scan can be made in 50 milliseconds). The challenge one expects would be the recall stage to improve the DG/RC efficiency. - For instance has RC control been optimally (within reason) developed? -Could the roll axis be manipulated for lateral correction or additional augers fitted to unify densification in the nip zone?	System design: The importance of a consistent path-length of the THZ probe-beam has been emphasised many time herein. In a practical environment this still remains true and would therefore demand the ejected ribbon is analysed whilst it is attached to a roller-wheel (beneficially alleviating low magnitude posterior reflection peaks), or the need for a bracing bracket for the ribbon to pass through. Beneficial to the second condition, the reflective Au/Ag reference reflector could be placed at the posterior face of the ribbon with the use of a spring assembly to press the mirror onto the invariably fluctuating ribbon width.
Upgrading the reflectivity of current stainless-steel rolls by means of potential Au/Ag plating would permit the THz probe-beam to continuously re-establish a reference measurement of reflectivity (said in regard to potential powder deposition upon the lens) to provide greater posterior registration very simply. Additionally, absence of a substrate could be used to flag down-time of the process.	Granulation/Ribbon quality correlation. Indicated by several sources previously, the quality of the ribbon is paramount to the quality of the granulate. Therefore, optimal granule properties would require additional investigation in tying a feedback mechanism of the ribbons properties to the milling attrition time and rate.
Analysis of the granulate in regard to o.o.s. size/density etc vs. THz uniformity output could be easily controlled to alert the DG/RC to 'send to waste'/'rework' if axial/auger conveyance systems are beyond the scope of development.	Given the statistical equivalence of the results for potential in-line use, results indicative of variation of RI and thickness require the use of new software within the granulator and processes to reject sections of ribbons or evoke a complex system to improve the consistent lateral delivery of the powder blend to the roller (i.e. with multiple feed augers of smaller diameter to convey powder to regions across the width of the nip zone.

Outlined in the obstacles and advancement of technologies (both RC's and THz analysis) indicate to the author that despite current issues, in-line application if not unfeasible and pivotal to this statement is the need for enhanced feedback control; particularly for lateral consistency.

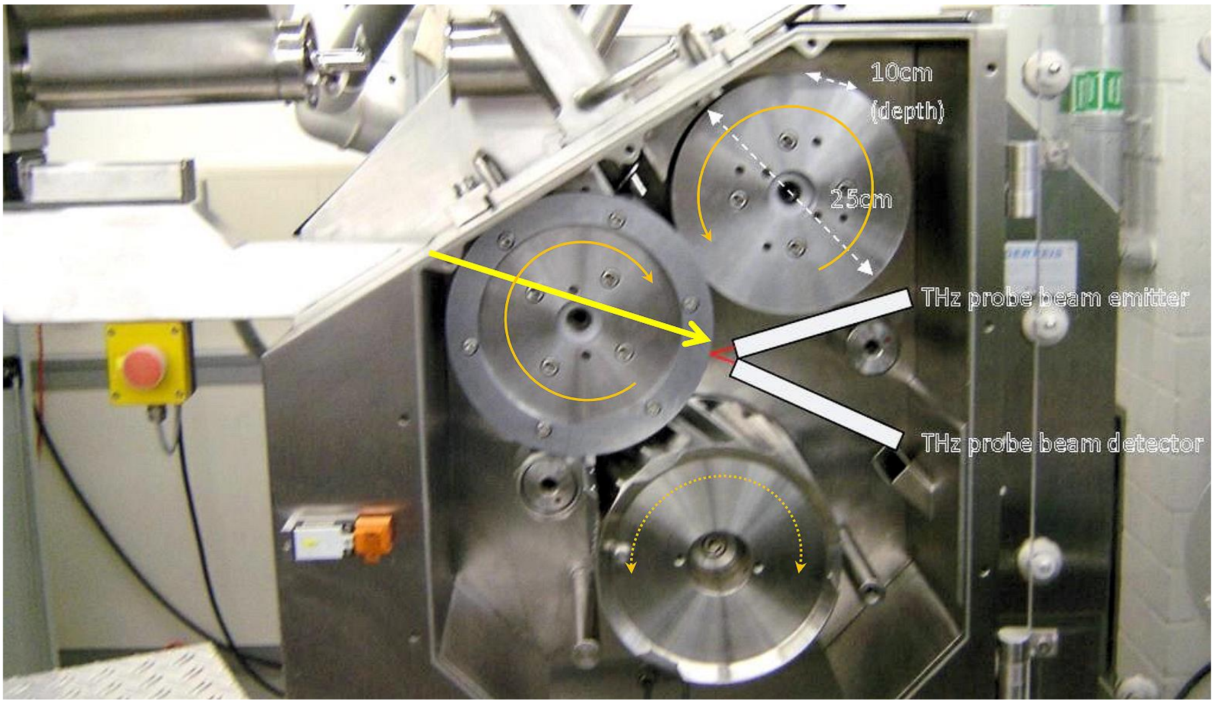

***Figure 108*: Hypothetical usage of current TeraView probe-beams for in-line use in a Gerteis Ultra compactor (sizes to scale).**

Part IV

10 Appendix

10.1 Classical Optics.

Acknowledgement is made to Hecht for the foundations to Maxwell's equations and the Fresnel equations [102].

Glossary of terms

E = Electric field ε = Permittivity σ = Conductivity μ = Permeability

H = Magnetic field $\mu_0/\ \varepsilon_0$ = Permeability/Permittivity in free-space or vacuum

10.1.1 Maxwell's wave equations of the coupling of *E & H-Fields*

Fusing Faraday's law of induction (not shown) and Ampere-Maxwell's law (not shown), the movement of EMR can be mathematically described with extensive derivation, as given in *Equation 20* and *Equation 21*, respectively.

$$\nabla \times \vec{E}(t) = \frac{\partial \mu(t)\vec{H}(t)}{\partial t}$$

Equation 20

$$\nabla \times \vec{H}(t) = \sigma(t)\vec{E}(t)\frac{\partial \varepsilon(t)\vec{E}(t)}{\partial t}$$

Equation 21

Through the above defining equations, the inherent relationship between *E-Fields* and *H-Fields* is shown, demonstrating propulsion of one field by collaboration with the other through free-space in vector form. Maxwell continued to purport the intrinsic entanglement of the *E-Fields* and *H-Fields* explicitly to time-dependent systems to produce the wave equations (*Equation 22*) to ostensibly model the behaviour of dynamic *E-Fields* and *H-Fields*, common also to THz wave generation [96].

$$\frac{1}{c^2}\frac{\partial^2 E}{\partial t^2} - \nabla^2 E = 0$$

$$\frac{1}{c^2}\frac{\partial^2 B}{\partial t^2} - \nabla^2 B = 0$$

Equation 22

Here, $H(t)$ describes magnetic flux $E(t)$, is the *E-Field* component and the materials permittivity $\mu(t)$, permeability $\varepsilon(t)$, and charge flow $\sigma(t)$ are shown. Noteworthy, Faraday's mentor (Maxwell) the first proved that light has a universal speed limit which cannot be exceeded with the yielding of *Equation 23*:

$$c_0 = \frac{1}{\sqrt{\varepsilon_0 \mu_0}}$$

Equation 23

10.1.2 Derivation of Fresnel's equations to a simple reflection coefficient

The *E-Field* (*t*) is the real-valued component of a complex valued signal and contained in the imaginary component includes the power spectrum, transmittance and phase information, which is accessible through a routine fast-Fourier transformation [108, 109, 105, 106]. During propagation through a medium which would retard c_0, the probe-beam becomes polarised, altering the Cartesian coordinates of signals *E* & *H* (*t*) phases as shown in *Figure 109* (*yz*), whereby the *E-Field* (*t*) is projected onto the *xy* axis and the *H-Field* onto the *xz* axis.

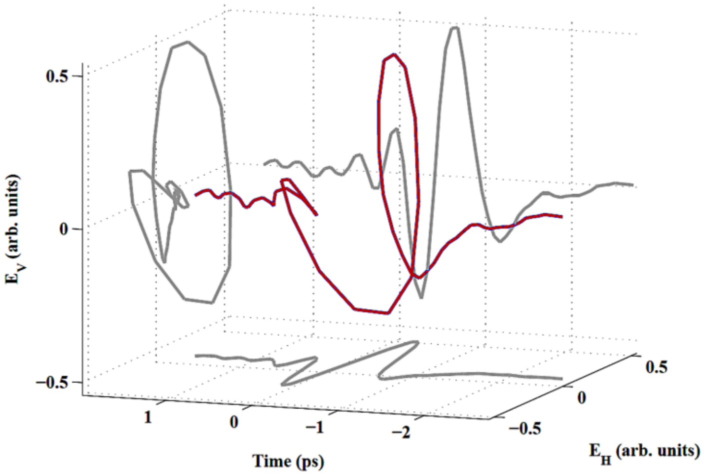

Figure 109: **Three-dimensional projection of a theoretical THz pulse as a superposition of two orthogonal fields, x^E_v (*t*) and y^E_H (*t*). Image adapted from source [154].**

The treatment of the *E-Field* (*t*) when it is either perpendicular (⊥), or parallel (‖) is necessarily illustrated in *Figure 110*. In the first instance when the *E-Field* is ⊥ to the incidence plane, (*see Figure 110A*), the magnetic component (*H-Field)* can be seen to traverse the *yz* plane. Similarly, the *E-Field* is ∥ to the incidence plane (*see Figure 110B*), the magnetic component (*B/H-Field)* can be seen to traverse in the *xy* plane.

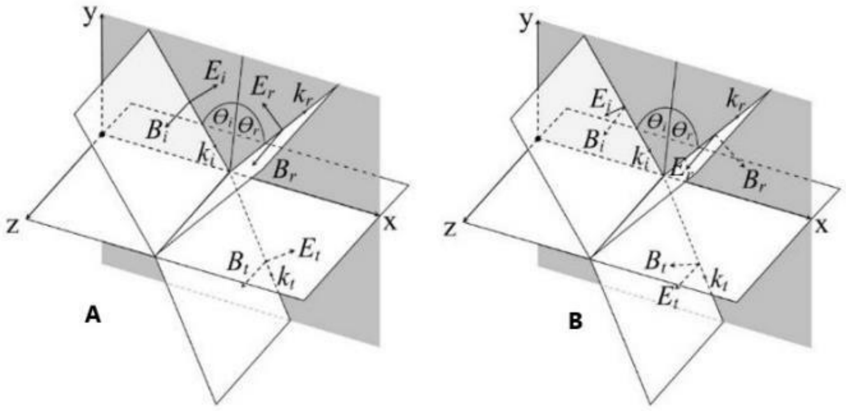

Figure 110: **Ray diagrams illustrating the travel of EMR wave along vector k_i in the *xy* plane to meet the substrate perpendicularly ('*A*') and parallel ('*B*') to the plane *xz* at oblique incidence.**

10.1.2.1 Perpendicular and Parallel *E-Fields* to the plane of incidence

Briefly, for materials of a dielectric nature (whereby $\mu_i \approx \mu_t \approx \mu_0$ [102]), the common form of the general perpendicular Fresnel reflection amplitude coefficient is yielded with understanding that the reflected and transmitted radiation is the sum of the emitted (i.e. $E_{0i} + E_{0r} = E_{0t}$), and θ_i° is assumed to be *0*° and $N_2 \sim 1$:

$$r_{\perp} \equiv \left(\frac{E_{0r^{\circ}}}{E_{0i^{\circ}}}\right)_{\perp} = \frac{\frac{n_i}{\mu_i}cos(\theta_i{}^{\circ}) - \frac{n_t}{\mu_t}cos(\theta_t{}^{\circ})}{\frac{n_i}{\mu_i}cos(\theta_i{}^{\circ}) + \frac{n_t}{\mu_t}cos(\theta_t{}^{\circ})} \Rightarrow r_{\perp} \equiv \left(\frac{E_{0r^{\circ}}}{E_{0i}{}^{\circ}}\right)_{\perp} = \frac{n_i\, cos(\theta_i{}^{\circ}) - n_t\, cos(\theta_t{}^{\circ})}{n_i\, cos(\theta_i{}^{\circ}) + n_t\, cos(\theta_t{}^{\circ})}$$

Equation 24

Using Snell's law, ($n_i \sin\theta_i^{\circ} = n_t \sin\theta_t^{\circ}$) and basic trigonometric identities, *Equation 24* can be expressed in terms of the angle of incident only [155, 156]:

$$r_{\perp} \equiv \left(\frac{E_{0r}{}^{\circ}}{E_{0i}{}^{\circ}}\right)_{\perp} = \frac{cos(\theta_i) - \sqrt{\left(\frac{n_t}{n_i}\right)^2 - sin^2(\theta_i{}^{\circ})}}{cos(\theta_i) + \sqrt{\left(\frac{n_t}{n_i}\right)^2 - sin^2(\theta_i{}^{\circ})}} \Rightarrow r_{\perp} \equiv \left(\frac{E_{0r}}{E_{0i}}\right)_{\perp} = \frac{cos(0^{\circ}) - \sqrt{\left(\frac{n_t}{1}\right)^2 - sin^2(0^{\circ})}}{cos(0^{\circ}) + \sqrt{\left(\frac{n_t}{1}\right)^2 - sin^2(0^{\circ})}} \Longrightarrow \frac{1 - \sqrt{n_t{}^2 - 0^{\circ}}}{1 + \sqrt{n_t{}^2 - 0^{\circ}}}$$

Equation 25

When the incident radiation is normal to the plane and propagates through free-space before interception, *Equation 25* can be further simplified to produce *Equation 26* for simple $r_{\perp}$ deduction:

$$r_{\perp} \equiv \left(\frac{E_{0r^{\circ}}}{E_{0i}{}^{\circ}}\right)_{\perp} = \frac{1 - n_t}{1 + n_t}$$

Equation 26

In a similar fashion to the perpendicular representation, the common form of the general parallel Fresnel reflection amplitude coefficient is yielded;

$$r_{\parallel} \equiv \left(\frac{E_{0r^{\circ}}}{E_{0i^{\circ}}}\right)_{\parallel} = \frac{\frac{n_t}{\mu_t} cos(\theta_i{}^{\circ}) - \frac{n_i}{\mu_i} cos(\theta_t{}^{\circ})}{\frac{n_i}{\mu_i} cos(\theta_i{}^{\circ}) + \frac{n_t}{\mu_t} cos(\theta_i{}^{\circ})} \Longrightarrow r_{\parallel} \equiv \left(\frac{E_{0r}{}^{\circ}}{E_{0i}{}^{\circ}}\right)_{\parallel} = \frac{n_t\, cos(\theta_i{}^{\circ}) - n_i\, cos(\theta_t{}^{\circ})}{n_i\, cos(\theta_t{}^{\circ}) + n_t\, cos(\theta_i{}^{\circ})}$$

Equation 27

Again, using Snell's law, ($n_i\sin\theta_i{}^{\circ} = n_t\sin\theta_t{}^{\circ}$) and basic trigonometric identities, *Equation 27* can be expressed in terms of the angle of incident only ($r_{\parallel}$),

$$r_{\parallel} \equiv \left(\frac{E_{0r^{\circ}}}{E_{0i}{}^{\circ}}\right)_{\parallel} = \frac{\sqrt{\left(\frac{n_t}{n_i}\right)^2 - sin^2(\theta_i{}^{\circ})} - \left(\frac{n_t}{n_i}\right)^2 cos(\theta_i{}^{\circ})}{\sqrt{\left(\frac{n_t}{n_i}\right)^2 - sin^2(\theta_i{}^{\circ})} + \left(\frac{n_t}{n_i}\right)^2 cos(\theta_i{}^{\circ})} \Rightarrow r_{\parallel} \equiv \left(\frac{E_{0r^{\circ}}}{E_{0i}{}^{\circ}}\right)_{\parallel} = \frac{\sqrt{\left(\frac{n_t}{1}\right)^2 - sin^2\, 0^{\circ}} - \left(\frac{n_t}{1}\right)^2 cos(0^{\circ})}{\sqrt{\left(\frac{n_t}{1}\right)^2 - sin^2\, 0^{\circ}} + \left(\frac{n_t}{1}\right)^2 cos(0^{\circ})} \Longrightarrow \frac{\sqrt{1^2} - n_t}{\sqrt{1^2} + n_t}$$

Equation 28

Analogous to *Equation 26*, when the incident radiation is normal to the plane and propagates through free-space prior be further simplification is possible for $r_{\parallel}$:

$$r_{\parallel} \equiv \left(\frac{E_{0r^{\circ}}}{E_{0i}{}^{\circ}}\right)_{\parallel} = \frac{1 - n_t}{1 + n_t}$$

Equation 29

As $r_{\parallel}$ and $r_{\perp}$ are assumed value *0*°, unification of the reflection coefficients *Equation 26* and *Equation 29* enable one to derive r_p in congruence with the measured *E-Field*.

$$r_p \equiv \left(\frac{E_{0r}{}^{\circ}}{E_{0i}{}^{\circ}}\right)_p = \frac{1 - n_t}{n_t + 1}$$

Equation 30

10.1.2.2 Derivation of Fresnel's coefficients [|½(⊥+||)|] for a simplified equation for predicting RI

Requiring the most reliable product of the mean coefficients of the reflection amplitude of Fresnel's equations for RI prediction, the angle of incidence ($\theta_i{}^{\circ}$) is assumed to be *0*°*;* and thus $\theta_r{}^{\circ} = 0°$ is used to yield n_t for when the RI for N_2 ~ 1:

$$\Longrightarrow r_p = \left(\frac{E_{r^{\circ}}}{E_i{}^{\circ}}\right) = \frac{1 - n_t}{1 + n_t}; \qquad multiply\ by\ (1 + n_t) \Longrightarrow r_{\perp}(1 + n_t) = \frac{1 - n_t}{\cancel{1 + n_t}} \times \cancel{1 + n_t}$$

$$\Longrightarrow r_p + r_p n_t = 1 - n_t;\ \ sub\left(-r_p - n_t\right) \Rightarrow r_p + r_p n_t - r_p - n_t = 1 - n_t - r_p - n_t$$

$$\Rightarrow r_p n_t + \cancel{r_p} - \cancel{r_p} - n_t = 1 - 2n_t - r_p \Rightarrow n_t(r_p + 1) - n_t = 1 - 2n_t - r_p;\ sub\ (n_t)$$

$$\Rightarrow n_t(r_p + 1) - \cancel{n_t} + \cancel{n_t} = 1 - n_t - r_p; \quad \div \cap (n_t) \Rightarrow \frac{\cancel{n_t}(r_p + 1)}{\cancel{n_t}} = \frac{(1 - n_t - r_p)}{n_t}$$

$$\Rightarrow (r_p + 1) = (1 - n_t - r_p); \quad \div \ (1 - r) \Rightarrow \frac{(1 + r_p)}{(1 - r_p)} = -n_t; - \times \ -1$$

$$\Rightarrow \frac{(-1 - r_p)}{(1 - r_p)} \equiv n_t \equiv \frac{\boldsymbol{(1 + r_p)}}{\boldsymbol{(1 - r_p)}} = \boldsymbol{n_t}$$

Equation 31

10.1.2.3 Limitations and constraints of data treatment

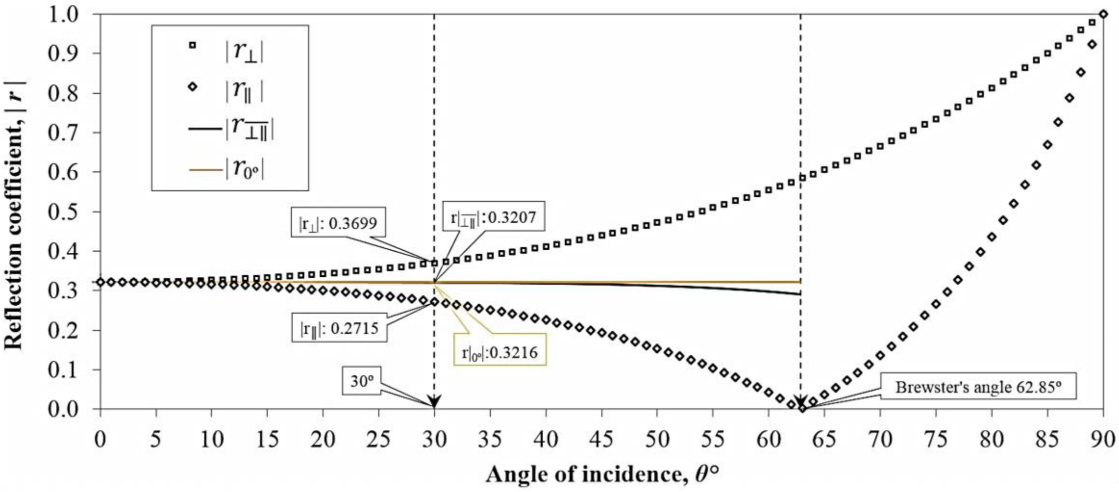

Figure 111: **Mathematical model displaying the effect of increasing the angle of incidence from *0°* to *90°* reflection of EMR with calculation of $r_{\perp}$ (squares) and $r_{\parallel}$ (diamonds) and r_p (mean). The substrate is of glass having an RI of 1.95.**

10.2 Illustrated TD waveform phase inversions in TDT and TPI

Introducing a planar substrate into the transmission chamber (*See Figure 112*: sketched as two white vertical lines), the red (incident) pulse is phase inverted at initial substrate interaction (resulting in reflection, refraction, and signal propagation, labelled '*2*') The reflection marked with a cross evades detection, following backward transmission following phase inversion. Pulse labelled '*A*' ('*3*') is visibly attenuated in comparison to the pulse in schematic '*1*'. The Fabry-Pérot originating pulse '*B*' has undergone two internal inversions (denoted *2* and *3*) and with propagation into the diffusive medium is significantly delayed and attenuated w.r.t. '*A*'.

Attenuation is much more marked because of transmittance, but also a substantial proportion of the THz signal is lost with evasion of detection (marked with the grey cross).

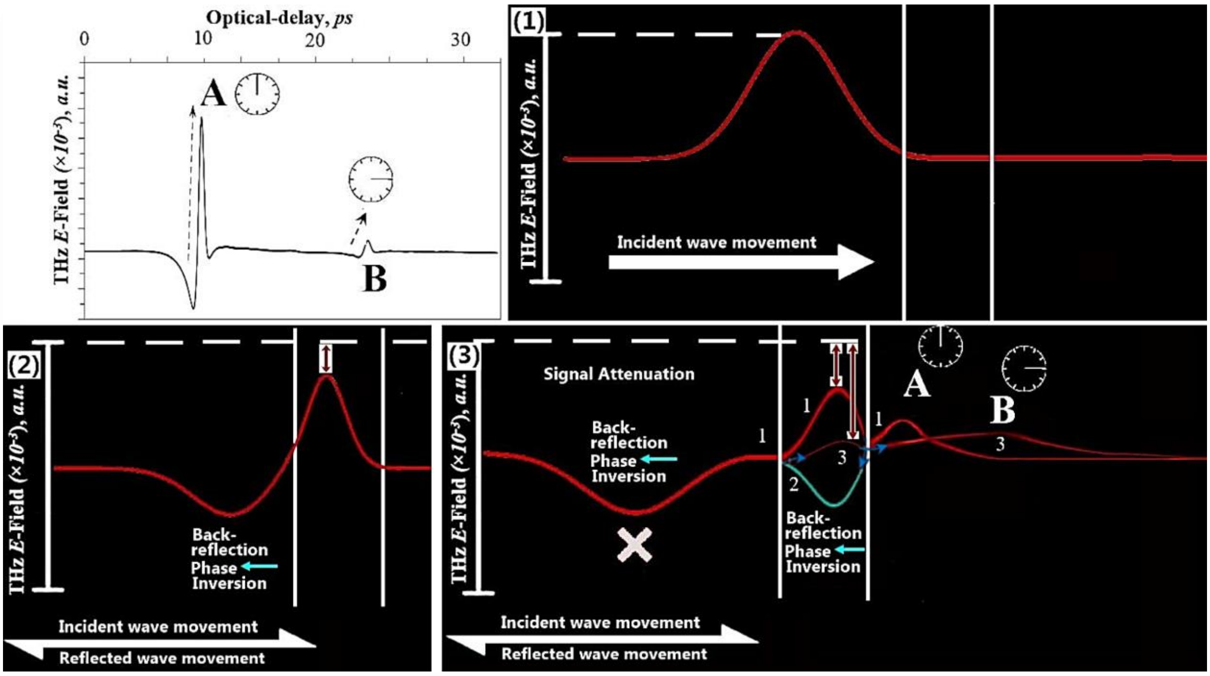

***Figure 112*: A typical transmission pulse (featuring silica). The top image labelled 'A' and 'B' and time symbols correspond to the sequential waves sketched 1, 2 and 3.**

Reflection imaging

Minimal signal attenuation is observed in *Figure 113* following near complete reflection form the mirror. To give similar waveform magnitudes in the ± regions to a baseline time denoted '*A*'. Although OD is normalised to *0 ps* the path-length of the THz signal is consequently much longer than witnessed in transmission methods.

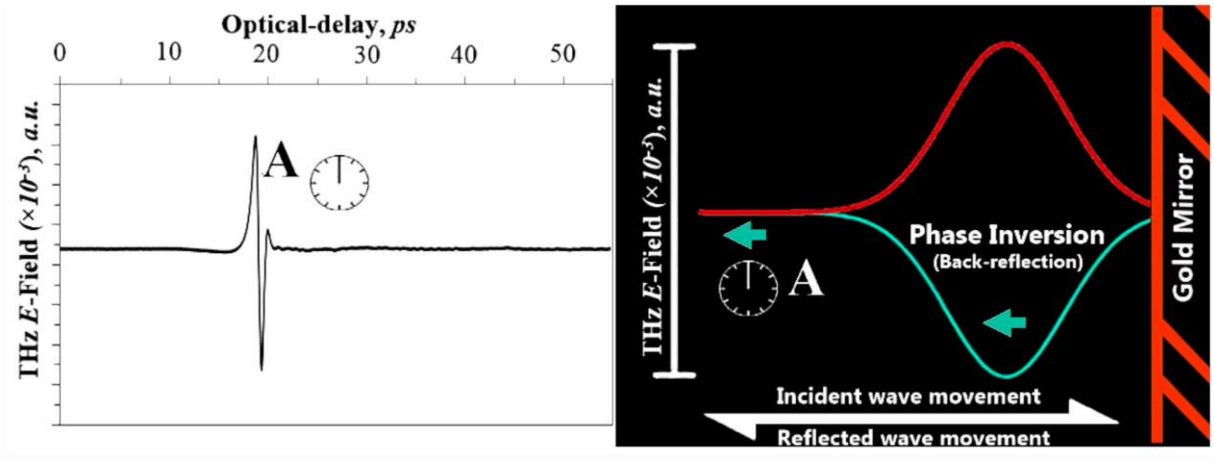

***Figure 113*: Representation of signal phase inversion point in reflection imaging. The red wave signifies the probe-beam (source) and the blue wave corresponds to the reflected 180º inverted signal returning from a specular gold plated polished mirror. In the situation of reflection from the first and second boundaries of a substrate, the *E-Field* again simply turns around as the wave arrives at the first interface, giving an inverted phase shift of 180º degree flip (see *Figure 114; 15-22 ps* and *bottom 'A'*). The first inverted reflection has a decreased amplitude/magnitude because a proportion of the light propagates into the slide (s*ee Figure 114; Δ B-A*). At the second boundary full inversion occurs again and the amplitude/magnitude is attenuated further, and detection is optically-delayed (labelled '*B*' and clock).**

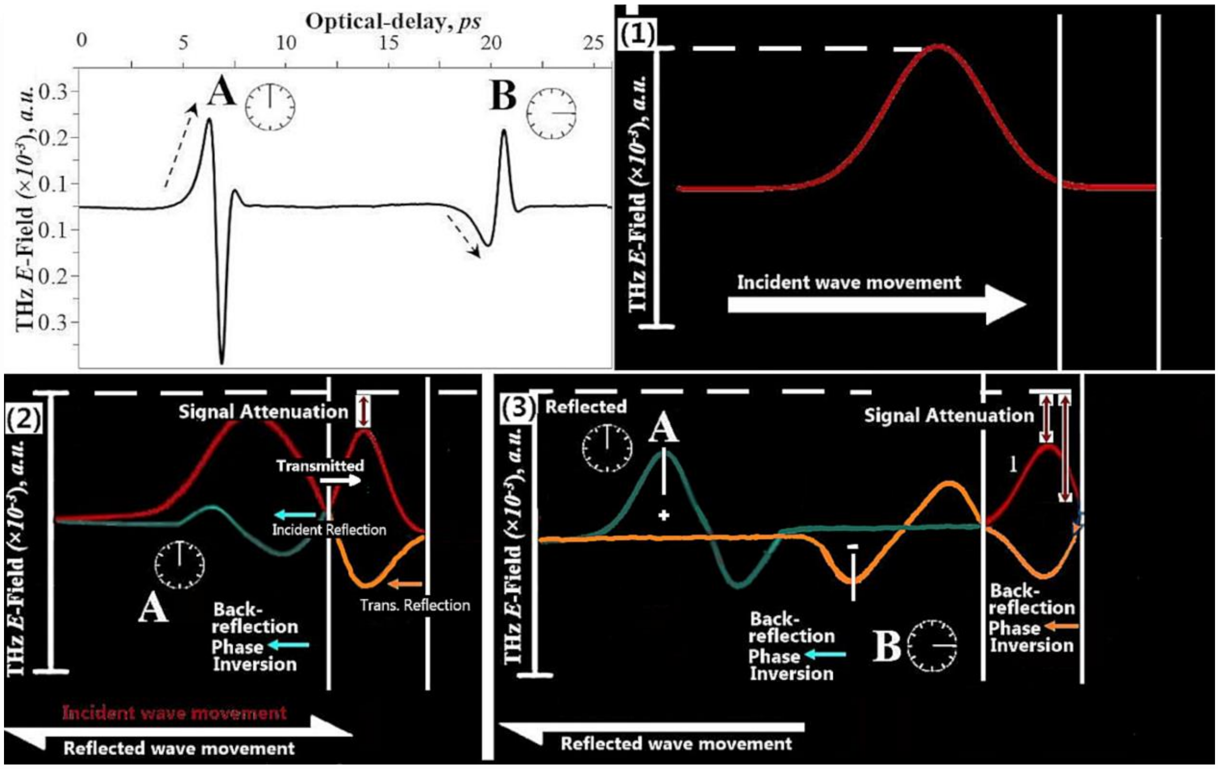

***Figure 114:* Representation of signal phase inversion points in reflection imaging with a silica substrate. The white wave signifies the source wave and the black waves correspond to reflected waves from the vertical representations of the substrate, with the grey second line representing the rear surface.**

10.2.1 Focal issues of TPI

THz radiation produced by the TPS-3000 is broadband, thus a distribution of light frequencies and subsequently, Δ index of refractive (function of λ) causes degrees of defocusing of the probe-beam imaging three dimensional structures of significant width/RI (*see Figure 115*).

The effects of light diffraction and echoes within the internal structure may account for temporal based discrepancies. For instance, images witnessed at a depth indicated at '*x*' *ps* may report peak-broadening and marginal inaccuracy if time-delay measures are crucial c. Non-specular nature of some materials can add further issues of imprecise imaging of the rear internal surface as an effect of light diffraction prior to interacting with either the anterior or posterior substrate interface.

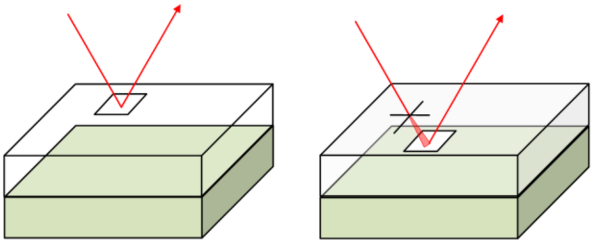

Figure 115: **During TPI. Substrates are typically positioned to give a focal plane representative of the anterior interface. Pictured is a demonstration that reflections for an artefact or posterior are consequently out of focus.**

10.2.2 Further conditions for good TPI derived RI's

Table 45: **Further conditions necessary for accurate prediction of RI using Fresnel's reflection amplitude coefficient.**

i. Flat and parallel surfaces of glass slides and no scattering
The substrate slides are considered as smooth and planar with no appreciable surface roughness. Subsequently, specular light diffusion is expected.
ii. Substrate homogeneity
The substrate slides are considered as smooth and planar with no appreciable surface roughness. Subsequently, specular light diffusion is expected. Each slide was equally homogenous in regard to physical thickness (as determined by multiple micrometer readings) and also in regard to chemical uniformity. The spatial positioning of network modifiers within two of the substrates is believed to be consistent.
iii. Dry atmosphere
The substrates are analysed on a gantry seated ~5 mm above the sample chamber. The passage of N_2 flows from the base of the exposed sample chamber (containing the additional module of OAP mirrors) to escape the system, predominately from the gap beneath the gantry and the chamber; because the density of nitrogen is ~3% less than air. The flow rate was therefore increased to 30

l/min (from 20 as used in sealed transmission studies) in order to compensate for the moisture present in the air from significantly effecting the THz pulse. It is also noted that the presence of moisture is of lesser detriment to waveform profiles (reflection resonance studies) than with spectrum analysis, where absorption peaks for water are observable.

10.3 Experimental chapter 2 data tables

Tablet design specifications and numerical results.

***Table 46*: Variable density MCC tablets.**

Summary of physical specifications		OD-derived RI's	
Mean Thk^n	Density, *ρ*	Signal-delay, *ps*	
n = 10	*mg/mm^3*	E^{max}-field OD, *ps*	RI's ‡
Reference	~ 0	311.5	-
4.62 (± 0.005)	0.586 (± 0.000)	316.6	1.330 (± 0.000)
4.62 (± 0.005)	0.660 (± 0.001)	317.3	1.373 (± 0.000)
4.62 (± 0.005)	0.691 (± 0.001)	317.4	1.383 (± 0.000)
4.62 (± 0.005)	0.712 (± 0.001)	317.7	1.399 (± 0.000)
4.61 (± 0.005)	0.758 (± 0.001)	318.1	1.425 (± 0.000)
4.62 (± 0.005)	0.786 (± 0.001)	318.3	1.439 (± 0.000)
4.63 (± 0.005)	0.817 (± 0.002)	318.5	1.456 (± 0.000)
4.62 (± 0.005)	0.857 (± 0.002)	318.9	1.481 (± 0.001)
4.64 (± 0.005)	0.894 (± 0.002)	319.3	1.504 (± 0.001)
4.65 (± 0.005)	0.927 (± 0.002)	319.5	1.517 (± 0.001)

‡Error margins are included for possible incorrect thickness deduction made with the callipers.

***Table 47*: Fixed mass**

Summary of physical spec's		**OD-derived RI's**				
Mean *Thk^n*	Density, *ρ*,	Signal-delay, *ps*		Internal-delay, *ps*		Combined RI's
n = 10	*mg/mm^3*	Δ E^{max}-field OD (with reference peak), *ps*	Thk^n/OD RI's	(2nd) E^{max}-field OD, *ps*	Thk^n/OD RI's	½ × SD+ID RI
Reference	~ 0					
1.10 (± 0.005)	0.995	2.097	1.572	11.573	1.577 (± 0.007)	1.574 (± 0.007)
1.12 (± 0.005)	0.983	2.107	1.564	11.532	1.543 (± 0.007)	1.544 (± 0.007)
1.15 (± 0.005)	0.958	2.077	1.541	11.615	1.514 (± 0.007)	1.528 (± 0.007)
1.15 (± 0.005)	0.951	2.077	1.541	11.635	1.517 (± 0.007)	1.529 (± 0.007)
1.16 (± 0.005)	0.952	2.140	1.533	11.759	1.520 (± 0.007)	1.536 (± 0.007)
1.19 (± 0.005)	0.922	2.073	1.522	11.718	1.476 (± 0.006)	1.499 (± 0.006)
1.22 (± 0.005)	0.905	2.150	1.528	12.461	1.531 (± 0.006)	1.530 (± 0.006)
1.21 (± 0.005)	0.915	2.153	1.533	12.482	1.546 (± 0.006)	1.540 (± 0.006)
1.24 (± 0.005)	0.886	2.140	1.517	12.728	1.514 (± 0.006)	1.513 (± 0.006)
1.26 (± 0.005)	0.869	2.150	1.512	12.728	1.514 (± 0.006)	1.513 (± 0.006)
1.33 (± 0.005)	0.823	2.090	1.471	12.791	1.442 (± 0.005)	1.456 (± 0.005)
1.35 (± 0.005)	0.811	2.063	1.458	12.894	1.432 (± 0.005)	1.445 (± 0.005)
1.37 (± 0.005)	0.799	2.080	1.439	13.678	1.444 (± 0.005)	1.441 (± 0.005)
1.42 (± 0.005)	0.777	2.057	1.408	13.904	1.380 (± 0.005)	1.394 (± 0.005)
1.51 (± 0.005)	0.728	2.071	1.408	14.255	1.406 (± 0.005)	1.410 (± 0.005)

***Table 48:* Fixed fill-weight MCC tablet specifications and results.**

Specification of physical characteristics		r_p and RI results	
Mean Thk^n, *mm*; n = 10	Density, *mg/mm^3*	r_p	RI
1.10 (± 0.005)	0.995 (±0.005)	0.2221	1.571
1.12 (± 0.005)	0.983 (±0.005)	0.2166	1.553
1.15 (± 0.005)	0.958 (±0.005)	0.2020	1.506
1.15 (± 0.005)	0.951 (±0.005)	0.2015	1.505
1.16 (± 0.005)	0.952 (±0.005)	0.2040	1.513

1.19 (± 0.005)	0.922 (±0.005)	0.2049	1.516
1.22 (± 0.005)	0.905 (±0.005)	0.2068	1.522
1.21 (± 0.005)	0.915 (±0.004)	0.1985	1.495
1.24 (± 0.005)	0.886 (±0.004)	0.1954	1.486
1.26 (± 0.005)	0.869 (±0.004)	0.1901	1.470
1.33 (± 0.005)	0.823 (±0.004)	0.1911	1.473
1.35 (± 0.005)	0.811 (±0.004)	0.1824	1.446
1.37 (± 0.005)	0.799 (±0.004)	0.1877	1.462
1.42 (± 0.005)	0.777 (±0.003)	0.1688	1.406
1.51 (± 0.005)	0.728 (±0.003)	0.1682	1.405
1.52 (± 0.005)	0.724 (±0.003)	0.1691	1.407
Empty system	~ 0	0.7845	

The effect of fill-weight to comparable thicknesses of ten MCC compacts (and thus ~ equal volume) was measured by spectral FDT-RI analysis in *Table 49*.

Table 49: **Summary and RI results (by FDT-FFT analysis) of variable density tablets of MCC.**

Physical characteristics					Mean RI between 0.75 – 1.25 THz	RI range as a product of micrometer sensitivity and high-low fluctuation within the frequency band.
Compaction Load, *kg*	Fill-weight, *mg*	Thk^n, *mm*	Volume, *mm^3*	Density, *ρ*, *g/cm^3*		
77.6 (± 0.05)	359.1	4.62 (± 0.005)	613.2 (± 0.005)	0.586 (± 0.000)	1.316	± 0.002
138.9 (± 0.05)	404.9	4.62 (± 0.005)	613.2 (± 0.005)	0.660 (± 0.001)	1.350	± 0.003
190.2 (± 0.05)	424.0	4.62 (± 0.005)	613.2 (± 0.005)	0.691 (± 0.001)	1.366	± 0.003
203.0 (± 0.05)	436.3	4.62 (± 0.005)	613.2 (± 0.005)	0.712 (± 0.001)	1.379	± 0.003
264.7 (± 0.05)	463.6	4.61 (± 0.005)	611.9 (± 0.005)	0.758 (± 0.001)	1.407	± 0.004
312.9 (± 0.05)	482.1	4.62 (± 0.005)	613.2 (± 0.005)	0.786 (± 0.001)	1.419	± 0.004
349.7 (± 0.05)	502.0	4.63 (± 0.005)	614.6 (± 0.005)	0.817 (± 0.001)	1.435	± 0.004
420.9 (± 0.05)	525.4	4.62 (± 0.005)	613.2 (± 0.005)	0.857 (± 0.001)	1.458	± 0.005
462.8 (± 0.05)	550.3	4.64 (± 0.005)	615.9 (± 0.005)	0.894 (± 0.001)	1.480	± 0.005
497.1 (± 0.05)	572.0	4.65 (± 0.005)	617.2 (± 0.005)	0.927 (± 0.001)	1.494	± 0.005

Table 50: **Summary of tablet specifications**

Summary of physical specifications				
Compaction Load, *kg*	Fill weight, *mg*	Mean Thk^n, *mm*	Volume, *mm^3*	Density, *ρ*, *mg/mm^3*
77.6 (± 0.05)	359.1	4.62 (± 0.005)	613.2 (± 1.14)	0.586 (± 0.001)
138.9 (± 0.05)	404.9	4.62 (± 0.005)	613.2 (± 1.14)	0.660 (± 0.001)
190.2 (± 0.05)	424.0	4.62 (± 0.005)	613.2 (± 1.14)	0.691 (± 0.001)
203.0 (± 0.05)	436.3	4.62 (± 0.005)	613.2 (± 1.14)	0.712 (± 0.001)
264.7 (± 0.05)	463.6	4.61 (± 0.005)	611.9 (± 1.13)	0.758 (± 0.001)
312.9 (± 0.05)	482.1	4.62 (± 0.005)	613.2 (± 1.14)	0.786 (± 0.001)
349.7 (± 0.05)	502.0	4.63 (± 0.005)	614.6 (± 1.14)	0.817 (± 0.002)
420.9 (± 0.05)	525.4	4.62 (± 0.005)	613.2 (± 1.14)	0.857 (± 0.002)
462.8 (± 0.05)	550.3	4.64 (± 0.005)	615.9 (± 1.14)	0.894 (± 0.002)
497.1 (± 0.05)	572.0	4.65 (± 0.005)	617.2 (± 1.14)	0.927 (± 0.002)

Table 51: **Results of fixed physical thickness**

FFT		TDT (SD)		FFT & TDT-SD RMSE %	TPI	FDT & TPI RMSE%
Mean RI (0.75 – 1.25 THz)	RI range *, **	Mean RI	RI range **		Mean RI	
1.316	± 0.002	1.330	(± 0.000)	0.020%	1.271	0.203%
1.350	± 0.003	1.373	(± 0.000)	0.053%	1.325	0.063%
1.366	± 0.003	1.383	(± 0.000)	0.029%	1.338	0.078%

1.379	± 0.003	1.399	(± 0.000)	0.040%	1.351	0.078%
1.407	± 0.004	1.425	(± 0.000)	0.032%	1.376	0.096%
1.419	± 0.004	1.439	(± 0.000)	0.040%	1.396	0.053%
1.435	± 0.004	1.456	(± 0.000)	0.044%	1.407	0.078%
1.458	± 0.005	1.481	(± 0.000)	0.053%	1.433	0.062%
1.480	± 0.005	1.504	(± 0.001)	0.058%	1.442	0.144%
1.494	± 0.005	1.517	(± 0.001)	0.053%	1.463	0.096%
			Total:	2.05%	Total:	3.09%

* As a product high-low fluctuation within the frequency band.

**As a product of micrometre sensitivity.

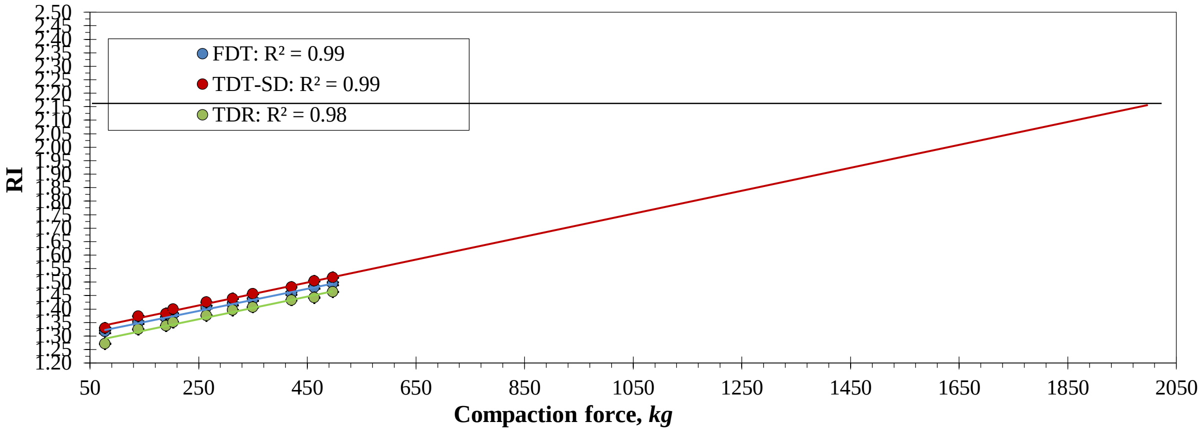

Figure 116: **A plot of the three RI determination methods for Avicel® (PH-101) tablets manufactured under increasing compaction forces.**

Table 52: **Summary of fixed mass MCC tablets.**

Summary of physical specifications					
Compaction Load, *kg*	Fill-weight, *mg*	Thk^n, *mm*	Diameter, *mm*	Volume, *mm^3*	Density, *ρ*, *mg/mm^3*
486.4 (± 0.05)	145.3	1.10 (± 0.005)	13.0 (± 0.005)	146.0 (± 1.289)	0.995 (± 0.003)
479.2 (± 0.05)	146.2	1.12 (± 0.005)	13.0 (± 0.005)	148.7 (± 1.285)	0.983 (± 0.005)
474.4 (± 0.05)	146.2	1.15 (± 0.005)	13.0 (± 0.005)	152.6 (± 1.280)	0.958 (± 0.003)
465.3 (± 0.05)	145.1	1.15 (± 0.005)	13.0 (± 0.005)	152.6 (± 1.280)	0.951 (± 0.004)
453.1 (± 0.05)	146.6	1.16 (± 0.005)	13.0 (± 0.005)	154.0 (± 1.279)	0.952 (± 0.005)
439.8 (± 0.05)	145.7	1.19 (± 0.005)	13.0 (± 0.005)	158.0 (± 1.274)	0.922 (± 0.005)
399.0 (± 0.05)	146.6	1.22 (± 0.005)	13.0 (± 0.005)	161.9 (± 1.269)	0.905 (± 0.004)
382.8 (± 0.05)	147.0	1.21 (± 0.005)	13.0 (± 0.005)	160.6 (± 1.270)	0.915 (± 0.005)
341.9 (± 0.05)	145.8	1.24 (± 0.005)	13.0 (± 0.005)	164.6 (± 1.265)	0.886 (± 0.004)
315.1 (± 0.05)	145.4	1.26 (± 0.005)	13.0 (± 0.005)	167.2 (± 1.262)	0.869 (± 0.004)
290.0 (± 0.05)	145.3	1.33 (± 0.005)	13.0 (± 0.005)	176.5 (± 1.251)	0.823 (± 0.004)
268.2 (± 0.05)	145.4	1.35 (± 0.005)	13.0 (± 0.005)	179.2 (± 1.248)	0.811 (± 0.004)
248.6 (± 0.05)	145.3	1.37 (± 0.005)	13.0 (± 0.005)	181.8 (± 1.244)	0.799 (± 0.003)
214.9 (± 0.05)	146.5	1.42 (± 0.005)	13.0 (± 0.005)	188.5 (± 1.237)	0.777 (± 0.004)
194.3 (± 0.05)	146.0	1.51 (± 0.005)	13.0 (± 0.005)	200.4 (± 1.223)	0.728 (± 0.004)
175.0 (± 0.05)	146.1	1.52 (± 0.005)	13.0 (± 0.005)	201.8 (± 1.221)	0.724 (± 0.003)

Table 53: **Results of fixed mass.**

FFT		TDT SD			TDT ID			TDT ID + SD			TPI	
Mean RI	RI range	RI	RI	FFT & TDT-SD	RI (ID)	RI	FFT & TDT-ID	Combined RI	RI	FFT & TDT-(ID+SD)	RI	FFT & TPI
0.75–1.25 THz	*,**	Mean	Range **	RMSE %	Mean	Range **	RMSE %	Mean	Range **	RMSE %	Mean	RMSE %
1.554	± 0.003	1.572	± 0.003	0.032%	1.577	± 0.007	0.053%	1.574	± 0.010	0.040%	1.571	0.029%
1.545	± 0.005	1.564	± 0.004	0.036%	1.543	± 0.007	0.000%	1.544	± 0.009	0.000%	1.553	0.006%
1.524	± 0.003	1.541	± 0.002	0.029%	1.514	± 0.007	0.010%	1.528	± 0.009	0.002%	1.506	0.032%
1.525	± 0.004	1.541	± 0.002	0.026%	1.517	± 0.007	0.006%	1.529	± 0.005	0.002%	1.505	0.040%
1.537	± 0.005	1.533	± 0.005	0.002%	1.520	± 0.007	0.029%	1.536	± 0.011	0.000%	1.513	0.058%
1.504	± 0.005	1.522	± 0.002	0.032%	1.476	± 0.006	0.078%	1.499	± 0.008	0.002%	1.516	0.014%
1.509	± 0.004	1.528	± 0.004	0.036%	1.531	± 0.006	0.048%	1.530	± 0.009	0.044%	1.522	0.017%
1.517	± 0.004	1.533	± 0.002	0.026%	1.546	± 0.006	0.084%	1.540	± 0.008	0.053%	1.495	0.048%
1.499	± 0.004	1.517	± 0.004	0.032%	1.514	± 0.006	0.022%	1.513	± 0.008	0.020%	1.486	0.017%
1.495	± 0.004	1.512	± 0.002	0.029%	1.514	± 0.006	0.036%	1.513	± 0.008	0.032%	1.470	0.063%
1.453	± 0.003	1.471	± 0.002	0.032%	1.442	± 0.005	0.012%	1.456	± 0.007	0.001%	1.473	0.040%
1.445	± 0.004	1.458	± 0.003	0.017%	1.432	± 0.005	0.017%	1.445	± 0.007	0.000%	1.446	0.000%
1.435	± 0.003	1.439	± 0.002	0.002%	1.444	± 0.005	0.008%	1.441	± 0.007	0.004%	1.462	0.073%
1.424	± 0.004	1.408	± 0.002	0.026%	1.380	± 0.005	0.194%	1.394	± 0.006	0.090%	1.406	0.032%
1.394	± 0.004	1.408	± 0.001	0.020%	1.406	± 0.005	0.014%	1.410	± 0.006	0.026%	1.405	0.012%
1.396	± 0.003	1.572	± 0.003	3.098%	1.577	± 0.007	3.276%	1.574	± 0.010	3.168%	1.407	0.012%
			Total	1.67%		Total	1.92%		Total	1.40%	Total	1.80%

* As a product high-low fluctuation within the frequency band.

** As a product of micrometre sensitivity.

10.4 Experimental Chapter 4 data

Table 54: **BMS wafer specifications, mathematical corrections used and relative *err*.in regard to FD vs TPI.**

ID/SF		***Thickness recording (caliper)***	***Geometric Density, (range)***	***FDT Benchmark bulk RI***	***Internal Transmitted angle***	***Thickness Correction factor***	***TPI Predicted surface RI***	***Relative Error, (THz FD-RI vs TPI)***
%		***mm***	***mg/mm^3***	***$\bar{x}$ 0.75-1.25 THz***	***θ_t°***	***Cos θ_t°***	***-***	***%***
ab	63 %	2.31 (± 0.005) *mm*	0.931 (± 0.002) *mm*	*1.542*	*18.920°*	0.946	1.538	**0.40 %**
cd	83 %	2.24 (± 0.005) *mm*	1.29, (± 0.003) *mm*	*1.743*	*16.670°*	0.958	1.741	**0.20 %**
ef	90 %	*2.27* (± 0.005) *mm*	1.361 (± 0.003) *mm*	*1.788*	*16.239°*	0.960	1.784	**0.40 %**

Table 55: **BMS wafer specifications, mathematical corrections used and relative errors in regard to FD vs reflectance (RI) and then thickness approximation.**

ID/SF		*FDT Benchmark bulk RI*	*TPI Predicted surface RI*	*Internal Transmitted angle*	*Thickness Correction factor*	*c_0*	*E^{MAX}1-field*	*E^{MAX}2-field*	*Caliper Thickness*	*Predicted thickness*	***Relative Error***
%		*$\bar{x}$ 0.75-1.25 THz*	*-*	*θ_t°*	*Cos θ_t°*	*m/s*	*ps*	*ps*	*mm*	$\left({}^{1}/_{2} \times \left(\frac{c_0}{RI_t^{\circ}}\right) \times \left(OD \times Cos\theta_t^{\circ}\right)\right)/10^8$	***%***
ab	**63 %**	**1.542**	**1.538**	***18.920°***	**0.946**	**$2.997{\times}10^8$**	**3.714 *ps***	**28.540 *ps***	**2.31 (± *0.005*) *mm***	**2.28 *mm***	**1.30 (0.43) *%***
cd	**83 %**	**1.743**	**1.741**	***16.670°***	**0.958**	**$2.997{\times}10^8$**	**1.044 *ps***	**28.433 *ps***	**2.24 (± *0.005*) *mm***	**2.26 *mm***	**-0.89 (0.45) *%***
ef	**90 %**	**1.788**	**1.784**	***16.239°***	**0.960**	**$2.997{\times}10^8$**	**1.020 *ps***	**29.532 *ps***	**2.27 (± *0.005*) *mm***	**2.29 *mm***	**-0.88 (0.44) *%***

10.4.1 Instrument specifications.

Table 56: **Operating specifications of the AW WP-120.**

Parameter	**Range**	**Unit/Description**
Throughput	8-40 [157]	*Kg/h*
Force or torque of the rolls:	0.3– 21.3 [157]	*kN/cm*
Roll-speed	2-60	*RPM*
Roll-gap	0.2-5	*mm*
Roll-wheel: Diameter and width	Ø; 120 (40)	*mm*
Feed auger (horizontal/single screw feed)	unknown	*RPM*
Cheek Plates	(Side) External of rolls	Steel
Roll design	Interchangeable	Smooth or Lattice
Additional Information		
Vacuum de-aeration?	Yes	
Granulator stage:	2 stage oscillating mill. Adjustable screen distance to mill/aperture size.	
Number of moving rolls	1	

Table 57**: Operational details of the Gerteis PolyGran.**

Parameter	**Range**	**Unit/Description**
Throughput	0.5-200	*Kg/h*
Force or torque of the rolls:	1 – 15	*kN/cm*
Roll-speed	1-30	*RPM*
Roll-gap	2-5	*mm*
Roll-wheel: Diameter and width	Ø 150; (30)	*mm*
Feed auger (diagonal/single axle screw feed)	0-2000	*RPM*
Cheek Plates	(Side) External of both rolls	Pyrex composite
Roll-wheel design	Interchangeable	Smooth or Lattice
Additional Information		
Vacuum de-aeration?	Yes	
Granulator stage:	Oscillating mill. Adjustable screen distance to mill/aperture size.	
Number of moving rolls	1	

Table 58: **Operational details of the Gerteis Macro-Pactor.**

Parameter	**Range**	**Unit/description**
Throughput	0.1 – 400	*Kg/h*
Force or torque of the rolls:	1 – 20	*kN/cm*
Roll-speed	1 – 30	*RPM*
Roll-gap	1 – 6	*mm*
Roll-wheel: Diameter and width	Ø 250; (100)	*mm*
Feed auger (diagonal/single screw feed)	0-2000	*RPM*
Cheek plates	(Side), overlapping ring attached to 1 roll	Steel
Roll design	Interchangeable	Smooth or Lattice
Additional Information		
Vacuum de-aeration?	Yes	
Granulator stage:	Oscillating mill. Adjustable screen distance to mill/aperture size.	
Number of moving rolls	1	

10.4.2 Eliminating lattice protrusions.

The raised lattice effect of knurling was removed and subsequently the samples can be measured with a calliper to ensure equal lateral and longitudinal thickness, using light abrasive forces involving level alignment of the wafer in a vice and applying minimal sanding with a high grain (*grain/cm*^{2}, *2400*) paper.

Table 59: **Methods to eliminate knurl/lattice protruisons**

In simply measuring RI of the compact, placement of the smooth face to the optics assembly during TPI analysis is a simple solution.
To evaluate the thickness as a secondary step (e.g. optical-delay) following RI prediction, 1 ribbon or wafer substrate was sacrificed in order to be braced level in a vice and lightly sanded with 2400 grain grit-paper to both achieve a near specular surface (i.e. greater distinguishment), and of consistent lateral and longitudinal dimensions. This allows variable SF ribbons to be accurately compared.
Alternatively, selective OD data analysis can be carried out with placement of mercury onto the upper latticed surface during spot imaging to act as a highly effective and strongly contrasting medium to highlight the internal surface. The technique was very effective yet, naturally required additional and timely preparation.
The reference mirror was balanced on top ribbons or wafers for similar magnification of the surface.

10.5 Conference participation.

10.5.1 Abstract for APS September 2010

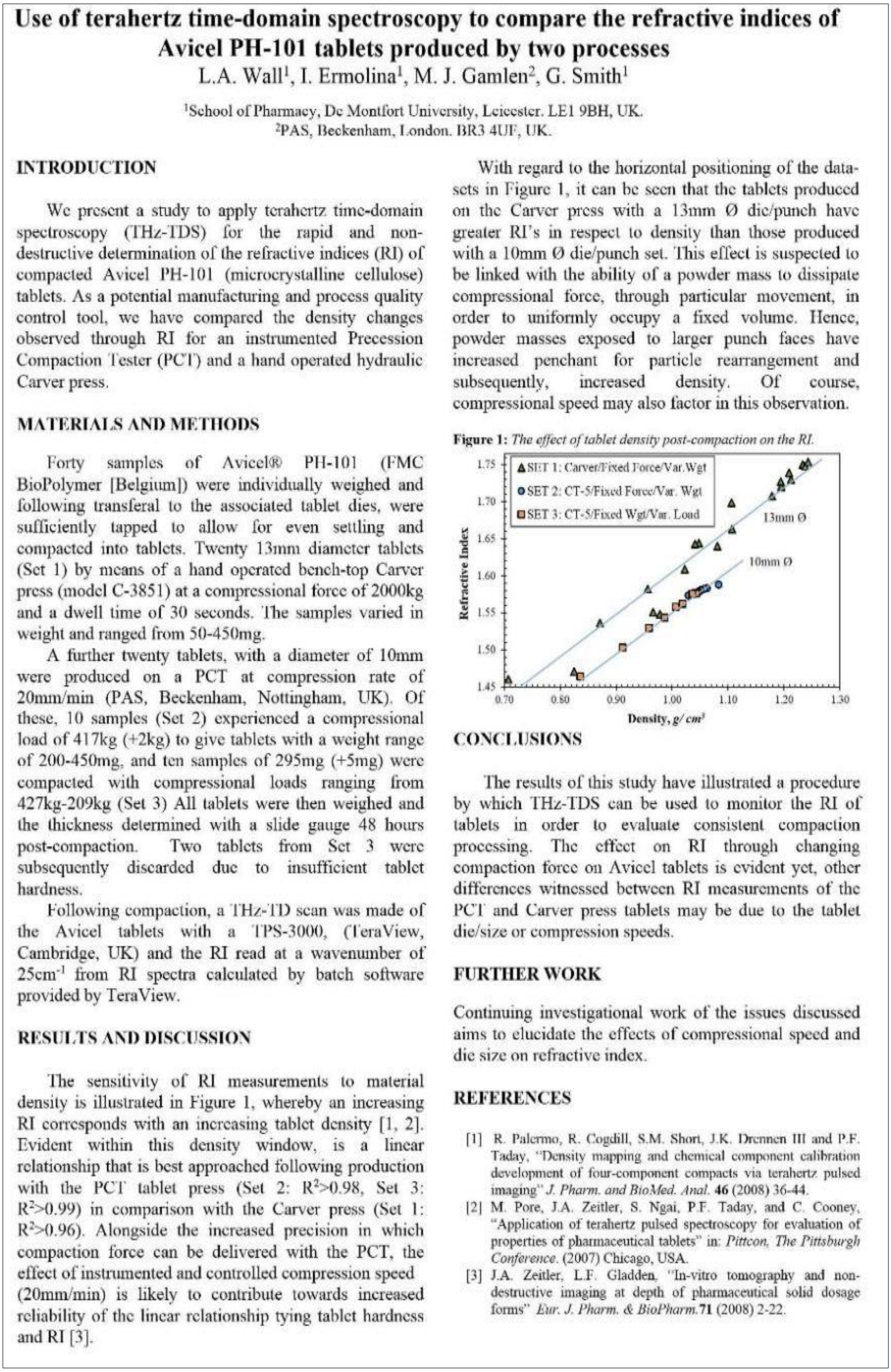

Use of terahertz time-domain spectroscopy to compare the refractive indices of Avicel PH-101 tablets produced by two processes

L.A. Wall[1], I. Ermolina[1], M. J. Gamlen[2], G. Smith[1]

[1]School of Pharmacy, De Montfort University, Leicester. LE1 9BH, UK.
[2]PAS, Beckenham, London. BR3 4UF, UK.

INTRODUCTION

We present a study to apply terahertz time-domain spectroscopy (THz-TDS) for the rapid and non-destructive determination of the refractive indices (RI) of compacted Avicel PH-101 (microcrystalline cellulose) tablets. As a potential manufacturing and process quality control tool, we have compared the density changes observed through RI for an instrumented Precession Compaction Tester (PCT) and a hand operated hydraulic Carver press.

MATERIALS AND METHODS

Forty samples of Avicel® PH-101 (FMC BioPolymer [Belgium]) were individually weighed and following transferal to the associated tablet dies, were sufficiently tapped to allow for even settling and compacted into tablets. Twenty 13mm diameter tablets (Set 1) by means of a hand operated bench-top Carver press (model C-3851) at a compressional force of 2000kg and a dwell time of 30 seconds. The samples varied in weight and ranged from 50-450mg.

A further twenty tablets, with a diameter of 10mm were produced on a PCT at compression rate of 20mm/min (PAS, Beckenham, Nottingham, UK). Of these, 10 samples (Set 2) experienced a compressional load of 417kg (+2kg) to give tablets with a weight range of 200-450mg, and ten samples of 295mg (+5mg) were compacted with compressional loads ranging from 427kg-209kg (Set 3) All tablets were then weighed and the thickness determined with a slide gauge 48 hours post-compaction. Two tablets from Set 3 were subsequently discarded due to insufficient tablet hardness.

Following compaction, a THz-TD scan was made of the Avicel tablets with a TPS-3000, (TeraView, Cambridge, UK) and the RI read at a wavenumber of 25cm^{-1} from RI spectra calculated by batch software provided by TeraView.

RESULTS AND DISCUSSION

The sensitivity of RI measurements to material density is illustrated in Figure 1, whereby an increasing RI corresponds with an increasing tablet density [1, 2]. Evident within this density window, is a linear relationship that is best approached following production with the PCT tablet press (Set 2: $R^2>0.98$, Set 3: $R^2>0.99$) in comparison with the Carver press (Set 1: $R^2>0.96$). Alongside the increased precision in which compaction force can be delivered with the PCT, the effect of instrumented and controlled compression speed (20mm/min) is likely to contribute towards increased reliability of the linear relationship tying tablet hardness and RI [3].

With regard to the horizontal positioning of the data-sets in Figure 1, it can be seen that the tablets produced on the Carver press with a 13mm Ø die/punch have greater RI's in respect to density than those produced with a 10mm Ø die/punch set. This effect is suspected to be linked with the ability of a powder mass to dissipate compressional force, through particular movement, in order to uniformly occupy a fixed volume. Hence, powder masses exposed to larger punch faces have increased penchant for particle rearrangement and subsequently, increased density. Of course, compressional speed may also factor in this observation.

Figure 1: *The effect of tablet density post-compaction on the RI.*

CONCLUSIONS

The results of this study have illustrated a procedure by which THz-TDS can be used to monitor the RI of tablets in order to evaluate consistent compaction processing. The effect on RI through changing compaction force on Avicel tablets is evident yet, other differences witnessed between RI measurements of the PCT and Carver press tablets may be due to the tablet die/size or compression speeds.

FURTHER WORK

Continuing investigational work of the issues discussed aims to elucidate the effects of compressional speed and die size on refractive index.

REFERENCES

[1] R. Palermo, R. Cogdill, S.M. Short, J.K. Drennen III and P.F. Taday, "Density mapping and chemical component calibration development of four-component compacts via terahertz pulsed imaging" *J. Pharm. and BioMed. Anal.* **46** (2008) 36-44.

[2] M. Pore, J.A. Zeitler, S. Ngai, P.F. Taday, and C. Cooney, "Application of terahertz pulsed spectroscopy for evaluation of properties of pharmaceutical tablets" in: *Pittcon, The Pittsburgh Conference.* (2007) Chicago, USA.

[3] J.A. Zeitler, L.F. Gladden, "In-vitro tomography and non-destructive imaging at depth of pharmaceutical solid dosage forms" *Eur. J. Pharm. & BioPharm.* **71** (2008) 2-22.

10.5.2 Poster presented for APS September 2010

Use of terahertz time-domain spectroscopy to correlate refractive index and hardness for Avicel PH-101 tablets

dmu.ac.uk
DE MONTFORT UNIVERSITY
LEICESTER

L.A. Wall[1], I. Ermolina[1], M. J. Gamlen[2], G. Smith[1]
[1]Leicester School of Pharmacy, De Montfort University, Leicester. LE1 9BH, UK.
[2]PAS, Beckenham, London. BR3

INTRODUCTION

The use of dry granulation during the tablet manufacturing process has recently drawn much attention in the strive to implement continuous processing through the use of roller compaction. Yet, this technique is not without its problems. This study aims to demonstrate RI as a surrogate measurement for hardness and consequently the potential use of terahertz pulsed time-domain spectroscopy (TP-TDS) following QbD principles as an in-line process control method.

The study has applied TP-TDS for the rapid and non-destructive determination of refractive indices (RI) of compacted Avicel® PH-101 tablets. A precision compaction tester (PCT tablet press) was used to produce fixed weight tablets under various compressional forces and another set under fixed compressional forces with variable masses. Following RI determination using TP-TDS, tablet thickness and geometric densities were deduced and used to correlate hardness and density with RI.

MATERIALS AND METHODS

Samples of Avicel® PH-101 (FMC BioPolymer, Belgium) were weighed, sufficiently tapped and compacted into 10mm diameter tablets at a rate of 20 mm/min on the PCT tablet press (PAS, Beckenham, UK).

Table 1: ***Schedule of production***

Batch		Load Force	Fill Weight	n
1.	△	320kg ±1kg	150-375mg	9
2.	▲	420kg ±2kg	195-395 mg	9
3.	🟠	83-427kg	295mg ±5mg	8
4.	🔵	113-456kg	200mg ±2mg	11

All tablets were weighed and thickness determined using a slide gauge 48 hours post-compaction.

Following thickness determination, TP-TDS scans were made of the Avicel tablets with a TPS-3000 (TeraView, Cambridge, UK), and RI read at a wavenumber of 25cm^{-1} from RI spectra calculated by the manufacturers batch software. Finally, the four batches of tablets were tested for hardness with use of a PharmaTest PTB 311E, crushing the tablets diametrically.

RESULTS AND DISCUSSION

Given a greater compressional force, displacement of intra-particulate-voids results in a more densely packed structure within tablets of a fixed fill weight (Fig. 1).

At a constant compressional force with ↑ fill-weight, density maybe expected to remain equal, yet a slight reduction of density with ↑ thickness is indicated in Fig. 1 (△).

This observation indicates an effect of resistive response to pressure as the powder mass becomes more massive.

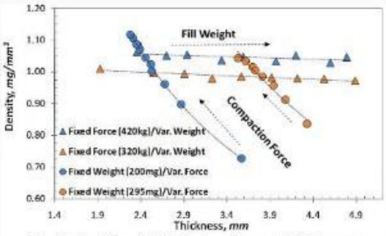

Fig. 1: ***Profile of tablet density and thickness***

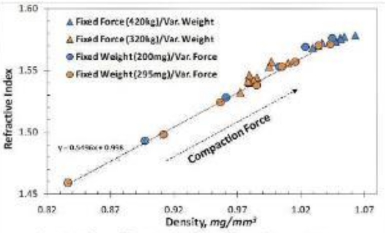

Fig. 2: ***The effect of tablet density on RI***

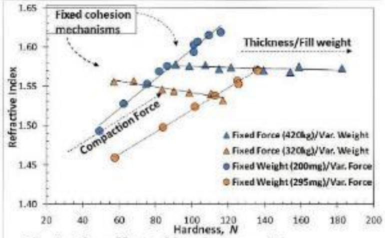

Fig. 3: ***The effect of hardness on RI***

The sensitivity of RI measurements to material density is illustrated in Figure 2, whereby an increasing RI corresponds with an increasing density in an apparent linear response over this scale [1]. As discussed, tablet density represents the material to air fraction within the packing structure and regression analysis of the fixed weight 295mg tablets 🟠($R^2>0.99$) predicts an RI approaching 1 (R.I. air ≈ 1) when density approaches zero. In previous work, the effect of compaction force on RI closely resembles the effect of density on RI and is also described by Palermo *et. al.* [2].

For any given compression force, the mechanisms/degree of internal cohesion forces are likely to remain similar. With reference to the tablets of fixed compressional forces (Fig. 3; △), the increased hardness results from the greater stress required to shear tablets of increasing thickness. Yet with the fixed weight tablets, as fill weights are equal, these mechanisms of internal cohesive forces vary with void fraction along with RI.

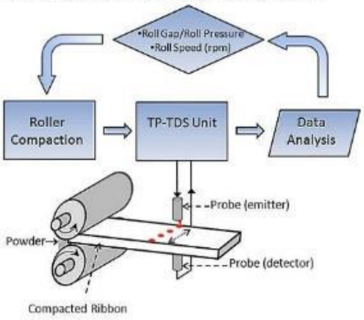

Figure 4: ***Schematic diagram representing the application of TP-TDS in-situ during continuous processing of roller-compacted ribbons***

CONCLUSION

As a controlled operating parameter during the roller-compaction process, roll gap greatly influences the thickness of the resultant ribbon. Coupling RI to the inferred thickness in-situ leads to a surrogate measurement for hardness and a platform for downstream QbD principles concerning hardness effects. For example, ribbon hardness may correlated with critical tablet characteristics, aswell as process qualities such as milling time and energetics, resultant granule size, and fines fraction.

ACKNOWLEDGMENTS

Gratitude is deserved for the East Midlands Development Agency for funding the acquisition of the TPS-3000.

REFERENCES

[1] M. Pore, J.A. Zeitler, S. Ngai, P.F. Taday, and C. Cooney, "Application of terahertz pulsed spectroscopy for evaluation of properties of pharmaceutical tablets" in: *Pittcon, The Pittsburgh Conference*. (2007) Chicago, USA.

[2] R. Palermo, R. Cogdill, S.M. Short, J.K. Drennen III and P.F. Taday, "Density mapping and chemical component calibration development of four-component compacts via terahertz pulsed imaging" *J. Pharm. and BioMed. Anal.* **46** (2008) 36-44.

PHARMACEUTICAL TECHNOLOGIES
Leicester School of Pharmacy

10.5.3 Abstract 1 for APS September 2011

Monitoring ribbon thickness in the roller compaction process with terahertz pulsed imaging

L.A. Wall[1], I. Ermolina[1], A. Dennis[2], J. Alton[3], G. Smith[1]

[1]School of Pharmacy, De Montfort University, Leicester. LE1 9BH, UK. [2] Bristol-Myers Squibb, Reeds Lane, Moreton, Wirral. CH46 1QW, UK.[3] TeraView, Cambridge, St John's Innovation Park, Cambridge CB4 0WS, UK.

INTRODUCTION

The density (or conversely the porosity) and thickness of a compressed ribbon has a significant impact on its tensile strength and subsequently the energy requirements during the milling process to achieve a consistent particle size distribution. It is therefore desirable to control ribbon properties and in particular ribbon porosity. A means to monitor these properties affords the potential for better process control.

THz pulsed imaging (TPI) techniques have begun to contribute to the growing range of process analytical techniques (PAT) for pharma process control. It has been demonstrated already that the diametric crushing strength of Avicel® tablets [1] (surrogates for roller-compacted ribbons) correlates with the measurement of terahertz (THz) refractive index (RI) thereby defining an opportunity for a new process control methodology in tablet compression and/or roller compaction. In comparison to the well established use of near-infrared (NIR) spectroscopy in PAT, TPI does not suffer from poor reproducibility relating to baseline shifts, resulting from surface smoothness. As most pharmaceutical materials are translucent to THz, TPI is better positioned to interrogate the entirety (i.e. thickness and density) of the ribbon rather than just its surface properties.

In this study, we investigate the effect of formulation on the terahertz pulsed waveform and the measurements of thickness that maybe extracted there from.

MATERIALS AND METHODS

Two roller compacted ribbons were prepared on an AlexanderWerk WP-120 with varying composition of Avicel PH-101 and anhydrous lactose (Table 1), plus 1.5% croscarmellose sodium and 0.25% magnesium stearate. Roller gap width was set at 2.2 mm in both cases, with equal feed vacuum pressures of 0.8 and roll pressures of 57.9bar ± 0.1.

TPI measurements of the roller compacted ribbons were made with a TPI™ Imaga 1000 (TeraView, Cambridge).

RESULTS AND DISCUSSION

Figure 1 shows a typical reflected waveform from a roller-compact. The exposed face of the ribbon corresponds to the substantial positive peak on the left-hand side of the diagram. The second, negative peak (right-hand side) shows the reflection from the interface associated with the back face of the ribbon.

In order to extract a measurement of ribbon thickness from the THz waveform it is first necessary to calculate a RI for each ribbon. The first step is to calculate the true densities and RI's of the blends of raw materials from the individual true densities and the relative proportions in each blend of powders (*Table 1, Step 1*).

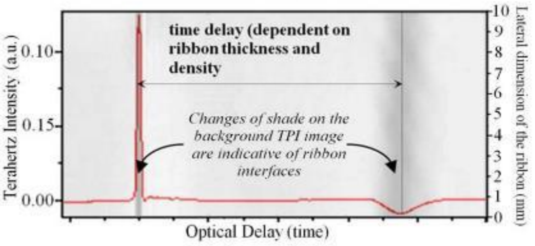

Figure 1: *Time-domain waveform of a typical roller-compacted ribbon at one pixel superimposed on a grayscale TPI lateral image across the ribbon.*

The second step is to use the measured density of the ribbon to estimate the RI of each ribbon. Co-incidentally the RIs calculated for each ribbon, via this method, approximate to 1.41.

Table 1: *Material attributes*

	Avicel PH -101	Anhydrous Lactose
True Density (g/cm^3)	1.590	1.589
R.I.	1.504	1.533
Batch A	58.95%	39.30%
Batch B	78.60%	19.65%
Step 1: Calculated values associated with true density of mixtures		
	A	**B**
Density(g/cm^3)	1.562	1.562
R.I.	1.489	1.483
Step 2: Estimated RI of ribbon from its measured density		
	A	**B**
Density (g/cm^3)	1.180	1.190
R.I.	1.370	1.368

From the estimate of RI it is then possible to convert the optical time delay between the peaks into estimates for ribbon thickness at each pixel of the scanned THz image (*Figure 2*).

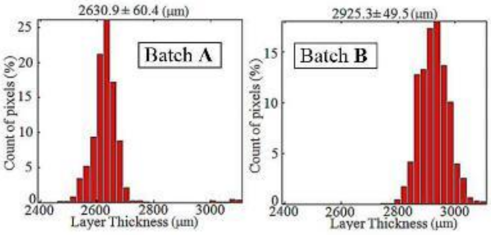

Figure 2: Processed TPI scans showing thickness distribution across two RC ribbons produced with different proportions of excipients.

CONCLUSION

The capability to measure ribbon thickness profiles has been demonstrated using TPI. From a comparison of the estimates for ribbon thickness with the roller gap width (of 2.2 mm) it is clear that 20-30% elastic recovery has taken place. The elastic recovery is greater in the case of the formulation containing a higher degree of Avicel® PH-101.

REFERENCES

[1] Wall, L.A., Ermolina, I., Gamlen, M.J., Smith, G., "Use of terahertz time-domain spectroscopy to correlate refractive index and hardness for Avicel PH-101 tablets" *Journal of Pharmacy and Pharmacology*, **62** (2010) 1485-1486

10.5.4 Poster 1 presented for APS September 2011

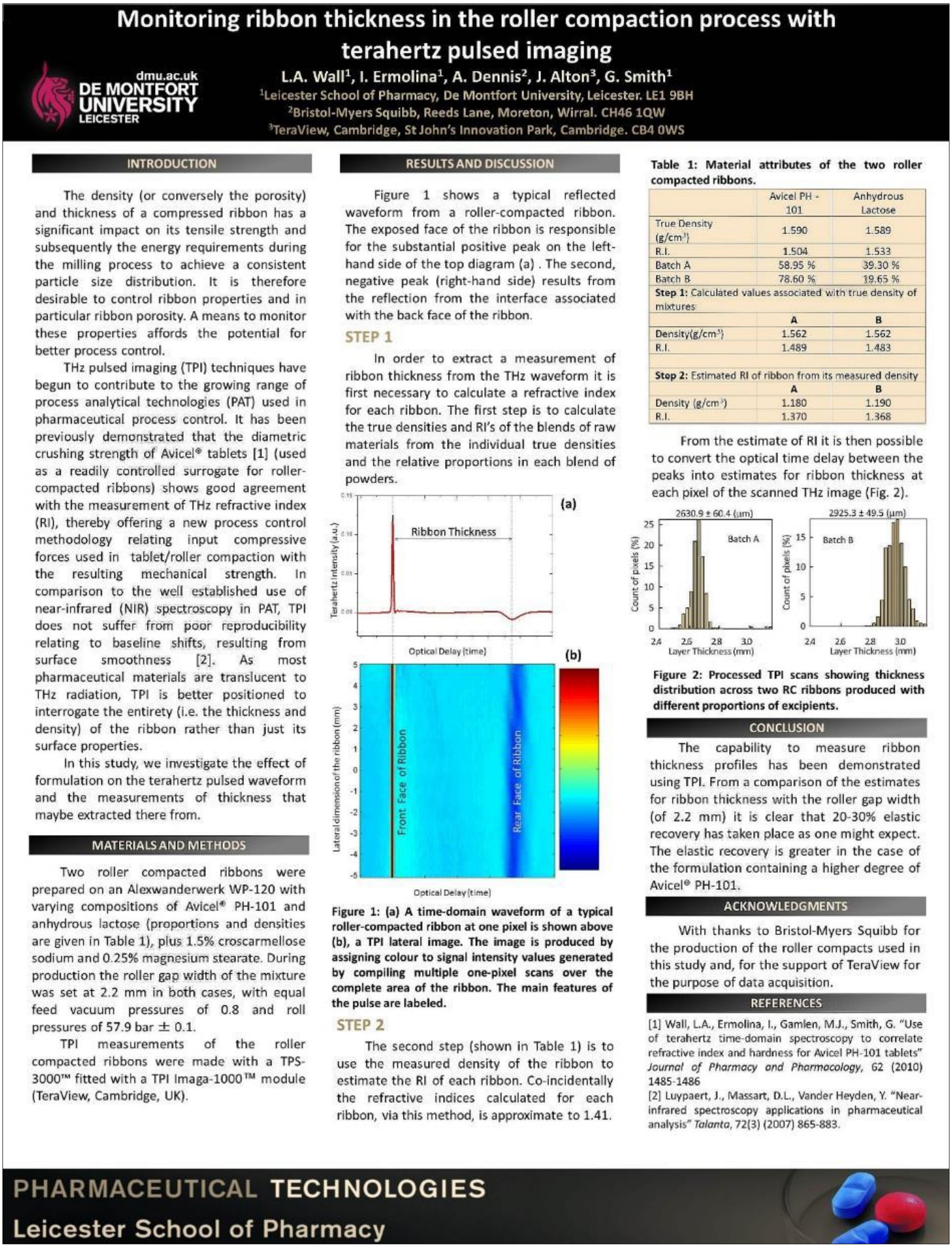

Monitoring ribbon thickness in the roller compaction process with terahertz pulsed imaging

dmu.ac.uk
DE MONTFORT UNIVERSITY
LEICESTER

L.A. Wall[1], I. Ermolina[1], A. Dennis[2], J. Alton[3], G. Smith[1]
[1]Leicester School of Pharmacy, De Montfort University, Leicester. LE1 9BH
[2]Bristol-Myers Squibb, Reeds Lane, Moreton, Wirral. CH46 1QW
[3]TeraView, Cambridge, St John's Innovation Park, Cambridge. CB4 0WS

INTRODUCTION

The density (or conversely the porosity) and thickness of a compressed ribbon has a significant impact on its tensile strength and subsequently the energy requirements during the milling process to achieve a consistent particle size distribution. It is therefore desirable to control ribbon properties and in particular ribbon porosity. A means to monitor these properties affords the potential for better process control.

THz pulsed imaging (TPI) techniques have begun to contribute to the growing range of process analytical technologies (PAT) used in pharmaceutical process control. It has been previously demonstrated that the diametric crushing strength of Avicel® tablets [1] (used as a readily controlled surrogate for roller-compacted ribbons) shows good agreement with the measurement of THz refractive index (RI), thereby offering a new process control methodology relating input compressive forces used in tablet/roller compaction with the resulting mechanical strength. In comparison to the well established use of near-infrared (NIR) spectroscopy in PAT, TPI does not suffer from poor reproducibility relating to baseline shifts, resulting from surface smoothness [2]. As most pharmaceutical materials are translucent to THz radiation, TPI is better positioned to interrogate the entirety (i.e. the thickness and density) of the ribbon rather than just its surface properties.

In this study, we investigate the effect of formulation on the terahertz pulsed waveform and the measurements of thickness that maybe extracted there from.

MATERIALS AND METHODS

Two roller compacted ribbons were prepared on an Alexwanderwerk WP-120 with varying compositions of Avicel® PH-101 and anhydrous lactose (proportions and densities are given in Table 1), plus 1.5% croscarmellose sodium and 0.25% magnesium stearate. During production the roller gap width of the mixture was set at 2.2 mm in both cases, with equal feed vacuum pressures of 0.8 and roll pressures of 57.9 bar ± 0.1.

TPI measurements of the roller compacted ribbons were made with a TPS-3000™ fitted with a TPI Imaga-1000™ module (TeraView, Cambridge, UK).

RESULTS AND DISCUSSION

Figure 1 shows a typical reflected waveform from a roller-compacted ribbon. The exposed face of the ribbon is responsible for the substantial positive peak on the left-hand side of the top diagram (a) . The second, negative peak (right-hand side) results from the reflection from the interface associated with the back face of the ribbon.

STEP 1

In order to extract a measurement of ribbon thickness from the THz waveform it is first necessary to calculate a refractive index for each ribbon. The first step is to calculate the true densities and RI's of the blends of raw materials from the individual true densities and the relative proportions in each blend of powders.

Figure 1: (a) A time-domain waveform of a typical roller-compacted ribbon at one pixel is shown above (b), a TPI lateral image. The image is produced by assigning colour to signal intensity values generated by compiling multiple one-pixel scans over the complete area of the ribbon. The main features of the pulse are labeled.

STEP 2

The second step (shown in Table 1) is to use the measured density of the ribbon to estimate the RI of each ribbon. Co-incidentally the refractive indices calculated for each ribbon, via this method, is approximate to 1.41.

Table 1: Material attributes of the two roller compacted ribbons.

	Avicel PH - 101	Anhydrous Lactose
True Density (g/cm^3)	1.590	1.589
R.I.	1.504	1.533
Batch A	58.95 %	39.30 %
Batch B	78.60 %	19.65 %
Step 1: Calculated values associated with true density of mixtures		
	A	**B**
Density(g/cm^3)	1.562	1.562
R.I.	1.489	1.483
Step 2: Estimated RI of ribbon from its measured density		
	A	**B**
Density (g/cm^3)	1.180	1.190
R.I.	1.370	1.368

From the estimate of RI it is then possible to convert the optical time delay between the peaks into estimates for ribbon thickness at each pixel of the scanned THz image (Fig. 2).

Figure 2: Processed TPI scans showing thickness distribution across two RC ribbons produced with different proportions of excipients.

CONCLUSION

The capability to measure ribbon thickness profiles has been demonstrated using TPI. From a comparison of the estimates for ribbon thickness with the roller gap width (of 2.2 mm) it is clear that 20-30% elastic recovery has taken place as one might expect. The elastic recovery is greater in the case of the formulation containing a higher degree of Avicel® PH-101.

ACKNOWLEDGMENTS

With thanks to Bristol-Myers Squibb for the production of the roller compacts used in this study and, for the support of TeraView for the purpose of data acquisition.

REFERENCES

[1] Wall, L.A., Ermolina, I., Gamlen, M.J., Smith, G. "Use of terahertz time-domain spectroscopy to correlate refractive index and hardness for Avicel PH-101 tablets" *Journal of Pharmacy and Pharmacology*, 62 (2010) 1485-1486

[2] Luypaert, J., Massart, D.L., Vander Heyden, Y. "Near-infrared spectroscopy applications in pharmaceutical analysis" *Talanta*, 72(3) (2007) 865-883.

PHARMACEUTICAL TECHNOLOGIES
Leicester School of Pharmacy

10.5.5 Abstract 2 for APS September 2011

Evaluating lactose content within Avicel® PH-101 tablets by computational analyses of terahertz waveforms

L.A. Wall[1], M. Mueller-Holtz[2], I. Ermolina[1], M.J. Gamlen[3], H. Seker[2], G. Smith[1]

[1]School of Pharmacy, De Montfort University, Leicester. LE1 9BH, UK. [2]Centre for Computational Intelligence, De Montfort University, Leicester. LE1 9BH, UK. [3] Gamlen Tableting Ltd, Nottingham. NG1 1GF, UK.

INTRODUCTION

Terahertz spectroscopy provides information on phonon modes in crystalline structures [1]. The phonon mode originates from van der Waals and hydrogen bonding between molecules within a crystal lattice structure. It represents an opportunity to fingerprint drug identity as well as assaying for content. Furthermore, the technique of terahertz pulsed technology has begun to contribute to in-process control of pharmaceutical manufacturing, in which drug uniformity in dry granulation procedures (e.g. roller compaction) may present certain issues for product quality.

The aim of this work was to evaluate two methods of terahertz (THz) time-domain waveform analysis for estimating the crystalline component of tablets. One method was based on the analysis of the time-domain waveform signal intensity and the second on principle component analysis (PCA) of the corresponding Fourier spectrum. A model tablet formulation was studied containing a crystalline component (lactose monohydrate) with known THz phonon vibrations, and another material (Avicel® PH-101) which does not display any phonon modes within the THz spectrum.

MATERIALS AND METHODS

Seven 200 mg samples of Avicel® PH-101 and lactose monohydrate were weighed separately and mixed for 5 minutes prior to transferring to a 13 mm diameter tablet die. The powder samples were pressed at 500 ± 1 kg at a rate of 20 mm/min on a single punch tablet press (Gamlen Tablet Press, Gamlen Tableting Ltd, Nottingham, UK) producing tablets with thickness 1.48 mm ±0.1 mm and densities of 1 mg/mm^3 ±0.03 mg/mm^3. Allowing 48 hours post-compaction for elastic recovery, the tablets were analysed with a TPS-3000™ (TeraView, Cambridge, UK) operating in transmission mode to record their time-domain waveform. ***Method 1*** Maximum peak intensities were read from the time-domain waveform (See Fig.1) over a time period in which a ripple in waveform is witnessed, free from visible shoulders and inflexions. ***Method 2*** PCA was performed on the corresponding Fourier spectrum of each time domain waveform (Fig. 2), between wavenumbers 0 to 75 cm^{-1}, where greater wavenumbers were considered as noise. The PCA method involves the transformation on the orthogonals of the input data to find similarities in the variances of a given dataset.

RESULTS AND DISCUSSION

Waveforms for the 7 samples are shown in figure 1, where greater lactose content is denoted with lighter lines with 0% represented as black. The corresponding Fourier spectra are shown in figure 2.

For each method the peak intensities in the chosen regions of the waveforms and Fourier spectrum (respectively, methods 1 and 2) are presented in figure 3.

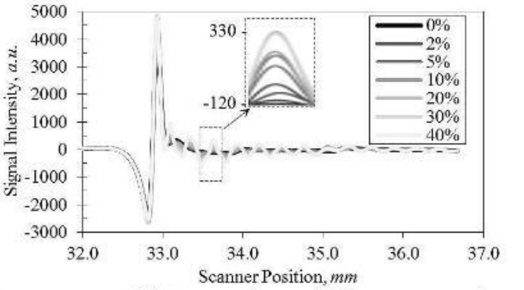

Figure 1: *Compiled THz waveforms of tablets comprising binary mixture of lactose (expressed in % w/w) and Avicel® PH-101. Inset shows exploded image of the time base analysed in Method 1.*

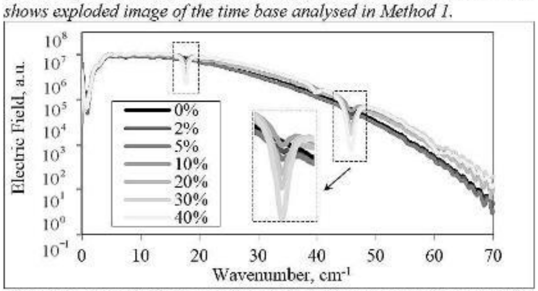

Figure 2: *Compiled THz spectrum with lactose concentrations % w/w. Inset boxes show wavenumber regions sensitive to lactose.*

In the PCA analysis, the second component was chosen for subsequent regression analysis because it showed a good correlation between the characteristic peaks in the spectra at approximately 46 cm^{-1} and 19 cm^{-1} and the concentration of lactose (See Fig. 3).

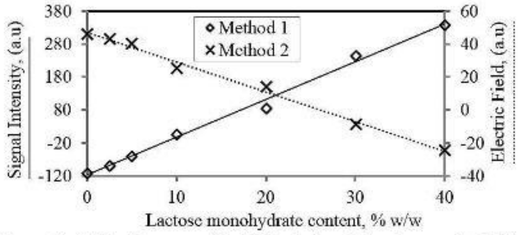

Figure 3: Calibration curve for Methods 1 and 2, where method 1 is measured against signal intensity and method 2, electric field.

From the root mean square error (RMS) in the calibration curve for methods 1 and 2, the uncertainty of any concentration in the range studied was ± 2.6% for method 1 and ± 2.0% for method 2.

CONCLUSION

Although the RMS errors for both methods are similar method 2 would be more suitable for the determination of concentration of one crystalline component in a binary mixture with another non-crystalline component. This is because PCA characterises the specific phonon vibrations from individual components directly on the Fourier spectrum and so has improved specificity.

REFERENCES

[1] Zhang, Y., *et al.*"A first principle study of THz) spectra of acephate" *Chemical Physics Letters* **452** (2008) pp. 59–66

10.5.6 Poster 2 presented APS September 2011

Evaluating lactose content within Avicel® PH-101 tablets by computational analysis of terahertz waveforms

dmu.ac.uk
DE MONTFORT UNIVERSITY LEICESTER

L.A. Wall[1], M. Mueller-Holtz[2], I. Ermolina[1], M.J. Gamlen[3], H. Seker[2], G. Smith[1]
[1]Leicester School of Pharmacy, De Montfort University, Leicester. LE1 9BH
[2]Centre for Computational Intelligence, De Montfort University, Leicester. LE1 9BH
[3]Gamlen Tableting Ltd, Nottingham. NG1 1GF

INTRODUCTION

Terahertz pulsed spectroscopy (TPS) provides information on phonon modes in crystalline structures [1]. The phonon mode originates from van der Waals and hydrogen bonding between molecules within a crystal lattice structure. Analysis of the phonon modes represents an opportunity to fingerprint drug identity of crystalline substances as well as assaying for content. The technique of TPS has been researched as a potential to monitor and control methodologies for pharmaceutical manufacturing in-situ, where blend uniformity might be an issue. One area of particular interest lies in dry granulation where the continuous nature of roller compaction makes live, in-line monitoring desirable.

In this study we evaluate two methods of terahertz-time domain (THz-TD) waveform analysis for estimating the crystalline component of binary blend tablets. One method was based on the analysis of the THz-TD waveform signal intensity and the second, on principle component analysis (PCA) of the corresponding Fourier spectrum. A model tablet formulation was studied containing a crystalline component (lactose monohydrate) with known THz phonon vibrations, and Avicel® PH-101 which does not display any phonon modes within the THz spectrum.

MATERIALS AND METHODS

Seven 200 mg samples of Avicel® and lactose monohydrate were weighed separately and mixed for 5 minutes before transferral into a 13 mm diameter die. The samples were pressed at 500 ±1 kg at a rate of 20 mm/min on a single punch Gamlen tablet press, (Gamlen Tableting Ltd, Nottingham, UK) producing tablets with thickness 1.48 mm ±0.1 mm and densities of 1 mg/mm^3 ±0.03 mg.mm^{-3}. Having allowed 48 hours post-compaction for potential elastic recovery, the tablets were analysed with a TPS-3000™ (TeraView, Cambridge, UK) in order to record their TD waveform.

METHOD 1

Maximum peak intensities were read from the TD waveforms at one time period (see Figure 1 where scanner position has equivalence with optical time delay) where a ripple in the waveform is witnessed. Ripples containing non-symmetrical shoulders or inflexions were not included in the analysis.

METHOD 2

PCA was performed on the corresponding Fourier spectrum of each time domain waveform (Figure 2), between wavenumbers 0 to 75 cm^{-1}.

The PCA method involves the transformation on the orthogonals of the input data to find similarities in the variances of a given dataset.

RESULTS AND DISCUSSION

Waveforms of the 7 samples are shown in Figure 1, where greater lactose concentration is denoted with a shift from red to green. With observation of the pure Avicel® waveform (0%) it is noted that the tablet is of sufficient thickness to avoid excessive front-to-rear Fabry-Pérot echo peaks. The corresponding Fourier spectra are shown in Figure 2.

For each method the peak intensities in the chosen regions of the waveforms and Fourier spectrum (respectively, Methods 1 and 2) are presented in Figure 3.

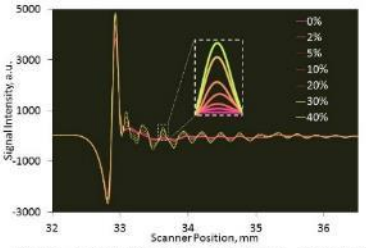

Figure 1: Compiled THz waveforms of tablets comprising of a binary mixture of lactose (expressed in % w/w) and Avicel® PH-101. Inset shows exploded image of the time region analysed in Method 1.

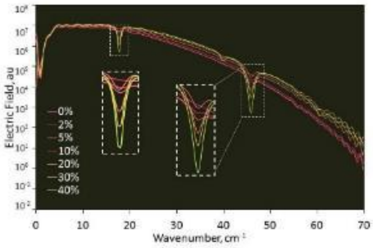

Figure 2: Compiled THz spectrum with lactose concentrations (expressed in % w/w). Inset boxes show wavenumber regions sensitive to lactose monohydrate, with exploded images of main peaks.

The PCA works as a signal filter eliminating regions of the spectra where repeated and similar data-points occur across the concentration range, while at the same time amplifying regions of interest. In the example shown the lactose-associated peaks are amplified.

By projecting the original frequency waveforms onto the second component, the method takes small fluctuations (i.e. at 40 cm^{-1}) into account, allowing use of the whole frequency spectrum for the final regression. Dimension reduction was applied by calculating the dot-product of the original waveforms with the second component.

The second component was chosen for subsequent regression analysis because it showed a good correlation between the characteristic peaks in the spectra at approximately 46 cm^{-1} and 19 cm^{-1} and the concentration of lactose (see Figure 3).

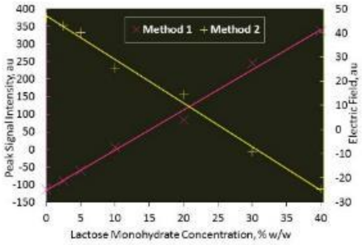

Figure 3: Calibration curve for Methods 1 and 2, where method 1 is measured against signal intensity and method 2, electric field.

From the RMS in the calibration curve for methods 1 and 2, the uncertainty of any concentration in the range studied was ±2.6% for method 1 & ±2.0% for method 2.

CONCLUSIONS

Although the RMS errors for both methods are similar, method 2 would be more suitable for the determination of concentration of one crystalline component in a binary mixture with another non-crystalline component. This is because PCA characterises the specific phonon vibrations from individual components directly on the Fourier spectrum and so has improved specificity.

Implicit to the 2.0% uncertainty described, the suitability of such uniformity analysis may only find utility for blends with a concentration of active above 10% w/w.

ACKNOWLEDGMENTS

Gratitude is deserved for the East Midlands Development Agency for funding the acquisition of the TPS-3000.

REFERENCES

[1] Zhang, Y., *et al.* "A first principle study of terahertz spectra of acephate" *Chemical Physics Letters*, 452 (2008) 59–66

PHARMACEUTICAL TECHNOLOGIES
Leicester School of Pharmacy

10.5.7 Abstract for APS September 2012

The application of terahertz pulsed spectroscopy in the evaluation of the radial tensile strength of Avicel® PH-101 tablets

LA Wall, G Smith, I Ermolina
School of Pharmacy, De Montfort University, Leicester, LE1 9BH

INTRODUCTION

The resistance of a tablet to fracture (diametrically) under pressure, between two converging plates is a quantitative compendial test to ensure that tablets possess sufficient tensile strength (TS). This strength is necessary to withstand post-production handling, yet if too strong; it will impact the disintegration process and the dissolution rate and ultimately the bioavailability of the drug. Therefore a limit for the optimal TS of the dosage unit must be present.

Here, we use terahertz-pulsed spectroscopy (TPS) to establish whether the refractive index (RI) at THz frequencies may be used to assess the radial tensile strength (RTS) of tablets. We have demonstrated previously that the RI of a tablet provides a convenient surrogate assessment for tablet density [1].

MATERIALS AND METHODS

Avicel® PH-101 (FMC, BioPolymer) was sufficiently tapped (for the purpose of de-aeration) prior to compaction within a 10mm die on an instrumented Precision Compression Tester (Gamlen Tabletting, Nottingham). Two populations of tablets were prepared, one at a fill-weight of 200 mg and the other at a fill-weight of 295 mg. In each case a range of compression-forces were used to generate tablets of varying thickness and hence density (Table 1). The geometric properties of each tablet were calculated 48 hours post-compaction and the THz RI (averaged over frequencies 0.3 - 1.5 THz) were measured on a TPS-3000 (TeraView, Cambridge).

Table 1: *Schedule of tablet production.*

Tablet Weight *mg*	*n*	Diameter, *mm*	Compression Rate, *mm/min*	Compression force range, *Kg*
200 mg ± 2	11	10 ± 0.01	20	110 – 460
295 mg ± 2	8	10 ± 0.01	20	85 - 430

The RTS of each tablet was calculated [2] using Equation 1, following the measurement of diametric crushing-force determination on a PharmaTest PTB 311E.

$$RTS = \frac{2p}{\pi d t} \qquad \text{(Equation 1)}$$

where p is the crushing force (N), and d and t denotes the diameter and thickness of the tablet (M).

RESULTS AND DISCUSSION

When presented together, both populations of tablets display a single, unified linear response between increasing RI and density ($R^2 > 98\%$) (*Figure 1*). This result is to be expected given that, during consolidation, the rearrangement and deformation of particles causes the removal of voids and increases the volume-fraction of the solid.

For any particular material, one might expect a direct correlation between RI/density and RTS given that particle-particle bonding is expected to increase proportionately alongside compaction-force.

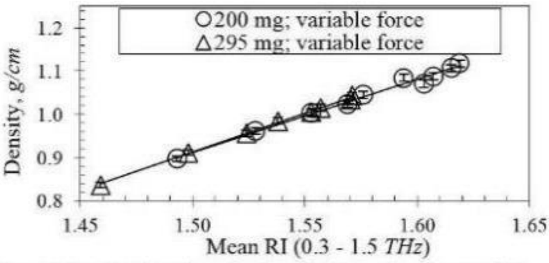

Figure 1: *Density plot with two batches of tablets made under variable compressional pressures [1].*

Figure 2 demonstrates that the hypothesis appears to hold (albeit independently) for both populations of tablets. The apparent-linear relationships between RI and RTS have different best-fit lines between the two populations. What is interesting is that the lines of best-fit appear to converge at a RI = 1.6 yet, at a RI = 1.5 (i.e. when the tablet thickness is greater) there is a 0.2 *MPa* difference in RTS.

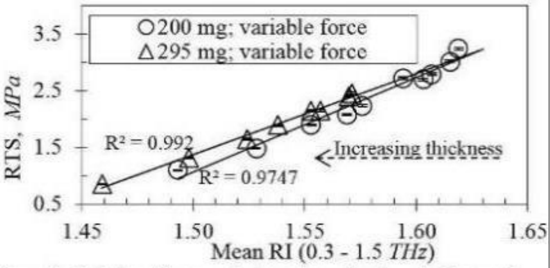

Figure 2 : *Radial tensile strength plot with two batches of tablets made under variable compressional pressures.*

We associate the differences between the two populations (with RI = 1.5) with the fact that the higher fill-weight tablet is approximately 50% thicker than the low fill-weight tablet and hence there will be greater forces applied to the tablet as it endeavours to undergo elastic and plastic consolidation. In contrast, tablets of lower fill-weight (and hence lower interfacial-contact) will experience similar consolidation mechanisms, yet recovery through elastic nature could result in internal flaws to the integrity of the tablet and therefore explain the reduced RTS.

CONCLUSION

With prior knowledge of the tablet fill-weight and the compaction-force, a calibration curve will provide a means to assess the RTS of 100% of produced tablets, non-destructively.

REFERENCES

[1] L.A. Wall, I. Ermolina, M.J. Gamlen, and G. Smith. "Use of terahertz time-domain spectroscopy to correlate refractive index and hardness for Avicel PH-101 tablets". *Journal of Pharmacy and Pharmacology*. **62**:10 (2010) 1485-86

[2] J.T. Fell and J.M. Newton. "Determination of tablet strength by the diametrical-compression test" *Journal of Pharmaceutical Sciences*. **59** (1970) 688-691

10.5.8 Poster presented APS September 2012

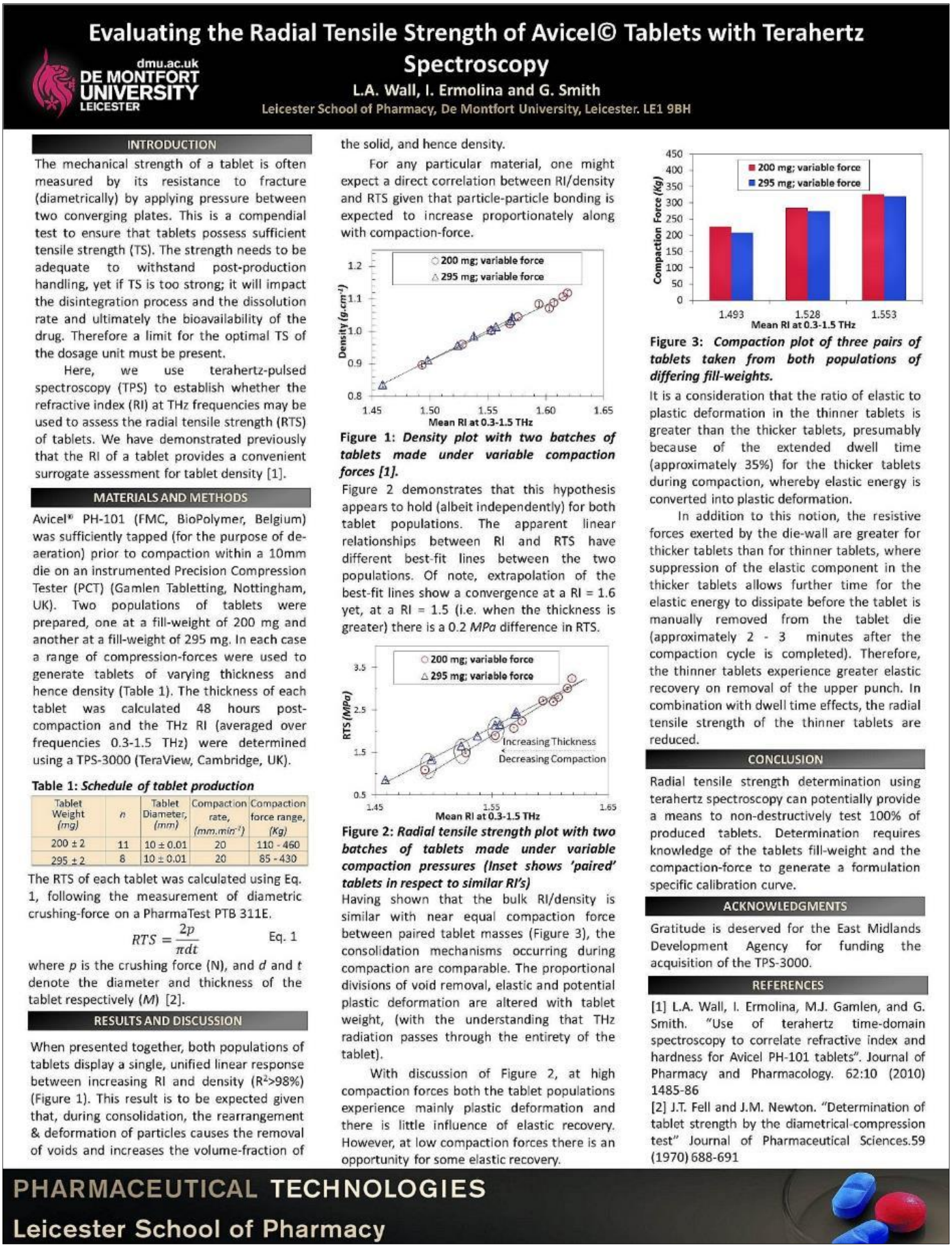

Evaluating the Radial Tensile Strength of Avicel© Tablets with Terahertz Spectroscopy

L.A. Wall, I. Ermolina and G. Smith
Leicester School of Pharmacy, De Montfort University, Leicester. LE1 9BH

INTRODUCTION

The mechanical strength of a tablet is often measured by its resistance to fracture (diametrically) by applying pressure between two converging plates. This is a compendial test to ensure that tablets possess sufficient tensile strength (TS). The strength needs to be adequate to withstand post-production handling, yet if TS is too strong; it will impact the disintegration process and the dissolution rate and ultimately the bioavailability of the drug. Therefore a limit for the optimal TS of the dosage unit must be present.

Here, we use terahertz-pulsed spectroscopy (TPS) to establish whether the refractive index (RI) at THz frequencies may be used to assess the radial tensile strength (RTS) of tablets. We have demonstrated previously that the RI of a tablet provides a convenient surrogate assessment for tablet density [1].

MATERIALS AND METHODS

Avicel® PH-101 (FMC, BioPolymer, Belgium) was sufficiently tapped (for the purpose of de-aeration) prior to compaction within a 10mm die on an instrumented Precision Compression Tester (PCT) (Gamlen Tabletting, Nottingham, UK). Two populations of tablets were prepared, one at a fill-weight of 200 mg and another at a fill-weight of 295 mg. In each case a range of compression-forces were used to generate tablets of varying thickness and hence density (Table 1). The thickness of each tablet was calculated 48 hours post-compaction and the THz RI (averaged over frequencies 0.3-1.5 THz) were determined using a TPS-3000 (TeraView, Cambridge, UK).

Table 1: ***Schedule of tablet production***

Tablet Weight *(mg)*	*n*	Tablet Diameter, *(mm)*	Compaction rate, *(mm.min^{-1})*	Compaction force range, *(Kg)*
200 ± 2	11	10 ± 0.01	20	110 - 460
295 ± 2	8	10 ± 0.01	20	85 - 430

The RTS of each tablet was calculated using Eq. 1, following the measurement of diametric crushing-force on a PharmaTest PTB 311E.

$$RTS = \frac{2p}{\pi d t} \qquad \text{Eq. 1}$$

where p is the crushing force (N), and d and t denote the diameter and thickness of the tablet respectively (*M*) [2].

RESULTS AND DISCUSSION

When presented together, both populations of tablets display a single, unified linear response between increasing RI and density (R^2>98%) (Figure 1). This result is to be expected given that, during consolidation, the rearrangement & deformation of particles causes the removal of voids and increases the volume-fraction of the solid, and hence density.

For any particular material, one might expect a direct correlation between RI/density and RTS given that particle-particle bonding is expected to increase proportionately along with compaction-force.

Figure 1: ***Density plot with two batches of tablets made under variable compaction forces [1].***

Figure 2 demonstrates that this hypothesis appears to hold (albeit independently) for both tablet populations. The apparent linear relationships between RI and RTS have different best-fit lines between the two populations. Of note, extrapolation of the best-fit lines show a convergence at a RI = 1.6 yet, at a RI = 1.5 (i.e. when the thickness is greater) there is a 0.2 *MPa* difference in RTS.

Figure 2: ***Radial tensile strength plot with two batches of tablets made under variable compaction pressures (Inset shows 'paired' tablets in respect to similar RI's)***

Having shown that the bulk RI/density is similar with near equal compaction force between paired tablet masses (Figure 3), the consolidation mechanisms occurring during compaction are comparable. The proportional divisions of void removal, elastic and potential plastic deformation are altered with tablet weight, (with the understanding that THz radiation passes through the entirety of the tablet).

With discussion of Figure 2, at high compaction forces both the tablet populations experience mainly plastic deformation and there is little influence of elastic recovery. However, at low compaction forces there is an opportunity for some elastic recovery.

Figure 3: ***Compaction plot of three pairs of tablets taken from both populations of differing fill-weights.***

It is a consideration that the ratio of elastic to plastic deformation in the thinner tablets is greater than the thicker tablets, presumably because of the extended dwell time (approximately 35%) for the thicker tablets during compaction, whereby elastic energy is converted into plastic deformation.

In addition to this notion, the resistive forces exerted by the die-wall are greater for thicker tablets than for thinner tablets, where suppression of the elastic component in the thicker tablets allows further time for the elastic energy to dissipate before the tablet is manually removed from the tablet die (approximately 2 - 3 minutes after the compaction cycle is completed). Therefore, the thinner tablets experience greater elastic recovery on removal of the upper punch. In combination with dwell time effects, the radial tensile strength of the thinner tablets are reduced.

CONCLUSION

Radial tensile strength determination using terahertz spectroscopy can potentially provide a means to non-destructively test 100% of produced tablets. Determination requires knowledge of the tablets fill-weight and the compaction-force to generate a formulation specific calibration curve.

ACKNOWLEDGMENTS

Gratitude is deserved for the East Midlands Development Agency for funding the acquisition of the TPS-3000.

REFERENCES

[1] L.A. Wall, I. Ermolina, M.J. Gamlen, and G. Smith. "Use of terahertz time-domain spectroscopy to correlate refractive index and hardness for Avicel PH-101 tablets". Journal of Pharmacy and Pharmacology. 62:10 (2010) 1485-86

[2] J.T. Fell and J.M. Newton. "Determination of tablet strength by the diametrical-compression test" Journal of Pharmaceutical Sciences.59 (1970) 688-691

11 References

1. Hsu, S., G.V. Reklaitis, and V. Venkatasubramanian, *Modelling and control of roller compaction for pharmaceutical manufacturing. Part I: Process dynamics and control framework.* Journal of Pharmaceutical Innovation, 2010. **5**(1-2): p. 14-23.
2. Bindhumadhavan, G., et al., *Roll compaction of a pharmaceutical excipient: Experimental validation of rolling theory for granular solids.* Chemical Engineering Science, 2005. **60**(14): p. 3891-3897.
3. Guigon, P., Simon, O., Saleh, K., Gururajan, B., Adams, M.J., Seville, J.P.K, *Roll Pressing*, in *Granulation*, A.D. Salman, Houndslow, M.J., Seville, J.P.K, Editor. 2007, Elsevier: London. p. 255-288.
4. Li. F, R.F. Meyer, and R. Chern. *Understanding Critical Parameters in Roller Compaction Process and Development of a Novel Scaling Method*. in *The Preliminary Program for 2006 Spring National Meeting*. 2006. Merck & Co. Inc., West Point, PA 19486
5. Jivraj, M., L.G. Martini, and C.M. Thomson, *An overview of the different excipients useful for the direct compression of tablets.* Pharmaceutical Science & Technology Today, 2000. **3**(2): p. 58-63.
6. Çelik, M., *The past, present, and future of tableting technology*. Drug Development and Industrial Pharmacy, 1996. **22**(1): p. 1-10.
7. Teng, Y., Qiu, Z., Wen, H., *Systematical approach of formulation and process development using roller compaction.* European Journal of Pharmaceutics and Biopharmaceutics, 2009. **73**(2): p. 219-229.
8. Herting, M.G., Kleinebudde, P., *Roll compaction/dry granulation: Effect of raw material particle size on granule and tablet properties.* International Journal of Pharmaceutics, 2007. **338**: p. 110-118.
9. Cavatur, N., et al., *Preformulation studies for tablet formulation development*, in *Pharmaceutical dosage form: Tablets*, L.L. Augsburger and S.W. Hoag, Editors. 2008, Informa Healthcare USA Inc.: New York. p. 465-485.
10. Augsburger, L.L. and S.W. Hoag, *Volume 1: Unit operations and mechanical properties*. Dosage forms: Tablets, ed. S.W. Hoag. 2008, New York: Informa Healthcare.
11. Peck, G.E., J.L.P. Soh, and K.R. Morris, *Dry Granulation*, in *Pharmaceutical Dosage Forms: Tablets*, L.L. Augsburger and S.W. Hoag, Editors. 2008, Informa Healthcare USA: New York. p. 303-336.
12. Parikh, D.M., *Roller compaction technology*, in *Handbook of Pharmaceutical Granulation Technology*, D.M. Parikh, Editor. 2005, Taylor & Francis Group: London. p. 1-7.
13. Shangraw, R.F., Demarest Jr., D.A., *A survey of current industrial practices in the formulation and manufacture of tablets and capsules.* Pharmaceutical Technology, 1993: p. 32-44.

14. Ennis, B.J. and J.D. Litster, *Particle Enlargement*, in *Perry's Chemical Engineer's Handbook*, D. Greens, Editor. 1997, McGraw Hill: New York. p. 20-56.
15. Dehont, F.R., et al., *Briquetting and granulation by compaction new granulator-compactor for the pharmaceutical industry*. Drug Development and Industrial Pharmacy, 1989. **15**(14-16): p. 2245-2263.
16. Miller, R.W., *A survey of current industrial practices and preference of roller compaction technology and excipients Year 2000*, in *Biennial Conference - Institute of Briquet and Aggloremation*. 2001. p. 41-58.
17. Sheskey, P., et al., *Roll compaction granulation of a controlled-release matrix tablet formulation containing HPMC.* Pharmaceutical Technology, 2000. **11**: p. 30-52.
18. Miller, R.W., *Roller compaction technology*, in *Handbook of Pharmaceutical Granulation Technology*, D.M. Parikh, Editor. 2005, Taylor & Francis Group: London. p. 159-191.
19. Kleinebudde, P., *Roll compaction/dry granulation: pharmaceutical applications.* European journal of pharmaceutics and biopharmaceutics, 2004. **58**(2): p. 317-326.
20. Singh, R., M. Ierapetritou, and R. Ramachandran, *An engineering study on the enhanced control and operation of continuous manufacturing of pharmaceutical tablets via roller compaction.* International Journal of Pharmaceutics, 2012. **438**: p. 307-326.
21. Miguélez-Morán, A.-M., *Roller compaction of pharmaceutical ingredients: On the understanding of the compaction and the use of knowledged based applications in the formulation of tablets*, in *Combined Faculties for the Natural Sciences and for Mathematics*. 2009, Ruperto-Carola University of Heidelberg, Germany. p. 239.
22. Arnaud, P., D. Brossard, and J.C. Chaumeil, *Effect of the granulation process on nitrofurantoin granule characteristics.* Drug Development and Industrial Pharmacy, 1998. **24**(1): p. 57-66.
23. Leuenberger, H., *New trends in the production of pharmaceutical granules: batch versus continuous processing.* European journal of pharmaceutics and biopharmaceutics, 2001. **52**(3): p. 289-296.
24. Schroeder, R., Steffens, K., *Continuous granulation technologies*, in *Handbook of Pharmaceutical Granulation Technology*, D.M. Parikh, Editor. 2005, Taylor & Francis Group: London. p. 431-459.
25. Leuenberger, H., *Scale-up of granulation processes with reference to process monitoring.* Acta Pharmaceutica Technologica, 1983. **29**(4): p. 274-280.
26. Faure, A., P. York, and R.C. Rowe, *Process control and scale-up of pharmaceutical wet granulation processes: A review.* European Journal of Pharmaceutics and Biopharmaceutics, 2001. **52**(3): p. 269-277.
27. Boswell, S., Smith, G., *Improving Solid Dosage Forms With Dry Granulation.* Pharmaceutical Technology, 2011. **?**(?): p.?
28. FDA/CDER, U.S., Food and Drug Administration, Center for Drug Evaluation and Research. *OPS process analytical technology initiative* 2005 [cited 2013 11/03]; Available from: http://www.fda.gov/AboutFDA/CentersOffices/OfficeofMedicalProductsand-Tobacco/CDER/ucm088828.htm.

29. Singh, R., et al., *A retrofit strategy to achieve fast, flexible, future (F3) pharmaceutical production processes.* Computer Aided Chemical Engineering, 2011. **29**: p. 291-295.

30. Woodcock, J., *The concept of pharmaceutical quality.* American Pharmaceutical Review, 2004. **7**(6): p. 10-15.

31. Troup, G.M. and C. Georgakis, *Process systems engineering tools in the pharmaceutical industry.* Computers & Chemical Engineering, 2013. **51**(0): p. 157-171.

32. Shi, Z., et al., *Process characterization of powder blending by near-infrared spectroscopy: Blend end-points and beyond.* Journal of pharmaceutical and biomedical analysis, 2008. **47**(4–5): p. 738-745.

33. Leuenberger, H., et al., *Manufacturing pharmaceutical granules: Is the granulation end-point a myth?* Powder Technology, 2009. **189**(2): p. 141-148.

34. Gupta, A., Peck, G.E., Miller, R.W., Morris, K.R., *Nondestructive measurements of the compact strength and the particle-size distribution after milling of roller compacted powders by near-infrared spectroscopy.* Journal of Pharmaceutical Sciences, 2004. **93**(4): p. 1047-1053.

35. Gupta, A., Peck, G.E., Miller, R.W., Morris, K.R., *Real-time near-infrared monitoring of content uniformity, moisture content, compact density, tensile strength, and young's modulus of roller compacted powder blends.* Journal of Pharmaceutical Sciences, 2005. **94**(7): p. 1589-1597.

36. Chen, Y., et al., *Prediction of Drug Content and Hardness of Intact Tablets Using Artificial Neural Network and Near-Infrared Spectroscopy.* Drug Development & Industrial Pharmacy, 2001. **27**(7): p. 623.

37. Kogermann, K., Zeitler, J.A., Heinämäki, J., Rades, T., Taday, P.F., Pepper, M., Heinamaki, J., Strachan C.J., *Investigating dehydration from compacts using pulsed, raman and NIR.* Applied Spectroscopy, 2007. **61**: p. 1265-1274.

38. Karande, A.D., P.W.S. Heng, and C.V. Liew, *In-line quantification of micronized drug and excipients in tablets by near infrared (NIR) spectroscopy: Real time monitoring of tabletting process.* International Journal of Pharmaceutics, 2010. **396**(1-2): p. 63-74.

39. Virtanen, S., O. Antikainen, and J. Yliruusi, *Determination of the crushing strength of intact tablets using Raman spectroscopy.* International Journal of Pharmaceutics, 2008. **360**(1-2): p. 40-46.

40. Ho, L., Müller, R., Gordon, K.C., Kleinebudde, P., Pepper, M., Rades, T., Shen, Y., Taday, P.F., Zeitler J.A., *Monitoring the film coating unit operation and predicting drug dissolution using terahertz pulsed imaging.* Journal of Pharmaceutical Sciences, 2009. **98**(12): p. 4866-4876.

41. Sekulic, S.S., et al., *Automated system for the on-line monitoring of powder blending processes using near-infrared spectroscopy: Part II. Qualitative approaches to blend evaluation.* Journal of pharmaceutical and biomedical analysis, 1998. **17**(8): p. 1285-1309.

42. Hailey, P.A., et al., *Automated system for the on-line monitoring of powder blending processes using near-infrared spectroscopy part I. System development and control.* Journal of pharmaceutical and biomedical analysis, 1996. **14**(5): p. 551-559.

43. Berntsson, O., et al., *Quantitative in-line monitoring of powder blending by near infrared reflection spectroscopy.* Powder Technology, 2002. **123**(2-3): p. 185-193.

44. Wall, L.A., Ermolina, I., Gamlen, M. J., Smith, G., *Use of terahertz time-domain spectroscopy to correlate refractive index and hardness for Avicel PH-101 tablets.* Journal of Pharmacy and Pharmacology, 2010. **62**(10): p. 1485-1486.

45. Grohganz, H., et al., *Role of excipients in the quantification of water in lyophilized mixtures using NIR spectroscopy.* Journal of Pharmaceutical and Biomedical Analysis, 2009. **49**: p. 901-907.

46. Verveat, C. and J.P. Remon, *Continuous granulation in the pharmaceutical industry.* Chemical Engineering Science, 2005. **60**: p. 3949-3957.

47. Funakoshi, Y., Asogawa, T., Satake, E., *The use of a novel roller compactor with a concavo-convex roller pair to obtain uniform compacting pressure.* Drug Development and Industrial Pharmacy, 1977. **3**(6): p. 555-573.

48. Miller, R.W., *Advances in pharmaceutical roller compactor feed design systems.* Pharmaceutical Technology Europe, 1994. **6**(5): p. 58-68.

49. Sheskey, P., et al., *Effect of roll compaction granulation of a controlled-release matrix tablet formulation containing HPMC: Effect of process scale-up on robustness of tablets and predicted in vivo performance.* Pharmaceutical Technology, 2000. **11**: p. 30-52.

50. *Introduction to artificial neural networks*. in *Electronic Technology Directions to the Year 2000*. 1995.

51. Miller, R.W., *Roller compaction technology*, in *Handbook of Pharmaceutical Granulation Technology*, D.M. Parikh, Editor. 1997, Marcel Dekker: New York. p. 99-150.

52. Nyström, C., et al., *Bonding surface area and bonding mechanism-two important factors for the understanding of powder comparability.* Drug Development and Industrial Pharmacy, 1993. **19**(17-18): p. 2143-2196.

53. Pietsch, W., *Agglomeration Processes: Phenomena, Technologies, Equipment*. 1991, London: John Wiley & Sons.

54. Teng, Y., Z. Qiu, and H. Wen, *Systematical approach of formulation and process development using roller compaction.* European journal of pharmaceutics and biopharmaceutics, 2009. **73**(2): p. 219-229.

55. Vervaet, C. and J.P. Remon, *Continuous granulation in the pharmaceutical industry.* Chemical Engineering Science, 2005. **60**(14): p. 3949-3957.

56. Swarbrick, J. and J.C. Boylan, *Encyclopaedia of pharmaceutical technology*, R.W. Miller, Sheskey, P.J., Editor. 2004, Informa Healthcare. Inc.: London. p. 397-415.

57. Kleinebudde, P., *Review article: Roll compaction/dry granulation: pharmaceutical applications.* European Journal of Pharmaceutics and Biopharmaceutics, 2004. **58**: p. 317-326.

58. Parrot, E.L., *Pharmaceutical Dosage Forms*. Vol. 2. 1990, New York: Marcel Dekker Inc.

59. Guigon, P. and O. Simon, *Roll press design - influence of force feed systems on compaction.* Powder Technology, 2003. **130**(1-3): p. 41-48.

60. *Gerteis Maschinen + Processengineering AG*. 2011.

61. Johanson, J.R., *A rolling theory for granular solids.* ASME Journal of applied mechanics, 1965. **32**: p. 842-848.

62. Johanson, J.R., *A rolling theory for granular solids.* Journal of Applied Mechanics, 1965. **32**(4): p. 842-848.

63. Cunningham, J.C., D. Winstead, and A. Zavaliangos, *Understanding variation in roller compaction through finite element-based process modelling.* Computers & Chemical Engineering, 2010. **34**(7): p. 1058-1071.

64. Guigon, P. and O. Simon. *Correlation between the geometry of feeding system and the stress distribution applied on the compact*. in *Proceedings of the 27th Institute for Briquetting and Agglomeration* 2001. Erie, PA, Gannon University, USA: Correlation between the geometry of feeding system and the stress distribution applied on the compact.

65. Bacher, C., Olsen, P.M., Bertelsen, P., Kristensen, J., Sonnergaard, J.M., *Improving the compaction properties of roller compacted calcium carbonate.* International Journal of Pharmaceutics, 2007. **342**: p. 115-123.

66. Kawashima, Y., et al., *Preparation of a sustained-release matrix tablet of acetaminophen with pulverized low-substituted hydroxypropylcellulose via dry granulation.* Chemical and Pharmaceutical Bulletin, 1993. **41**(10): p. 1827-1831.

67. Inghelbrecht, S. and J.P. Remon, *Roller compaction and tableting of microcrystalline cellulose/drug mixtures.* International Journal of Pharmaceutics, 1998. **161**(2): p. 215-224.

68. Sun, C. and M.W. Himmelspach, *Reduced tabletability of roller compacted granules as a result of granule size enlargement.* Journal of pharmaceutical sciences, 2006. **95**(1): p. 200-206.

69. Malkowska, S. and K.A. Khan, *Effect of re-compression on the properties of tablets prepared by dry granulation.* Drug Development and Industrial Pharmacy, 1983. **9**(3): p. 331-347.

70. Wu, S.-J. and C.C. Sun, *Insensitivity of compaction properties of brittle granules to size enlargement by roller compaction.* Journal of pharmaceutical sciences, 2007. **96**: p. 1445-1448.

71. Schonert, K., *The characteristics of comminution with high pressure roller mills.* KONA, 1991. **9**: p. 149-158.

72. Daugherity. P.D. and J.H. Chu, *Investigation of serrated roll surface differences on ribbon thickness during roller compaction.* Pharmaceutical Development & Technology, 2007. **12**: p. 603-608.

73. Dec, R., *Problems with processing of fine powders in roll press*, in *25th Biennial Conference, International Briquet Association.* 1995: Philadelphia.

74. David, S.T. and L.L. Augsburger, *Plastic flow during compression of directly compressible fillers and its effect on tablet strength.* Journal of pharmaceutical sciences, 1977. **66**(2): p. 155-159.

75. Kirsch, J.D. and J.K. Drennen, *Nondestructive tablet hardness testing by near-infrared spectroscopy: a new and robust spectral best-fit algorithm.* Journal of pharmaceutical and biomedical analysis, 1999. **19**(3-4): p. 351-362.

76. Luypaert, J., D.L. Massart, and Y. Vander Heyden, *Near-infrared spectroscopy applications in pharmaceutical analysis.* Talanta, 2007. **72**(3): p. 865-883.

77. Lim, H., et al., *Assessment of the critical factors affecting the porosity of roller compacted ribbons and the feasibility of using NIR chemical imaging to evaluate the porosity distribution.* International Journal of Pharmaceutics, 2011. **410**: p. 1-8.

78. Herting, M.G., Kleinebudde, P., *Studies on the reduction of tensile strength of tablets after roll compaction/dry granulation.* European Journal of Pharmaceutics and Biopharmaceutics, 2008. **70**(1): p. 372-379.

79. Donoso, M., D. Kildsig, and E. Ghaly, *Prediction of Tablet Hardness and Porosity Using Near-Infrared Diffuse Reflectance Spectroscopy as a Nondestructive Method.* Pharmaceutical Development & Technology, 2003. **8**(4): p. 357-366.

80. Shen, Y.C., P.F. Taday, and M. Pepper, *Elimination of scattering effects in spectral measurement of granulated materials using terahertz pulsed spectroscopy.* Applied Physics Letters, 2008. **92**(5): p. 051103 1-3.

81. Blanco, M. and M. Alcalá, *Content uniformity and tablet hardness testing of intact pharmaceutical tablets by near infrared spectroscopy: A contribution to process analytical technologies.* Analytica Chimica Acta, 2006. **557**(1–2): p. 353-359.

82. Morisseau, K.M. and C.T. Rhodes, *Pharmaceutical Uses of Near-Infrared Spectroscopy.* Drug Development and Industrial Pharmacy, 1995. **21**(9): p. 1071-1090.

83. Guo, J.-H., et al., *Application of Near-Infrared Spectroscopy in the Pharmaceutical Solid Dosage Form.* Drug Development & Industrial Pharmacy, 1999. **25**(12): p. 1267.

84. Johansson, J., S. Pettersson, and S. Folestad, *Characterization of different laser irradiation methods for quantitative Raman tablet assessment.* Journal of pharmaceutical and biomedical analysis, 2005. **39**(3–4): p. 510-516.

85. Wang, H., C.K. Mann, and T.J. Vickers, *Effect of Powder Properties on the Intensity of Raman Scattering by Crystalline Solids.* Appl. Spectrosc., 2002. **56**(12): p. 1538-1544.

86. Moore, M.D., STeinbach, A.M., Buckner, I.S., WIldfrog, P.L.D., *A structural Investigation into the Compaction Behaviour of Pharamaceutical Composites Using Powder-X-Ray Diffreaction andd Total Scattering Analysis.* Pharmaceutical Research, 2009. **26**(11): p. 2429-2437.

87. Sinka, I.C., et al., *Measurement of density variations in tablets using X-ray computed tomography.* International Journal of Pharmaceutics, 2004. **271**(1-2): p. 215-224.

88. Cairns, D., *Essentials of Pharmaceutical Chemistry*. 3 ed, ed. D. Cairns. 2008, London: Pharmaceutical Press.

89. Wallace, V.P., et al., *Terahertz pulsed imaging of basal cell carcinoma ex vivo and in vivo.* British Journal of Dermatology, 2004. **151**(2): p. 424-432.

90. Han, P.Y., G.C. Cho, and X.C. Zhang, *Time-domain transillumination of biological tissues with terahertz pulses.* Optics Letters, 2000. **25**(4): p. 242-244.

91. Taday, P.F., et al., *Using terahertz pulse spectroscopy to study the crystalline structure of a drug: A case study of the polymorphs of ranitidine hydrochloride.* Journal of pharmaceutical sciences, 2003. **92**(4): p. 831-838.

92. Taday, P.F., *Applications of terahertz spectroscopy to pharmaceutical sciences.* Phil. trans. R. Soc. Lond. A. , 2004. **362**: p. 351-364.

93. Zeitler, J.A., Shen, Y., Baker, C., Taday, P.F., Pepper, M., Rades, T., *Analysis of coating structures and interfaces in solid oral dosage forms by three dimensional terahertz pulsed imaging.* Journal of Pharmaceutical Sciences, 2007. **96**(2): p. 330-340.

94. Kang, B., et al., *Polarization angle control of coherent coupling in metamaterial superlattice for closed mode excitation.* Opt. Express, 2010. **18**(11): p. 11552-62.

95. Cheville, R.A., ed. *Terahertz Time-Domain Spectroscopy with Photoconductive Antennas*. Terahertz Spectroscopy: Principles and applications, ed. S.L. Dexheimer. 2008, CRC Press: London. 1-41.

96. Dexheimer, S.L., *Terahertz Spectroscopy: Principles and Applications*. 2007: CRC Press.

97. El Haddad, J., et al., *Review in terahertz spectral analysis.* TrAC Trends in Analytical Chemistry, 2013. **44**(0): p. 98-105.

98. Cheville, R.A., Grischkowsky, D., *Far-infrared terahertz time-domain spectroscopy of flames.* Optics Letters, 1995. **20**(15): p. 1646-1648.

99. Shen, Y.-C., *Terahertz pulsed spectroscopy and imaging for pharmaceutical applications: A review.* International Journal of Pharmaceutics, 2011. **417**(1–2): p. 48-60.

100. Wu, H., et al., *Process analytical technology (PAT): Effects of instrumental and compositional variables on terahertz spectral data quality to characterize pharmaceutical materials and tablets.* International Journal of Pharmaceutics, 2007. **343**(1-2): p. 148-158.

101. Kono, S., et al., *Detection of up to 20 THz with a low-temperature-grown GaAs photoconductive antenna gated with 15 fs light pulses.* Applied Physics Letters, 2000. **77**: p. 4104-4106.

102. Hecht, E., *Optics*. 3 ed. 1998, Harrow: Addison-Wesley.

103. Chan, W.L., J. Deibel, and D.M. Mittlemann, *Imaging with terahertz radiation* Reports on Progress in Physics, 2007. **70**: p. 1325-1379.

104. Lee, K., et al., *Polarization shaping of few-cycle terahertz waves.* Optical Society of America, 2012. **20**(11): p. 12463-12472.

105. Naftaly, M. and R.E. Miles, *Terahertz Time-Domain Spectroscopy for Material Characterization.* Proceedings of the IEEE, 2007. **95**(8): p. 1658-1665.

106. Naftaly, M. and R.E. Miles, *Terahertz time-domain spectroscopy of silicate glasses and the relationship to material properties.* Journal of Applied Physics, 2007. **102**: p. 043517.

107. Wu, H. and M. Khan, *THz spectroscopy: An emerging technology for pharmaceutical development and pharmaceutical Process Analytical Technology (PAT) applications.* Journal of Molecular Structure, 2012. **1020**(0): p. 112-120.

108. Zeitler, J.A., Kogermann, K., Rantanen, J., Rades, T., Taday, P.F., Pepper, M., Aaltonen, J., Strachan C.J., *Drug hydrate systems and dehydration processes studied by terahertz pulsed spectroscopy.* International Journal of Pharmaceutics, 2007. **334**: p. 78-84.

109. Cogdill, R.P., Forcht, R.N., Shen, Y., Taday, P.F., Creekmore, J.R., Anderson, C.A., Drennen, J.K., *Comparison of terahertz pulse imagining and near-infrared*

spectroscopy for rapid, non-destructive analysis of tablet coating thickness and uniformity. Journal of Pharmaceutical Innovation, 2007. **2**: p. 29-36.

110. Fitzgerald, A.J., Cole, B.E., Taday, P.F., *Nondestructive analysis of tablet coating thicknesses using terahertz pulsed imaging.* Journal of Pharmaceutical Sciences, 2005. **94**(1): p. 177-183.

111. Umarunisha, A.M., et al., *Design and Evaluation of Famotidine Controlled Release Tablets.* International Journal of Pharmaceutical Sciences, 2010. **2**(2): p. 574-582.

112. Akseli, I., et al., *A quantitative correlation of the effect of density distributions in roller-compacted ribbons on the mechanical properties of tablets using ultrasonics and X-ray tomography.* American Association of Pharmaceutical Scientists, 2011. **12**(3): p. 834-853.

113. Spencer, J.A., Gao, Z., Moore, T., Bushe, L.F., Taday, P.F., Newnham, D.A., Shen, Y., Portieri, A., Husain, A., *Delayed release tablet dissolution related to coating thickness by terahertz pulsed image mapping.* Journal of Pharmaceutical Sciences, 2008. **97**(4): p. 1543-1550.

114. Ho, L., Müller, R., Gordon, K.C., Kleinebudde, P., Pepper, M., Rades, T., Shen, Y., Taday, P.F., Zeitler J.A., *Applications of terahertz pulsed imaging to sustained-release tablet film coating quality assessment and dissolution performance.* Journal of Controlled Release, 2008. **127**: p. 79-87.

115. Schmuttenmaer, C.A., *Exploring Dynamics in the Far-Infrared with Terahertz Spectroscopy.* Chemical Review, 2004. **104**: p. 1759-1779.

116. Cao, X., et al., *Estimating the refractive index of pharmaceutical solids using predictive methods.* International Journal of Pharmaceutics, 2009. **368**(1-2): p. 16-23.

117. Watanabe, A., Y. Yamaoka, and K. Kuroda, *Study of crystalline drugs by means of polarizing microscope. III. Key refractive indices of some crystalline drugs and their measurement using an improved immersion method.* Chem Pharm Bull, 1980. **28**(2): p. 372-8.

118. Piñeiro, A., et al., *Prediction of excess volumes and excess surface tensions from experimental refractive indices.* Physics and Chemistry of Liquids, 2000. **38**(2): p. 251-260.

119. Lawson, D.D. and J.D. Ingham, *Estimation of solubility parameters from refractive index data [14].* Nature, 1969. **223**(5206): p. 614-615.

120. Bartels, A., et al., *High-resolution THz spectrometer with kHz scan rates.* Optics express, 2006. **14**: p. 430-437.

121. Jin, Y.-S., G.-J. Kim, and S.-G. Jeon, *Terahertz Dielectric Properties of Polymers.* Journal of Korean Physical Society, 2006. **49**(2): p. 513-517.

122. Yasui, T., et al., *Terahertz paintmeter for noncontact monitoring of thickness and drying progress in paint film.* Applied Optics, 2005. **44**: p. 6849-6856.

123. Scheller, M. and M. Koch, *Fast and Accurate Thickness Determination of Unknown Materials using Terahertz Time Domain Spectroscopy.* Journal of Infrared, Millimetre and Terahertz Waves, 2009. **30**(7): p. 762-769.

124. Pupeza, I., R. Wilk, and M. Koch, *Highly accurate optical material parameter determination with THz time-domain spectroscopy*. Opt. Express, 2007. **15**(7): p. 4335-4350.

125. Withayachumnankul, W., Fischer, B.M., and Abbott, D., *Material thickness optimization for transmission-mode terahertz time-domain spectroscopy.* Optics Express, 2008. **16**(10): p. 7382-7396.

126. Ho, L., Müller, R., Gordon, K.C., Kleinebudde, P., Pepper, M., Rades, T., Shen, Y., Taday, P.F., Zeitler J.A., *Terahertz pulsed imaging as an analytical tool for sustained-release tablet film coating.* European Journal of Pharmaceutics and Biopharmaceutics, 2009. **71**(117-123).

127. Ho, L., Cuppok, Y., Muschert, S., Gordon, K.C., Pepper, M., Shen, Y., Siepmann, F., Siepmannd, J., Taday, P.F., Rades, T., *Effects of film coating thickness and drug layer uniformity on in vitro drug release from sustained-release coated pellets: A case study using terahertz pulsed imaging.* International Journal of Pharmaceutics, 2009.

128. Maurera, L., Leuenberger, H., *Terahertz pulsed imaging and near infrared imaging to monitor the coating process of pharmaceutical tablets.* International Journal of Pharmaceutics, 2009. **370**: p. 8-16.

129. Haaser, M., et al., *Terahertz Pulsed Imaging as a PAT Tool for Evaluating the Effect of Coating Methods and Application of Stress Conditions on Applied Film Quality*, in *The Electronic Conference on Pharmaceutical Sciences ECPS2011*, M. AG, Editor. 2011: Basel, Switzerland.

130. Gendre, C., et al., *Development of a Process Analytical Technology (PAT) for in-line monitoring of film thickness and mass of coating materials during a pan coating operation.* European Journal of Pharmaceutical Sciences, 2011. **43**(4): p. 244-250.

131. Malaterre, V., Pedersen, M., Ogorka, J., Gurny, R., Loggia, N., Taday, P.F., *Terahertz pulsed imaging, a novel process analytical tool to investigate the coating characteristics of push–pull osmotic systems.* European Journal of Pharmaceutics and Biopharmaceutics, 2009.

132. TeraView *Using Terahertz Pulsed Imaging as a Process Analytical Technology (PAT) for Online Monitoring of Tablet Coating*. Application note, 2012.

133. Müller, J., et al., *Prediction of dissolution time and coating thickness of sustained release formulations using Raman spectroscopy and terahertz pulsed imaging.* European journal of pharmaceutics and biopharmaceutics, 2012. **80**(3): p. 690-697.

134. Palermo, R., Cogdill, R.P., Short, S.M., Drennen III, J.K., Taday, P.F., *Density mapping and chemical component calibration development of four-component compacts via terahertz pulsed imaging.* Journal of pharmaceutical and biomedical analysis, 2008. **46**(1): p. 36-44.

135. Haaser, M., et al., *Terahertz pulsed imaging as an advanced characterisation tool for film coatings–a review.* International Journal of Pharmaceutics, (0).

136. Wagh, M.P., Sonawane, Y.H., Joshi, O.U., *Terahertz technology: A boon to tablet analysis.* Indian Journal of Pharmaceutical Sciences, 2009. **71**(3): p. 235-241.

137. Naftaly, M. and R.E. Miles, *Terahertz time-domain spectroscopy: A new tool for the study of glasses in the far infrared.* Journal of Non-Crystalline Solids, 2005. **351**(40–42): p. 3341-3346.

138. Rehouma, F. and K. Aiadi, *Glasses for ion-exchange technology.* Int. J. Commun, 2008. **1**(6): p. 148-155.

139. Pupeza, I., Wilk, R., and Koch, M., *Highly accurate optical material parameter determination with THz time-domain spectroscopy.* Optics Express, 2007. **15**(7): p. 4335-4350.

140. Guy, A., *Cellulose, Microcrystalline*, in *Handbook of Pharmaceutical Excipients: 6th edition*, R.C. Rowe, P.J. Sheskey, and M.E. Quinn, Editors. 2009, Pharmaceutical Press: London.

141. Alderborn, G., *Tablets and compaction*, in *Aulton's Pharaceutics: The Design and Manufacture of Medicines*, M.E. Aulton, Editor. 2007, Churchill Livingstone: London. p. 441-482.

142. Fell, J.T. and J.M. Newton, *Determination of tablet strength by the diametrical-compression test. J Pharm Sci, 59, 688–91.* Journal of Pharmaceutical Sciences, 1970. **59**: p. 688-691.

143. Busignies, V., et al., *Quantitative measurements of localized density variations in cylindrical tablets using X-ray microtomography.* European journal of pharmaceutics and biopharmaceutics, 2006. **64**(1): p. 38-50.

144. Miguélez-Morán, A.M., et al., *Characterisation of density distributions in roller-compacted ribbons using micro-indentation and X-ray micro-computed tomography.* European journal of pharmaceutics and biopharmaceutics, 2009. **72**(1): p. 173-182.

145. Zinchuk, A.V., Mullarney, M.P., Hancock, B.C., *Simulation of roller compaction using a laboratory scale compaction simulator.* International Journal of Pharmaceutics, 2004. **269**: p. 403-415.

146. Hoag, S.W., V.S. Dave, and V. Moolchandani, *Compression and Compaction*, in *Pharmaceutical Dosage Forms: Tablets*, L.L. Augsburger and S.W. Hoag, Editors. 2008, Informa Healthcare USA, Inc.: New York. p. 555-619.

147. Zinchuk, A.V., M.P. Mullarney, and B.C. Hancock, *Simulation of roller compaction using a laboratory scale compaction simulator.* International Journal of Pharmaceutics, 2004. **269**(2): p. 403-415.

148. Abdel-Hamid, S. and G. Betz, *Study of radial die-wall pressure changes during compaction.* Drug Development & Industrial Pharmacy, 2011. **37**(4): p. 387-395.

149. Sun, C., *True density of microcrystalline cellulose.* Journal of pharmaceutical Science, 2005. **94**(10): p. 2132-2134.

150. Strachan, C.J., Taday, P.F., Newnham, D.A., Gordon, K.C., Zeitler, J.A., Pepper, M., Rades, T., *Using terahertz pulsed spectroscopy to quantify pharmaceutical polymorphism and crystallinity.* Journal of Pharmaceutical Sciences, 2005. **94**(4): p. 837-846.

151. Hervieu, P. and F. Dehont, *Granulation of pharmaceutical powders by compaction. An experimental study.* Drug Development and Industrial Pharmacy, 1994. **20**(1): p. 65-74.

152. Bultmann, J.M., *Multiple compaction of microcrystalline cellulose in a roller compactor.* European Journal of Pharmaceutics and Biopharmaceutics, 2002. **54**(1): p. 59-64.

153. Korter, T.M., et al., *Terahertz spectroscopy of solid serine and cysteine.* Chemical Physics Letters, 2006. **418**(1–3): p. 65-70.

154. Castro-Camus, E., *Polarisation-resolved terahertz time-domain spectroscopy*. Journal of Infrared, Millimeter, and Terahertz Waves, 2012. **33**(418): p. 418-425.

155. Fisika, *Oblique Incidence*, in *EM Waves and Antennas*.

156. Chiou, C.-P., et al., *SIGNAL MODELING IN THE FAR-INFRARED REGION FOR NONDESTRUCTIVE EVALUATION APPLICATIONS.* AIP Conference Proceedings, 2011. **1335**(1): p. 581-588.

157. Kaur, G., D.B. Sridhar, and M. Gera, *Optimization of Roll Compaction/Dry Granulation Process for Poorly Flowable Antiviral Formulation.* American Journal of PharmTech Research, 2012. **2**(4): p. 544-557.